UNIVERSITY OF LJUBLJANA

FACULTY OF MATHEMATICS AND PHYSICS,
DEPT. OF ASTROPHYSICS

PHOEBE Scientific Reference

PHOEBE version 0.30

Andrej Prša
andrej.prsa@fmf.uni-lj.si

January 2006

Abstract

Eclipsing binary stars are among most attractive objects in stellar astrophysics. Their particular geometrical layout and well known governing laws of dynamics and radiative physics enable a detailed and accurate modeling and analysis of the acquired observational data. Accuracy is crucial, because the results obtained from the model are used by the community to obtain reliable calibrations, tests on evolutionary sequences and distance estimates. The book thorougly reviews the modeling principles of the Wilson-Devinney code. On these foundations several physical, numerical and technical advancements that have never before been used in modeling eclipsing binaries are introduced. These include obtaining individual temperatures objectively by means of color-constraining, imposing sets of conditional constraints to the model, rigorous treatment of interstellar extinction, using spectra as a native data source, powerful heuristical minimization algorithms, a flexible scripting facility, an intuitive graphical user interface. We demonstrate most important novel features on a synthetically created test star as well as on several real, astrophysically challenging binaries.

Keywords: methods: data analysis — methods: numerical — binaries: eclipsing — stars: fundamental parameters — stars: individual: BF Aurigae, UV Leonis, GK Draconis, V945 Centauri

PACS: 97.80Hn

Contents

1 Preface **1**

2 Introduction to the Field **3**

2.1 Why binaries are important 3

2.2 Why eclipsing binaries are even more important 4

2.3 Observations and data acquisition 5

2.3.1 Photometry 5

2.3.2 Spectroscopy 8

2.3.3 Radial velocities 12

2.3.4 Doppler tomography 13

2.3.5 Astrometry 14

2.3.6 Polarimetry 17

3 System geometry **19**

3.1 The Roche model 19

3.2 Shapes and sizes of stars in a binary system 24

3.3 Morphological classification of close binaries 25

3.4 Orbital properties of close binaries 28

3.5 Dynamical aspects of binary systems 32

3.5.1 The Kepler problem 32

3.5.2 Solving the Kepler problem for binary stars 34

3.6 Eclipses 37

3.7 Measuring time: heliocentric Julian date 40

3.8 Ephemeris parameters and phase plots 41

4 Radiative properties of binary stars 45

4.1 Emergent intensity 47

4.2 Kurucz's model atmospheres 51

4.3 Gravity darkening 53

4.4 Limb darkening 55

4.5 Reflection effect 58

4.6 Ellipsoidal variations 61

4.7 Stellar spots 63

5 The model of an eclipsing binary 65

5.1 The point-sampling strategy 67

5.2 Computation of local geometrical quantities 68

5.3 Computation of local radiative quantities 74

5.4 Computation of aspect-dependent quantities 81

6 Approaches to solving the inverse problem 85

6.1 Local and global minima in hyperspace valleys 85

6.2 Differential Corrections 87

6.2.1 Method of Multiple Subsets 88

6.2.2 Levenberg-Marquardt algorithm 89

6.3 Powell's Direction Set method 90

6.4 Nelder and Mead's downhill Simplex 91
6.5 Adaptive Simulated Annealing 93
6.6 Formal errors of the fit 94
6.7 Handling degeneracies efficiently 96
6.7.1 Heuristic Scanning 98
6.7.2 Parameter kicking 100
6.7.3 What happens to those oblivious of degeneracy? 101

7 PHOEBE - PHysics Of Eclipsing BinariEs 105

7.1 What is it all about? 105
7.2 What is different? 106
7.2.1 Building a synthetic binary 107
7.2.2 Color-indices and effective temperatures 107
7.2.3 Spectra as independent data source 116
7.2.4 Main sequence constraints 118
7.2.5 Interstellar and atmospheric extinction 121
7.2.6 Suggested optimizations to WD solving method 126

8 Using PHOEBE on real data 131

8.1 BF Aurigae: a near-contact textbook binary 131
8.2 UV Leonis: a spotted star 135
8.3 GK Draconis: an intrinsically variable component 139
8.4 V945 Centauri: an ellipsoidal binary 144

9 Prospects for the future **149**

9.1 In situ stellar atmospheres 149

9.2 More minimization algorithms 150

9.2.1 Principal component analysis 150

9.3 Planetary transits 151

9.4 Automated analysis of large data-sets 154

9.4.1 Gaia 155

9.5 Get people to join in 158

10 Wrapping it up **159**

A Mathematical symbols used in the book **171**

1 Preface

Science in general differs little, if at all, from the game of puzzles. The grand picture being built of small building blocks is an analogy that goes beyond simple words: the tedious job of seeking the right piece, the cleverness of fitting it in, the attention of recognizing and removing a displaced piece and the sense of accomplishment once that piece is settled in are exactly what science is all about. The edges of the picture have been laid out by brilliant scientists in the past and it is up to us to choose and concentrate on a small area of the overall picture which we want to build. Having someone that has experience in putting the puzzles together advises you to be attentive of the shapes and colors of the pieces. Joining forces with others not only makes the picture grow faster, it also enables you to share experience and have more fun. Persistence is the only aid when it seems that a piece is lost, and patience when many pieces seem to fit a given tile. Yet settling the right piece is such a fulfilling experience that it outweights all the trouble of finding it, enabling you and others to search and attach all subsequent pieces to the puzzle. That is science.

§

This work differs in form and content from conventional scientific reference books: instead of concentrating only on particularities of our acomplished work, we attempt to present a consistent picture of the whole field of modeling eclipsing binary stars. We do not go into all the details that would be typical for a textbook, yet we do not omit common definitions and the description of the analytical formalism either. There are several reasons for this: the manuscript is conceived to become a solid scientific reference for a wider astronomical community, as a bridge between obscure and undocumented concepts upon which the modeling code is built and the results yielded by the code. Any omissions from the manuscript would result in a partial picture with possible mis-interpretations and erroneous conclusions. Furthermore, there are no textbooks currently available that would cover the modeling aspects with due vigilance and rigor which are absolutely crucial for a self-consistent overall picture.

2 Introduction to the Field

Contrary to the popular belief, binary star systems are as common as single stars in the Universe. A review paper by Abt (1983) and subsequent studies by Latham et al. (1992), Pinfield et al. (2003) and many others have established that at least 50% of all stellar systems are binary or multiple. This fact alone makes binaries appealing and worthy of studying and research.

2.1 Why binaries are important

Binary stars prove to be ideal testbeds for a number of astrophysical studies. Since they represent a significant portion of the celestial fauna, they are found throughout our galaxy, in open and globular clusters, in the halo, and in other galaxies. There have been numerous studies based on binary stars, the new ones are emerging constantly. We outline below some general properties of binary stars along with prominent references that are crucial to the Field.

- The only practical way to obtain stellar masses of individual stars without external calibration (i.e. color-magnitude diagrams or mass-luminosity relations) is from binary systems. See e.g. Martin et al. (1998) for an assembled catalog of stellar masses of astrometric binaries.

- Stellar evolution warrants the exact coevality (equal age) of both binary system components. This is of particular importance for detached binaries, because the lives of both components are asserted to be decoupled, enabling us to study the dependence of evolutionary stages on stellar mass and luminosity. It is also important for close binaries, where the interaction influence (presence of mass transfer, circumstellar clouds) on evolution isochrones may be studied. See e.g. Tohline (2002) for a review of theoretical models of binary system genesis.

- Depending on the morphological type of the binary, stellar shapes may further determine the values of physical parameters via tidal interaction, see e.g. Giménez et al. (1998).

- Binarity is not reserved for "ordinary" stars; all kinds of stellar, substellar, variable and peculiar components may appear and thus be thoroughly studied, which might otherwise not be possible at all. See e.g. Verbunt (1993) for review of X-Ray binaries, Mathieu (1994) for pre-main-sequence binaries, Taam and Sandquist (2000) for massive

binaries with common envelopes, Pinfield et al. (2005) for binarity in brown dwarf systems etc.

- Binary stars are ideal distance estimators, since absolute magnitudes of the components may be readily obtained from their luminosities. See e.g. Munari et al. (2004b) as an example of determining the distance to the Pleiades and Ribas et al. (2004) for the distance to M31 using binary stars; Guinan et al. (2004) demonstrates how to calibrate the cosmic distance scale to the local group using binaries.

2.2 Why eclipsing binaries are even more important

Because of their geometrical layout, eclipsing binaries exhibit specific features in observational data that are easily recognized: since the part of the light is blocked as one component passes in front of the other, the observed flux is diminished. Such a time-dependent change in flux enables us to further constrain physical parameters of a binary system: all binary-nature features pertain to eclipsing binaries, with eclipses as a bonus. Eclipses can, in principle, be used to obtain the following information:

- in addition to stellar masses, eclipsing binaries directly yield stellar radii – other methods such as interferometry or stellar occultation are much less practical because of their sensitivity to distance and unique point in time, respectively;
- shape of the eclipses indicates the inclination;
- duration of the eclipses and their relative position indicates orbital eccentricity and the sum of the radii of both components in units of their separation;
- ratio of depths of the two eclipses indicates the degree of surface coverage and the relation between individual surface temperatures of both components;
- ratio of in-and-out-of eclipse levels in different passbands indicates the amount of interstellar extinction;
- timing of eclipses indicates the ephemeris (orbital period and, if significant, a period change rate);
- secular features during eclipses reveal surface brightness variations (gravity darkening, limb darkening, reflection, spots, circumstellar matter).

These points hold only in principle and may not always yield the attributed information, depending on morphology and individual properties of the given eclipsing binary type. We will discuss them in detail in the following Sections.

2.3 Observations and data acquisition

To be able to extract a complete set of physical parameters, one needs diverse and accurate observational data. Diversity is crucial because different physical parameters are more sensitive to different data types. This section overviews most common data acquisition techniques used for observing eclipsing binaries.

2.3.1 Photometry

The most popular and accessible data acquisition method in astronomy is undoubtedly photometry. The principal instrument for acquiring photometric observations is a photoelectric photomultiplier; recently the CCDs are taking over because of their wide spectral response and large fields that enable observers to take measurements of many stars simultaneously.

Photometric measurements consist of acquiring a flux on a given passband in a given exposure time. Such instrumental flux is only a part of the total (bolometric) flux that reaches our atmosphere: it depends on the passband transmission curve, the CCD response curve (dependence of quantum efficiency on the wavelength), the telescope optics response curve (dependence of reflection on the wavelength) and the sky transmission and quality (air-mass, seeing, cloudiness, ...):

$$J_\lambda^{\text{instrumental}} = \mathcal{T}_\lambda^{\text{passband}}\, R_\lambda^{\text{ccd}}\, R_\lambda^{\text{optics}}\, X_\lambda^{\text{atmosphere}}\, J_\lambda^{\text{bolometric}}. \tag{2.1}$$

Variations of the atmosphere $X_\lambda^{\text{atmosphere}}$ may be corrected by monitoring the flux variation of comparison stars that are present in the field. The remaining factors depend on the optical layout of the instrumental system and are calibrated using standard stars in the field during data reduction. The ultimate goal is to transform this instrumental flux (or more commonly the magnitude) onto a standard photometric system, i.e. Johnson (1965), Cousins (1976), Bessell (1990) or similar. Fig. 1 depicts transmission curves of the Bessell (1990) UBVRI series (left) and CCD response curve of the University of Ljubljana's 70 cm telescope Vega (right).

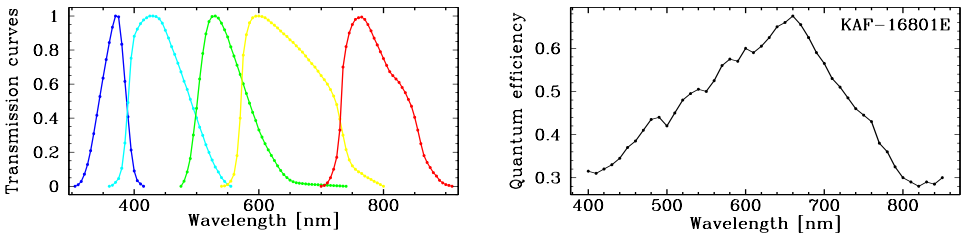

Figure 1: Filter and CCD response curves. Left: transmission curves for the Bessell (1990) UBVRI filter-set. Right: quantum efficiency of Kodak's KAF-16801E CCD chip mounted on 70cm telescope Vega at University of Ljubljana's observatory Golovec. Taken from Eastman Kodak Company (2000) report.

Consecutive photometric measurements given as a function of time (usually heliocentric Julian date, HJD) constitute a **photometric light curve**. Inspecting light curves reveals variability of the source, be it intrinsic or aspect-dependent. If a variability is periodic, it is customary to fold the observational data to the phase interval $[0, 1]$:

$$\Phi = \mathrm{mod}\left[\frac{\mathrm{HJD} - \mathrm{HJD}_0}{P_0}\right], \tag{2.2}$$

where HJD_0 is a reference point in time (usually set to heliocentric Julian date of the primary minimum) and P_0 is the orbital period of the binary. Such a transformation constitutes a **phased light curve**. It is sometimes preferable to use the interval $[-0.5, 0.5]$ for phased data, to center the primary minimum that occurs near $\Phi = 0$. Fig. 2 shows an example of photometric and phased light curves for an eclipsing binary AW Virginis; the data were adopted from Lapasset et al. (1996).

Photometric accuracy is represented in terms of the signal-to-noise ratio: the power ratio between a signal (meaningful information) and the background noise:

$$\mathrm{S/N} = \frac{P_{\mathrm{signal}}}{P_{\mathrm{noise}}}. \tag{2.3}$$

The amount of photometric noise present in the signal depends on the photon regime of the observations:

Seeing-limited regime is inherent to bright sources, where the atmospheric scintillation is the dominant source of error. The noise scales *linearly* with the light level.

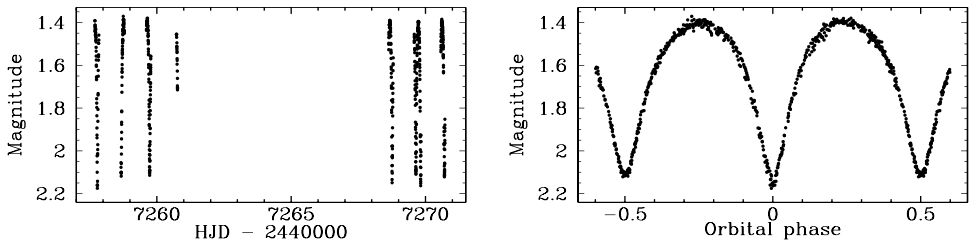

Figure 2: Photometric data of the eclipsing binary AW Virginis (taken from Lapasset et al., 1996). Left: timed photometric light curve connects observed magnitudes with times of observation. Right: phased photometric curve connects observed magnitudes with phase. The data are folded to the $[-0.5, 0.5]$ interval and aliased to $[-0.6, 0.6]$ interval for better visibility of the secondary minimum. Note that in both cases the magnitude axis is inverted.

Shot-limited regime is inherent to the sources from which enough photons are acquired that Poissonian scattering dominates. The noise scales with the *square root* of the light level.

Sky-limited regime is inherent to faint sources, where background fluctuations are of the same order of magnitude as the signal. The noise scales *linearly* with the light level.

Most photometrically attractive objects (not too bright, not too dark) fall into the shot-limited regime, which makes photometry one of the most accurate data acquisition methods in astronomy.

Fluxes are transformed to magnitudes using the usual relation:

$$m - m_0 = -\frac{5}{2} \log \left(\frac{J}{J_0} \right), \tag{2.4}$$

where m_0 is the magnitude zero-point that corresponds to the flux J_0. It is important to realize that the errors in measured flux do not symetrically transform to errors in magnitudes. Standard flux error $\pm 1\sigma_J$ deviates may be written as:

$$J^{\pm} = J \pm \sigma_J = J \left(1 \pm \frac{1}{\mathrm{S/N}} \right), \tag{2.5}$$

where J is the individual measured flux data point. Dividing $J^{\pm}$ with J yields:

$$\frac{J^{\pm}}{J} = 1 \pm \frac{1}{\mathrm{S/N}} = 1 \pm \frac{\sigma_J}{J}, \tag{2.6}$$

which may be readily transformed to a stanard magnitude error using Eq. (2.4):

$$\sigma_m^{\pm} = -\frac{5}{2}\log\left(1 \pm \frac{1}{\mathrm{S/N}}\right) = -\frac{5}{2}\log\left(1 \pm \frac{\sigma_J}{J}\right). \tag{2.7}$$

These two values, σ_m^+ and σ_m^-, are not equal, the former's absolute value always being larger than the latter's. For practical purposes, an average is usually taken as reference standard magnitude error:

$$\sigma_m = \frac{1}{2}(\sigma_m^- - \sigma_m^+), \tag{2.8}$$

where the difference in signedness comes from the fact that σ_m^+ is always negative.

2.3.2 Spectroscopy

Spectroscopic measurements are based on dispersing the beam of light into the wavelength-distributed spectrum. The resolution of the spectrum is defined as:

$$R = \frac{\lambda}{\Delta\lambda}, \tag{2.9}$$

where $\Delta\lambda$ is the width of the smallest discernible unit of wavelength around λ. Resolved features thus directly depend on the resolving power of the spectrograph: for $R \sim 500$ (low-resolution spectroscopy) only continuum features are typically discerned; for $R \sim 5000$ (medium-resolution spectroscopy), equivalent widths of strong spectral lines may be studied; for $R \gtrsim 20000$ or more (high-resolution spectroscopy), narrow spectral lines may also be studied and, with increasing resolution, finer features such as line-broadening may be observed. Modern echelle spectrographs typically reach well over $R \sim 20\,000$. Fig. 3 shows a part of the reduced (wavelength-calibrated, flux-normalized) echelle spectrum near H_α of the eclipsing binary UV Leonis. The spectrum was acquired using 1.82m telescope on Mt. Ekar, Asiago.

There are four principal physical parameters that may be obtained from spectra directly by cross-correlation techniques against synthetic spectra:

Effective temperature T_{eff} of the source is the dominant parameter revealed both by the shape and position of the peak of the spectral energy distribution (SED) and by the presence and strength of spectral lines.

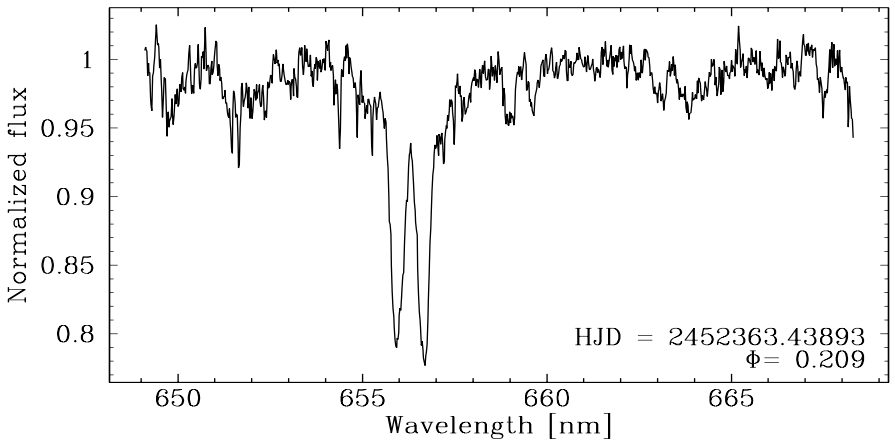

Figure 3: A part of the echelle spectrum of the eclipsing binary UV Leonis. The Doppler-splitting of H_α is clearly visible. The spectrum was acquired with echelle spectrograph mounted on 1.82m telescope at Mt. Ekar, Asiago and reduced by `IRAF` (Tody, 1986).

Surface gravity $\log g/g_0$ of the source indicates the size of the star and is revealed by the shapes of spectral lines. Note that surface gravity is usually denoted simply with $\log g$, where g is given in cgs units, yet this work, along with all of our other published work, tries to establish a rectified convention where $g_0 = 1\,\mathrm{cm/s^2}$ is introduced so that the logarithm acts on a dimensionless variable.

Metallicity [M/H] of the source indicates the abundance of heavy elements compared logarithmically to Solar abundances; it is revealed by the presence and strength of metallic spectral lines. Metallicity [M/H]$= 0$ corresponds to solar abundances, [M/H]$= -1.0$ means 10 times more metal-poor and [M/H]$= 1.0$ means 10 times more metal-rich. Symbol M in [M/H] stands for all elements heavier than Helium; sometimes other abundances are published, i.e. [Fe/H] for iron, [α/H] for α-particle capturing elements etc.

Rotational velocity v_{rot} of the source is revealed by the amount of Doppler broadening of spectral lines. The actually measured quantity is *radial* rotational velocity $v_{\mathrm{rot}} \sin i$.

Astronomers often use spectral types instead of effective temperatures: spectral type O corresponds to the hottest blue stars ($T_{\mathrm{eff}} \sim 50000$K), following in decreasing temperature are B ($T_{\mathrm{eff}} \sim 20000$K), A ($T_{\mathrm{eff}} \sim 8500$K), F ($T_{\mathrm{eff}} \sim 6600$K), G ($T_{\mathrm{eff}} \sim 5700$K), K ($T_{\mathrm{eff}} \sim 4600$K); finally, M corresponds

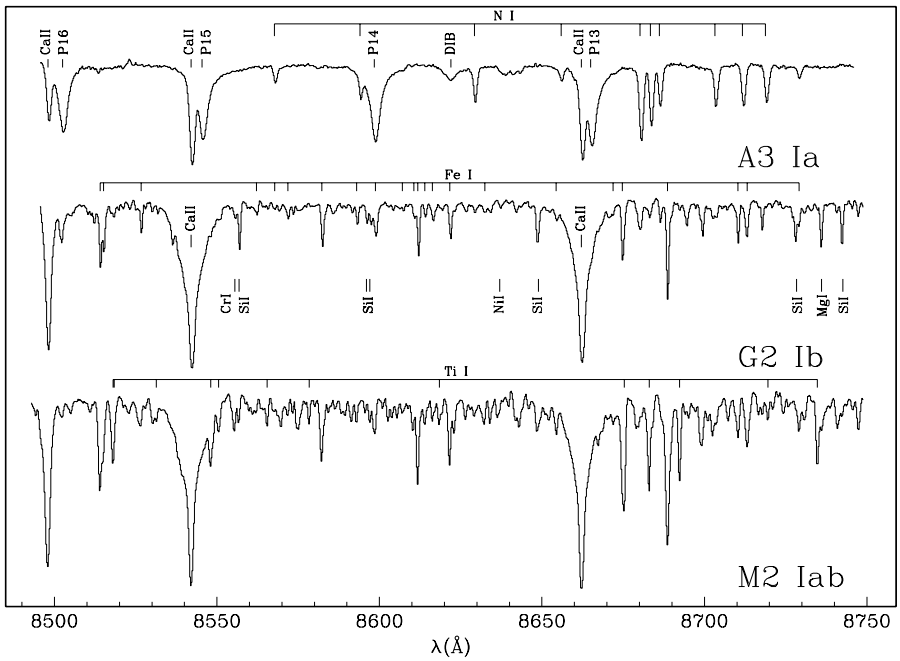

Figure 4: Temperature influence on stellar spectra. Adopted from Munari and Tomasella (1999).

to the coolest red stars ($T_{\rm eff} \sim 3200$K). This spectral taxonomy is due to Pickering and Fleming (1895). Closely related to spectral classification are luminosity classes that are used instead of $\log g/g_0$: type V corresponds to main-sequence (dwarf) stars (and thus largest $\log g/g_0$), IV to sub-giants, III to normal giants, II to bright giants and I to super-giants (and thus smallest $\log g/g_0$). This classification is due to Morgan et al. (1943).

Figs. 4-7 depict the influence of the four mentioned parameters on true stellar spectra.

Given that the observations are acquired with high resolving power ($R \sim 20\,000$ or more), there's much more to be revealed from spectra than just those 4 parameters. From measuring the changes of spectral line positions in time (or phase), one can obtain radial velocity of the source. From measuring the changes in spectral line shapes in time (or phase), one can do Doppler tomography of the source. Since these two approaches are crucial to analysis and modeling of eclipsing binaries, they are presented here separately.

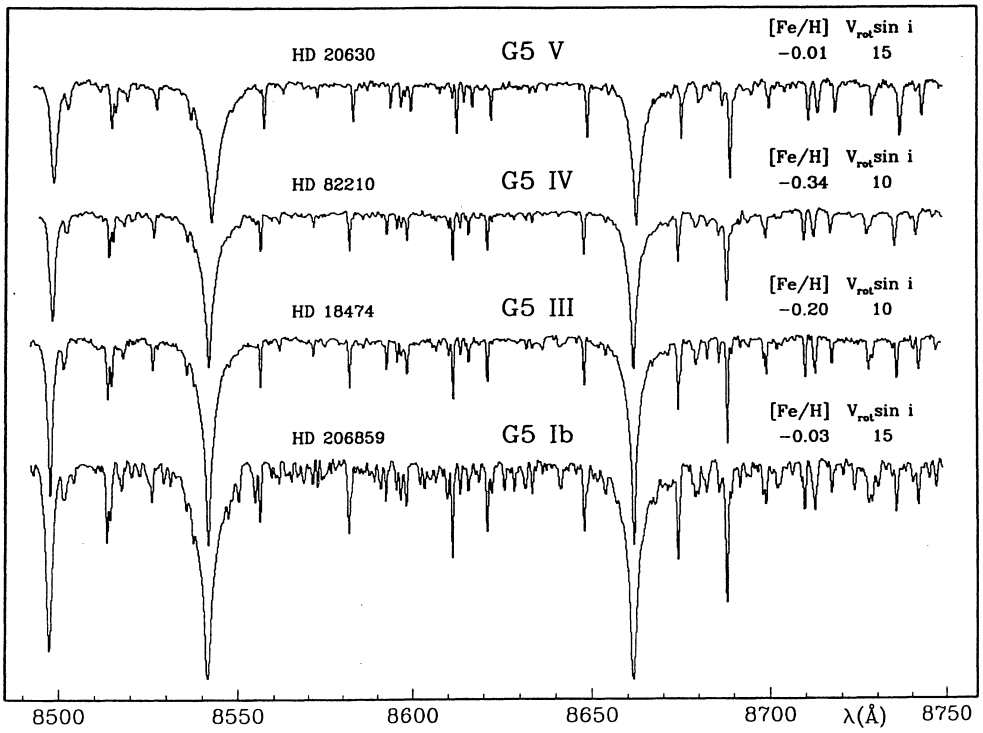

Figure 5: Gravity ($\log g/g_0$) influence on stellar spectra. Adopted from Marrese et al. (2003).

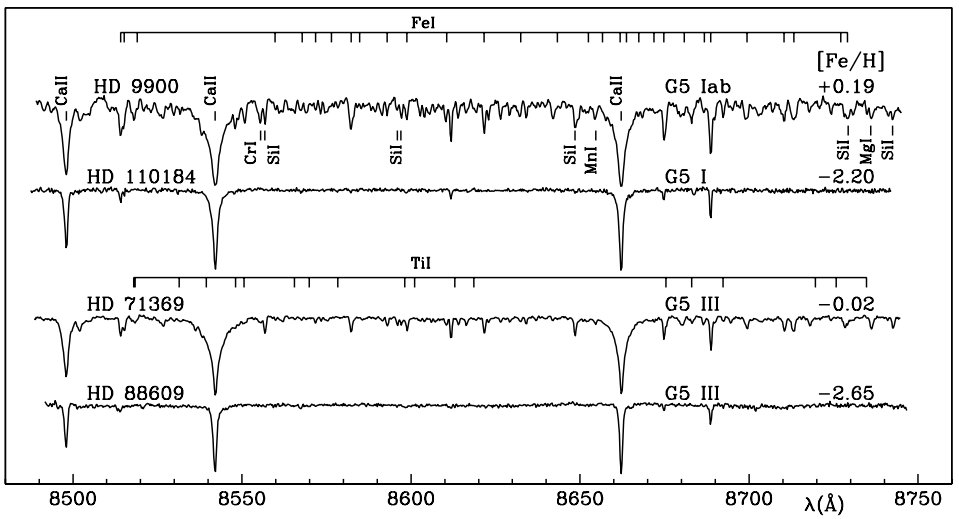

Figure 6: Metallicity influence on stellar spectra. Adopted from Marrese et al. (2003).

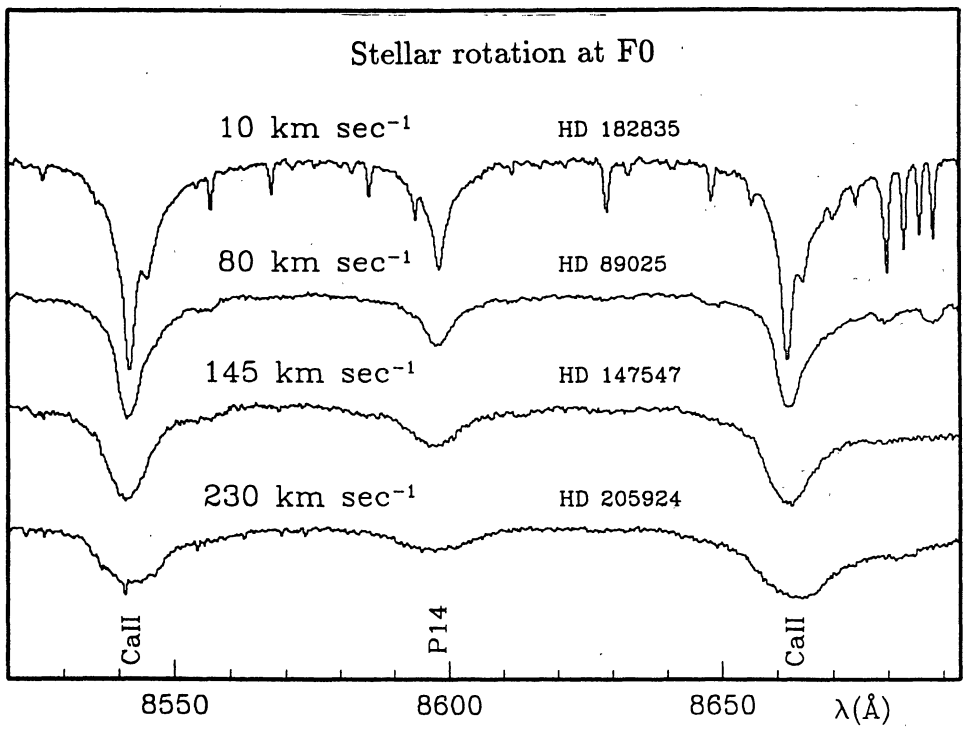

Figure 7: Rotational velocity influence on stellar spectra. Adopted from Munari (1999).

2.3.3 Radial velocities

Consider an acquired spectrum with the $R = 20\,000$ resolution as depicted in Fig. 8, with the inset magnifying a portion of the whole spectrum to show Doppler-split spectral lines. Extracting radial velocity data from spectra may seem straight-forward, but it is not. People have historically fitted Gaussian profiles to individual spectral lines and deduced radial velocities from the obtained Gaussian means, yet this approach is very inaccurate, especially in the vicinity of eclipses (Rossiter, 1924). Fitting two Gaussians simultaneously improves the accuracy and this is the technique used in IRAF (Tody, 1986). A new special technique `TODCOR` has been devised recently that uses the cross-correlation of two template (synthetic) spectra against the observed spectra (Zucker and Mazeh, 1994): it finds the Doppler shift of each template and luminosity ratio of the two templates that best fit the observed spectrum.

Once the radial velocities are extracted, a **radial velocity curve** may be assembled by listing radial velocities as function of time or phase. This curve is in a sense similar to a light curve, but it carries information on different physical parameters, e.g. the mass ratio, center-of-mass velocity, semi-major

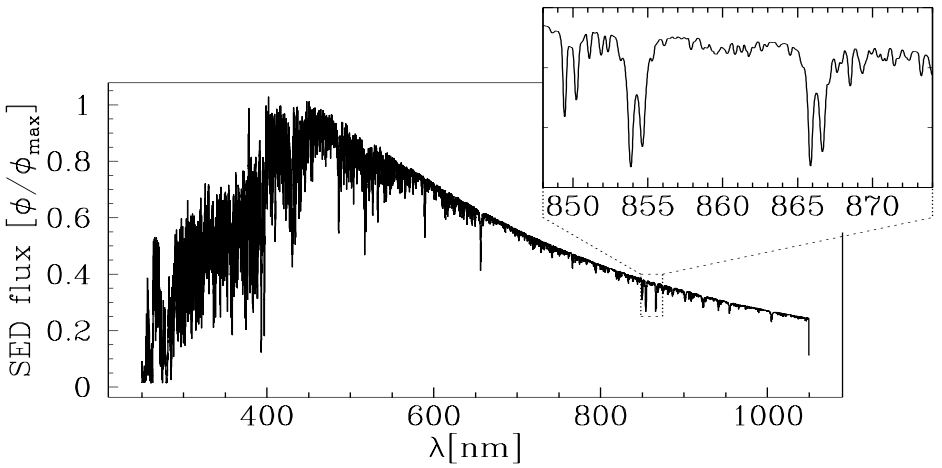

Figure 8: An example of a synthetically created eclipsing binary spectrum at quarter-phase with the inset magnifying the Gaia RVS window. Spectral lines are visibly split because of binarity. Adopted from Prša and Zwitter (2005a).

axis etc. Fig. 9 shows an example of extracted radial velocities for V945 Centauri; observations taken from Aerts et al. (2005).

2.3.4 Doppler tomography

When very high resolution spectra are available ($R = 50\,000$ or higher) and good phase coverage is acquired, accurate measurements of spectral line shapes may be performed for rotating stars. The idea is to map distortions of spectral lines onto particular features on the stellar surface. As such, the method is convenient for rapidly rotating single stars and, to our benefit, most types of close binary stars. Doppler tomography (sometimes referred to also as Doppler imaging) was first proposed to astronomical application by Deutsch (1958); with improved mathematical and numerical techniques, Doppler tomography is gaining significance in many astronomical problems: chemical analysis of Ap stars (Rice and Wehlau, 1990), temperature imaging (Piskunov and Wehlau, 1990), rapid stellar rotation (Vogt et al., 1987), gravity darkening (Kõvári and Weber, 2004), eclipsing binaries (Vincent et al., 1993) etc.

Doppler tomography of eclipsing binaries aims to detect and map the presence of stellar spots, center-to-limb intensity variation (limb darkening), rotational ellipticity (gravity darkening) effects and other non-uniform struc-

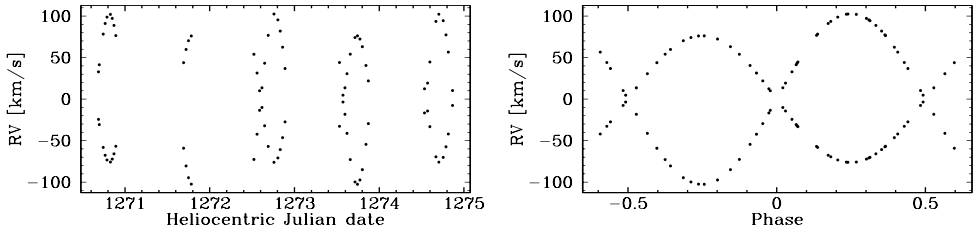

Figure 9: Radial velocity curve of V945 Centauri (taken from Aerts et al. (2005)). Left: timed radial velocity curve connects observed radial velocities with times of observation. Right: phased radial velocity curve connects observed radial velocities with phase. The data are folded to $[-0.5, 0.5]$ interval and aliased to $[-0.6, 0.6]$ interval for better sense of periodicity of the curve.

tures on stellar surfaces of both components. Doppler shift of the distortion is determined by the position of the mapping feature on the surface (stellar latitude and longitude). Tomography uses the Method of Maximum Entropy (Vogt et al., 1987) to solve the inverse problem. Fig. 10 shows an example of a Doppler tomography reconstruction of the synthetic pattern "OA_A"; the results are taken from Vincent et al. (1993). The results indicate that Doppler tomography of eclipsing binaries performs even better than in the case of single rapidly rotating stars, because the orbital movement and eclipses break the degeneracy of the choice of hemisphere that the feature is on.

2.3.5 Astrometry

Astrometry is an observational method that is based on measuring the position of celestial bodies in the sky. Since astrometry relies on resolving powers of instrumentation, it is diffraction-limited, and as such it wasn't really practical for objects that are not in our immediate vicinity; yet once the astrometric instrument is lifted above the atmosphere, a major limitation to resolving distant objects is removed. Space astrometry is also able to provide a non-rotating stellar reference frame to which the motions of objects in the Solar System and stars in the Galaxy may be referred. Pioneering results of the Hipparcos satellite (ESA SP-402, 1997) have reached the accuracy of 1 mas, beating the ground-based record of 50 mas (Johnston, 2000). The forthcoming space mission Gaia (Perryman et al., 2001) will be equipped with an astrometric instrument with a few μas accuracy, which is several hundreds of times better than that of Hipparcos!

Astrometry is usually applied to extract distances to celestial objects.

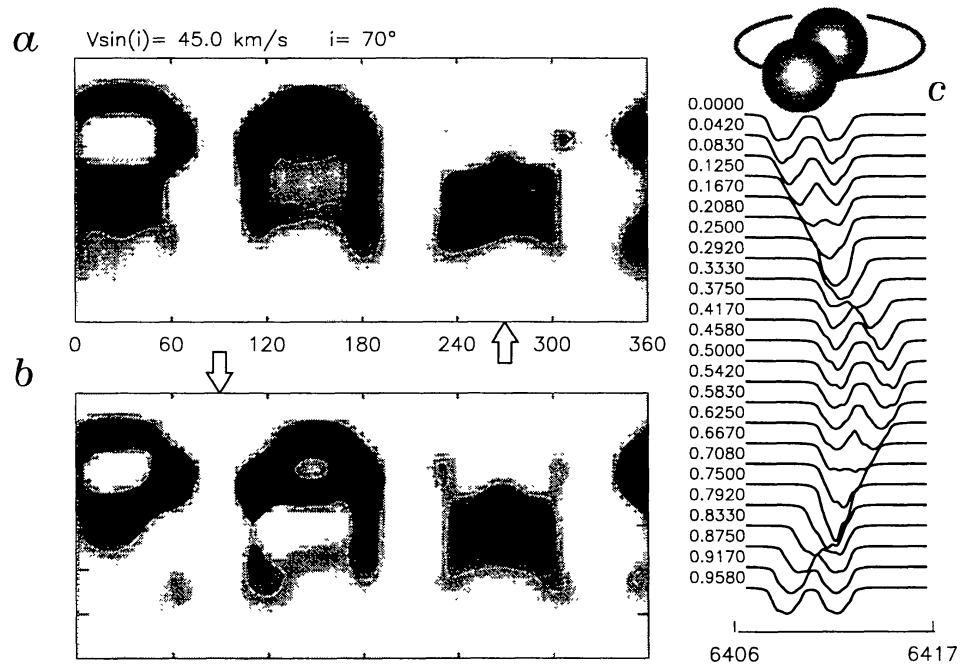

Figure 10: Doppler image of the pattern "OA_A". The pattern was synthetically created to be 1000 K cooler than the stellar surface and was impregnated to the spectra with $R = 90\,000$. Arrows mark the phase of the eclipse for each component, letters a and b refer to the inversion of the primary and secondary component, respectively. It is shown that Doppler tomography of eclipsing binaries yields better results than single stars, because the known orbital movement removes the ambiguity of the position of features with respect to the equator (the so-called equatorial reflection). Adopted from Vincent et al. (1993).

Known distances to eclipsing binary stars enable us to determine component luminosities in the absolute sense, which is not otherwise observable. This distance may either enter the modeling process independently or be compared to the value yielded by the model. In both cases the uncertainties decrease and interstellar extinction may be readily evaluated (Prša and Zwitter, 2005b).

By observing proper motions, astrometric measurements of visual binaries have long been utilized with remarkable results in obtaining accurate masses of individual stars (Pourbaix, 2002). Apart from visual binaries, astrometric data, when accompanied by the radial velocity observations, can also provide masses from the photocentric orbits of double-lined spectroscopic binaries based purely on observations, without any underlying physical model.

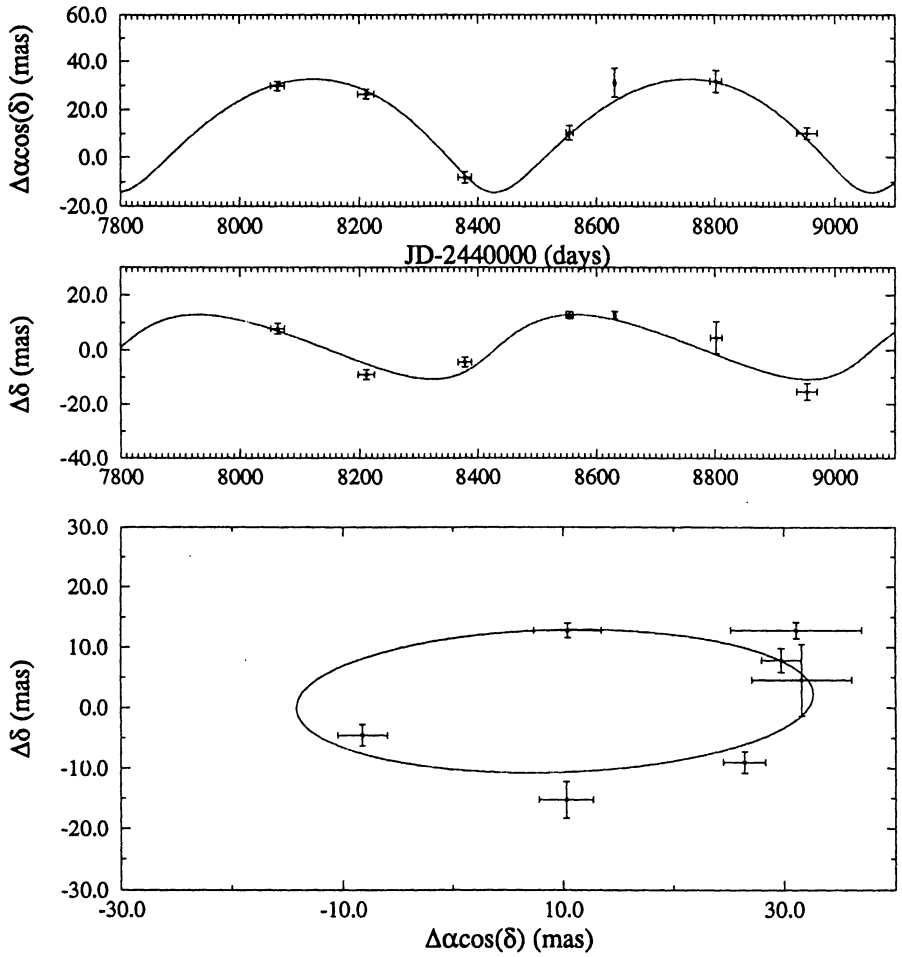

Figure 11: The orbit of the photocenter of the double-lined spectroscopic binary HIP 111170, adopted from Halbwachs and Arenou (1999). The upper two panels show astrometric changes in projected right ascension and declination and the bottom panel shows a reconstructed orbit of the photocenter. Astrometric accuracy of Gaia will vastly improve the detection and determination of the orbit for such binary stars.

Fig. 11 summarizes the results obtained by Halbwachs and Arenou (1999) for a double-lined spectroscopic binary HIP 111170: measuring the changes in the position of the star in the sky enabled them to reconstruct its orbit and obtain the masses of both components to a $\sim 15\%$ accuracy.

2.3.6 Polarimetry

A polarimetric measurement is essentially equal to photometry, with an additional polarimetric analyser inserted in the input beam. This analyser transmits only a fraction of the light with the matching polarization. By rotating the polarimetric analyser, the degree of polarization may be measured for the given source.

Within the astronomical context, the degree of polarization coming from celestial sources is often low, typically up to a few percent (Tinbergen, 1996). Sources of polarization in close binaries could be (Shakhovskoi, 1965):

- emergent light scattered on the star's photosphere due to shape distortion,
- light of one star scattered at the surface of the other star (reflection effect),
- light scattered by the accretion disk, streams and/or circumstellar clouds,
- electron scattering in gas flows, flares, high-temperature atmospheres and
- magnetic surface fields.

To avoid systematic bias and drift errors, polarimetric observations are usually given in *fractional* polarization (Tinbergen, 1996):

$$\mathcal{P} = \frac{J_1 - J_2}{J_1 + J_2}, \tag{2.10}$$

where J_1 and J_2 are observed fluxes at two orthogonal positions of the polarimetric analyser. Typically one finds the minimal and maximal values of the transmitted flux:

$$\mathcal{P}_{\max} = \frac{J_{\max} - J_{\min}}{J_{\max} + J_{\min}}. \tag{2.11}$$

Since polarimetric observations discard significant portions of the input flux, considerable observing time on a large telescope is generally needed in order to reduce the photometric noise. Polarimetry should therefore not be used indiscriminately, but only when it provides insights which other methods cannot give (Tinbergen, 1996).

Polarimetric observations of eclipsing binaries are seldom carried out despite their potential value. Kallrath and Milone (1999) speculate on several reasons for this, concluding that it is mostly due to the lack of sophisticated instrumentation needed to perform polarimetry. So, while the theoretical basis for polarimetry, along with several applications for eclipsing binaries, have already been laid by Landi degl'Innocenti et al. (1988) and Wilson and Liou (1993), it remains to be seen whether future observers will find polarimetry a worthy observational technique.

3 System geometry

There have been many attempts to accurately describe geometry of binary stars. One of the most accurate approximations, the **Roche** model, is based on the principle of equipotential surfaces; it implies the following assumptions (Kallrath and Milone, 1999):

1. both stars of the binary system gravitationally interact as point sources surrounded by massless envelopes. This allows a relatively simple analytical representation of the potential;

2. the periods of free non-radial oscillations are negligible when compared to the orbital period P, so that the shape of the components is determined by the instantaneous force field. The time scale of these oscillations is of the order of time required for a star to re-establish the hydrostatic equilibrium, which is $\sim$15 minutes for Solar-type stars (Hilditch, 2001). This assumption effectively states that the shape of the star in a binary system is fully determined by the instantaneous force field.

3. the star rotates around its axis as a rigid body, without any differential rotation.

The model was first formulated by the French astronomer Édouard Albert Roche (1820-1883) in 1849.

3.1 The Roche model

The *principle of equipotential surfaces* states that the shape and physical characteristics of both stars in a binary system are fully determined by the given effective potential on that surface. Fig. 12 depicts a typical binary system layout. M_1 and M_2 are point-source masses of individual stars, a is the separation between the two, m is the test mass and s_1 and s_2 are respective distances to M_1 and M_2. The origin of the coordinate system is set to star 1. The system revolves about the axis that goes through the center-of-mass (COM) and is parallel with z-axis. The discussion hereafter concentrates on obtaining the shapes of both stars in a binary system with circular orbits and synchronous rotation (for the purpose of brevity and simplicity). The result will be generalized to elliptical orbits and asynchronous rotation in the end of the Section.

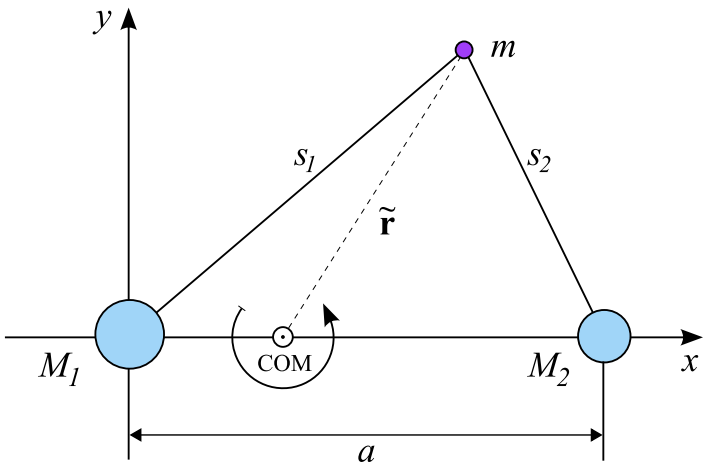

Figure 12: Binary system geometry. Note that the origin of the coordinate system is in star 1, not in the center-of-mass.

The net force exerted on a particle m within or at the surface of either star is given by Newton's law:

$$\mathbf{F_p} + \mathbf{F_g} = -m\omega^2\tilde{\mathbf{r}}, \tag{3.1}$$

where $\mathbf{F_p}$ is the force of the pressure gradient, $\mathbf{F_g}$ is the gravitational force, ω is the angular velocity of the system and $\tilde{\mathbf{r}}$ is the vector from the rotation axis to the test particle m. As long as the particle is located within or at the surface of the star, it will be at rest in the rotating coordinate system because of the rigid rotation approximation and no Coriolis force will be exerted. $\mathbf{F_p}$ per unit volume V may be written as the gradient of pressure:

$$\mathbf{F_p} = -V\nabla p, \tag{3.2}$$

and the remaining two terms from Eq. (3.1) may be written as the gradient of an effective potential ψ:

$$\mathbf{F_g} + m\omega^2\tilde{\mathbf{r}} = -m\nabla\psi. \tag{3.3}$$

Combining Eqs. (3.1)–(3.3) yields:

$$-V\nabla p = m\nabla\psi \Rightarrow \nabla p = -\rho\nabla\psi. \tag{3.4}$$

This means that ∇p and $\nabla\psi$ are parallel. It quickly follows from Eq. (3.4) that $\nabla\rho$ is also parallel with the two when we evaluate the curl of the above expression:

$$\nabla \times \nabla p = -\nabla \times \rho\nabla\psi = -\rho\nabla \times \nabla\psi - \nabla\rho \times \nabla\psi. \tag{3.5}$$

Since the curl of the gradient is 0 for any given function, it immediately follows that:

$$\nabla\rho \times \nabla\psi = 0 \Rightarrow \nabla\rho \parallel \nabla\psi \parallel \nabla p. \tag{3.6}$$

This implies that surfaces of constant density, effective potential and pressure coincide. Once ψ is known, we can obtain the shape of the corresponding equipotential surface, and the shape of the star directly follows from Eq. (3.6).

The effective potential ψ may be easily obtained from Eq. (3.3) if a spherically symmetric distribution of mass is attributed to M_1 and M_2:

$$\psi = -\frac{GM_1}{s_1} - \frac{GM_2}{s_2} - \frac{1}{2}\omega^2\tilde{r}^2. \tag{3.7}$$

It should be stressed at this point that the potential ψ has limited validity: it is not at all applicable for stellar interiors, nor does it encompass the tidal interaction that would be described by the quadruple term. Such a term would arise if the assumption of a massless envelope (and thus a spherically symmetric distribution of mass) was dropped. Observations show that such interaction clearly exists, and we shall return to this towards the end of Section 3.4.

Because of system geometry, it proves useful to use spherical coordinates (Fig. 13):

$$\begin{aligned} x &= r\sin\theta\cos\phi = \lambda r, \\ y &= r\sin\theta\sin\phi = \mu r, \\ z &= r\cos\theta = \nu r. \end{aligned} \tag{3.8}$$

Following such convention, the polar angle θ goes from 0 at $+z$ pole to 180° at $-z$ pole; the azimuth angle ϕ goes from 0 to 360° in a positive (CCW) sense, starting from the x-axis. The x-axis points toward the companion star within a binary system (Fig. 12). Parameters λ, μ and ν in Eq. (3.8) are the direction cosines.

The COM of the system lies on the x-axis and its position depends on the mass ratio $q = M_2/M_1$ of the binary:

$$x_{\rm COM} = \frac{\sum_i M_i x_i}{\sum_i M_i} = \frac{qa}{1+q}. \tag{3.9}$$

Effective potential ψ can now be readily written in spherical coordinates following Eqs. (3.7) and (3.8), and by noting that:

$$s_1 = r, \quad s_2 = \sqrt{r^2 - 2xa + a^2} \text{ and } \tilde{r} = \sqrt{(x - x_{\rm COM})^2 + y^2}: \tag{3.10}$$

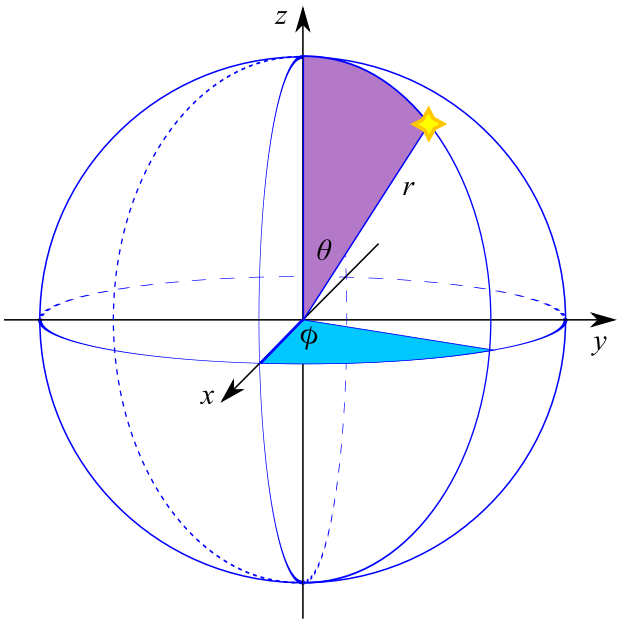

Figure 13: Spherical coordinate convention: the polar angle θ goes from 0 at $+z$ pole to 180° at $-z$ pole; the azimuth angle ϕ goes from 0 to 360° in a positive (CCW) sense, starting from the x-axis.

$$\psi(r,\lambda,\nu) = -\frac{GM_1}{r} - \frac{GM_2}{\sqrt{r^2-2ar\lambda+a^2}} - \frac{1}{2}\omega^2\left(r^2(1-\nu^2) - 2r\lambda x_{\mathrm{COM}} + x_{\mathrm{COM}}^2\right). \tag{3.11}$$

Finally, we use Kepler's law $\omega^2 a^3 = G(M_1+M_2)$ and Eq. (3.9) to derive the full form of the effective potential:

$$\psi(r,\lambda,\nu) = -\frac{GM_1}{a}\left[\frac{a}{r} + q\left(\frac{a}{\sqrt{r^2-2ar\lambda+a^2}} - \frac{r\lambda}{a}\right) + \right.$$
$$\left. + \frac{1}{2}\frac{r^2}{a^2}(1+q)(1-\nu^2) + \frac{1}{2}\frac{q^2}{1+q}\right]. \tag{3.12}$$

A dimensionless potential may be introduced that relates to the potential $\psi(r,\lambda,\nu)$ by the following expression:

$$\Omega = -\frac{a\psi}{GM_1} - \frac{1}{2}\frac{q^2}{1+q}, \tag{3.13}$$

which by substituting ψ with Eq. (3.12) and introducing the dimensionless

variable $\varrho = r/a$ expands to:

$$\Omega = \frac{1}{\varrho} + q\left(\frac{1}{\sqrt{\varrho^2 - 2\varrho\lambda + 1}} - \rho\lambda\right) + \frac{1}{2}(1+q)(1-\nu^2)\varrho^2. \tag{3.14}$$

This form was first suggested by Kopal (1959) and the potential Ω is often referred to as the *modified* Kopal potential. One should keep in mind that the origin of the coordinate system is at the center of star M_1, not the center-of-mass of the system. The potential with respect to star M_2 is obtained by symmetrical inversion of Ω and q:

$$\Omega' = \frac{\Omega}{q} + \frac{1}{2}\frac{q-1}{q}, \quad q' = \frac{1}{q}. \tag{3.15}$$

Ω and Ω' apply only to circular orbits and synchronous rotation. The generalization to elliptical orbits and asynchronous case was first done by Wilson (1979):

$$\Omega = \frac{1}{\varrho} + q\left(\frac{1}{\sqrt{\delta^2 + \varrho^2 - 2\varrho\lambda\delta}} - \frac{\varrho\lambda}{\delta^2}\right) + \frac{1}{2}F^2(1+q)\varrho^2(1-\nu^2), \tag{3.16}$$

where $\delta = D/a$ is the instantaneous separation between the two stars normalized to the semi-major axis and F is the synchronicity parameter, defined as the ratio between the axial and orbital revolution period:

$$F = \frac{P_{\text{axial}}}{P_{\text{orbital}}}. \tag{3.17}$$

Synchronicity parameter is a single number for the whole star, in accordance with the approximation that the star is treated as a rigid body. Value $F = 1$ corresponds to a synchronous rotation in a circular orbit. In case of elliptical orbits the rotation tends to synchronize because of tidal interactions between the two components. In eccentric cases one can define pseudo-synchronous rotation, where the angular rotation rate of the star is equal to the orbital angular velocity *at periastron*. Following the angular momentum conservation, angular velocity ω at the given point on the orbit is given by the following expression:

$$\omega(t) = \frac{1}{\delta^2}\left(\frac{2\pi}{P}\right)\sqrt{1-\varepsilon^2}, \tag{3.18}$$

where ε is the orbital eccentricity. Since the synchronicity parameter is defined with respect to periastron, $\delta = 1 - \varepsilon$, introducing this into Eq. (3.18)

yields that for pseudo-synchronous rotation the synchronicity parameter is given by:

$$F = \sqrt{\frac{1+\varepsilon}{(1-\varepsilon)^3}}. \tag{3.19}$$

The formalism of asynchronous rotation was first developed by Limber (1963); for observational tests on real binaries see e.g. van Hamme and Wilson (1986).

Having elliptical orbits and asynchronous rotation effectively means that additional approximations were assumed with respect to the circular orbit case, most notable being that the now present Coriolis force is neglected. For a thorough discussion on error estimates due to this approximation please refer to Limber (1963).

Generalized Kopal potentials Ω and Ω' *uniquely* determine the shapes and sizes of individual stars in a binary system at any point of the orbit. Exactly how this is done will now be explained.

3.2 Shapes and sizes of stars in a binary system

The previous section has shown that the surfaces of constant pressure and density coincide with equipotential surfaces. This in turn implies that the stellar shape is fully determined by its effective potential Ω: given the value of Ω, Eq. (3.16) has to be iteratively inverted to obtain the radius ϱ for the given λ and ν. This is most easily achieved by expressing the potential at the star's pole ($\theta = 0, \lambda = 0, \nu = 1$):

$$\Omega = \frac{1}{\varrho_{\rm pole}} + q\left(\frac{1}{\sqrt{\delta^2+\varrho_{\rm pole}^2}}\right), \tag{3.20}$$

solving for ϱ_p and asserting that Ω is constant over the surface of the star:

$$\frac{1}{\varrho} + q\left(\frac{1}{\sqrt{\delta^2+\varrho^2-2\varrho\lambda\delta}} - \frac{\varrho\lambda}{\delta^2}\right) + \frac{1}{2}F^2(1+q)\varrho^2(1-\nu^2) =$$

$$= \frac{1}{\varrho_{\rm pole}} + q\left(\frac{1}{\sqrt{\delta^2+\varrho_{\rm pole}^2}}\right). \tag{3.21}$$

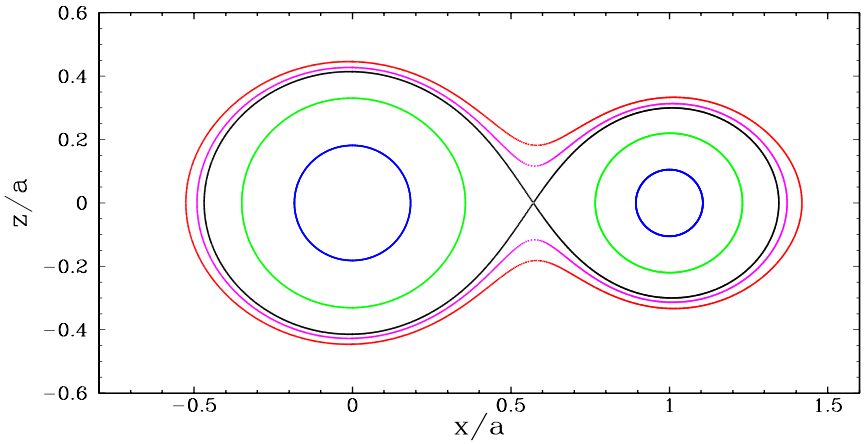

Figure 14: The xz cross-section of the space of Roche equipotentials. Five color-coded examples are all depicted for the mass ratio $q = M_2/M_1 = 0.5$. They correspond to five different values of Ω: the innermost (blue) equipotential corresponds to $\Omega = 6.0$, the green equipotential corresponds to $\Omega = 3.5$, the black equipotential corresponds to the critical Roche lobe, $\Omega = 2.87584$, the magenta corresponds to $\Omega = 2.8$ and finally, the red equipotential corresponds to $\Omega = 2.7$.

Solving this equation iteratively for each λ and ν determines the shape and the size of the star. Fig. 14 depicts 5 color-coded examples of an xz cross-section of stellar shapes that correspond to the constant mass ratio $q = 0.5$ and different values of Ω. A shape of the star is determined by the equipotential it fills, so the value of potential Ω determines the morphology of the binary. The most important equipotential on Fig. 14 is drawn in black and corresponds to the value $\Omega = 2.87584$: both stars have a typical teardrop shape and they are in contact in only one point. This particular equipotential is referred to as the **Roche lobe** and it plays a significant role in morphological classification of close binaries.

3.3 Morphological classification of close binaries

Morphology of binary stars is very important because it strongly influences both the evolution and observational appearence of the system. As we have shown in the previous Section, the shapes of stars in a binary system depend solely on the value of Kopal potentials Ω and Ω'. Depending on their value, compared to the critical value of the Roche lobe, close binaries are classified into three distinct groups:

Detached binaries are systems in which both stars are bound within separate equipotential surfaces. Their evolution is more-or-less independent from one another, that is why detached binaries may be used as ideal physical laboratories for studying the properties of individual stars.

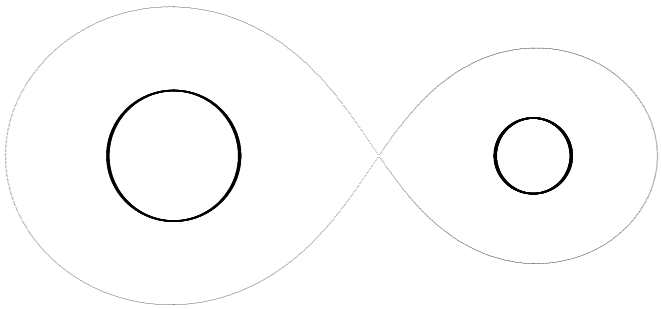

Semi-detached binaries are systems in which one star fills the Roche lobe and the other is bound within a separate equipotential surface. Semi-detached binaries frequently exhibit mass transfer, magnetic coupling of both stars and circumstellar clouds.

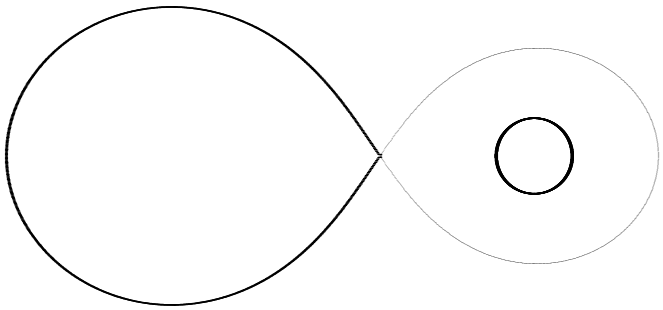

Overcontact binaries are systems in which both stars overfill the Roche lobe and share a common envelope. They may or may not be in a thermal equilibrium. Their evolution is closely coupled.

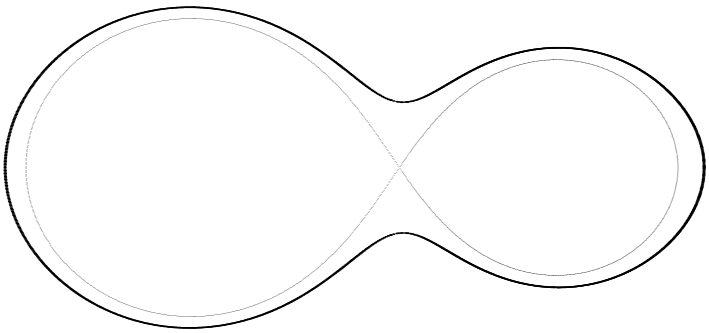

The Roche lobe is thus the limiting equipotential surface that distinguishes between different morphologies of close binary stars. The contact point of the Roche lobe is the **Lagrangian point** L_1.

Lagrangian points are those points in a rotating two-body system where the net force exerted on a particle mass is 0. There are 5 such points, shown on Fig. 15: L_1, L_2 and L_3 are located on the x-axis and are always unstable; L_4 and L_5 are displaced in $\pm y$-direction and may be either stable or unstable, depending on the mass ratio of the binary. These points are obtained by demanding that a gradient of Eq. (3.16) is 0:

$$\mathbf{F} = -m\nabla\Omega = 0: \qquad \text{Lagrangian points.} \tag{3.22}$$

This equation cannot be solved analytically, but the useful approximations to the 10^{-6} fractional accuracy given by Taff (1985) may be used:

$$\begin{aligned} x(L_1) &= z - \frac{1}{3}z^2 - \frac{1}{9}z^3 + \frac{58}{81}z^4, \\ x(L_2) &= z + \frac{1}{3}z^2 - \frac{1}{9}z^3 + \frac{50}{81}z^4, \\ x(L_3) &= 1 - \frac{7}{12}\mu - \frac{1127}{20736}\mu^3 - \frac{7889}{248832}\mu^4, \end{aligned} \tag{3.23}$$

where $\mu = M_2/(M_1 + M_2)$ and $z = (\mu/3)^{1/3}$. Of practical interest for the morphology of close binaries are the approximations for L_1 and L_2, the one for L_3 is given for sake of completion.

Once the position of L_1 is known, the Kopal potential $\Omega_{\text{crit}}^{L_1}$ at that point can be calculated by using Eq. (3.16), substituting ϱ with x_{L_1}. Following the

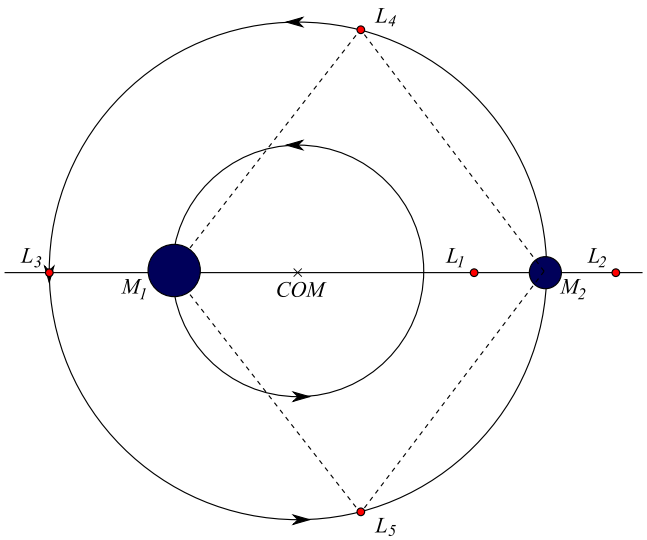

Figure 15: Lagrangian points in a rotating two-body system. The first three points (L_1 through L_3) lie on the straight line that passes through the center of the two stars. The remaining two points (L_4 and L_5) form equilateral triangles with the two stars.

same argument, $\Omega_{\text{crit}}^{L_2}$ may be obtained from the position of L_2. These are inner and outer critical values of potential that may be used as reference to define the **filling factor** of the system:

$$\mathcal{F} = \frac{\Omega - \Omega_{\text{crit}}^{L_1}}{\Omega_{\text{crit}}^{L_2} - \Omega_{\text{crit}}^{L_1}}. \tag{3.24}$$

It immediately follows that $\mathcal{F} = 0$ corresponds to the semi-detached case, $\mathcal{F} < 0$ to the detached case and $\mathcal{F} \in (0, 1]$ to the overcontact case. Values $\mathcal{F} > 1$ are not physically plausible, since the star would be overfilling L_2 and would therefore lose its outer envelope on a dynamical timescale.

3.4 Orbital properties of close binaries

Within the Roche approximation, the motion of stars in a binary system around the mutual center-of-mass constitutes a classical two-body problem. Fig. 16 shows two types of orbits, circular (left) and elliptical (right).

Kepler's 2$^{\text{nd}}$ law assures that the line connecting the centers of both stars must go through the center-of-mass, which in turn implies that orbital periods of both stars must be the same: $P := P_1 = P_2$. Semi-major axis and period

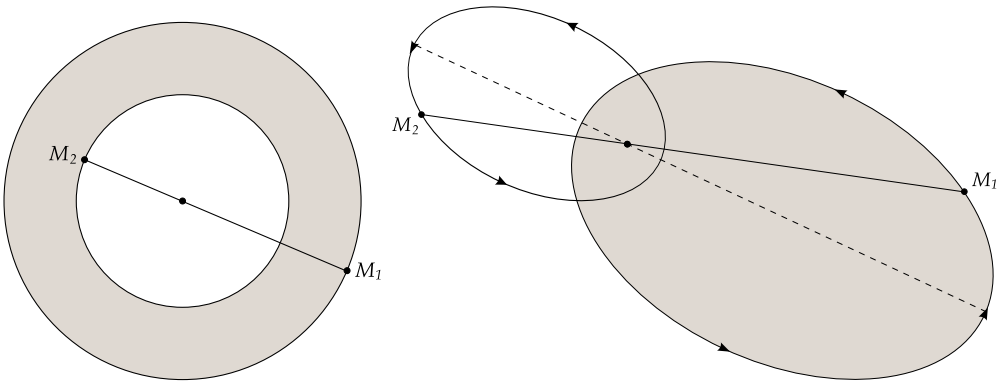

Figure 16: Binary star orbits. Left: an example of a circular orbit. Right: an example of an elliptical orbit. The line that connects both stars goes through the center-of-mass in each point on orbit.

are connected by the 3rd Kepler law:

$$\frac{(a_1 + a_2)^3}{P^2} = \frac{G(M_1 + M_2)}{4\pi^2}, \quad a := a_1 + a_2, \quad M := M_1 + M_2. \tag{3.25}$$

Finally, both orbital eccentricities ε must be equal: $\varepsilon := \varepsilon_1 = \varepsilon_2$; both orbits are co-planar and their orientations differ by 180° within that plane.

As a consequence, we refer to the *relative* orbit of the binary as a whole, with its semi-major axis a, orbital eccentricity ε and orbital period P. The sizes of all three orbits are thus in proportions $a_1 : a_2 : a = M_2 : M_1 : (M_1 + M_2)$.

Let us now inspect parameters which determine geometrical *orientation* of the orbit with respect to the observer: the *inclination* i, *argument of periastron* ω, and the *longitude of the ascending node* Ω. Fig. 17 depicts these three orbital parameters. The new coordinate system with respect to the observer (direction u) that is perpendicular to the plane-of-sky (v, w) is also depicted.

Inclination i is the angle between the orbital plane and plane-of-sky. It can assume any value on the interval $[0, \pi]$. For any inclination different than $\pi/2$, the two planes intersect at two orbital points: *ascending* and *descending* nodes. In these two nodes the orbiting body approaches to and recedes from the observer, respectively. If the inclination is exactly $\pi/2$, the two planes are perpendicular.

Argument of periastron ω is the angle from ascending node to periastron, measured in the direction of motion. It can assume any value on

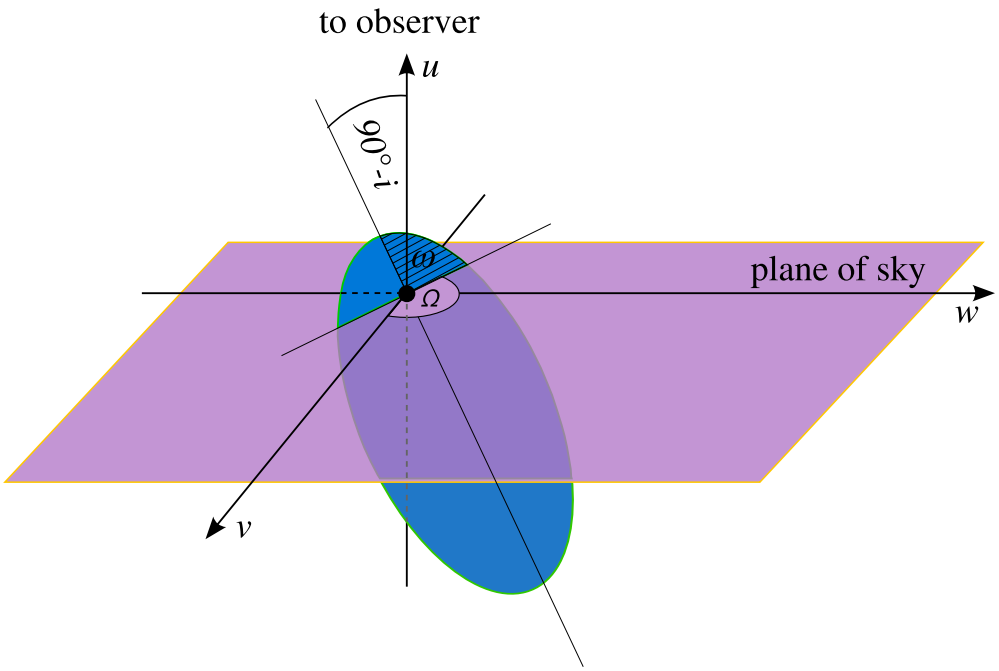

Figure 17: Orbital parameters determining the orientation of the orbit: inclination i, the argument of periastron ω and the longitude of the ascending node Ω. The observer is in the direction of u-axis and vw is the plane-of-sky. It is immediately evident that rotations about u axis do not have physical significance, so Ω may be arbitrarily fixed; by convention we set $\Omega = 0$.

the interval $[0, 2\pi]$.

Longitude of the ascending node Ω is the angle from the reference direction axis v to the ascending node, measured in a positive (CCW) mathematical sense.

There are three important points that should be stressed for eclipsing binary stars:

1. since the vw plane-of-sky may be arbitrarily rotated to establish the v and w directions, the longitude of the ascending node Ω is also arbitrary (as is evident from Fig. 17). By convention we set $\Omega = 0$, which in turn determines the position of v and w axes; and

2. the transitions of individual stars through the nodes are opposite: while one star passes through the ascending node, the other star passes

through the descending node. The argument of periastron of the secondary star thus differs by π radians. By definition, the argument of periastron of the binary corresponds to the *primary* star.

3. the inclination change from below to over $\pi/2$ interchanges the role of the ascending and descending node. It is customary, due to this point, to use the term **reference node** instead of ascending node in the field of binary stars; for inclinations smaller than $\pi/2$, the reference node is the ascending node and for those larger than $\pi/2$, the reference node is the descending node. This assures that regardless of the value of inclination, only one node is consistently used as reference for the argument of periastron.

The $1/s$ dependence of the gravitational potential, c.f. Eq. (3.7), is exact only if the star is spherically symmetric. In reality, however, the stars are distorted by tidal interactions and rotation; Chandrasekhar (1933) has shown that the distortion of a binary system component is the same as if it rotated like a rigid body about its own axis with the Kepler angular velocity ω and then tidally distorted by a secondary at a distance a from its center of gravity, the two effects being simply added. This superposition theorem is true to (and including) the fifth order in $\langle R\rangle/s$, where $\langle R\rangle$ is the mean stellar radius. To see this, let us add a quadruple term[1] to the gravitational potential of the secondary star:

$$\psi_2^G = -G\left(\frac{M_2}{s_2} + \frac{J_x + J_y + J_z - 3I}{2s_2^3} + \dots\right), \tag{3.26}$$

where J_x, J_y and J_z are the principal components of inertia of the secondary star at its center of gravity, and I is the moment of intertia about the radius vector. These moments of inertia are of the order of $M_2\langle R_2\rangle^2$ and tidal interaction is of the order $\langle R_2/s_2\rangle^3$, which yields the second term in the equation above of the order $M_2/\langle R_2\rangle\,(\langle R_2\rangle/s_2)^6$.

The potential ψ_2^G in the vicinity of the primary star may be expanded in terms of Legendre polynomials up to the fifth order (Sterne, 1939):

$$\psi_2^G = \frac{GM_2}{a^2}s_1\cos\theta + \frac{GM_2}{a}\sum_{i=2}^{4}\left(\frac{s_1}{a}\right)^i P_i(\cos\theta) + \text{const.} \tag{3.27}$$

where θ is the angle between the direction along a towards the secondary star and the direction along s_1. The first term on the right describes the orbital acceleration of the primary star as a whole; by placing the origin of

[1]This is a good approximation for any point that is sufficiently receeded from the star itself (Chandrasekhar, 1933).

the corotating coordinate system in the primary star this term is neutralized and the center of gravity of the primary will always be at the origin. The remaining terms ($2 \leq i \leq 4$) constitute a tidal potential which causes the deviation from a spherically symmetric potential. To properly solve this problem, an assumption on the density distribution of the star needs to be stated. We instead proceed phenomenologically to stress the immediate consequence: these terms cause a torque that is exerted on the star and consequentially a precession of the whole orbit. To this we refer to as **apsidal motion**, due to the rotation of the line of apsides (line of nodes). Apsidal motion is very common in close binaries and should thus be carefully handled: if ω changes, then the effective period of the binary no longer corresponds to the true sidereal period but to the anomalistic period (the time between two consecutive periastron passages). In addition, if ω changes, the phasing of the eclipses will also change. That is why special care should be excercised when defining the orbital phase. That is the topic of our next Section.

3.5 Dynamical aspects of binary systems

The formulation of dynamical aspects of binary stars differs from the historical (Russell's) formulation given e.g. by Smart (1977); textbooks and papers that are paving the field of binary stars (e.g. Hilditch 2001, Kallrath and Milone 1999, Etzel 1981, Wilson 1998; Wilson and Van Hamme 2003, Hadrava 1990 and others) typically do not include this formulation, that is why we present this topic here in some detail.

3.5.1 The Kepler problem

We start the discussion by overviewing the well-known approach to solving the Kepler problem by introducing *anomalies*. Fig. 18 shows an elliptical orbit that is described by the equation:

$$r(\upsilon) = \frac{r_0}{1 + \varepsilon \cos \upsilon} = \frac{a(1 - \varepsilon^2)}{1 + \varepsilon \cos \upsilon}. \tag{3.28}$$

Here r_0 is half-parameter, a is the semi-major axis and ε is the numerical eccentricity of the ellipse.

True anomaly υ is the angle measured from periastron to the position of the star on its orbit relative to the focal point of the ellipse. Since its

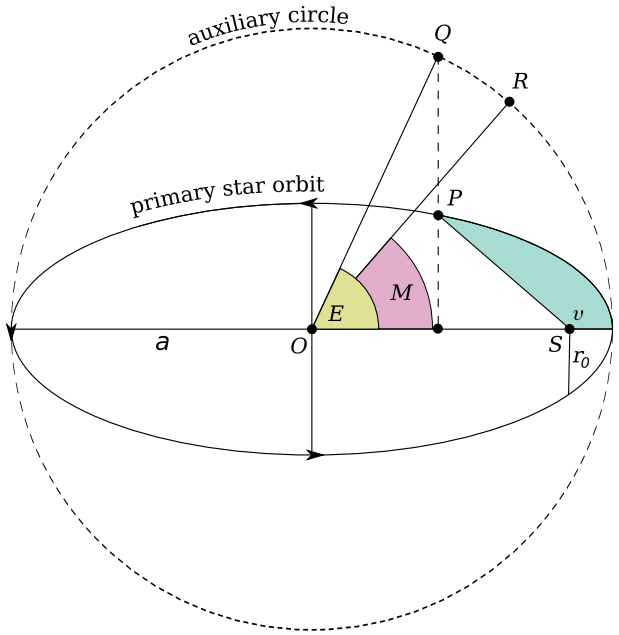

Figure 18: Graphical representation of the true anomaly υ, eccentric anomaly E and the mean anomaly M. The star is on point P at the orbit, rotating in a counter-clockwise direction around the focal point S. Point Q is the vertical projection of the star's position to the auxiliary circle. The angle ROS is proportional to the time elapsed since the star's passage through periastron.

rate of change varies with time and this variation cannot be expressed analytically in terms of time, we use an auxiliary circle depicted in Fig. 18.

Eccentric anomaly E is the angle from periastron to the projected point Q on the auxiliary circle relative to the center of the ellipse. The relation between the two anomalies is shown to be (e.g. by Smart, 1977):

$$\tan\frac{\upsilon}{2} = \sqrt{\frac{1+\varepsilon}{1-\varepsilon}}\tan\frac{E}{2}. \tag{3.29}$$

Mean anomaly M introduces time dependency and is defined as:

$$M = 2\pi\frac{t-\tau}{P}, \tag{3.30}$$

where τ is the time of periastron passage and P is the orbital period of the binary.

Mean anomaly is a measure of time and as such it cannot be geometrically constructed from the true and/or eccentric anomaly on Fig. 18.

However, this does not mean that M cannot be represented by an angle: given an auxiliary circle within the plane depicted on Fig. 18 with an arbitrary center point, the mean anomaly can be represented with the steadily increasing angle from the direction that corresponds to $M = 0$. Since all such representations are equivalent, we select the one that is most convenient to visualize: we set the auxiliary circle's center to the center of the ellipse and the direction $M = 0$ towards the periastron. This way we may depict the mean anomaly as an angle rather than only an abstract unit of time.

Mean anomaly is related to the eccentric anomaly by the transcendental[2] relation that needs to be solved iteratively:

$$M = E - \varepsilon \sin E. \tag{3.31}$$

Thus, to obtain $\upsilon(t)$, a set of equations (3.29)–(3.31) is used. We refer to these equations as solving the Kepler problem.

3.5.2 Solving the Kepler problem for binary stars

Instead of using mean anomaly directly to describe the time dependence of motion of the stars in a binary system, it is customary to use the orbital phase of the system.

Orbital phase Φ is a fraction of the orbital period that has elapsed since the last completed revolution cycle. It changes linearly in time on the $[0, 1]$ interval and is connected to the mean anomaly by the following relation:

$$M = 2\pi(\Phi - \Phi_{\mathrm{per}}). \tag{3.32}$$

Zero phase is set by convention. People were traditionally taking one of the eclipses (usually the deeper one) as reference for the zero point; this convention would be suitable if it weren't for apsidal motion (the rotation of the line of apsides). Apsidal motion causes excursions of *both* eclipses in opposite directions with respect to uniformly advancing time. For the model to conform to this, a slightly revised definition of zero phase is accordingly needed[3]: zero phase corresponds to the far intersection between the projection of the line-of-sight through the

[2] This is the very reason why solving $r(t)$ analytically is not possible for eccentric Keplerian orbits.

[3] Modeling a binary with constant real period and apsidal motion would show a fictitious period change under the convention of fixing zero phase at eclipses.

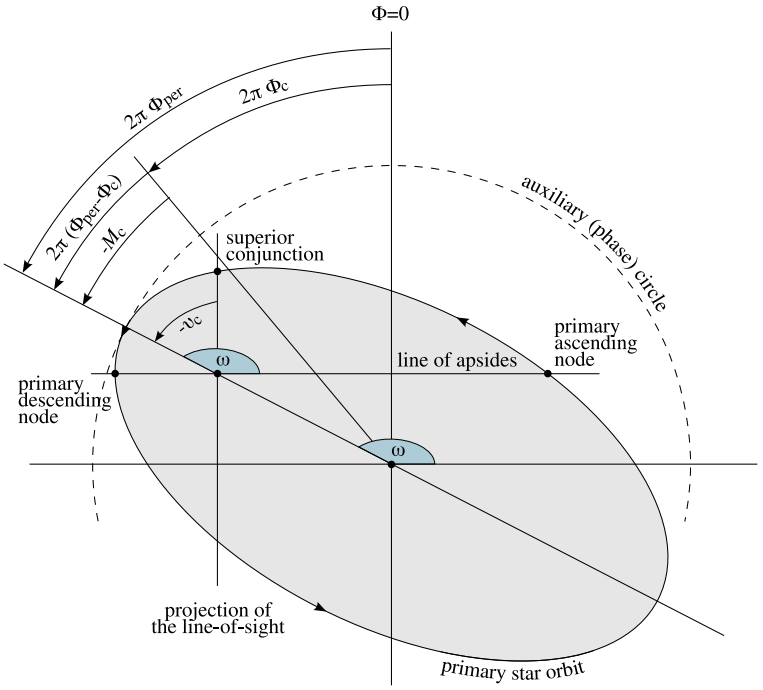

Figure 19: Schematic view of the orbital plane of the primary star. To derive the relationship between the phase of conjunction Φ_C and the argument of periastron ω, the Kepler problem needs to be solved.

center of the ellipse on the orbital plane and the ellipse itself. *Zero phase is the conjunction phase when the argument of periastron is $\pi/2$*, that is when the observer is looking along the semi-major axis. In case of circular orbits zero phase always coincides with the conjunction phase.

Orbital phase may be visualized similarly to the mean anomaly: by an angle with the origin at the center of the ellipse, increasing steadily with time from the zero point.

Having the phase defined, a naming convention for individual stars in a binary system needs to be set:

Primary star is the one at superior conjunction near orbital phase 0. It will be the one eclipsed near orbital phase 0 if there are eclipses.

Secondary star is the one at inferior conjunction near orbital phase 0. It will be the one eclipsing near orbital phase 0 if there are eclipses.

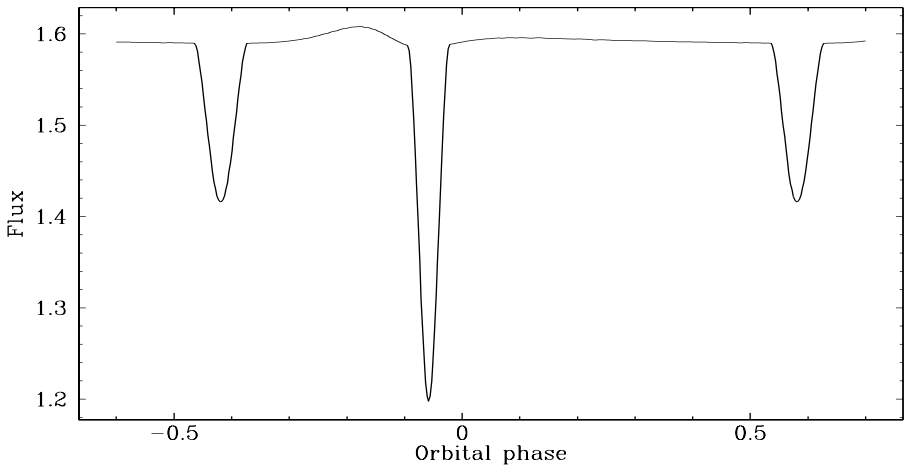

Figure 20: A synthetic light curve of an eccentric binary. Orbital eccentricity is $\varepsilon = 0.3$ and the argument of periastron is $\omega = \pi/4$. The figure stresses 3 points: 1) zero-phase $\Phi = 0$ does *not* in general coincide with eclipses, 2) the duration of the primary and the secondary eclipse is different and 3) although effective temperatures of both components are the same, the depths of both eclipses differ because of different surface coverage during the primary and the secondary minimum.

The phase of conjunction is computed by solving the Kepler problem. Fig. 19 shows three important points: the zero phase $\Phi = 0$, the conjunction phase $\Phi = \Phi_C$ and the periastron phase $\Phi = \Phi_{\rm per}$. These phases are referred to as *critical epochs*. The first step is to write the true anomaly of superior conjunction, which may be easily inferred from Fig. 19:

$$\upsilon_C = -\left(\omega - \frac{\pi}{2}\right) = \frac{\pi}{2} - \omega. \tag{3.33}$$

Once the true anomaly of the conjunction is known, Eqs. (3.29)–(3.31) may be used to obtain the mean anomaly at conjunction, M_C. Inspecting Fig. 19 again it is immediately evident that:

$$2\pi(\Phi_{\rm per} - \Phi_C) = -M_C \quad \text{and} \quad 2\pi\Phi_{\rm per} = \omega - \frac{\pi}{2}. \tag{3.34}$$

The phase of conjunction may then be computed by the following expression:

$$\Phi_C = \frac{M_C + \omega}{2\pi} - \frac{1}{4}. \tag{3.35}$$

To demonstrate this formalism on a particular example, consider a light curve depicted in Fig. 20: it is a light curve of a detached eclipsing binary with

orbital eccentricity $\varepsilon = 0.3$ and the argument of periastron $\omega = \pi/4$. From Eq. (3.33) we see that the true anomaly of conjunction $\upsilon_C = \pi/2 - \pi/4 = \pi/4$. Using Eqs. (3.29–3.31) we obtain $E_C = 0.59$ and $M_C = 0.42$. Using Eqs. (3.34–3.35) we get the phase of periastron $\Phi_{\rm per} = -0.125$ and the phase of (superior) conjunction, $\Phi_C = -0.06$.

3.6 Eclipses

The crucial advantage of eclipsing over non-eclipsing binary systems is the presence of eclipses, which are used as indicators of sizes and surface structure of individual components. Depending on the orbital inclination, eclipsing binaries may exhibit:

Partial eclipses, where the stars partially overlap. The shape of eclipses is typically sharp, V-shaped. Figs. 21 and 22 show an example of a partially eclipsing binary: its shape and orientation for the orbital phase cycle $[-0.6, 0.6]$ and the corresponding light curve.

Total eclipses, where the stars fully overlap. The profile of eclipses is typically box-shaped, since the eclipses are either total or annular. Figs. 23 and 24 show an example of a totally eclipsing binary: its shape and orientation for the orbital phase cycle $[-0.6, 0.6]$ and the corresponding light curve. Note that the primary (annular) eclipse is *not* flat: this is due to non-uniform distribution of normal emergent intensity over the primary star.

The condition for the eclipse on circular orbits is most easily determined by expressing[4] the position of the eclipsing star in the plane-of-sky coordinates:

$$u = a\cos\Phi\sin i, \quad v = a\sin\Phi, \quad w = -a\cos i\cos\Phi. \tag{3.36}$$

The projection onto the plane-of-sky vw is then:

$$\Delta^2 = v^2 + w^2 = a^2\left(\sin^2\Phi + \cos^2\Phi\cos^2 i\right). \tag{3.37}$$

The condition for the eclipse is now easily written out:

$$\begin{array}{rcccll} R_1 + R_2 & < & \Delta & & : & \text{no eclipses} \\ R_1 - R_2 & < & \Delta & < R_1 + R_2 & : & \text{partial eclipse} \\ & & \Delta & < R_1 - R_2 & : & \text{total eclipse} \end{array} \tag{3.38}$$

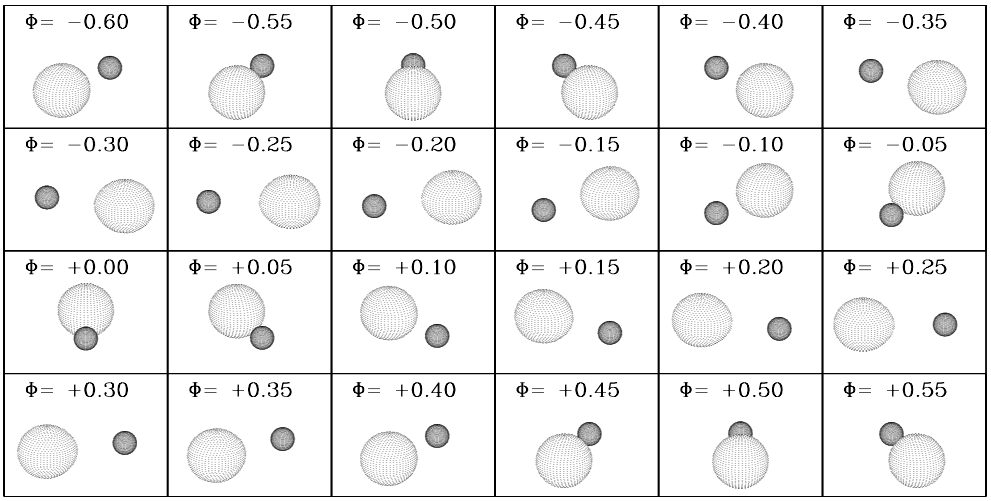

Figure 21: Collage of a partially eclipsing binary system. Mass ratio of the binary is $q = 1.0$, effective potentials of individual components are $\Omega_1 = 4.0$ and $\Omega_2 = 8.0$ and the inclination is $i = 70°$. Primary star is the one eclipsed at phase $\Phi = 0.0$.

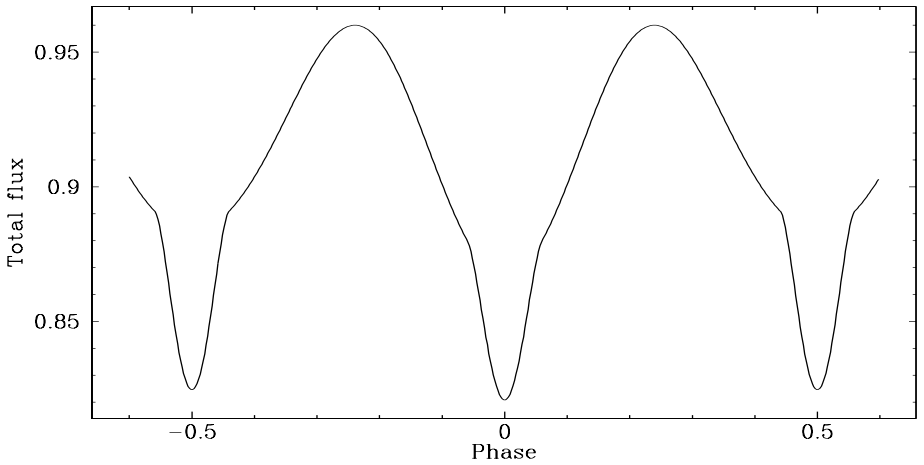

Figure 22: Light curve of a partially eclipsing binary system. System parameters are identical to those in Fig. 21.

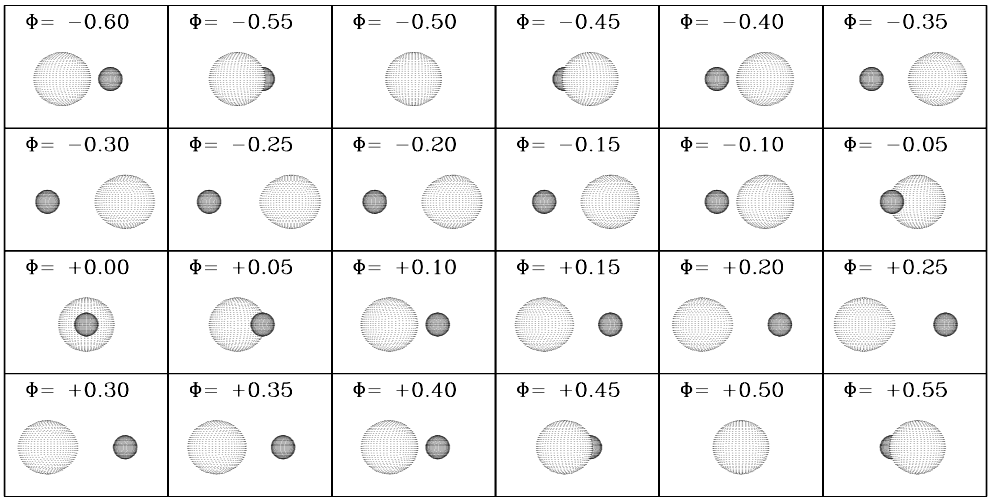

Figure 23: Collage of a totally eclipsing binary system. Mass ratio of the binary is $q = 1.0$, effective potentials of individual components are $\Omega_1 = 4.0$ and $\Omega_2 = 8.0$ and the inclination is $i = 90°$. Primary star is the one eclipsed at phase $\Phi = 0.0$.

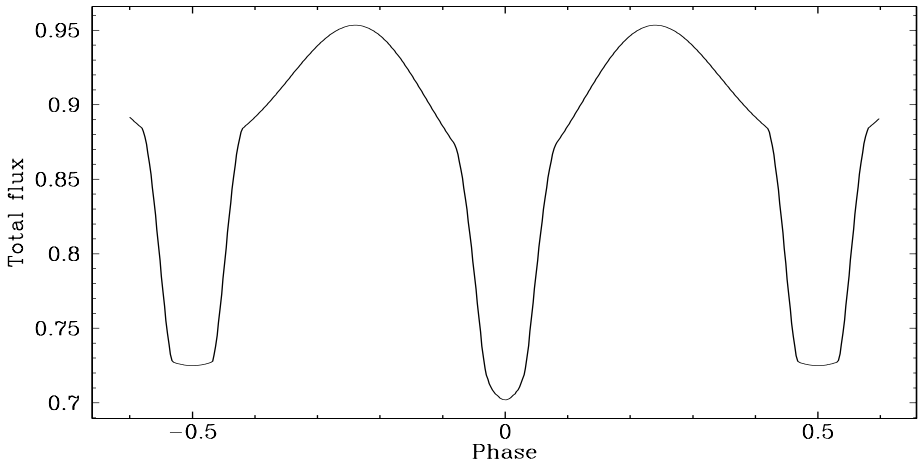

Figure 24: Light curve of a totally eclipsing binary system. System parameters are identical to those in Fig. 23.

The same expression for Δ may be used for eccentric orbits if a in Eq. (3.37) is replaced by the instantaneous separation D:

$$D = \frac{a(1-\varepsilon^2)}{1+\varepsilon\cos\upsilon}; \tag{3.39}$$

the true anomaly υ may be converted to phase Φ as explained in Section 3.5.2.

There is another important point to be realized when dealing with eccentric orbits: even if the effective temperatures of both components are the same, the depths of the minima are different. This is due to the fact that the fraction of the eclipsed stellar surface depends on the distance between the stars on orbit. It is also possible due to this point to have only one eclipse, when the stars are near periastron, and that the other eclipse is completely missing.

3.7 Measuring time: heliocentric Julian date

Civil time that we are used to from our daily lives is not practical to time astronomical events; instead, a common practice is to use Julian date (JD). JD gives the number of mean solar days that have passed since the mean Greenwich noon on January 1, 4713 BC. To correct for the Earth's motion, the center of gravity of the Solar system is used as a reference point: this corrects for the fact that a star on the far side of the Sun requires nearly 16 more minutes for its light to reach the Earth than when the Earth is on the same side of the Sun as that star, approximately six months later. For stellar observations where timing to the minute or second is important, it is essential to apply this heliocentric correction: *heliocentric* Julian date is the Julian date referenced to the center of the Sun and can be found using the following equation (Smart, 1977):

$$\begin{aligned}\mathrm{HJD} = \mathrm{JD}\ (\mathrm{Geoc.}) + TR\,[&\cos\lambda_\odot\cos\alpha\cos\delta + \\ &\sin\lambda_\odot\,(\sin\epsilon\sin\delta + \cos\epsilon\cos\delta\sin\alpha)]\,,\end{aligned} \tag{3.40}$$

where $T = 499$ seconds is the light travel time for 1 au, $R = 1$ au is the Sun–Earth distance, $\lambda_\odot$ is the longitude of the Sun, α and δ are the star's right ascension and declination, respectively, and $\epsilon = 23.45°$ is the angle between the ecliptic and the equator. Eq. (3.40) and values of the above given constants are only approximate; one needs to consult accurately computed values published e.g. in Nautical Almanac (2005).

[4] We defer the derivation of these expressions to Section 5.4.

Using HJD corrections is also very important for radial velocities, since the contribution of Earth's motion around the Sun must be properly subtracted. Astronomical data reduction software like `IRAF` (Tody, 1986) compute the HJD correction to sufficient accuracy for most binary star modeling requirements, but it may be deficient for e.g. pulsar timing in X-ray binaries (Galičič, 1999). In such cases it is necessary to apply the barycentric correction: *barycentric* Julian date is the Julian date referenced to the center of gravity of the Solar system. Such correction is computed numerically for each point in time due to significant influence of many celestial bodies on Earth's motion.

3.8 Ephemeris parameters and phase plots

As we have seen in Section 3.5.2, orbital phase Φ needs to be carefully defined to be consistent with the description of apsidal motion and Eq. (2.2) needs to be further refined.

There are 4 parameters that determine the ephemeris of the observed object:

Zero point HJD_0 is a unique point in time that sets the origin of the ephemeris. Adhering to the same convention as the orbital phase, HJD_0 does not in general correspond to superior conjunction of the primary star.

Orbital period P_0 is the sidereal time of revolution of both components in a binary system around the center-of-mass.

Rate of period change dP/dt is the first time derivative of the orbital period:

$$P(\mathrm{HJD}) = P_0(\mathrm{HJD}_0) + \frac{dP}{dt}(\mathrm{HJD} - \mathrm{HJD}_0). \tag{3.41}$$

Phase shift $\Delta\Phi$ is a constant offset to the whole ephemeris introduced as a matter of convenience:

$$\Phi = \mathrm{mod}\left[\frac{\mathrm{HJD} - \mathrm{HJD}_0}{P_0 + \frac{dP}{dt}(\mathrm{HJD} - \mathrm{HJD}_0)}\right] + \Delta\Phi. \tag{3.42}$$

The value of $\Delta\Phi$ is usually 0, but there are several cases when its value is different from 0:

1. a number of people still prefer to set the value of HJD_0 to correspond to the primary minimum because of very efficient methods for determining the times of minima (e.g. Kwee and van Woerden, 1956): $\Delta\Phi$ should then be set to the value of Φ_C;
2. the data supplied to the program may already have been transformed to phases and the original HJDs of observations are not available: $\Delta\Phi$ is then a free variable that may then be determined by the model;
3. the roles of both stars may need to be exchanged: $\Delta\Phi = 0.5$ should then be applied to the ephemeris.

To compute the phase as function of time, we need to solve the following differential equation:

$$d\Phi = \mathrm{mod}\left[\frac{d\mathrm{HJD}}{P(\mathrm{HJD})}\right]. \tag{3.43}$$

If $P \neq P(\mathrm{HJD})$, solving this by simple integration yields exactly Eq. (2.2). If on the other hand P changes linearly in time, we have:

$$\begin{aligned}\Phi(\mathrm{HJD}) &= \mathrm{mod}\left[\int \frac{d\mathrm{HJD}}{P_0 + \dot{P}(\mathrm{HJD} - \mathrm{HJD}_0)}\right] \\ &= \mathrm{mod}\left[\frac{1}{\dot{P}}\log[P_0 + \dot{P}(\mathrm{HJD} - \mathrm{HJD}_0)]\right].\end{aligned} \tag{3.44}$$

The direct consequence of this time-to-phase transformation is that phase points will be smeared if apsidal motion is present in the system. Since apsidal motion changes the argument of periastron ω_0, the conjuntion phase changes according to Eqs. (3.34-3.35). *This is exactly what is being observed and is not a consequence of a poor phase definition.* If we defined zero phase to coincide with conjunctions, we would be measuring the *anomalous* period of the binary rather than the true period and the changes in light curve shape due to the changing value of the argument of periastron would cause *artificial* noise in the phased light curve (c.f. Fig. 25).

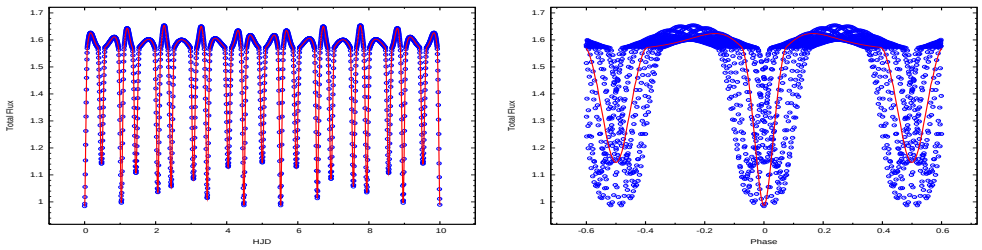

Figure 25: Influence of the changing argument of periastron ω_0 on phased light curve. The data correspond to a fictitous binary with a 1-day period and periastron rate of change $\dot{\omega_0} = 36°/\text{day}$. This value is chosen to best demonstrate the effect of the changing argument of periastron (it takes 10 binary cycles to complete one apsidal cycle) rather than to reflect a typical value of $\dot{\omega_0}$, which is of course orders of magnitude smaller. **Left:** light curve in time space, spanning 10 cycles. **Right:** light curve in phase space, with a theoretical light curve corresponding to the 0th cycle (around $\text{HJD} - \text{HJD}_0 = 0$). Phase smearing is an observational fact rather than a consequence of a flakey phase definition.

4 Radiative properties of binary stars

When we set to quantify the amount of light that hits the detector mounted on a given optical system, we are basically counting photons that reach the detector from the given direction in a given unit of time. The number of detected photons depends on many factors: the intrinsic properties of the observed source of radiation, its inferred distance, the amount of absorption between the source and the observer (e.g. interstellar and atmospheric extinction), response function of the optical system, quantum efficiency of the detector etc. Although several of these contributions may be readily quantified, not all of them can and because of that it is not always straight-forward to draw conclusions about the light source itself. Yet photon counting is all we have and it is up to the model to determine intrinsic properties of the light source.

In a binary star field, a common practice is to reverse this logic and set up a model in such a way that it describes the light intrinsically, i.e. independently of the position of the observer. This somewhat specific approach enables us to build the model on physical and geometrical properties of the system alone, obtaining the relative measure of the light that is emitted by the binary in a given direction and a given moment in time. Once the distance to the observer is inferred, the number of photons that reach the observer's detector will have been possible to predict. That is why, as it shall be elaborated later in this section, the description of radiative properties of binary stars is based on intensity rather than flux. This is also why special care must be taken to properly introduce these photometric quantities.

§

The light we observe from the components of a binary system depends not only on the geometrical configuration, but also on the distribution of physical parameters (such as temperature and gravity acceleration) over the stellar surface. The distribution is non-uniform because of tidal and rotational distortion of both stars.

The amount of distortion of the stellar surface depends on the value of effective potential Ω. We have already discussed in Section 3.3 the implications of different values of Ω on morphological types of binary stars; the deviation from a spherical form also causes non-uniform distribution of the normal[5] emergent intensity. To study it, we need to relate a local surface element normal $\hat{\mathbf{e}}_\mathbf{n}$ with the unity radius vector $\hat{\mathbf{e}}_\mathbf{r}$. Fig. 26 shows a semi-detached,

[5]Emergent intensity along the normal to the surface element.

lobe-filling component with a distorted surface element. Since the gradient of the potential is always perpendicular to equipotential surfaces and it points inward, the surface element normal may be written as:

$$\hat{\mathbf{e}}_{\mathbf{n}} = -\frac{\nabla\Omega(\lambda,\mu,\nu)}{\|\nabla\Omega(\lambda,\mu,\nu)\|}, \tag{4.1}$$

where λ, μ and ν are the direction cosines as defined by Eq. (3.8). On the other hand, the unity radius vector is simply given by:

$$\hat{\mathbf{e}}_{\mathbf{r}} = (\lambda,\mu,\nu). \tag{4.2}$$

To determine the angle γ between the two vectors, we need to evaluate a dot-product of the two:

$$\cos\gamma = \hat{\mathbf{e}}_{\mathbf{n}}\cdot\hat{\mathbf{e}}_{\mathbf{r}} = -\frac{\lambda\frac{\partial\Omega}{\partial x}+\mu\frac{\partial\Omega}{\partial y}+\nu\frac{\partial\Omega}{\partial z}}{\|\nabla\Omega(\lambda,\mu,\nu)\|}, \tag{4.3}$$

where the gradient magnitude $\|\nabla\Omega(\lambda,\mu,\nu)\|$ is given by:

$$\|\nabla\Omega(\lambda,\mu,\nu)\| = \sqrt{\left(\frac{\partial\Omega}{\partial x}\right)^2+\left(\frac{\partial\Omega}{\partial y}\right)^2+\left(\frac{\partial\Omega}{\partial z}\right)^2} \tag{4.4}$$

and individual partial derivatives of effective potential follow from Eq. (3.16):

$$\begin{aligned}
\frac{\partial\Omega}{\partial x} &= -\frac{x}{(x^2+y^2+z^2)^{3/2}}+\frac{q(d-x)}{([d-x]^2+y^2+z^2)^{3/2}}+F^2(1+q)x-\frac{q}{d^2},\\
\frac{\partial\Omega}{\partial y} &= -y\left[\frac{1}{(x^2+y^2+z^2)^{3/2}}+\frac{q}{([d-x]^2+y^2+z^2)^{3/2}}-F^2(1+q)\right],\\
\frac{\partial\Omega}{\partial z} &= -z\left[\frac{1}{(x^2+y^2+z^2)^{3/2}}+\frac{q}{([d-x]^2+y^2+z^2)^{3/2}}\right].
\end{aligned} \tag{4.5}$$

This allows us to explicitly write the surface element $d\sigma$:

$$d\sigma(\lambda,\mu,\nu) = \frac{\varrho^2(\lambda,\mu,\nu)\sin\theta}{\cos\gamma(\lambda,\mu,\nu)}d\theta d\phi, \tag{4.6}$$

where $\varrho = r/a$ is the dimensionless radius as defined on page 23. Integrating this equation over all surface elements yields the total surface of the distorted star:

$$S = \int_{\partial V} d\sigma(\lambda,\mu,\nu) = \int_0^{2\pi}\int_0^{\pi}\frac{\varrho^2(\theta,\phi)\sin\theta}{\cos\gamma(\theta,\phi)}d\theta d\phi. \tag{4.7}$$

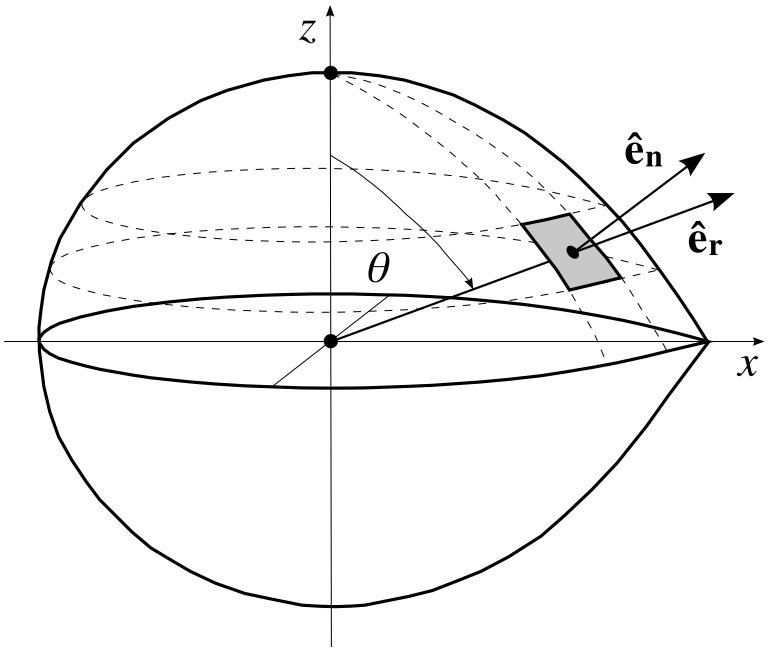

Figure 26: Surface distortion of a lobe-filling component. Unit vectors $\hat{\mathbf{e}}_\mathbf{r}$ and $\hat{\mathbf{e}}_\mathbf{n}$ enclose an angle γ that increases with distortion of the stellar surface.

In a similar fashion, the volume of the star may be obtained by integrating over all volume elements:

$$V = \int_V dV(\lambda,\mu,\nu) = \int_0^{2\pi}\int_0^{\pi}\int_0^{\varrho(\theta,\phi)} \varrho^2(\theta,\phi)\sin\theta dr d\theta d\phi. \tag{4.8}$$

Surface S determines an important global property of the distorted star: its effective temperature. For the given bolometric luminosity, effective temperature is given by:

$$L_{\rm bol} = \sigma S T_{\rm eff}^4 \Rightarrow T_{\rm eff} = \left(\frac{L_{\rm bol}}{\sigma S}\right)^{1/4}. \tag{4.9}$$

It is a *single* quantity for the whole star.

4.1 Emergent intensity

Distortion of stellar surfaces does not only influence the appearence of the star, it also causes a non-uniform distribution of emergent intensity over the surface. Monochromatic intensity (c.f. Fig. 27) is given by:

$$I_\lambda = \frac{dE}{d\lambda dA\cos\theta d\Omega dt}, \tag{4.10}$$

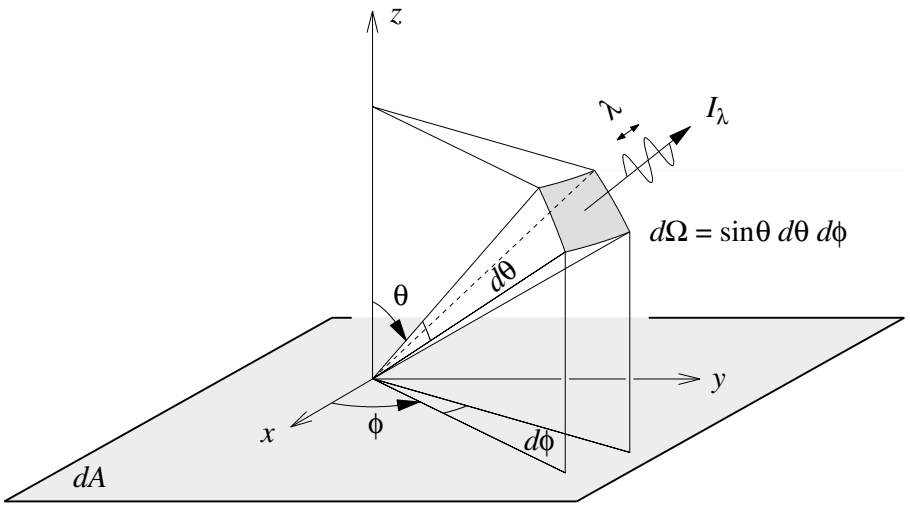

Figure 27: Monochromatic emergent intensity I_λ. It gives the amount of energy dE emitted by the star to a solid angle $d\Omega$, on the wavelength interval $[\lambda, \lambda + d\lambda]$, passing through a projected surface $dA\cos\theta$ in a time interval dt. Adopted from Carroll and Ostlie (1995).

where dE is the amount of energy emitted by the star to a solid angle $d\Omega$, on the wavelength interval $[\lambda, \lambda + d\lambda]$, passing through a projected surface $dA\cos\theta$ in a time interval dt (Carroll and Ostlie, 1995). The units of intensity I_λ are thus $\mathrm{J\,m^{-3}\,sr^{-1}\,s^{-1}}$ (or $\mathrm{erg\,cm^{-3}\,sr^{-1}\,s^{-1}}$ in cgs units). Since the intensity is given per solid angle cone $d\Omega \to 0$, the energy dE of the light ray that travels in vacuum does not dissipate and the intensity remains constant along the whole ray.

Integrating monochromatic intensity over solid angle and normalizing by 4π yields the *mean* monochromatic intensity:

$$\langle I_\lambda \rangle = \frac{1}{4\pi} \int I_\lambda d\Omega = \frac{1}{4\pi} \int_0^{2\pi} \int_0^{\pi} I_\lambda \sin\theta d\theta d\phi. \tag{4.11}$$

Another important photometric quantity is monochromatic flux. It is defined by the amount of overall energy emitted along the surface normal (z-axis) in the wavelength interval $[\lambda, \lambda + d\lambda]$ in time interval dt:

$$J_\lambda d\lambda dA dt = \int dE = \int I_\lambda \cos\theta d\Omega. \tag{4.12}$$

Depending on whether the light source is resolved or not, the instrument measures intensity or flux, respectively. Since flux is the integral over the

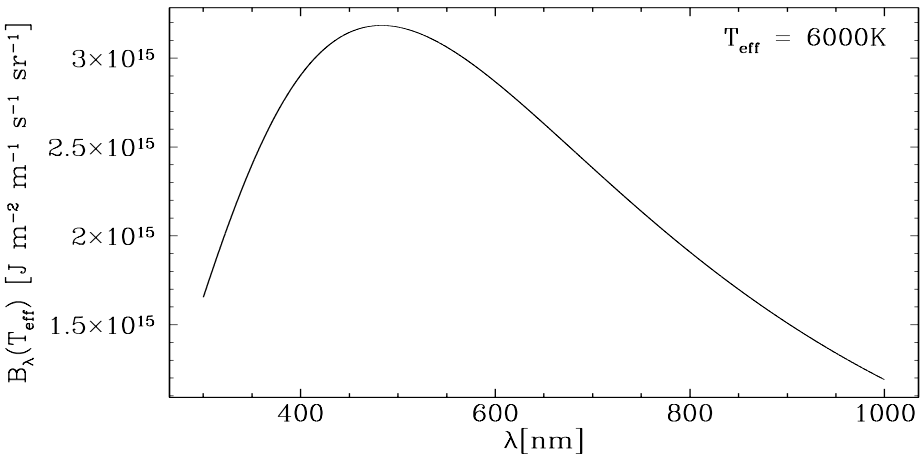

Figure 28: Planck function B_λ for $T_{\text{eff}} = 6000\text{K}$ black-body radiation.

solid angle, it depends on the distance: $J \propto d^{-2}$. By integrating monochromatic flux over a certain wavelength range, we obtain the *passband* flux (or bolometric flux, in case we integrate over all wavelengths):

$$J_{\text{passband}} = \int_\lambda J_\lambda \mathcal{T}_\lambda d\lambda, \tag{4.13}$$

where $\mathcal{T}_\lambda$ is the passband transmission function.

§

To demonstrate the application of radiation formalism to binary stars, consider a simplistic example of a black-body radiation that is described by the Planck's function:

$$B_\lambda(T) = \frac{2hc^2}{\lambda^5} \frac{1}{e^{hc/\lambda kT} - 1}, \tag{4.14}$$

where $h = 6.6262 \cdot 10^{-34}\,\text{J s}$ is the Planck constant, $k = 1.3806 \cdot 10^{-23}\,\text{J/K}$ is the Boltzmann constant, $c = 2.99793 \cdot 10^8\,\text{m/s}$ is the speed of light, T is the effective temperature and λ is the wavelength. Planck's function $B_\lambda(T)$ has the units of intensity, namely $\text{J m}^{-3}\,\text{sr}^{-1}\,\text{s}^{-1}$. Fig. 28 depicts the $T = 6000\,\text{K}$ black-body radiation curve.

In this simplistic approach, stellar atmospheres may be regarded as layers stacked on top of one another, where the flux on the stellar surface is only outward oriented. Rewriting Eq. (4.12) as a contribution of two integrals, one outward and the other inward of the stellar surface:

$$J_\lambda = \int_0^{2\pi} \int_0^{\pi/2} I_\lambda \cos\theta \sin\theta d\theta d\phi + \int_0^{2\pi} \int_{\pi/2}^{\pi} I_\lambda \cos\theta \sin\theta d\theta d\phi \tag{4.15}$$

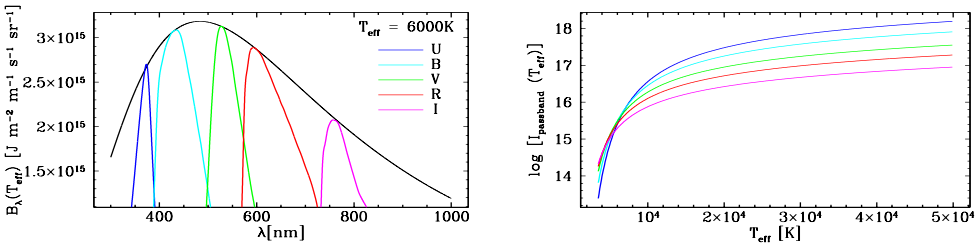

Figure 29: Normal emergent intensity of the passband. Left: a convolution between the Planck function for $T_{\rm eff} = 6000\,{\rm K}$ (dotted line) and the Bessell (1990) UBVRI filter-set transmission functions. Right: logarithm of the normal emergent intensity of the five passbands in the same units. Passband data taken from Moro and Munari (2000), electronically available from `http://ulisse.pd.astro.it/Astro/ADPS/`.

we notice that the second term vanishes since there is no inward flux. Assuming that intensity is direction-independent, we may perform the integration of the remaining term to obtain Lambert's law:

$$J_\lambda = 2\pi I_\lambda \int_0^{\pi/2} \sin\theta\cos\theta d\theta = \pi I_\lambda. \tag{4.16}$$

To obtain the flux that is passed in a particular passband, the monochromatic flux 4.12 has to be convolved with the passband transmission function $\mathcal{T}_\lambda$ and integrated over the passband's wavelength span:

$$J_{\rm passband} = \pi \int_\lambda B_\lambda(T_{\rm eff})\mathcal{T}_\lambda d\lambda, \tag{4.17}$$

where the factor π comes from Eq. (4.16).

This flux is transformed back into intensity by dividing the flux with the integral of the passband transmission function:

$$I_{\rm passband} = \frac{J_{\rm passband}}{\int \mathcal{T}_\lambda d\lambda}. \tag{4.18}$$

This way we obtain normal emergent intensity of the passband. Fig. 29 shows a convolution between the black-body spectrum and the Bessell (1990) UBVRI filter-set transmission functions (left) and the logarithm of the normal emergent intensity of the passband as function of effective temperature (right).

4.2 Kurucz's model atmospheres

In the actual every-day modeling black body approximation is only seldom appropriate: real spectra are far from being adequately described by the continuum without any line blanketing. For that reason people have been building numerical codes capable of producing sophisticated synthetic spectra based on huge databases of spectral lines. These codes are usually referred to as model atmospheres.

There have been many attempts to model stellar atmospheres; a fairly recent review over this overwhelming field was done by Hubeny et al. (2003). Out of the crowd emerge three particular model atmospheres, Kurucz (1996)'s `ATLAS12`, Gustafsson (1983)'s `MARCS` and Hauschildt et al. (1999)'s `NextGen`. Although the latter two are arguably more sophisticated, they are not publicly available and their usage is restrictive. That is why a somewhat older, yet still powerful, Kurucz's model atmospheres are the most prominent numerical code of today. For a fair comparison between `ATLAS` and `NextGen` refer to Bertone et al. (2004).

Kurucz's model atmospheres are built on the formalism of radiative equilibrium, with the following assumptions (Kurucz, 1970):

Plane-parallel layers. The thickness of the photosphere is much smaller than the radius of the star. The photosphere may thus be approximated with a plane model, where values of all physical quantities depend on a single spatial coordinate, the height.

Homogeneous layers. All physical properties of a given layer are constant throughout that layer. Any fine-structure features like granulation, spots and similar are neglected.

Hydrostatic equilibrium. The outward pressure force on the photosphere is exactly balanced by gravity. Any net vertical movement of the gas, buoyancy and/or mass-loss are neglected.

Local thermodynamic equilibrium (LTE). Individual small volumes of the photosphere act as black bodies, so that their state depends only on local thermodynamic variables (temperature, pressure, density) that are related by the equation of state.

Steady state. Any time-changing dynamical properties of the gas are discarded.

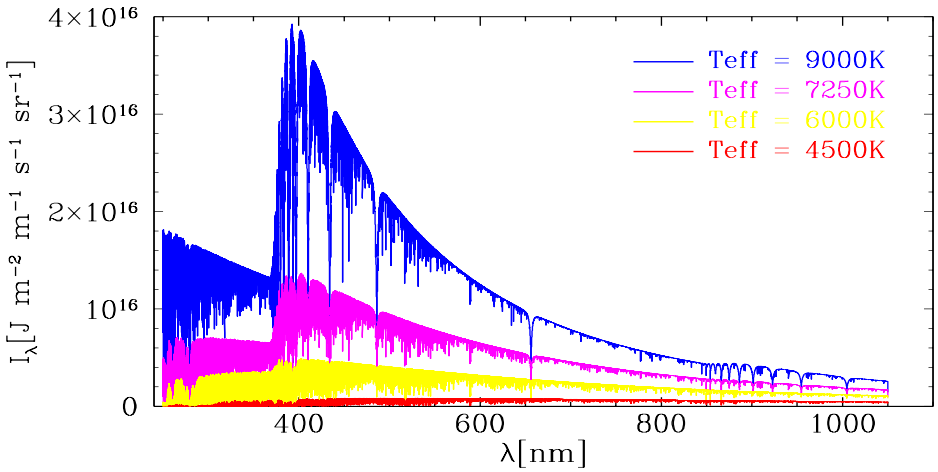

Figure 30: Kurucz's synthetic spectra. Colors denote effective temperatures of the model. Other parameters are the same for all four models: $v_{\rm rot} = 0$, $\log g/g_0 = 4.0$ and [M/H]= 0.0.

Radiative and/or convective equilibrium. There are no sources or sinks of energy within the photosphere: the total flux that passes through the photosphere is conserved from layer to layer.

Chemical balance. Abundance of chemical elements is constant througout the photosphere.

Fig. 30 depicts four synthetic spectra for different effective temperatures. It is evident that the spectral energy distribution doesn't resemble that of a black-body radiation depicted on Fig. 28, particularly in the vicinity of the Balmer jump.

Kurucz's model atmospheres have been well studied and applied to numerous astrophysical problems. They are far from being ideal for binary stars, since due to the above cited assumptions their validity for distorted binary system components is clearly broken. Still, they are quite satisfactory for describing detached binaries, as was shown by dedicated photospheric studies by Terrell et al. (2003), Marrese et al. (2004b), Siviero et al. (2004) and others.

4.3 Gravity darkening

The distribution of intensity over the stellar disk depends on the dominant energy transfer mechanism in a stellar envelope. The mechanism is primarily determined by the effective temperature of the star: for $T_{\text{eff}} > 8000\,\text{K}$ the envelope is in a predominantly radiative equilibrium, for $T_{\text{eff}} < 5000\,\text{K}$ the envelope is in a predominantly convective equilibrium (Claret, 1999); in-between, both mechanisms significantly contribute to the energy transfer.

For a rotating star in a strict radiative equilibrium, a pioneering work by von Zeipel (1924) has shown that the flux distribution over the surface is proportional to the effective gravity:

$$J_\lambda = -\frac{16\sigma T^3}{3\bar{\kappa}\rho}\frac{dT}{d\Omega}g^\beta, \tag{4.19}$$

where $\sigma = 5.67 \cdot 10^{-8}\text{W}\,\text{m}^{-2}\,\text{K}^{-4}$ is the Stefan-Boltzmann constant, T is the local surface temperature, $\bar{\kappa}$ is the Rosseland opacity coefficient, ρ is the density of the gas, g is the local gravity acceleration and β is the introduced gravity darkening coefficient, for which von Zeipel (1924) rigorously showed that $\beta = 1$ for strictly radiative envelopes. Eq. (4.19) implies that the equatorial regions are darker than the polar ones, hence the name gravity darkening[6]. The local temperature may also be coupled to the gravitational acceleration:

$$T \propto J^{1/4} \Rightarrow T \propto g^{1/4}. \tag{4.20}$$

The generalized formalism of computing the value of the gravity darkening coefficient β for radiative envelopes was presented later by Kippenhahn (1977).

Predictions on gravity darkening of purely convective envelopes were first done by Lucy (1967), who used convective stellar envelope models to compute the average value $\beta = 0.32$ for Solar-type stars. The driving idea of Lucy's study was that within the fully convective zone the gradient of the specific entropy is 0. His predictions for the gravity darkening coefficient were later confirmed observationally by Rafert and Twigg (1980), who have obtained the average value $\beta = 0.31$ for the sample of 28 stars.

Putting the two results for radiative and convective equilibrium together, gravity darkening is given by:

$$J = J_{\text{pole}}\left(\frac{g}{g_{\text{pole}}}\right)^\beta, \quad \beta = \begin{cases} 1.00 & \text{for radiative envelopes} \\ 0.32 & \text{for convective envelopes} \end{cases} \tag{4.21}$$

[6]There is a tendency to change the naming convention from gravity darkening to gravity *brightening* (e.g. Kallrath et al., 1998), but this work retains the original nomenclature as set by von Zeipel (1924) and Lucy (1967).

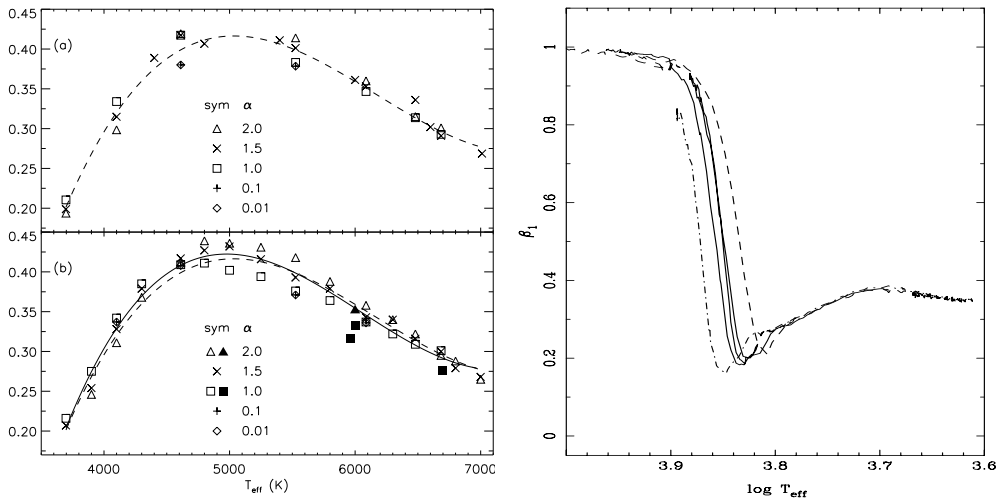

Figure 31: Temperature dependence of the gravity darkening coefficient β for convective envelopes. Left: results for grey (continuum) and non-grey (line-blanketed) model atmospheres computed by Alencar and Vaz (1997). Different symbols correspond to different convection efficiency coefficients $\alpha = 1/H_p$. Right: results of stellar evolution models computed by Claret (1999). Different lines denote different hydrogen abundances: solid line depicts $X = 0.7$, dashed line depicts $X = 0.6$ and dot-dashed line depicts $X = 0.8$.

Factor:

$$\mathcal{G} = \frac{J}{J_{\rm pole}} = \left(\frac{g}{g_{\rm pole}}\right)^{\beta} \tag{4.22}$$

is called the gravity darkening correction. Eq. (4.21) may be rewritten in terms of local temperature:

$$T = T_{\rm pole}\left(\frac{g}{g_{\rm pole}}\right)^{\beta/4}. \tag{4.23}$$

Two later studies by Alencar and Vaz (1997) and Alencar et al. (1999) followed Lucy's approach of attributing gravity darkening to stellar atmospheres; they used non-illuminated and illuminated Uppsala model atmospheres (Gustafsson, 1983) respectively, deriving an empirical formula for $\beta(T_{\rm eff})$, depicted in Fig. 31 (left). The results indicate agreement with Lucy's estimate only at temperatures $\sim 6500\,$K, although the discrepancy for other temperatures is not strikingly strong.

Since gravity darkening effect depends on the circumstances in stellar envelopes, it is related not only with atmospheric parameters ($T_{\rm eff}$ and $\log\, g/g_0$),

but also with the internal stellar structure and the star's rotation properties. This point was first stressed by Claret (1999), who introduced the computation of gravity darkening coefficients into the stellar evolution code. Statistical studies based on this new formalism (Claret, 2000b, Fig. 1 therein) yielded a more accurate theoretical prediction for stellar envelopes where both radiation and convection contribute significantly to the energy transfer. Fig. 31 (right) shows the results of Claret's study, depicting the dependency of β for three different hydrogen abundances. It should be emphasized that at the actual level of light curve quality of eclipsing binaries it is not possible to discriminate effects of third order in the gravity darkening exponents such as chemical composition, theory of convection, irradiation, etc.

4.4 Limb darkening

Picking up the discussion from Section 4.1, we need to take into consideration that emergent light from the star passes through the stellar atmosphere, where a fraction of it is absorbed[7] by means of bound-bound transitions, bound-free absorption (photoionization), free-free absorption and electron scattering:

$$dI_\lambda = -\kappa_\lambda \rho I_\lambda dx, \tag{4.24}$$

where κ_λ is the absorption coefficient, ρ is the density of the gas that forms the atmosphere, and dx is the travelled distance. Absorption coefficient is generally a function of the composition, density and temperature of the gas: $\kappa_\lambda = \kappa_\lambda([\mathrm{M/H}], \rho, T_{\mathrm{eff}})$. Typical values of κ_λ for solar-type stars are $2.64 \cdot 10^{-2}\,\mathrm{m^2\,kg^{-1}}$ at $\lambda = 500\,\mathrm{nm}$ (Carroll and Ostlie, 1995).

Since we are observing intensity *back along* the emergent path, it is convenient to define optical depth τ_λ as:

$$d\tau_\lambda = -\kappa_\lambda \rho dx \quad \Rightarrow \quad dI_\lambda = I_\lambda\, d\tau_\lambda. \tag{4.25}$$

The τ_λ defined in this way assumes $\tau_\lambda = 0$ at the top of the photosphere, growing gradually towards the interior of the star. Connected to the definition of optical depth is the optical thickness of the gas: for $\tau_\lambda \gg 1$ the gas is said to be optically *thick*, while for $\tau_\lambda \ll 1$ it is said to be optically *thin*.

The opposite mechanism to gas absorption is gas emission, which is due to scattering, bound-bound emission and recombination:

$$dI_\lambda = j_\lambda \rho dx, \tag{4.26}$$

[7]Detailed description of the absorption processes may be found in any textbook on stellar atmospheres, e.g. Gray (1992), Chapters 8 and 11.

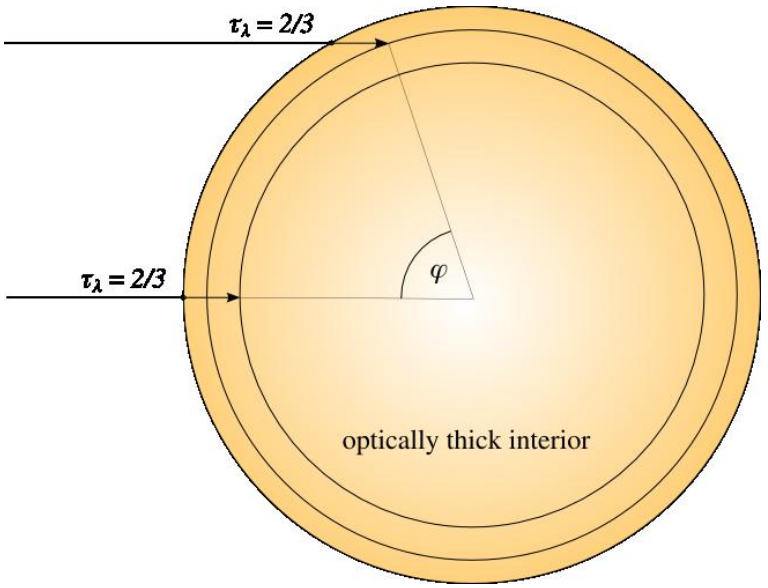

Figure 32: Limb darkening effect. A common way to analytically quantify the optical depth of the visible photospheric surface is to adopt a model of a plan-parallel grey atmosphere: planar layers are stacked on top of each other and the absorption coefficient κ_λ is assumed to be wavelength-independent, hence grey (this is not a realistic model, since all absorption processes except Thompson scattering are wavelength-dependent, but it does a good job in setting the basic principles). Following Eddington's approximation (see Carroll and Ostlie (1995) for details on derivation), we find that the reference surface where $T = T_{\rm eff}$ is at $\tau_\lambda = 2/3$.

where j_λ is the emission coefficient of the gas. Note that the contribution of emission to the emergent intensity is independent of the intensity I_λ itself.

The *net* change in emergent intensity is the sum of both emission and absorption:

$$dI_\lambda = j_\lambda \rho dx - \kappa_\lambda \rho I_\lambda dx. \tag{4.27}$$

The ratio of the rates at which the competing processes of emission and absorption occur determine how rapidly the intensity of the beam changes. Dividing Eq. (4.27) by $-\kappa_\lambda \rho dx$ yields:

$$\frac{dI_\lambda}{d\tau_\lambda} \equiv -\frac{1}{\kappa_\lambda \rho}\frac{dI_\lambda}{dx} = I_\lambda - \frac{j_\lambda}{\kappa_\lambda} \equiv I_\lambda - \mathcal{S}_\lambda, \tag{4.28}$$

where $\mathcal{S}_\lambda = j_\lambda/\kappa_\lambda$ is called the source function and Eq. (4.28) is called the equation of radiative transfer.

If the dependence of the source function $\mathcal{S}_\lambda$ on the optical depth τ_λ was known, Eq. (4.28) could be integrated to find emergent intensity as a function of position on the stellar disk, φ (c.f. Fig. 32). Since it is not, this dependence needs to be assumed. The simplest assumption is a linear dependence:

$$\mathcal{S}_\lambda = a_\lambda + b_\lambda \tau_\lambda, \tag{4.29}$$

where a_λ and b_λ are wavelength-dependent coefficients that need to be determined. Integrating[8] Eq. (4.28) yields the intensity at the top of the atmosphere:

$$I_\lambda(\varphi) = a_\lambda + b_\lambda \cos\varphi. \tag{4.30}$$

The ratio between the intensity at the given value of φ and the normal emergent intensity at $\varphi = 0$:

$$\mathcal{L}(\varphi) = \frac{I_\lambda(\varphi)}{I_\lambda(0)} \tag{4.31}$$

is called the limb darkening correction. The normal emergent intensity $I_\lambda(0)$ is computed by Eq. (4.14) when using a black-body approximation, and by the corresponding analogue of Eq. (4.18) for the passband intensity computed from model atmospheres (c.f. Section 4.2). Writing out Eq. (4.31) explicitly for the linear dependence given by Eq. (4.30) yields:

$$\mathcal{L}(\varphi) = 1 - x_\lambda + x_\lambda \cos\varphi, \qquad x_\lambda := \frac{b_\lambda}{a_\lambda + b_\lambda}. \tag{4.32}$$

Note that here only one limb-darkening coefficient suffices to describe the modeled law. This is the simplest, linear version of the limb-darkening law. Two of the more commonly used laws are the logarithmic limb darkening law due to Klinglesmith and Sobieski (1970):

$$\mathcal{L}(\varphi) = 1 - x_\lambda + x_\lambda \cos\varphi - y_\lambda \cos\varphi \log(\cos\varphi) \tag{4.33}$$

and the square-root limb darkening law due to Diaz-Cordoves and Gimenez (1992):

$$\mathcal{L}(\varphi) = 1 - x_\lambda + x_\lambda \cos\varphi - y_\lambda(1 - \sqrt{\cos\varphi}). \tag{4.34}$$

Thorough studies by Diaz-Cordoves and Gimenez (1992) and van Hamme (1993) have shown that towards the longer wavelengths and in the IR, a square root law gives the best results. In the UV the roles are reversed and a logarithmic law is better for all types of stars. In the optical region,

[8]The actual integration is prolonged and is omitted here on account of brevity. For details please refer e.g. to Carroll and Ostlie (1995) or any other similar textbook.

better results are obtained using a logarithmic law in the case of late-type stars ($T < 9000\,\mathrm{K}$) and a square root law in the case of early-type stars ($T > 9000\,\mathrm{K}$). These two laws are an order of magnitude more precise than the linear law. van Hamme (1993) has also shown that any additional terms to the linear law of the form $y_\lambda(1 - \cos\varphi)^p$ for the given value of p yield results of a comparable accuracy to the two non-linear laws, with the notable drawback that the exponent p is wavelength-dependent.

4.5 Reflection effect

When components of the binary system are close, i.e. when their radii are of the order $\sim 15 - 20\%$ of their separation or more (Wilson, 1990), the surface irradiation of one component by another becomes important. The irradiating flux heats the surface of the irradiated star, increasing the temperature. This effect is somewhat confusingly[9] called the reflection effect.

Before we develop the formalism to account for reflection effect, one may ask in how many cases does the reflection effect play a significant role in contributing to the overall flux of the irradiated component; it has been shown throughout the literature that there is indeed quite a number of such cases, particularly when the stars are close and comparable in size and effective temperature (Hilditch et al., 1996), in cataclysmic and pre-cataclysmic binaries (Pigulski and Michalska, 2002), and rapidly-rotating Algols (Olson and Etzel, 1994).

Reflection effect was first derived moderately recently by Wilson (1990); before only approximative solutions existed of limited value – see e.g. a thorough review by Vaz (1985) on this topic.

Consider a close binary as depicted on Fig. 33. If we are to properly account for the heating of a given surface element $d\sigma_1$ on the primary star, contributions to irradiation of all surface elements $d\sigma_2$ on the secondary star must be taken into account. Following the energy conservation principle, let us recall that heating is a bolometric process, whereas reradiation is a wavelength-dependent process, according to the given spectral energy distribution function (Planck, Kurucz, ...). Bolometric emergent intensity I_2^{bol} from surface element $d\sigma_2$ may be expressed with normal bolometric emergent

[9]Term "reflection" would insinuate a more geometrical meaning, whereas reflection effect, as traditionally named in the field of binary stars, refers to the heating of the surface of irradiated star.

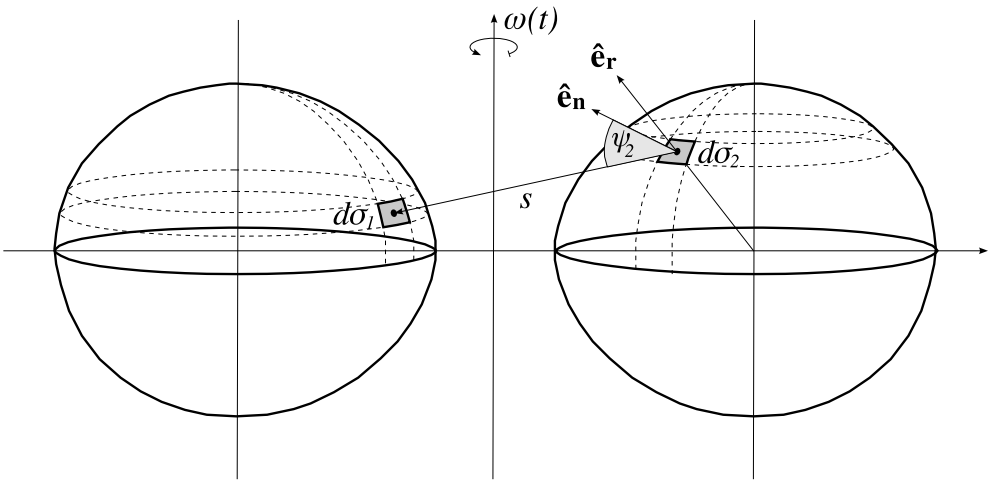

Figure 33: Irradiation of the primary star (left) by the secondary star (right). To properly account for the heating of the surface element $d\sigma_1$ on the primary star, contributions to irradiation of all surface elements $d\sigma_2$ on the secondary star must be summed up. Angle ψ_2 is the angle between the surface normal $\hat{\mathbf{e}}_\mathbf{n}$ and the line connecting the two surface elements s. Its counterpart ψ_1 is omitted for sake of Figure clarity. Angles γ_1 and γ_2 between $\hat{\mathbf{e}}_\mathbf{n}$ and $\hat{\mathbf{e}}_\mathbf{r}$ are also omitted. The depicted binary consists of two equal stars with $\Omega = 4.0$ on circular orbit.

intensity $I^{\rm bol}_{2\perp}$ and bolometric limb darkening correction $\mathcal{L}^{\rm bol}_2(\psi_2)$:

$$I^{\rm bol}_2 = I^{\rm bol}_{2\perp} \cos\psi_2 \mathcal{L}^{\rm bol}_2(\psi_2), \tag{4.35}$$

where ψ_2 is the angle between the $d\sigma_2$ surface normal and the line s that connects the two surface elements. Normal emergent intensity $I^{\rm bol}_\perp$ at surface element $d\sigma_1$ is computed from the polar emergent intensity $I^{\rm bol}_{\rm polar}$ and the gravity darkening correction[10] given by Eq. (4.22), following the same procedure as outlined in the black-body example in Section 4.1, namely using Eq. (4.18), but integrating over all wavelengths and using Kurucz's spectral energy distribution function instead of the Planck function. The term $\cos\psi_2$ in Eq. (4.35) projects only the fraction of the normal emergent intensity $I^{\rm bol}_{2\perp}$ that is radiated toward the surface element $d\sigma_1$. Finally, the term $\mathcal{L}^{\rm bol}_2(\psi_2)$ is the bolometric limb-darkening correction of intensity coming from the surface element $d\sigma_2$ as seen from the surface element $d\sigma_1$, due to a different optical depth visible at different surface elements over the irradiating star.

The obtained emergent intensity contributes to the flux according to the

[10]Note that Eq. (4.22) defines gravity darkening correction with respect to *flux* and not intensity, but since these are bolometric values (integrated over all wavelengths), this correction is still rigorous.

bolometric counterpart of Eq. (4.12), where the projection toward $d\sigma_1$ was already taken into account in Eq. (4.35):

$$dJ_2^{\rm bol} = I_2^{\rm bol} d\Omega = I_2^{\rm bol} \frac{d\sigma_2}{s^2}, \tag{4.36}$$

where $d\sigma$ is given by Eq. (4.6), yielding:

$$dJ_2^{\rm bol} = I_{2\perp}^{\rm bol} \cos\psi_2 \mathcal{L}_2^{\rm bol}(\psi_2) \frac{\varrho^2 \sin\theta}{s^2 \cos\gamma} d\theta d\phi. \tag{4.37}$$

The amount of flux $dJ_2^{\rm bol}$ emitted from $d\sigma_2$ that is perpendicular to $d\sigma_1$ is then given simply by:

$$dJ_{2\to1}^{\rm bol} = dJ_2^{\rm bol} \cos\psi_1 = I_{2\perp}^{\rm bol} \cos\psi_1 \cos\psi_2 \mathcal{L}_2^{\rm bol}(\psi_2) \frac{\varrho^2 \sin\theta}{s^2 \cos\gamma} d\theta d\phi. \tag{4.38}$$

What remains to be done is to integrate this expression over the surface of the irradiating star, where we need to take into account that the irradiating star is also heated by the irradiated star (in the exactly analogous way), causing the excess of the emergent flux:

$$J_{2\to1}^{\rm irradiating} = \mathcal{R}_2 \int dJ_{2\to1}^{\rm bol}, \tag{4.39}$$

where $\mathcal{R}_2$ is the excess of the total radiated flux over the flux that would be radiated in absence of heating. It is a single coefficient for each star that needs to be determined iteratively in such a way that the total energy is conserved.

The fraction of $J_{2\to1}^{\rm irradiating}$ that actually heats the irradiated star depends on the bolometric albedo A_1, which is the local ratio of reradiated energy to irradiance energy:

$$\begin{aligned} J_{2\to1}^{\rm entrant} &= A_1 J_{2\to1}^{\rm irradiating} \\ &= A_1 \mathcal{R}_2 \iint I_{2\perp}^{\rm bol} \cos\psi_1 \cos\psi_2 \mathcal{L}_2^{\rm bol}(\psi_2) \frac{\varrho^2 \sin\theta}{s^2 \cos\gamma} d\theta d\phi. \end{aligned} \tag{4.40}$$

The entrant bolometric flux heats the star, causing its local temperature at surface element $d\sigma_1$ to raise. To quantify how much, we need to evaluate the ratio of entrant bolometric flux to the total intrinsic emergent flux $J_1^{\rm tot}$ from $d\sigma_1$. The latter is given by:

$$J_1^{\rm tot} = I_{1\perp}^{\rm bol} \int_{2\pi} \mathcal{L}_1^{\rm bol}(\psi) \cos\psi d\Omega, \tag{4.41}$$

where we have again implicitly used gravity darkening correction to obtain local emergent intensity $I_{1\perp}^{\rm bol}$. The ratio between the two gives the excess in total emergent flux:

$$\mathcal{R}_1 = 1 + \frac{J_{2\to1}^{\rm entrant}}{J_1^{\rm tot}}, \qquad \mathcal{R}_2 = 1 + \frac{J_{1\to2}^{\rm entrant}}{J_2^{\rm tot}}. \tag{4.42}$$

It follows immediately that the new effective temperature at a given surface element follows from the conservation of energy:

$$T_{\rm eff\,1}^{\rm new} = T_{\rm eff\,1}^{\rm orig}\mathcal{R}_1^{1/4}, \tag{4.43}$$

$$T_{\rm eff\,2}^{\rm new} = T_{\rm eff\,2}^{\rm orig}\mathcal{R}_2^{1/4}. \tag{4.44}$$

Eqs. (4.40) and (4.42) are solved iteratively, from the chosen values $\mathcal{R}_1 = \mathcal{R}_2 = 1$ to their converged values, so they are invisible to the outside; the only change that is exhibited by the star is the change of local temperature at irradiated surface elements.

The above procedure may be repeated iteratively any number of times to accomodate for multiple reflections: the emergent flux from the primary star is now attributed with heating by the secondary star, which in turn causes stronger irradiation of the secondary star by the primary. Unfortunately, Wilson (1990) has shown that this limit cannot be computed analytically, so numerical approaches must be applied.

4.6 Ellipsoidal variations

Another significant effect arises due to stellar surface distortion, which is aspect-dependent: variation of the overall flux caused by the variation of the size of visible parts of the star. Since the star is oblate due to tidal forces and rotation, we see a larger surface cross-section when the stars are oriented side-ways, hence around quarter-phases. On the other hand we see a smaller surface cross-section when we are looking along the semi-major axis, hence around phases 0.0 and 0.5. This effect is referred to as ellipsoidal variation of the light curve; Fig. 34 shows an example of ellipsoidal variation of a non-eclipsing semi-detached binary with depicted orientation of both components in critical phases. The effect is present even if a binary isn't eclipsing, for as long as the inclinations are not too low (i.e. smaller than 10°, c.f. Fig. 35). When we are observing a binary face-on, there can be no ellipsoidal variations, because we are seeing a constant surface cross-section.

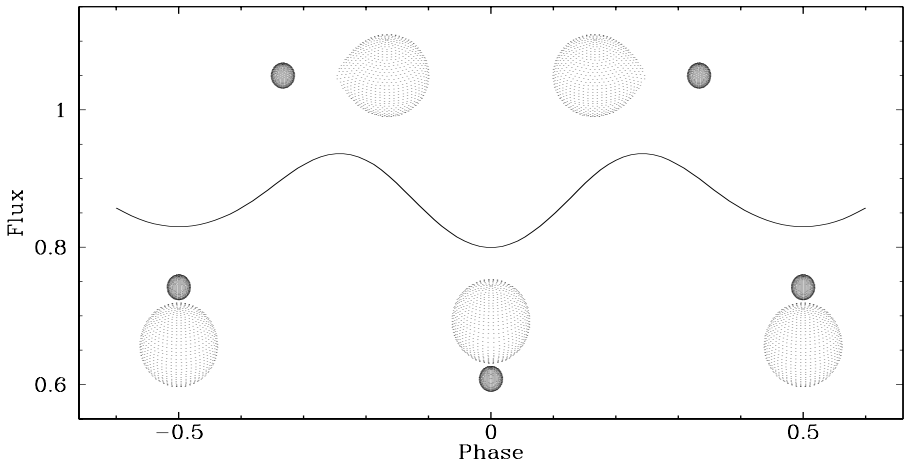

Figure 34: Light curve variation of a semi-detached binary due to ellipsoidal variations. Shape distortion of the lobe-filling component causes the total surface that is visible to the observer to change with phase. Stellar shapes are depicted in phases -0.5, -0.25, 0.0, 0.25 and 0.5, that correspond to minima and maxima of the light curve. The inclination of the system $i = 60°$ is chosen so that the light curve exhibits no eclipses: the variation is exclusively due to ellipsoidal variations.

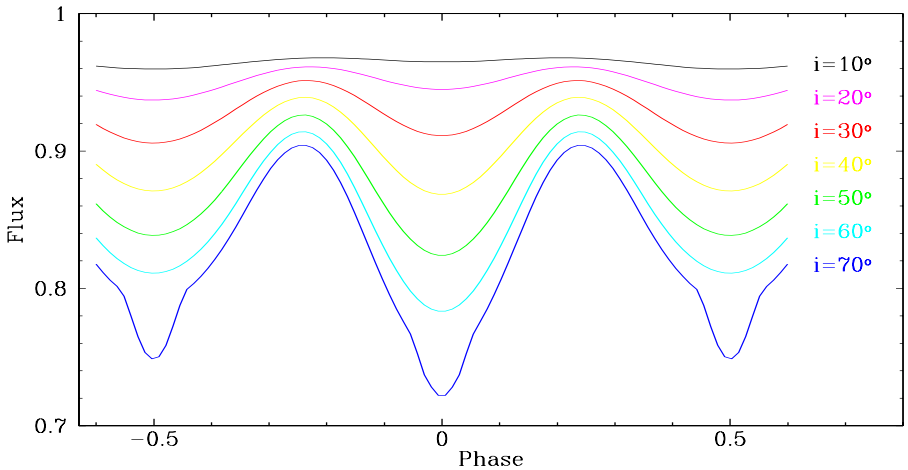

Figure 35: Ellipsoidal variation of a semi-detached binary at different system inclinations. Inclination $i = 70°$ implies eclipses and is represented with a blue line. All other inclinations correspond to non-eclipsing systems. The effect of ellipsoidal variation is observable for inclinations down to 10°.

4.7 Stellar spots

Stellar surfaces may feature cool or hot spots, usually attributed to magnetic activity of one or both components and/or mass transfer, e.g. hot spots in cataclysmic variables (Warner, 2003). Spots may be described by 4 parameters:

Spot latitude $\theta_{\rm sp}$: the latitude of the spot on the stellar surface. Latitude does not need to coincide with the grid point of the surface element. It is described in the same coordinate system as the star itself.

Spot longitude $\phi_{\rm sp}$: the longitude of the spot on the stellar surface. As latitude, longitude does not need to coincide with the grid point surface element. It is described in the same coordinate system as the star itself.

Spot angular radius $\varrho_{\rm sp}$: angular radius of the spot, expressed in radians. Please note that for spots the size of which is so small that it does not cover any sampled point on the stellar surface it won't have any effect at all.

Spot temperature factor $\tau_{\rm sp}$: the ratio between the temperature of the spot and the local temperature of the underlying photosphere. Values $\tau_{\rm sp} > 1$ correspond to hot spots, while values $\tau_{\rm sp} < 1$ correspond to cool spots.

The adequacy of this simplistic approach has a fair argument: to properly model spots, advanced and reliable methods of data acquisition (polarimetry, Doppler tomography) are required (see Section 2.3). It is thus *not* straight-forward to submit acquired data to the sophisticated treatment of spots (e.g. non-uniform spot brightness, magneto-hydrodynamic effects etc.), especially since reckless modeling of spots may easily reproduce *any* physical effect - the degeneracy is simply too strong. Even such a simplified treatment is thus still ahead of current observational capabilities.

It is, however, evident how modeling spots is included in the model: the local temperature of the surface element covered by the spot is multiplied by the $\tau_{\rm sp}$ factor, thus changing the local emergent intensity in that point. If two or more spots overlap, the respective temperature is obtained by the product of the individual spot temperature factors.

5 The model of an eclipsing binary

There are many models that have been more-or-less successfully applied to eclipsing binaries. In the last 40 years the EB field was overwhelmed by many approaches to solution seeking; Kallrath and Milone (1999) give an overview of the most important ones. The widely used `WD` code (Wilson and Devinney, 1971) underwent many expansions, improvements and fine-tuning (Wilson and Biermann (1976); Wilson (1979); Wilson (1990); Milone et al. (1992); Kallrath et al. (1998); van Hamme and Wilson (2003) and many others), which firmly established it as the most prominent software available for EBs. The list of geometrical and physical parameters that enter the model reflects on the level of sophistication and is given in Table 1. Our work builds on an unmodified version of `WD` (namely `WD2003`), so in the following discussion we limit ourselves to the modeling principles of `WD` and extensions that have been introduced by Prša and Zwitter (2005a). As such, the discussion most accurately applies to the modeling package `PHOEBE`, which will be formally introduced in the next Section.

§

To adequately describe geometrical and physical properties of a binary star system, it is necessary to estimate the potential gain in model accuracy and compare it to its computational cost. Having fully analytic expressions built into the model that describe smooth variations in parameter values across stellar surfaces would be ideal in terms of accuracy, but at the same time they would be a show-stopper in terms of time required for the computation. On the other hand, having a simple predefined geometry of triaxial ellipsoids and predetermined distribution of physical quantities over such surfaces would be ideal in terms of speed, but at the severe expense of accuracy. We seek an intermediate solution: without making any a priori assumptions about the shape of the stars or parameter variations over their surfaces, the model is built on a Roche equipotential geometry formalism and *samples* parameter values across the surface in a discrete set of points uniformly distributed along the latitude and longitude of the star. The underlying physics is there in all its analytical might, but it is used only in these discrete sampling points. The number of points that are required to reach a given level of accuracy depend on the problem at hand: if a modeled binary is well-detached, then a small number of sampling points is enough for accurate results. If the modeled binary is in contact and features spots, then a number of sampling points should be noticeably larger.

Parameter:	Description:
HJD_0	Zero-point of HJD
P_0	Orbital period of the binary
dP/dt	Time derivative of the orbital period
$\Delta\Phi$	Phase shift
ε	Orbital eccentricity
ω_0	Argument of periastron
$d\omega/dt$	Time derivative of the argument of periastron
a	Semi-major axis
q	Mass ratio (secondary over primary)
i	Orbital inclination
v_γ	Center-of-mass radial velocity
$\mathcal{R}$	Reddening factor
$E\,(\mathrm{B}-\mathrm{V})$	Reddening color excess
T_{eff_1}, T_{eff_2}	Effective temperatures
Ω_1, Ω_2	Surface potentials
$\log g_1/g_0$, $\log g_2/g_0$	Surface gravity accellerations
$[\mathrm{M/H}]_1$, $[\mathrm{M/H}]_2$	Metallicities
A_1, A_2	Surface albedoes
g_1, g_2	Gravity darkening coefficients
F_1, F_2	Synchronicity parameters
L_1^i, L_2^i	Passband luminosities
$x_1^{\mathrm{ld},i}$, $x_2^{\mathrm{ld},i}$	Linear limb darkening coefficients
$y_1^{\mathrm{ld},i}$, $y_2^{\mathrm{ld},i}$	Non-linear limb darkening coefficients
L_3^i	3^{rd} light
κ^i	Circumstellar cloud opacity
ϕ_{sp}^k	k^{th} spot longitude
θ_{sp}^k	k^{th} spot latitude
ϱ_{sp}^k	k^{th} spot angular radius
τ_{sp}^k	k^{th} spot temperature factor

Table 1: A list of geometrical and physical parameters that enter the model. Parameters are grouped together for easier reference: ephemeris parameters, orbital parameters, system parameters, component parameters, limb darkening coefficients, third light and circumstellar matter parameters, and spot parameters. Superscript i denotes that the given parameter is wavelength-dependent, i.e. a different value applies to each light and/or RV curve. Superscript k appearing at spot parameters denotes the spot number.

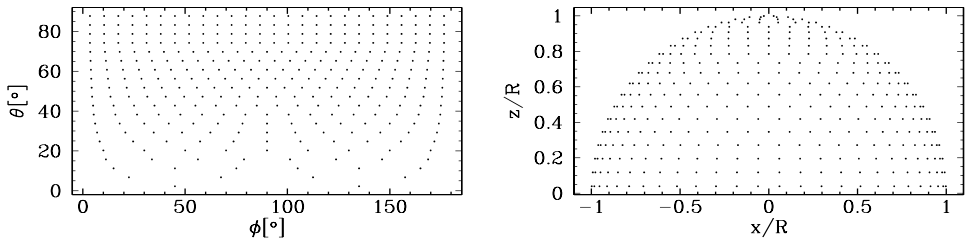

Figure 36: Sampling the stellar surface. Left: sampled points in latitude (θ) and longitude (ϕ) according to Eqs. (5.1–5.3) and $N = 20$. Right: the same plot, converted into xz plane.

5.1 The point-sampling strategy

Points on a stellar surface are sampled uniformly in latitude and longitude. You may recall from Section 3, Fig. 13 that latitude is by definition measured from $+z$ axis direction ($\theta = 0$) to $-z$ axis direction ($\theta = \pi$). Since the star shape is symmetric with respect to the equator, it suffices to sample only half of the hemisphere of the star and copy the points to other three quarters. Given the number of points N, the latitude is divided in equidistant intervals:

$$\theta_k = \frac{\pi}{2}\frac{k-0.5}{N}, \quad k = 1 \ldots N. \tag{5.1}$$

Given the θ_k, the longitude circle at that θ_k is further divided in equidistant intervals:

$$M_k := 1 + \mathrm{int}\,(1.3N \sin\theta_k), \tag{5.2}$$

$$\phi_l = \pi\frac{l-0.5}{M_k}, \quad l = 1 \ldots M_k. \tag{5.3}$$

The longitude ϕ is by definition measured from the direction to the companion star in a counter-clockwise direction (c.f. Fig. 13 and Eqs. (3.8)). Since the star shape is symmetric about the orientation toward its companion, it suffices to sample only the interval $[0, \pi]$. The factor 1.3 in Eq. (5.2) means that 30% more points will be sampled in longitude than in latitude. The reason for this are corrections of the partially eclipsed surface elements, which are done only in longitude directions. We shall further discuss this point in Section 5.4. Fig. 36 shows the distributions of sampled points in latitude and longitude for $N = 20$.

5.2 Computation of local geometrical quantities

Once the points have been sampled, the model needs to compute the values of geometrical and radiative parameters at those points. Since they depend on the position on the stellar surface, they are *local*, defined with respect to some reference point. There are 4 prospective reference points on the stellar surface that are shown on the lobe-filling component on Fig. 37: $r_{\rm pole}$ is measured toward the pole, $r_{\rm back}$ toward L_2, $r_{\rm side}$ toward the side, perpendicular to the xz plane, and $r_{\rm point}$ is measured toward the other component. Any point on the stellar surface could be selected as a reference point, yet the most natural choice would be the polar radius $r_{\rm pole}$, because it doesn't depend significantly on the morphology of the given binary. Hereafter we shall use the radii normalized to the semi-major axis, $\varrho = r/a$.

Local intrinsic quantities, such as local effective temperature or local surface brightness, depend on the local gravitational force. Below we outline the procedure that computes all local geometrical properties. The results are valid for both circular and elliptical orbits, the only difference being that the first 3 steps are phase-independent in case of circular orbits and apply to the periastron passage phase in case of elliptical orbits.

1. Compute polar radius $\varrho_{\rm pole}$ of the given star.

As was discussed in Section 3, polar radius $\varrho_{\rm pole}$ may be easily computed by solving Eq. (3.20) for $\varrho_{\rm pole}$ from the given value of the surface potential Ω. Since the expression cannot be analytically inverted, a Newton-Raphson method is used to solve it.

2. Compute the polar gradient magnitude $\|\nabla\Omega_{\rm pole}\|$.

Effective gravitational acceleration is the driving quantity for distributing local intrinsic quantities over the stellar surface. To compute its polar value (which we need as reference), the model needs to evaluate a gradient of the gravitational potential at the star's pole:

$$\Upsilon_{\rm pole} \equiv \|\nabla\Omega_{\rm pole}\| = \sqrt{\left(\frac{\partial\Omega}{\partial x}\right)^2 + \left(\frac{\partial\Omega}{\partial y}\right)^2 + \left(\frac{\partial\Omega}{\partial z}\right)^2}, \qquad (5.4)$$

where partial derivatives are given by Eq. (4.5). Evaluating them at

the star's pole ($\theta = 0$) yields:

$$\begin{aligned}\frac{\partial\Omega}{\partial x} &= \frac{q\delta}{(\delta^2+\varrho_{\rm pole}^2)^{3/2}} - \frac{q}{\delta^2},\\ \frac{\partial\Omega}{\partial y} &= 0,\\ \frac{\partial\Omega}{\partial z} &= -\frac{1}{\varrho_{\rm pole}^2} + \frac{q\varrho_{\rm pole}}{(\delta^2+\varrho_{\rm pole}^2)^{3/2}},\end{aligned} \tag{5.5}$$

where δ is the instantaneous separation between the two stars, normalized to the semi-major axis. The gravitational acceleration $\Upsilon_{\rm pole}$ computed in this manner is unitless, since both $\varrho_{\rm pole}$ and δ are given in units of semi-major axis a.

3. Compute gravity acceleration $g_{\rm pole}$ in physical units.

The next step is to compute gravitational acceleration $g_{\rm pole}$ in physical units, which will in turn provide a scaling constant to its unitless value $\Upsilon_{\rm pole}$. Fig. 37 depicts a semi-detached binary star layout; there are three forces acting on the polar surface point of the lobe-filling star: gravity of the primary star, gravity of the secondary star and centrifugal force. Putting them together yields:

$$\mathbf{g}_{\rm pole} = -\frac{GM_1}{r_{\rm pole}^2}\frac{\mathbf{r}_{\rm pole}}{r_{\rm pole}} - \frac{GM_2}{h^2}\frac{\mathbf{h}}{h} - \omega^2(t)d_{\rm cf}\frac{\mathbf{d}_{\rm cf}}{d_{\rm cf}}, \tag{5.6}$$

where $r_{\rm pole} = a\varrho_{\rm pole}$ is the polar radius in physical units, $h = \sqrt{r_{\rm pole}^2 + d^2}$ is the distance between the star's pole and other star's center, $\omega(t)$ is the angular velocity and $d_{\rm cf}$ is the perpendicular distance from star's pole to the axis of rotation of the binary.

Once $g_{\rm pole}$ is known, a scaling factor between $g_{\rm pole}$ and $\Upsilon_{\rm pole}$ may be computed:

$$\zeta = \frac{g_{\rm pole}}{\Upsilon_{\rm pole}} = \frac{g_{\rm pole}}{\|\nabla\Omega_{\rm pole}\|}. \tag{5.7}$$

4. Start the loop.

Now that the reference point is established, the algorithm proceeds to compute local intrinsic quantities at every sampled point on stellar surface. If orbits are elliptical, all reference quantities computed in steps **1**–**3** ($\varrho_{\rm pole}$, $\Upsilon_{\rm pole}$ and $g_{\rm pole}$) are essentially phase-dependent and are recomputed at each phase. The only constraint to which both components by assumption must adhere is the preservation of the volume

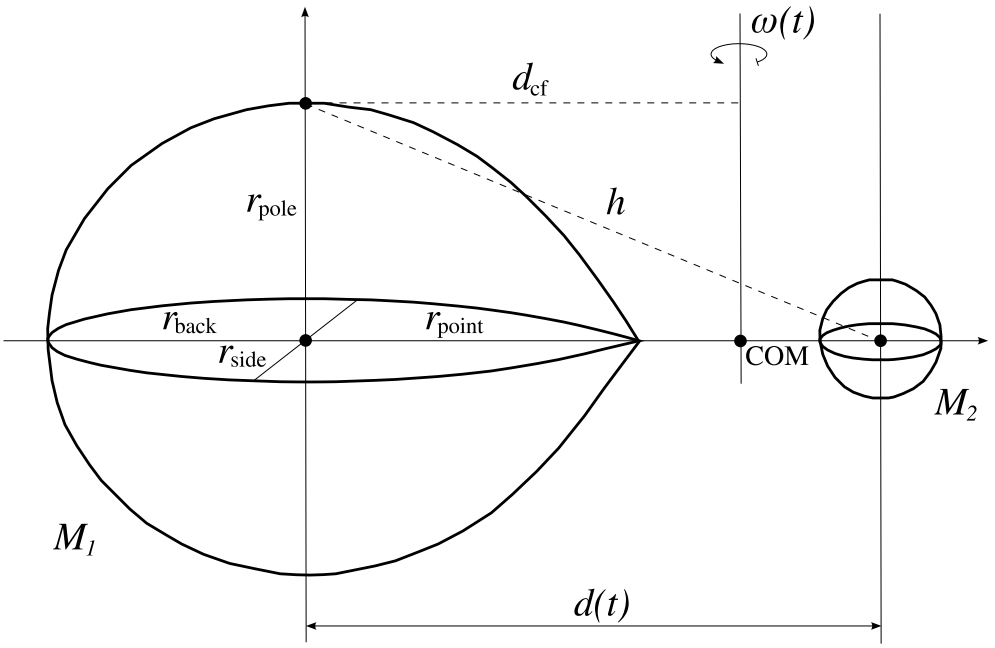

Figure 37: Schematic view of a semi-detached binary. There are 4 reference radii labelled on the lobe-filling binary (left): $r_{\rm pole}$, $r_{\rm back}$, $r_{\rm side}$ and $r_{\rm point}$; the semi-detached morphology is depicted to stress the difference between those 4 radii. When a binary orbit is elliptical, the instantaneous separation $d(t)$ between the two components and the angular velocity $\omega(t)$ are functions of phase. This implies that the 4 radii are phase-dependent as well, bound by the constraint that the volume of each component must by assumption be preserved in every phase.

throughout the period cycle. In reality the volume is not strictly preserved, but the errors induced by this approximation were shown to be practically negligible (Wilson, 1993).

4a. Compute temporal polar quantities.

This step is skipped when we are dealing with circular orbits. Computing polar radius and relative gravitational acceleration follows the procedure outlined in steps **1** and **2** in detail and it does not require any additional consideration. The computation of absolute gravitational acceleration on the other hand needs to take into account time dependence of the instantaneous separation $\delta = \delta(t)$ and angular velocity $\boldsymbol{\omega}(t)$, given by Eq. (3.18):

$$\omega(t) = \frac{2\pi}{P}\frac{1}{\delta^2}\sqrt{(1+\varepsilon)(1-\varepsilon)}. \tag{5.8}$$

In this way the scaling factor ζ given by Eq. (5.7) also changes in phase and must be recomputed in each step of the loop.

4b. Compute the local radius $\varrho(\theta_k, \phi_l)$.

Any point on the stellar surface is fully determined by the given surface potential and the chosen direction (θ_k, ϕ_l). To compute the local radius, the model solves Eq. (3.21) numerically by the Newton-Raphson method. Fig. 38 depicts the results of such computation for the lobe-filling star and grid size $N = 20$.

4c. Compute the norm of the local gradient potential $\|\nabla\Omega(\theta_k, \phi_l)\|$.

The computation of the local gradient yields the local gravitational acceleration $\Upsilon(\theta_k, \phi_l)$. The model makes use of the gradient derivatives given by Eq. (4.5), where x, y and z are given by Eq. (3.8) and ϱ was obtained in step **4b**. Fig. 39 depicts the distribution of the local gravity acceleration normalized to its polar value for the lobe-filling star and grid size $N = 20$.

4d. Compute the local gravity acceleration $g(\theta_k, \phi_l)$.

Instead of repeating the lengthy and time-consuming computation outlined in step **3**, here the algorithm makes use of the scaling factor ζ, given by Eq. (5.7):

$$g(\theta_k, \phi_l) = \zeta\Upsilon(\theta_k, \phi_l) = \frac{\Upsilon(\theta_k, \phi_l)}{\Upsilon_{\text{pole}}} g_{\text{pole}}. \tag{5.9}$$

It is common to take the logarithm of the obtained value, since the gravity acceleration is by convention described in terms of $\log g/g_0$ instead plainly of g.

4e. Compute the gravity darkening correction $\mathcal{G}(\theta_k, \phi_l)$.

Although gravity darkening is in a sense a radiative correction, the model can compute its distribution over the surface using the results of steps **3** and **4d**. Since the gravity darkening coefficient β is one of the passed parameters to the model, Eq. (4.22) may be used to obtain the gravity darkening correction:

$$\mathcal{G}(\theta_k, \phi_l) = \left(\frac{g(\theta_k, \phi_l)}{g_{\text{pole}}}\right)^{\beta}. \tag{5.10}$$

This correction will later be used to obtain the temperature distribution over the stellar surface.

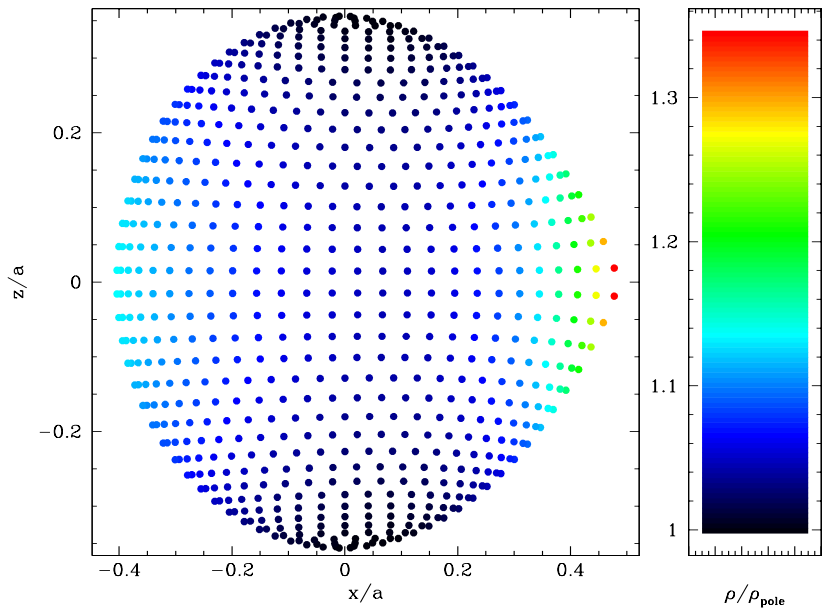

Figure 38: The distribution of local radii normalized to the polar radius on the lobe-filling star in circular orbit and $q = 1$. The grid size is $N = 20$.

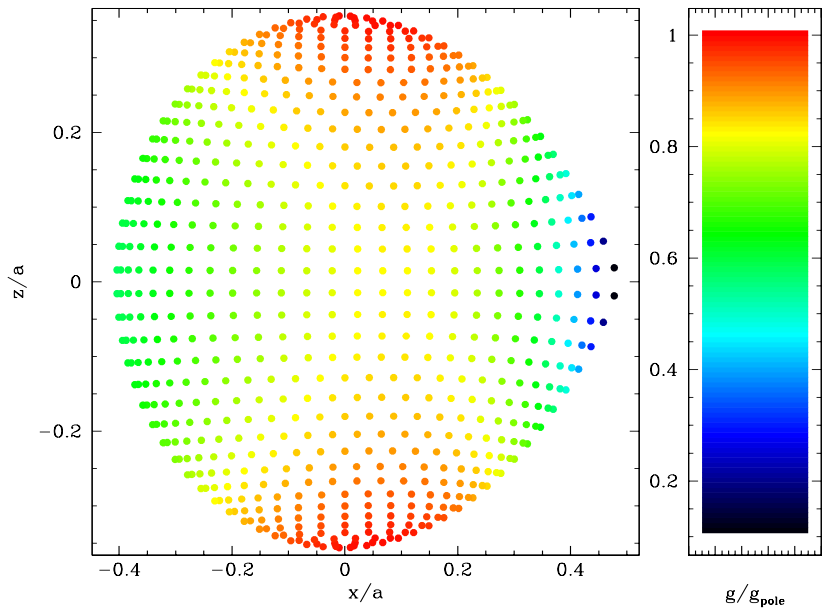

Figure 39: The distribution of local gravitational acceleration normalized to the polar gravitational acceleration on the lobe-filling star from the figure above. The grid size is $N = 20$.

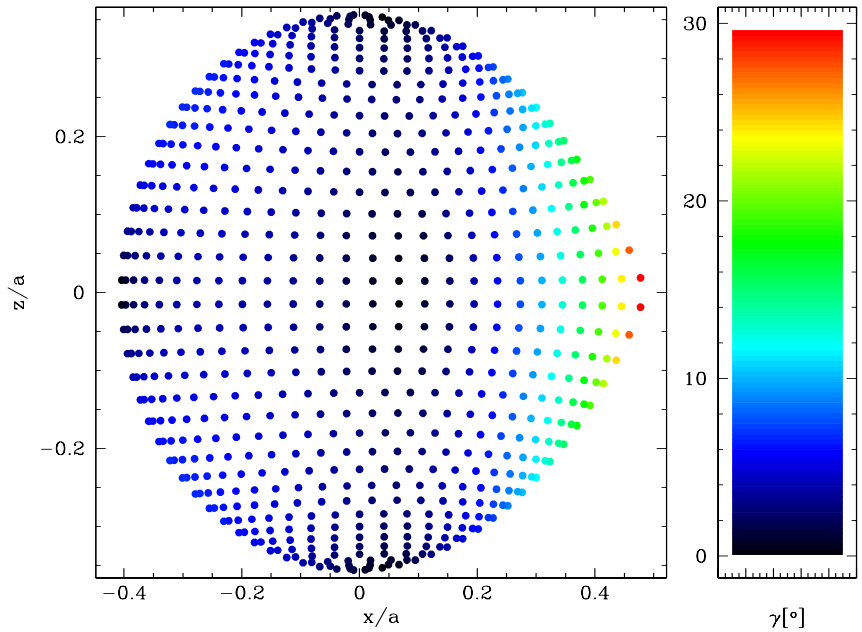

Figure 40: The distribution of the angle γ between the surface normal and the radius vector for the lobe-filling star.

4f. Compute the surface angle $\gamma(\theta_k, \phi_l)$.

Following our discussion in the beginning of Section 4, the model computes the angle γ between the surface normal vector $\hat{\mathbf{e}}_\mathbf{n}$ and unit radius vector $\hat{\mathbf{e}}_\varrho$ by using Eq. (4.3) in each sampled point. Fig. 40 depicts the values of γ for the lobe-filling star.

5. Compute the stellar surface, volume and the mean radius.

Shape distortion implies that the total surface S and the total volume V of the star generally differ from $4\pi(a\varrho_{\rm pole})^2$ and $4\pi(a\varrho_{\rm pole})^3/3$, respectively. A measure of the *local* distortion is the angle γ between the surface normal $\hat{\mathbf{e}}_\mathbf{n}$ and unit radius vector $\hat{\mathbf{e}}_\mathbf{r}$, which has been computed in step **4f**. The model is now in position to compute the total surface of the star by using the discretized version of Eq. (4.7):

$$S = 4\sum_{k=1}^{N}\sum_{l=1}^{M_k} \frac{\varrho^2(\theta_k,\phi_l)\sin\theta_k}{\cos\gamma(\theta_k,\phi_l)}\Delta\phi_l\Delta\theta_k, \tag{5.11}$$

where N and M_k are latitude and longitude grid dimensions as defined in Section 5.1, Eqs. (5.1)–(5.3), $\Delta\phi_l$ and $\Delta\theta_k$ are the discrete step

sizes in longitude and latitude, respectively. The factor 4 is due to the adopted sampling strategy of placing the grid only on 1/4 of the star and assuming symmetry with respect to xy and xz planes.

Similarly, a discretized version on Eq. (4.8) may be used to obtain the total volume of the star:

$$V = \frac{4}{3}\sum_{k=1}^{N}\sum_{l=1}^{M_k} \varrho^3(\theta_k,\phi_l)\sin(\theta_k)\Delta\phi_l\Delta\theta_k. \tag{5.12}$$

Stellar radii do not enter the model explicitly, they are computed from the surface potential in step **1**. This means that we do not need to transform any input quantity as we had to do with the mean surface temperature. Mean stellar radius is defined as the radius of a sphere with the same volume as the star in question:

$$\langle R\rangle = \left(\frac{3V}{4\pi}\right)^{1/3}. \tag{5.13}$$

Having computed all local geometrical quantities, the algorithm proceeds with modeling local radiative properties of each star.

5.3 Computation of local radiative quantities

Now that the local geometry is put in place, we are in position to compute the distribution of other intrinsic properties of the binary system. Their computation is not in any way distinct from the computation of geometrical quantities; the reason why we present them separately is only to make the overall algorithm flow more transparent to the reader. For that reason we pick up with the enumeration where we left off.

6. Compute the polar surface temperature.

Binary stars in eccentric orbits change not only their shape as function of orbital phase Φ but also their surface temperature distribution; it is particularly important to clearly specify what the input temperature really means. The temperature input parameter is the *mean* effective temperature, defined with respect to the bolometric luminosity of the star:

$$L_{\rm bol} = S\sigma T_{\rm eff}^4 = \int_{\partial V} \sigma T^4(\theta,\phi)dS, \tag{5.14}$$

where $T(\theta,\phi)$ is the local surface temperature. The model internally uses *polar* surface temperature as reference and the algorithm needs to compute it from the mean temperature using Eq. (4.23):

$$T_{\rm eff}^{\rm pole} = T_{\rm eff}\left(\frac{S}{\int_{\partial V}\mathcal{G}(\theta,\phi)dS}\right)^{1/4}. \tag{5.15}$$

The discretized form of Eq. (5.15) is:

$$T_{\rm eff}^{\rm pole} = T_{\rm eff}S^{1/4}\left[\sum_{k=1}^{N}\sum_{l=1}^{M_k}\mathcal{G}(\theta_k,\phi_l)\frac{\varrho^2(\theta_k,\phi_l)\sin\theta_k}{\cos\gamma(\theta_k,\phi_l)}\Delta\theta_k\Delta\phi_l\right]^{-1/4}. \tag{5.16}$$

There are two reasons why polar surface temperature is not chosen for the input parameter: 1) there is a slight difference between the observed temperature (e.g. revealed by the color index) and the polar temperature, so one would need to apply a correction to compare the two; 2) for binaries on eccentric orbits, the polar surface temperature can vary significantly, whereas the mean temperature does not.

7. Compute the polar passband intensity $I_{\rm passband}^{\rm pole}$.

A definition of the passband intensity and an overview for the black-body radiation has already been given in Section 4.1, Eq. (4.18). To save on computing time, normal emergent intensities for individual passbands have been approximated by the expansion in Legendre series to the $10^{\rm th}$ order (van Hamme and Wilson, 2003), with polynomial coefficients stored in a separate file. This allows the model to completely skip the integration of a spectral energy distribution function (be it black-body or model atmospheres) and to reduce the required operations to a simple data table readout. Instead of temperatures in absolute units, Legendre polynomials take relative temperature factors ϖ that are given by:

$$\varpi = \frac{T - T_{\rm ll}}{T_{\rm ul} - T_{\rm ll}}, \tag{5.17}$$

where $T_{\rm ll}$ and $T_{\rm ul}$ are prescribed lower and upper limits of the predefined temperature intervals summarized in Table 2 (van Hamme and Wilson, 2003).

Since model atmospheres depend on more than just effective temperature (recall the discussion in Section 2.3.2), the data tables must be multi-dimensional. In particular, Kurucz's atmospheres provide intensities at 1221 wavelengths[11] that span from 9nm to 160 000 nm, 11

[11] Their sampling is equidistant over the near-UV, visible and near-IR part of the spectrum with 2 nm step size (Kurucz, 1993).

Temperature interval [K]:	$T_{\rm ll}$ [K]	$T_{\rm ul}$ [K]
$[500, 1900)$	500	2000
$[1900, 5500)$	1800	5600
$[5500, 20000)$	5400	20100
$[20000, 100000)$	19900	100100
$[100000, 500000)$	99900	500300

Table 2: Temperature intervals for different Legendre polynomials. The argument to Legendre polynomials ϖ is always strictly in the $(0, 1)$ range, c.f. Eq. (5.17). Adopted from `WD` source code.

values of $\log g/g_0$ ranging from 0.0 to 5.0, effective temperatures ranging from 3 500K to 50 000K and 19 metallicities from -5.0 to 5.0, given for 21 different passbands (van Hamme and Wilson, 2003). Such a scheme, although practical from the computational point of view, is not practical if photometry is acquired in any other (unsupported, i.e. not pre-calculated) passband. A better approach is to supply passband transmission functions and to do the integration once during the overall analysis and use the data dynamically, independent of any external data files. This approach is implemented in `PHOEBE`.

8. Start the loop.

Now that all radiative polar quantities have been computed, the algorithm enters a loop to compute their local counterparts over the whole stellar surface grid.

8a. Compute the local surface temperature $T(\theta_k, \phi_l)$.

As the polar temperature is computed in step **6** and the gravity darkening correction is computed in step **4e**, the model is able to compute the gravity-corrected local temperature:

$$T(\theta_k, \phi_l) = [\mathcal{G}(\theta_k, \phi_l)]^{1/4} T_{\rm pole}. \tag{5.18}$$

Figs. 41 and 42 depict local temperature distribution for radiative and convective envelopes, respectively. It is clear that gravity darkening causes equatorial regions to be cooler than polar regions. As expected, the effect is more pronounced for radiative envelopes.

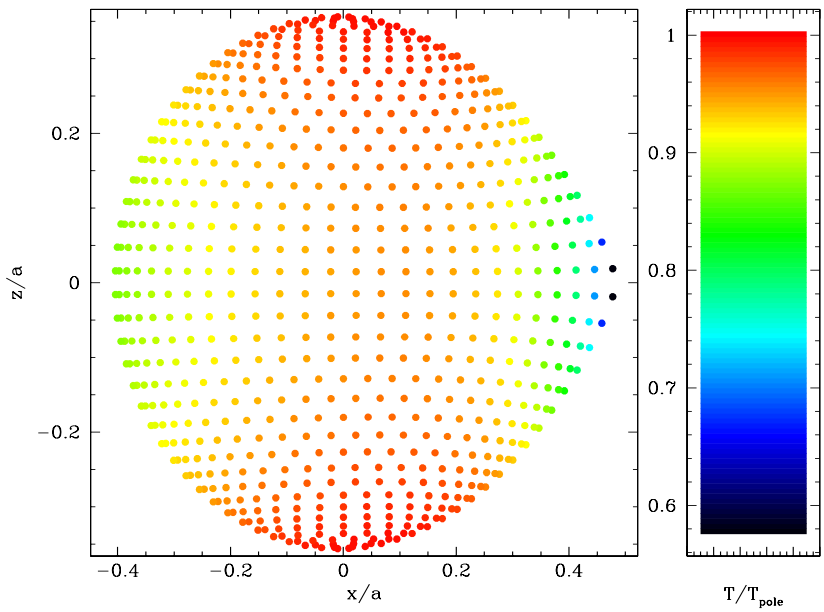

Figure 41: The distribution of local temperature normalized to the polar temperature on the lobe-filling star with the assumed radiative envelope.

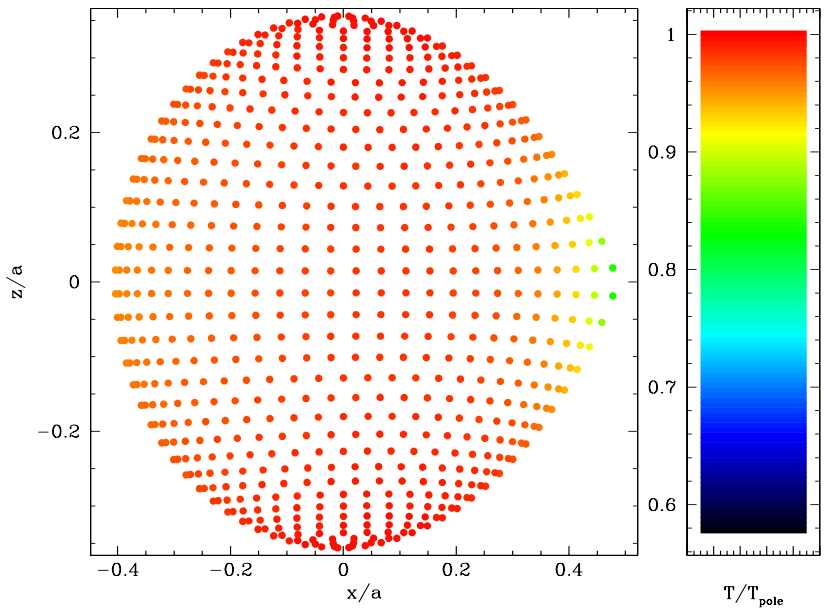

Figure 42: The distribution of local temperature normalized to the polar temperature on the lobe-filling star with the assumed convective envelope.

8b. Compute the local passband intensity $I_{\text{passband}}(\theta_k, \phi_l)$.

Similar to step **7**, obtaining the local passband intensity $I_{\text{passband}}(\theta_k, \phi_l)$ is a matter of querying external data tables to obtain Legendre coefficients for the given values of local surface temperature $T(\theta_k, \phi_l)$ and local gravity acceleration $\log(g/g_0)(\theta_k, \phi_l)$, which were obtained in steps **8a**, Eq. (5.18) and **4d**, Eq. (5.9).

8c. Compute discontinuous surface effects: spots

You may recall from Section 4.7 that the local temperature of the surface element covered by the spot is described by the τ_{sp} factor:

$$T_s(\theta_k, \phi_l) = \tau_{\text{sp}} T(\theta_k, \phi_l), \tag{5.19}$$

where $T(\theta_k, \phi_l)$ is the temperature of the underlying surface element. The spot-corrected normal passband intensity is obtained from the external Legendre tables for the corrected temperature $T_s(\theta_k, \phi_l)$. The correction factor $\mathcal{X}(\theta_k, \phi_l)$ is the ratio between the spot-corrected passband intensity and the passband intensity which would exist without a presence of a spot:

$$\mathcal{X}(\theta_k, \phi_l) = \frac{I^{\text{spot}}_{\text{passband}}(\theta_k, \phi_l)}{I_{\text{passband}}(\theta_k, \phi_l)}. \tag{5.20}$$

9. Compute the reflection effect correction $\mathcal{R}(\theta_k, \phi_l)$.

The main difference between reflection effect and other surface brightness phenomena computed in the previous loop is that a given surface element on each star receives integrated radiation from many surface elements on the other star. That is why the distribution of surface temperature and intensity had to be computed before reflection is treated. The number of computations required for the accurate treatment of reflection scales essentially with the square of the grid size, so computing it for dense grids can become the dominant computational expense of the model.

When we are dealing with circular orbits, intrinsic reflection does not depend on the orbital phase, except regarding the aspect: it is fully characterized by its value attached to a given surface element. The model then needs to compute the local intrinsic effect over the stellar surface only once and then perform aspect-dependent transformations to compute the flux as seen by the observer. This advantage is lost for eccentric orbits, where even local intrinsic reflection is phase dependent.

9a. Compute bolometric limb darkening correction $\mathcal{L}^{\rm bol}(\theta_k, \phi_l)$.

Limb darkening with respect to the observer is inherently aspect-dependent, so the model cannot perform any limb darkening computations at this point yet. However, to compute the amount of heating received by mutual irradiation of the components, the model needs to compute *bolometric* limb darkening coefficients. In contrast to the limb darkening effect seen by the observer, this bolometric limb darkening effect is intrinsic to the system. When modeling binaries with eccentric orbits, stellar shapes and the instantaneous distance change in phase and bolometric limb darkening correction must be recomputed at each phase. The evaluated expression depends on the adopted limb darkening law (linear, logarithmic or square-root, c.f. Section 4.4) and the bolometric limb darkening coefficients $x_1^{\rm bol}$, $y_1^{\rm bol}$, $x_2^{\rm bol}$ and $y_2^{\rm bol}$ passed as parameters to the model; for the simplest case of the linear law the correction is given by:

$$\begin{aligned} \mathcal{L}_1^{\rm bol}(\psi_1) &= (1 - x_{\rm bol} + x_{\rm bol}\cos\psi_1)\,, \\ \mathcal{L}_2^{\rm bol}(\psi_2) &= (1 - x_{\rm bol} + x_{\rm bol}\cos\psi_2)\,, \end{aligned}$$

where ψ_1 and ψ_2 are the angles of view from the reflecting element on the primary and secondary star, respectively (c.f. Fig. 33). Note that ψ_1 and ψ_2 depend on coordinates $(\theta_k, \phi_l)_{1,2}$ on *both* stars, that is why the computation time scales with the square of the grid size.

9b. Compute the reflection coefficients $\mathcal{R}_{1,2}(\theta_k, \phi_l)$.

Now that $\mathcal{L}_{1,2}^{\rm bol}$ corrections are available, the model computes the flux by which one star irradiates the other and the total flux emitted by the irradiated star – Eqs. (4.40) and (4.41), respectively:

$$J_{2\to1}^{\rm entrant} = A_1\mathcal{R}_2 \sum_{k=1}^{N}\sum_{l=1}^{M_k} I_{2\perp}^{\rm bol}\cos\psi_1\cos\psi_2\mathcal{L}_2^{\rm bol}(\psi_2)\cdot \cdot\frac{\varrho^2\sin\theta_k}{\cos\gamma(\theta_k,\phi_l)}\Delta\phi_l\Delta\theta_k, \tag{5.21}$$

$$\begin{aligned} J_1^{\rm tot} &= I_{1\perp}^{\rm bol}\int_{2\pi}(1 - x_{\rm bol} + x_{\rm bol}\cos\psi)\,d\Omega \\ &= \pi I_{1\perp}^{\rm bol}\left(1 - \frac{x_{\rm bol}}{3}\right). \end{aligned} \tag{5.22}$$

The $I_{1\perp}^{\rm bol}$ and $I_{2\perp}^{\rm bol}$ are obtained from Legendre series; Eq. (5.22) was integrated by assuming a simple linear limb-darkening law given

by Eq. (4.32). A similar step is applied to the secondary star, obtaining $J_{1\to 2}^{\text{entrant}}$ and J_2^{tot}. The model now *iteratively* computes the reflection coefficients $\mathcal{R}_1(\theta_k, \phi_l)$ and $\mathcal{R}_2(\theta_k, \phi_l)$ from Eq. (4.42), adhering to the energy conservation law.

10. Compute the scaled polar passband intensity $\mathcal{I}_{\text{passband}}^{\text{pole}}$.

The model now has to provide a link between the passband luminosity (a single number for a given star and a global quantity) and passband intensity (a direction-dependent local quantity). The computation of observable flux involves the integration of the local passband intensity over the solid angle – c.f. Eq. (4.12) – so the model needs local intensities as immediate input. Local intensity is obtained from the polar passband intensity by applying the gravity darkening correction, but polar passband intensity as computed in step **7** needs to be made accordant with the passband luminosity. The model takes passband luminosity as input parameter (Table 1, L_i^1 and L_i^2) and treats polar passband intensity as an auxiliary quantity that is guaranteed to produce a specified luminosity upon integrating the resulting surface flux over the entire star. Since the luminosity must obviously be proportional to the polar passband intensity, it is only necessary to presume unity for the intensity, perform the luminosity integration, compare the provisionally computed luminosity with the specified input luminosity, and re-scale the polar passband luminosity so as to make the two luminosities agree.

The provisional luminosity is computed by the following expression:

$$L_{\text{model}} = \int_{2\pi} \mathcal{L}(\theta)\cos\theta d\Omega \cdot \sum_{k=1}^{N}\sum_{l=1}^{M_k} \mathcal{G}(\theta_k,\phi_l)\frac{\rho^2\sin\theta}{\cos\gamma(\theta_k,\phi_l)}\Delta\theta_k\Delta\phi_l, \tag{5.23}$$

where the integration of the limb darkening correction $\mathcal{L}(\theta)$ is done over the outgoing hemisphere. The polar passband intensity does not appear in the sum because its tentative value is unity. After computing this expression, the model re-scales the polar passband intensity:

$$\mathcal{I}_{\text{passband}}^{\text{pole}} = \frac{L_1^i}{L_{\text{model}}}. \tag{5.24}$$

With the above outlined scheme we have computed all intrinsic locally defined geometrical and radiative quantities of an eclipsing binary system. The total flux seen by the observer will be found by summing the flux in his direction contributed by all stellar surface elements, excluding those which lie over the horizons and those in eclipse.

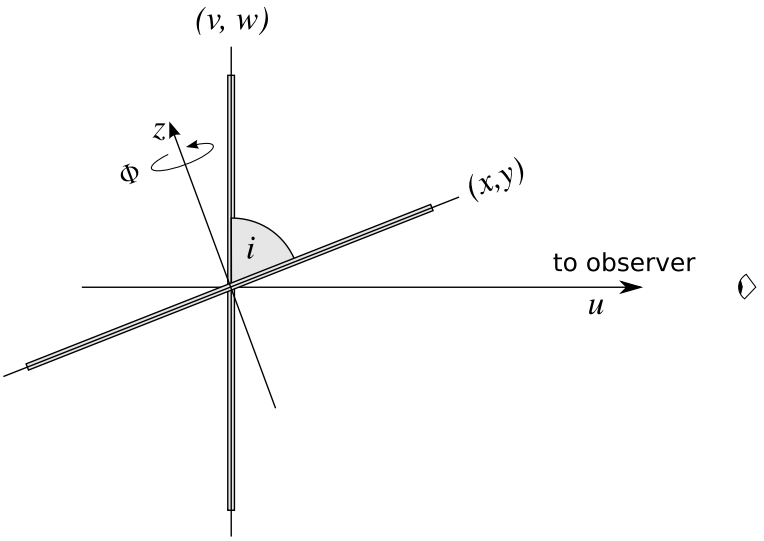

Figure 43: Projection of the orbital plane xy to the plane-of-sky vw. Angle i is the inclination and Φ is the orbital phase.

5.4 Computation of aspect-dependent quantities

The formalism to mathematically describe eclipses within our model is very simple: only visible surface elements contribute to the total flux. The model treats the star in front first, to obtain the area that blocks the star in the back. To test which star is in front, the model evaluates the following expression for the given phase:

$$(\Phi - 0.5)^2 \leq 0.25^2 \equiv 0.0625. \tag{5.25}$$

If it is true, then the primary star is in front, otherwise the secondary is in front. Once we know which star to handle first, we only need to figure out which surface elements are visible in the given phase. The easiest way to describe the distance between the centers of the two stars as function of phase is to transform stellar coordinates (x, y, z) to plane-of-sky coordinates (u, v, w) with simple rotations (c.f. Fig. 43). For the primary star this will be:

$$\begin{pmatrix} u \\ v \\ w \end{pmatrix}_{\mathrm{P}} = \begin{pmatrix} \sin i & 0 & \cos i \\ 0 & 1 & 0 \\ -\cos i & 0 & \sin i \end{pmatrix} \begin{pmatrix} \cos\Phi & -\sin\Phi & 0 \\ \sin\Phi & \cos\Phi & 0 \\ 0 & 0 & 1 \end{pmatrix} \begin{pmatrix} x \\ y \\ z \end{pmatrix}, \tag{5.26}$$

where i is the inclination and Φ is the orbital phase with the factor 2π omitted

for simpler notation. Multiplying the matrices yields:

$$\begin{pmatrix} u \\ v \\ w \end{pmatrix}_{\mathrm{P}} = \begin{pmatrix} \sin i \cos\Phi & -\sin i \sin\Phi & \cos i \\ \sin\Phi & \cos\Phi & 0 \\ -\cos i \cos\Phi & \cos i \sin\Phi & \sin i \end{pmatrix} \begin{pmatrix} x \\ y \\ z \end{pmatrix}. \tag{5.27}$$

The transformation of stellar coordinates to the plane-of-sky coordinates for the secondary star consists of the analogous two-matrix rotation and a translation by instantaneous separation δ along x-axis:

$$\begin{aligned} \begin{pmatrix} u \\ v \\ w \end{pmatrix}_{\mathrm{S}} &= \begin{pmatrix} \sin i & 0 & \cos i \\ 0 & 1 & 0 \\ -\cos i & 0 & \sin i \end{pmatrix} \begin{pmatrix} -\cos\Phi & \sin\Phi & 0 \\ -\sin\Phi & -\cos\Phi & 0 \\ 0 & 0 & 1 \end{pmatrix} \begin{pmatrix} x' \\ y' \\ z' \end{pmatrix} + \begin{pmatrix} \delta \\ 0 \\ 0 \end{pmatrix} \\ &= \begin{pmatrix} -\sin i \cos\Phi & \sin i \sin\Phi & \cos i \\ -\sin\Phi & -\cos\Phi & 0 \\ \cos i \cos\Phi & -\cos i \sin\Phi & \sin i \end{pmatrix} \begin{pmatrix} x' \\ y' \\ z' \end{pmatrix} + \begin{pmatrix} \delta \\ 0 \\ 0 \end{pmatrix}, \end{aligned} \tag{5.28}$$

where x', y' and z' are the stellar coordinates with the origin in the center of the secondary star.

It is now straight-forward to write the distance $\boldsymbol{\delta} = (\delta, 0, 0)$ between the centers of both stars in the plane-of-sky coordinates:

$$\begin{pmatrix} u_\delta \\ v_\delta \\ w_\delta \end{pmatrix} = \delta \begin{pmatrix} \sin i \cos\Phi \\ \sin\Phi \\ -\cos i \cos\Phi \end{pmatrix}. \tag{5.29}$$

Its projection on the plane of sky is then:

$$\delta_\perp^2 = v_\delta^2 + w_\delta^2 = \delta^2 \left(\sin^2\Phi + \cos^2 i \cos^2\Phi\right). \tag{5.30}$$

The model may now test whether the sum of relative radii $\varrho_1^{\max} + \varrho_2^{\max}$ is smaller than $\delta_\perp$ for the given phase. If it is not, there will be no eclipses; if it is, accurate sumation over surface elements due to shape distortion must be done to see whether eclipses occur or not. For this reason the model computes the angle φ between the line-of-sight vector $\hat{\mathbf{u}}$ and the surface normal $\hat{\mathbf{n}}$ in each sampled point:

$$\hat{\mathbf{u}} = \begin{pmatrix} \sin i \cos\Phi \\ -\sin i \sin\Phi \\ \cos i \end{pmatrix}, \qquad \cos\varphi = \hat{\mathbf{u}} \cdot \hat{\mathbf{n}}, \tag{5.31}$$

where $\hat{\mathbf{n}}$ is given by Eq. (4.1). The visible horizon of the star in front is bounded by the limiting value $\cos\varphi > 0$ (see Fig. 44); if this condition is not fulfilled, the given surface element is *not* visible.

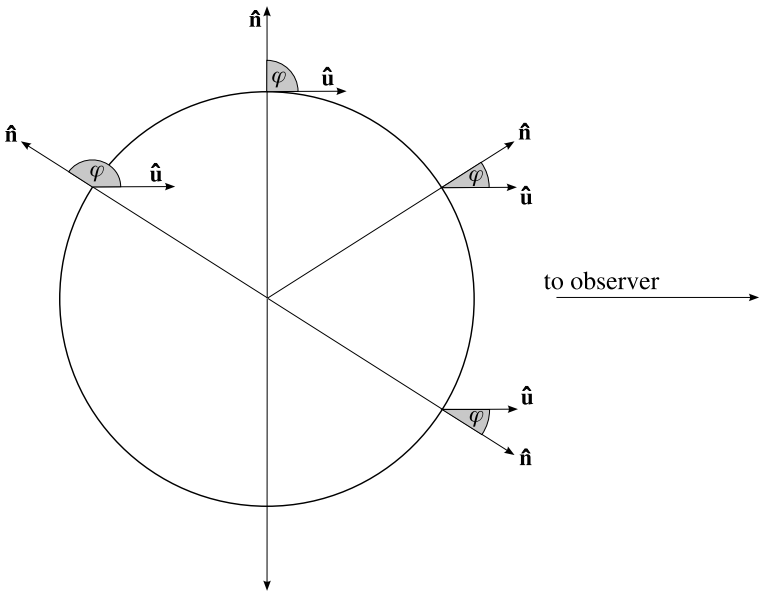

Figure 44: Angle φ between the surface normal $\hat{\mathbf{n}}$ and the line-of-sight vector $\hat{\mathbf{u}}$. If $-90^\circ < \varphi < 90^\circ$ or, alternatively, if $\cos\varphi > 0$, the corresponding surface element will be visible, otherwise it will not. This condition thus determines the horizon of the star in question.

Coordinates (θ_H, ϕ_H) of surface elements that are on the boundary (i.e. the transition from $\cos\varphi > 0$ to $\cos\varphi < 0$ occurs in-between) are kept for horizon determination. An analytical function for the boundary is then obtained by interpolating among these points to get equal spacing and then computing the Fourier series to the 5^{th} order:

$$\theta(\phi_l) = \sum_{n=0}^{5} \left[a_n \cos(n\phi_l) + b_n \sin(n\phi_l) \right], \tag{5.32}$$

$$a_n = \frac{\Delta\phi}{\pi} \sum_{l=0}^{5} \theta(\phi_l) \cos n\phi_l, \tag{5.33}$$

$$b_n = \frac{\Delta\phi}{\pi} \sum_{l=0}^{5} \theta(\phi_l) \sin n\phi_l. \tag{5.34}$$

Once the horizon is determined, the model proceeds with the total flux integration of the star in the back. Taking as origin the center of the eclipsing component, the model simply compares the projected radius to the Fourier boundary function obtained by Eqs. (5.32)-(5.34). Next to this boolean characterization the model also computes the correction due to fractional eclipse of a boundary surface element; as we mentioned earlier in Section 5.1, this

correction is only done along longitudes ϕ and that is why point sampling strategy prefers higher-density sampling in longitudes than in latitudes. The flux for the given star is computed by the following expression that accounts all corrections to the normal emergent intensity that have been computed:

$$J_{i,\text{total}}(\Phi) = \sum_{\text{visible } \theta,\phi} \mathcal{GRDX}\mathcal{I}^{\text{pole}}_{\text{passband}} \cos\varphi \frac{\varrho^2 \sin\theta_k}{\cos\gamma} \Delta\phi_l \Delta\theta_k, \tag{5.35}$$

where φ is the angle between the surface element normal $\hat{\mathbf{e}}_\mathbf{n}$ and the direction toward the observer. Finally:

$$J_{\text{total}}(\Phi) = J_{1,\text{total}}(\Phi) + J_{2,\text{total}}(\Phi). \tag{5.36}$$

This is the total intrinsic flux emitted at the given phase into the steradian's worth of area. To obtain a synthetic light curve, the model computes this flux at every observed phase (or HJD). Such a synthetic light curve is then compared with the observed light curve. To reach agreement, the model needs to adjust the values of parameters. How this is done is the topic of our next Section.

6 Approaches to solving the inverse problem

In the previous two Sections we have shown that the number of geometrical and physical parameters entering the model is substantial: you may recall from Table 1 on page 66 that the complete list comprises of more than 40 parameters. The task of the model is to take these arguments and compute synthetic curves (light curves, radial velocity curves, spectra...) as predicted by the theory. This is referred to as the **direct** problem: given the list of parameters, synthetic curves are *uniquely* determined.

In practice, however, we need to do exactly the opposite: given the observational data, we need to determine a set of parameters for which the model yields a matching synthetic curve. This is referred to as the **inverse** problem: given the curve, determine parameters that yield it. Unfortunately, due to parameter correlation and data noise, there may be many combinations of parameters that yield the same synthetic curve within the given accuracy; the inverse problem may *not* be uniquely solvable. This is referred to as **solution degeneracy**: right combination of the wrong parameters may perfectly satisfy observational data (Kopal, 1951).

Despite this initial pitfall, there is a consolation for those wary of degeneracy: with accurate and diverse observations, advanced numerical methods and, beyond all, a fair amount of common sense, the effects of degeneracy may be diminished to the point where the obtained solution is reliable and accurate to $\sim 1\%$. The aim of this Section is to introduce numerical methods for solving the inverse problem and to pronounce the caveats associated with them.

6.1 Local and global minima in hyperspace valleys

The job of any minimization algorithm deployed for solving the inverse problem is to minimize the discrepancy between observational data and synthetic curves. The discrepancy can most easily be quantified in terms of χ^2 or similar cost function:

$$\chi^2_k = \sum_{i=1}^{N_k} w_k w_i \left(J_i^{\rm obs} - J_i^{\rm syn}\right)^2 = \frac{1}{\sigma_k^2} \sum_{i=1}^{N_k} w_i \left(J_i^{\rm obs} - J_i^{\rm syn}\right)^2 \qquad (6.1)$$

for the $k^{\rm th}$ passband, where N_k and σ_k are the number and standard deviation of observational data points in that passband, respectively; w_i are individual weights, $w_k = 1/\sigma_k^2$ are passband weights; $J^{\rm obs}$ is the observed flux at the

given phase and $J^{\rm syn}$ is a synthetically-computed flux at the same phase. Since the weighted variance is given by:

$$s_k^2 = \frac{1}{N_k - 1} \sum_{i=1}^{N_k} w_i \left(J_i^{\rm obs} - J_i^{\rm syn} \right)^2, \tag{6.2}$$

the passband cost function χ_k^2 may be readily expressed as:

$$\chi_k^2 = (N_k - 1) \frac{s_k^2}{\sigma_k^2}. \tag{6.3}$$

The overall cost function is a sum of individual cost functions for each observed curve:

$$\chi^2 = \sum_{k=1}^{M} \chi_k^2 = \sum_{k=1}^{M} (N_k - 1) \left(\frac{s_k}{\sigma_k} \right)^2, \tag{6.4}$$

where M is the number of curves. If σ_k are properly estimated, the ratio s_k/σ_k is of the order unity and χ^2 of the order $N_{\rm tot} = \sum_k N_k$. We use this to parameterize χ^2 values (Prša and Zwitter, 2005a):

$$\lambda := \left(\chi^2 / N_{\rm tot} \right). \tag{6.5}$$

The cost coefficient λ will now directly measure the goodness of the fit: if the value is ~ 1, the discrepancy between the model and observations is small and the fit it satisfactory. If λ is large, the discrepancy is large and the fit is not satisfactory. Note that we use the word *fit* instead of *solution*, since a good fit to the data does not necessarily imply a good solution.

As we have seen in the previous Section, the model for eclipsing binaries is highly non-linear, with some strong parameter correlations. Inherent observational data noise adds to this, making the inverse problem very difficult to solve. Parameters span a high-dimensional hyperspace which, due to constraints and correlations, has a very complicated topology. This in turn implies that such a hyperspace is bound to have many minima with respect to the cost parameter λ. The discernible property of these minima is their depth: there are many shallow minima that occupy certain areas of the hyperspace to which we refer to as **local**: a small displacement in parameter values may knock the fit out of the minimum and enable the minimizer to further reduce the value of the cost function. On the other hand, there is an area of the deepest minimum within the hyperspace to which we refer to as **global**: a small displacement in parameter values won't cause any further improvement of the fit.

Parameter λ may thus be regarded as a qualifier for the depth of the minimum. If a minimization method converges and λ is still large, chances

are that the method had converged to a local minimum, where it got stuck. If λ is small, the method got close to a global minimum. The smaller the λ, the deeper the minimum. This is an important point that we will further build upon at the end of this Section, when we discuss on how to handle degeneracies of the solution.

The minimizer's task to objectively discern these minima and to find the deepest one is very demanding: any naive approaches of fitting the whole spectrum of parameters will surely fail. It is of utmost importance to have a system of control imposed on a minimizer that guides it in its solution-seeking process. We proceed with overviewing the most successful minimization algorithms that have been deployed for solving the inverse problem of eclipsing binaries.

6.2 Differential Corrections

One of the most straight-forward numerical methods for driving the χ^2 minimization is the method of differential corrections (DC), first proposed by Euler (1755). The method is based on replacing partial derivatives with finite differences:

$$\frac{\partial f(p_1,\ldots,p_k,\ldots,p_n)}{\partial p_k} \rightarrow \frac{f(\cdots p_k+\Delta p_k\cdots)-f(\cdots p_k\cdots)}{\Delta p_k}, \tag{6.6}$$

where $f(p_1,\ldots,p_n)$ is a scalar function in n-dimensional hyperspace. At the expense of calculation time, the accuracy of Eq. (6.6) may be slightly improved by symmetrization:

$$\frac{\partial f(p_1,\ldots,p_k,\ldots,p_n)}{\partial p_k} \rightarrow \frac{f(\cdots p_k+\Delta p_k/2\cdots)-f(\cdots p_k-\Delta p_k/2\cdots)}{\Delta p_k}. \tag{6.7}$$

The result of this discretization is the correction Δp_k to the starting value p_k which, provided that the corrections are small enough and the model is sufficiently accurate, yields the most probable value and its corresponding uncertainty for Δp_k. The same approach may be applied to more than just one parameter at a time, thus evaluating partial derivative with respect to a subspace of parameters set for adjustment.

Pioneering work on introducing DC to the field of eclipsing binary stars was done by Wyse and Kron (1939) and further facilitated by Irwin (1947) with his least square lookup tables; first computer implementation was done by Wilson and Devinney (1971) in their groundbreaking code `WD`. In context of eclipsing binaries, function $f(p_1,\ldots,p_n)$ is a model function that generates

synthetic curves (light curves, RV curves, spectra, ...) at the given phase and Δp_k are corrections to parameter values that reduce the value of the χ^2 cost function.

A notorious problem of differential corrections is the divergence in cases when the discrepancy between synthetic and observational curves is substantial. There are three distinct causes to this divergence (Prša and Zwitter, 2005a):

Computation of numerical derivatives decreases convergence accuracy because of limited precision of finite diferences, which introduces systematic errors.

Unconstrained minimization in n-dimensional hyperspace can diverge or give physically implausible results even in stable convergency domains.

Non-linearity of the problem at hand is being solved by the first-order differential corrections, which discards any higher-order derivatives. This means that the computation of the cost function does not *sense* their influence, while parameter correlations do. The divergence or, even worse, false convergence may occur when the two conditions (the lack of higher-order differences and parameter correlation) interact together (Wilson and Van Hamme, 2003).

These deficiencies are worked around by the absence of automatic iterations: the users are forced to manually verify convergency and resubmit the data to the minimizer (Wilson, 1993). In addition, two methods for improving convergence stability have been implemented: the Method of Multiple Subsets (Wilson and Biermann, 1976) and the Levenberg-Marquardt algorithm (Levenberg, 1944; Marquardt, 1963).

6.2.1 Method of Multiple Subsets

Failing convergence due to non-linearity of the problem and parameter correlations may be remedied to some extent by breaking the full parameter set into several subsets and thus reduce the complexity of the correlations in a given iteration (Wilson and Biermann, 1976). We refer to this as the Method of Multiple Subsets (MMS).

Let us presume that the full parameter set consists of six parameters, p_1 through p_6 and that the correlation between them is so strong that it causes bad convergency behavior. MMS breaks this set into two or more subsets,

i.e. $A = (p_1, p_2, p_3)$ and $B = (p_4, p_5, p_6)$. Subsets A and B are submitted to the minimizer separately, where each subsequent run is based on the results of the previous run:

$$AB \rightarrow \text{failure}; \quad A \rightarrow B \rightarrow A \rightarrow B \rightarrow \cdots \rightarrow \text{success}, \tag{6.8}$$

with the output from A being input for B and vice versa. This method shows a significant convergence improvement whenever the correlation between parameters is strong. The drawback to MMS is prolongation of the computation time and the under-estimation of standard errors of the determined solution. The latter may be fixed by submitting the whole set to the minimizer at the very end of the minimization process, only for reading out standard errors from the covariance matrix.

6.2.2 Levenberg-Marquardt algorithm

Levenberg-Marquardt algorithm (Levenberg, 1944; Marquardt, 1963) is one of most widely used and appreciated numerical methods for minimizing a function. It has become a standard technique for nonlinear least-squares problems and can be thought of as a combination of steepest descent and the Gauss-Newton methods[12].

To start a minimization, the user has to provide an initial guess for the parameter vector $\mathbf{p}$. In many cases, even an uninformed standard guess will work fine; in other cases, the algorithm converges only if the initial guess is already somewhat close to the final solution.

In each iteration step, the parameter vector $\mathbf{p}$ is replaced by a new estimate $\mathbf{p} + \mathbf{q}$. To determine $\mathbf{q}$, the function $f(\mathbf{p} + \mathbf{q})$ is approximated by its linearization:

$$f(\mathbf{p} + \mathbf{q}) \approx f(\mathbf{p}) + \mathbf{J} \cdot \mathbf{q}, \tag{6.9}$$

where $\mathbf{J}$ is the gradient of f at $\mathbf{p}$.

At a function minimum, the gradient $\nabla_{\mathbf{q}} f = 0$ and thus:

$$(\mathbf{J}^\dagger \mathbf{J}) \cdot \mathbf{q} = -\mathbf{J}^\dagger f, \tag{6.10}$$

from which $\mathbf{q}$ can be obtained by inverting $\mathbf{J}^\dagger \mathbf{J}$. The key to the Levenberg-Marquardt algorithm is to replace this equation by a damped counterpart:

$$(\mathbf{J}^\dagger \mathbf{J} + \lambda) \cdot \mathbf{q} = -\mathbf{J}^\dagger f \tag{6.11}$$

[12]For more information on these general numerical methods see e.g. Press et al. (1986) or a similar textbook on numerical mathematics.

by introducing a (non-negative) damping factor λ that is adjusted at each iteration. If reduction of S is too rapid, a smaller value can be used, bringing the algorithm closer to the Gauss-Newton method, whereas if an iteration gives insufficient reduction in the residual, λ can be increased, bringing it closer to the steepest descent. If a retrieved step length or the reduction of sum of squares to the latest parameter vector $\mathbf{p}$ falls short to predefined limits, the iteration is aborted and the last parameter vector $\mathbf{p}$ is considered to be the solution.

The Levenberg-Marquardt algorithm was first applied to eclipsing binaries by Djurasevic (1992) and later by Hill and Rucinski (1993). Now all major modeling codes, including WD, support it.

6.3 Powell's Direction Set method

Often neglected and overlooked, Powell's Direction Set method[13] (Brent, 1973, Chapter 7) is a derivativeless multi-dimensional method that utilizes 1-dimensional minimization algorithm along a chosen direction in parameter hyperspace. It is quadratically convergent, which makes it one of the fastest methods for solving non-linear minimization problems. It has never before been applied to eclipsing binaries.

The basic idea of Powell's method is to select a starting point $\mathbf{P}(p_1, \ldots, p_n)$ in parameter hyperspace, and minimize the cost function along some chosen direction vector $\mathbf{n}$ using 1-D minimizer such as bracketing or Brent's parabolic method (Brent, 1973, Chapter 5). There is a wealth of direction set method derivatives which differ only on how and at which point of iteration is the next direction vector $\mathbf{n}$ chosen (Press et al., 1986). The most appreciated scheme for choosing successive directions is the conjugate gradient method, which we now briefly describe.

When the cost function is minimized along the direction $\mathbf{n}$, the gradient in the obtained minimum is necessarily perpendicular to that direction. If it were not, that would mean that the projection of the gradient to that direction is non-null, which would in turn mean that the point was not really a minimum. The cost function may be expanded in Taylor series around that

[13] Although the method is still referred to as Powell's method, the algorithm actually used is due to Brent (1973), who has pointed out and corrected several serious flaws of Powell's original algorithm.

minimum:

$$f(\mathbf{p}) = f(\mathbf{P}) + \sum_i \frac{\partial f(\mathbf{P})}{\partial p_i} p_i + \frac{1}{2} \sum_i \sum_j \frac{\partial^2 f(\mathbf{P})}{\partial p_i \partial p_j} p_i p_j + \cdots =$$

$$= f(\mathbf{P}) - \mathbf{b} \cdot \mathbf{p} + \frac{1}{2} \mathbf{p}^\dagger \cdot \mathbf{H} \cdot \mathbf{p}, \tag{6.12}$$

where $\mathbf{b}$ is the negative gradient of f and $\mathbf{H}$ is the Hessian matrix of second partial derivatives of f at $\mathbf{P}$. The gradient is then simply expressed as:

$$\nabla f(\mathbf{P}) = \mathbf{H} \cdot \mathbf{p} - \mathbf{b}. \tag{6.13}$$

From Eq. (6.13) we may immediately deduce the change of the gradient along the chosen direction:

$$\delta \left(\nabla f(\mathbf{P}) \right) = \delta \left(\mathbf{H} \cdot \mathbf{p} - \mathbf{b} \right) = \mathbf{H} \cdot \left(\delta \mathbf{p} \right). \tag{6.14}$$

To adopt the best possible direction from the found minimum $\mathbf{P}$, the method must seek an orthogonal (conjugate) direction to the former direction vector, which obviously has to point along the direction of the gradient. If the former direction is denoted with $\mathbf{n}$ and the new direction is denoted with $\mathbf{m}$, then:

$$\mathbf{n} \cdot \delta \left(\nabla f(\mathbf{P}) \right) = \mathbf{n} \cdot \mathbf{H} \cdot \mathbf{m} = 0. \tag{6.15}$$

When Eq. (6.15) holds for vectors $\mathbf{n}$ and $\mathbf{m}$, they are said to be *conjugate*. For as long as the minimization is done *only* in conjugate directions, a single minimization along a given direction is necessary, which implies quadratic convergence. Note that the gradients need not be calculated at any point, we only use the orthogonality implication. This enables Powell's direction set method to preserve a derivativeless nature. The discussion on the success of the implementation for eclipsing binaries (automatic handling of large data-sets in particular) will be discussed in Section 7.

6.4 Nelder and Mead's downhill Simplex

As we have seen, Powell's method (similar to most multi-dimensional minimization methods) uses multiple 1-D minimizers to achieve convergence. The notable exception to this scheme is Nelder and Mead's downhill Simplex method (Nelder and Mead, 1965), hereafter NMS, which gives remarkable results when the parameter hyperspace is flat and correlations between parameters are strong (Press et al., 1986). The method requires only function

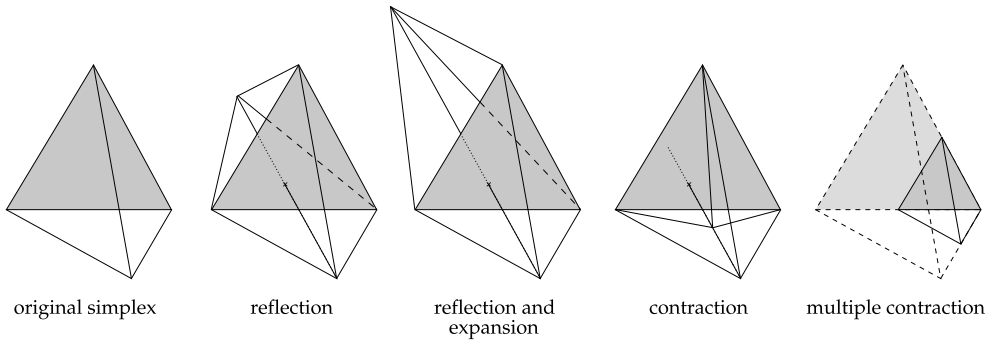

Figure 45: Four possible transformations of the 3D simplex: reflection, reflection followed by expansion, contraction and multiple contraction. The vertex being transformed is the one with the highest functional value. Using these transformations the simplex moves through the parameter hyperspace towards the closest minimum, where it contracts itself. At the end of each iteration a vertex with the lowest functional value is returned.

evaluations, not derivatives; it is thus not very efficient in terms of the number of evaluations that it requires, but its *generality* pays off for solving difficult non-linear problems where other methods fail.

NMS acts in n-dimensional parameter hyperspace. It constructs n vectors $\mathbf{p}_i$ from the vector of initial parameter values $\mathbf{x}$ and the vector of step-sizes $\mathbf{s}$ as follows:

$$\mathbf{p}_i = (x_0, x_1, \ldots, x_{i-1}, x_i + s_i, x_{i+1}, \ldots, x_n) \tag{6.16}$$

These vectors form $(n+1)$ vertices of an n-dimensional simplex. During each iteration the algorithm tries to improve parameter vectors $\mathbf{p}_i$ by modifying the vertex with the highest function value by simple geometrical transformations (Fig. 45): reflection, reflection followed by expansion, contraction and multiple contraction (Galassi et al., 2003). Using these transformations, the simplex moves through parameter space towards the closest minimum, where it contracts itself.

The basic form of NMS was first applied to eclipsing binaries by Kallrath and Linnell (1987). This implementation, although novel to the field of eclipsing binaries, suffered from some serious setbacks:

- the code is based on Numerical Recipes (Press et al., 1986); although Numerical Recipes were groundbreaking at the time of publication, their restrictive license and outdated algorithms made it obsolete;
- the implementation preserves its generic, *unconstrained* attitude, which

allows the minimizer to lead the solution to unphysical regions of the parameter hyperspace;

- the stopping criterion of that implementation uses *absolute* values of parameters to assess convergence. Numerical Recipes' NMS was conceived for normalized hyperspaces (i.e. all parameters have the same order of magnitude), which is obviously not the case for eclipsing binaries. To see this, just imagine what an *absolute* accuracy of 10^{-2} means for the mass ratio and what it means for effective temperature – while it might be a perfectly acceptable accuracy limit for the mass ratio, which is of the order unity, it is absolutely unacceptable for temperatures, which are of the order 10^4 K.

These setbacks were worked out in our implementation, which we present in Section 7.

6.5 Adaptive Simulated Annealing

A recently emerging numerical method for finding a *global* (in contrast to closest) minimum is derived from classical Simulated Annealing (Metropolis et al., 1953) and Monte-Carlo methods and is called Adaptive Simulated Annealing (ASA; Ingber, 1989, 1996).

The general idea of all SA algorithms is to minimize the cost function according to the three-step procedure:

- Given a state $\mathbf{p}$ (a set $\mathbf{p}$ of parameters p_i), a change is imposed to each parameter according to some prescribed probability distribution function $G(y_i, T_i)$, where $y_i \in [-1, 1]$ is a random variable and T_i is a simulated temperature that determines the strength of the displacement.
- If the imposed change increased the cost function, the new state is rejected. If the imposed change decreased the cost function, a new state is accepted *or* rejected, based on another probability function.
- A simulated temperature parameter is decreased by the amount that is governed by the annealing scheduling function and the state is submitted to the next iteration.

Such a logic enables SA to escape from local minima, since even if the solution lies within a local minimum, there is still a chance that the algorithm

will displace it. ASA differs only little from this general scheme, by providing a hyperspace-dependent probability distribution functions and annealing scheduling. This adapts the algorithm to the problem at hand automatically.

A serious down-side to any SA and similar algorithm is the computational time cost. In order to preserve statistical properties that guarantee the optimal solution to the problem and to remove ambiguity in minima locality, temperature annealing has to be done slowly enough.

Simulated annealing has been applied to eclipsing binaries by Nightfall[14]. Currently, tests are under way to adapt ASA to eclipsing binaries (Prša, 2004), yet the merits are still to be confirmed.

6.6 Formal errors of the fit

Regardless of the minimizing method used, the χ^2 cost function features a ready way to estimate errors that correspond to the determined parameters and to examine the shape of the hyperspace around the reached minimum (Press et al., 1986). To see how this is done, consider again Eq. (6.1):

$$\chi^2(\mathbf{p}) = \sum_i \frac{\left[J_i^{\rm obs} - J_i^{\rm syn}(\mathbf{p})\right]^2}{\sigma_i^2}, \tag{6.17}$$

where $\mathbf{p}$ is the vector of all parameters of the model. The χ^2 function is taken to be smooth and that its second derivatives exist. When a local minimum is reached (i.e. the local value of χ^2 is minimized), Eq. (6.17) may be linearized. Written in the matrix form:

$$\chi^2(\mathbf{p}) = (\mathbf{J}^{\rm obs} - \mathbf{A}\mathbf{p})^\top \mathbf{W} (\mathbf{J}^{\rm obs} - \mathbf{A}\mathbf{p}), \tag{6.18}$$

where $[\mathbf{A}]_{ij} = \partial J_i^{\rm syn}/\partial p_j$ is the matrix of partial derivatives of the model function with respect to the parameters and $[\mathbf{W}]_{ii} = 1/\sigma_i^2$ is the weight matrix (Avery, 1991). Taking the partial derivative of $\chi^2(\mathbf{p})$ with respect to $\mathbf{p}$ and requiring it to be zero enables us to compute the values of parameters:

$$\mathbf{A}^\top \mathbf{W} \left(\mathbf{J}^{\rm obs} - \mathbf{A}\mathbf{p}\right) = 0 \Rightarrow \mathbf{p} = \mathbf{V}\mathbf{A}^\top \mathbf{W}\mathbf{J}^{\rm obs}, \tag{6.19}$$

where $\mathbf{V} = (\mathbf{A}^\top \mathbf{W}\mathbf{A})^{-1}$ is the covariance matrix:

$$[\mathbf{V}]_{ij} = \langle (p_i - \bar{p}_i)(p_j - \bar{p}_j) \rangle = \langle \delta p_i \delta p_j \rangle. \tag{6.20}$$

[14] A freely available amateur code for modeling eclipsing binary stars from `http://www.lsw.uni-heidelberg.de/users/rwichman/Nightfall.html`

The symbol $\langle\rangle$ refers to a weighted average taken over all possible values of the enclosed expression. It is immediately evident from Eq. (6.20) that the diagonal elements of the covariance matrix are standard deviations σ_{p_i}; the off-diagonal elements correspond to the correlation between parameters:

$$[\mathbf{V}]_{ij} = [\boldsymbol{\rho}]_{ij}\sigma_{p_i}\sigma_{p_j}, \tag{6.21}$$

where $\boldsymbol{\rho}$ is the correlation matrix and ρ_{ij} are the correlation coefficients.

§

To characterize the shape of the hyperspace in the vicinity of the reached minimum, Eq. (6.17) is expanded in Taylor series up to the quadratic term (Press et al., 1986):

$$\begin{aligned}\chi^2(\mathbf{p}) &= \chi^2(\mathbf{p_0}) + \sum_k \frac{\partial\chi^2}{\partial p_k}(p_k - p_{k,0}) + \frac{1}{2}\sum_{i,j}\frac{\partial^2\chi^2}{\partial p_k \partial p_l}(p_k - p_{k,0})(p_l - p_{l,0}) \\ &= \chi^2(\mathbf{p_0}) - \mathbf{b}\cdot\mathbf{p} + \mathbf{p}\cdot\mathbf{H}\cdot\mathbf{p},\end{aligned} \tag{6.22}$$

where $\mathbf{b} = -\nabla\chi^2(\mathbf{p})$ and $\mathbf{H}$ is the Hessian matrix of second derivatives. The gradient of χ^2 may be written out explicitly:

$$\frac{\partial\chi^2}{\partial p_k} = -2\sum_i \frac{\left[J_i^{\rm obs} - J_i^{\rm syn}(\mathbf{p})\right]}{\sigma_i^2}\frac{\partial J_i^{\rm syn}(\mathbf{p})}{\partial p_k}, \tag{6.23}$$

where the index k goes over all parameters of the model. Evaluating the second derivative yields:

$$\frac{\partial^2\chi^2}{\partial p_k \partial p_l} = 2\sum_i \frac{1}{\sigma_i^2}\left[\frac{\partial J_i^{\rm syn}(\mathbf{p})}{\partial p_k}\frac{\partial J_i^{\rm syn}(\mathbf{p})}{\partial p_l} - \left(J_i^{\rm obs} - J_i^{\rm syn}(\mathbf{p})\right)\frac{\partial^2 J_i^{\rm syn}(\mathbf{p})}{\partial p_l \partial p_k}\right]. \tag{6.24}$$

When computing the Hessian matrix using Eq. (6.24) to step towards the minimum, the term containing a second derivative of $J_i^{\rm syn}(\mathbf{p})$ will be neglected; for a thorough discussion why this may be done without any drawbacks please refer to Press et al. (1986).

The following test can be applied at a non-degenerate critical point $\mathbf{P}$, in which the gradient of χ^2 is zero: if the Hessian is positive definite at $\mathbf{P}$, then χ^2 attains a local minimum at $\mathbf{P}$. If the Hessian is negative definite at $\mathbf{P}$, then χ^2 attains a local maximum at $\mathbf{P}$. If the Hessian has both positive and negative eigenvalues, then $\mathbf{P}$ is a saddle point for χ^2 (this is true even if $\mathbf{P}$ is degenerate). Otherwise the test is inconclusive.

	i	Ω_1	Ω_2	$T_{\rm eff_1}$	$T_{\rm eff_2}$	q	a
i	0.321155	-0.003557	-0.003371	0.003958	0.021218	0.000576	0.000002
Ω_1	-0.003557	0.029753	-0.002312	1.712314	-1.842537	-0.000985	-0.000009
Ω_2	-0.003371	-0.002312	0.028974	-1.637029	1.524242	-0.003917	-0.000009
$T_{\rm eff_1}$	0.003958	1.712314	-1.637029	0.001368	-0.001186	0.000000	0.000000
$T_{\rm eff_2}$	0.021218	-1.842537	1.524242	-0.001186	0.000950	-0.000000	-0.000000
q	0.000576	-0.000985	-0.003917	0.000000	-0.000000	0.015099	0.000042
a	0.000002	-0.000009	-0.000009	0.000000	-0.000000	0.000042	-0.000000

Table 3: An example of the Hessian matrix. The model consists of a single light curve that is computed synthetically with Poissonian scatter 0.02 mag. The Hessian is evaluated at the global minimum. It is evident that the last two parameters, namely q and a, make the Hessian singular; this is expected, because the shape of the light curve is marginally sensitive to the value of q and completely insensitive to the value of a. To isolate such parameters, singular value decomposition (SVD) method may readily be used (Galassi et al., 2003).

Unfortunately, this test cannot sense the distinct minima in the whole hyperspace – it is confined to the given local minimum that is reached by the minimizer. Furthermore, the test is often rendered inconclusive because of the noise and parameter correlations; Table 3 lists coefficients of the Hessian matrix for a synthetically created light curve with Poissonian scatter 0.02 mag, evaluated at the global minimum. As we have stressed in the opening of this Section, we need diverse data-sets, because different types of data are not equally sensitive to different parameters; this is immediately evident by inspecting the coefficients of the Hessian matrix: parameters q and a make the matrix singular, because both parameters have little-to-no effect on the shape of a light curve. Had we also used a radial velocity curve, the Hessian would have been different. The Hessian test can thus help the analysis of the shape of the local minimum, but it cannot aid us in handling degeneracies in any thorough-going way.

6.7 Handling degeneracies efficiently

We have already stressed in the opening discussion of this Section how important it is to discern between local and global minima and to guide the minimizer towards the deepest minimum. The degeneracy that is inherent to the problem due to non-linearity and parameter correlation needs to be analysed *for every single modeled data-set* if error estimates and solution reliability are to be recovered properly.

One of the common misconceptions found in literature about degeneracy is the claim of having many minima within the global minimum valley

and that significant effort should be invested into finding the right minimum. Such a claim is invalid because it suggests that the model is able to discern between *physically undiscernible* minima: the shape and layout of the parameter hyperspace within minima regions is *not* determined by the data signal, it is determined by the data noise. If a single observational data point changes, the shape of the minima valleys would also change. Yet the difference between these two solutions is physically irrelevant – whenever a solution changes by the amount less than is the level of accuracy of the data, individual minima within are *all* equivalent. The co-dimension[15] of the minimum is always larger than 1 and can span up to the dimension of the hyperspace itself: the minima are bound regions rather than points, within which all solutions are equivalent. This does not constitute a physical degeneracy of the model that would in any way need to be addressed.

Another common misconception is to try and extract physical parameters of the model from the data which are not sensitive to that parameter. A good example for this is the attempt to obtain the semi-major axis a from photometric light curves; another such example would be to discern between two symmetric values of inclination with respect to 90°, i.e. 80° and 100°, for circular[16] orbits. Since such cases do not contain any physical information (other than the fact that there *is* no physical content in the given observational data-set), they do not constitute a physical degeneracy.

Apart from those two cases, *any other* effect that causes the value of the cost function to be (roughly) the same for different sets of parameters constitutes a physical degeneracy that we must learn to recognize and handle properly. An example of a true (and often present) degeneracy is between the inclination i and surface potentials Ω_1 and Ω_2, depicted on Fig. 46: smaller inclination may be compensated by enlarging the radius of the star, which corresponds to lower values of Ω_1 – according to Eq. (3.16). This degeneracy is difficult to handle without additional data sources or external conditional constraints (i.e. the ones imposed by the user, not by the model).

To be able to tackle such problems, two heuristic approaches have been developed and incorporated in our model: heuristic scanning and parameter kicking (Prša and Zwitter, 2005a).

[15]The codimension is defined as the number of mutually independent directions in which the gradient of the cost function is 0. This may be easily visualized in the 3D case: a minimum may be either a point, as the lowest part of the sinclination, a line, as a V-shaped canyon or a region, as a flat bottom of the valley.

[16]You may recall from Section 3 that the value of inclination determines the direction of rotation as projected on the plane-of-sky: clock-wise for $i < 90°$ and counterclock-wise for $i > 90°$. It is thus impossible to discern symmetric values of inclination with respect to $i = 90°$ when orbits are circular.

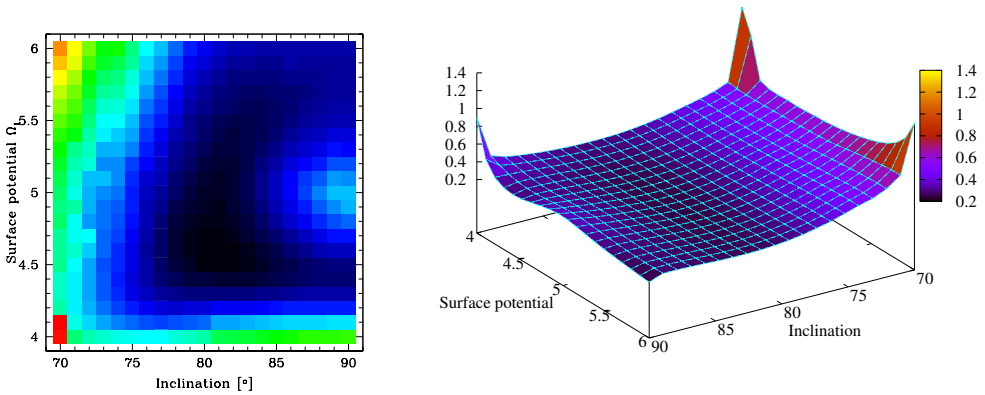

Figure 46: Degeneracy between the inclination i and the surface potential of the primary star Ω_1. Left: mesh plot of the i-Ω_1 cross-section. Right: 3D plot of the i-Ω_1 cross-section. Color coding corresponds to the value of the cost function, black being the lowest. The plots were computed for simulated binary data with two light-curves with Poissonian scatter 0.02 mag. The degeneracy may be easily understood: smaller inclinations may be compensated by enlarging the star's radius, which directly affects the value of surface potential, according to Eq. (3.16).

6.7.1 Heuristic Scanning

EB minimization algorithms, including even NMS with its property of guaranteed convergence, can be stuck in a local minimum, particularly since parameter hyperspace in the vicinity of the global minimum is typically very flat, with lots of local minima. In addition, global minimum may be shadowed by data noise and degeneracy.

Heuristic scanning is an enhancement method to any minimization algorithm we have discussed so far (DC, NMS, Powell, ASA, ...) that selects a set of starting points in the parameter hyperspace and starts the minimization from each such point. The user defines how starting points are selected – they may be gridded, stochastically dispersed, distributed according to some probability distribution function etc. The algorithm then sorts all solutions by the cost function (λ or χ^2, for example) and weights the obtained parameter values accordingly: heuristic runs with smallest values of the cost function correspond to the deepest minima and should thus have a higher weight – they are most suitable candidates for the global minimum.

The weighted values of adjusted parameters are then put into histograms, from which the mean and standard deviation of parameter values are calcu-

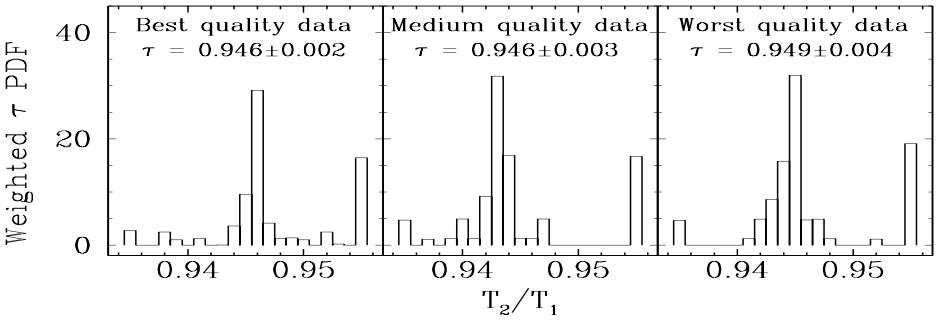

Figure 47: Temperature ratio histogram obtained as a result of heuristic scan. Plots show $\tau = T_2/T_1$ histograms for three different observational datasets: $\sigma_{\rm LC} = 0.005$, $\sigma_{\rm RV} = 5\,{\rm km\,s^{-1}}$ (left), $\sigma_{\rm LC} = 0.015$, $\sigma_{\rm RV} = 15\,{\rm km\,s^{-1}}$ (middle) and $\sigma_{\rm LC} = 0.025$, $\sigma_{\rm RV} = 25\,{\rm km\,s^{-1}}$ (right). First and last bins hold all other outlying points. Heuristic scanning is practically insensitive to the observational data accuracy as long as there are sufficient data points to determine both eclipse depths. Obtained values of temperature ratios are purely statistical and may be compared to the true value of $\tau = 0.9452$ that was used to create the data-set. Adopted from Prša and Zwitter (2005a).

lated. These estimates are truly statistical, since they do not depend on formal errors of the numerical method. Fig. 47 shows an example of such histograms for the effective temperature ratio $\tau = T_2/T_1$, adopted from Prša and Zwitter (2005a). Heuristic scan results for this particular example are virtually insensitive to observational data accuracy: for three significantly different cases (labelled *best*, *medium* and *worst* quality data on Fig. 47), the outcome of the histogram fit is approximately the same. Histograms for other parameters have somewhat larger standard deviations because of degeneracy. It should be noted that reliable statistics implies many starting points of heuristic scan, which in turn implies significant prolongation of the algorithm computation time: each additional scan linearly contributes to the time cost.

Because of data noise and degeneracy, the global minimum is essentially never a single point (with its corresponding uncertainty), it is actually a *region* (with its corresponding uncertainty) in parameter hyperspace. Such a region encompasses many adjacent minima, the depths of which are physically indistinguishable – a single observed data point with its individual weight may change the identity of the deepest minimum within that region. To identify these regions, we compute *convergence tracers* – selected 2D cross-sections of the parameter hyperspace, tracing parameter values from each starting point, iteration after iteration, all the way to the converged solution. Attractors – regions that attract most convergence traces – within

these cross-sections reveal parameter correlations and degeneracy. Inspecting such convergence tracers offers additional insight into the quality and integrity of the solution. Local minima are those that lie outside of the deepest attractor(s); those are the ones that need to be identified and avoided. Fig. 49(a) shows the i-Ω_1 convergence tracer computed for the same simulated data as in Fig. 46. The correlation between i and Ω_1 is evidently very flat at inclinations close to 90°, which may be easily understood: the model is able to compensate smaller inclinations by enlarging the radius of the star and vice versa. Therefore we should not trust light curve analysis to disentangle these parameters by itself – additional constraints are needed. This issue will be further discussed in the next Section.

6.7.2 Parameter kicking

Another possible approach to detect and escape from local minima is to use a stochastic method such as Simulated Annealing (SA). However, such methods are notoriously slow. Thus, instead of full-featured SA scan, a simple new procedure has been developed that achieves the same effect as stochastic methods, but in significantly shorter time. The idea is as follows: whenever a minimum is reached within a given fractional accuracy, the algorithm runs a globality assessment on that minimum.

Parameter kicking is a way of knocking the obtained parameter-set out of the minimum: using the Gaussian PDF, the method randomly picks an offset for each parameter. The strength of the kick is determined by the Gaussian dispersion $\sigma_{\rm kick}$, which depends on the minimum globality assessment parameter λ, Eq. (6.5). If λ is high, then the kick should be strong, but if it is low, i.e. around $\lambda \sim 1$, then only subtle perturbations should be allowed. Tests have shown that a simple expression such as:

$$\sigma^2_{\rm kick} = \frac{0.5\lambda}{100} \tag{6.25}$$

works very efficiently in case of partial eclipses (Prša and Zwitter, 2005a). This causes $\sigma^2_{\rm kick}$ to assume a value of 0.5 for 10σ offsets and 0.005 for 1σ offsets, being linear in between. Note that this $\sigma_{\rm kick}$ is *relative*, i.e. given by:

$$\sigma^{\rm abs}_{\rm kick} = x\,\sigma^{\rm rel}_{\rm kick}, \tag{6.26}$$

where x is the value of the given parameter. When convergence within the given fractional accuracy is reached, parameters are kicked with respect to the depth of the minimum and the minimization is restarted from displaced points. The influence of consecutive parameter kicking with NMS is depicted

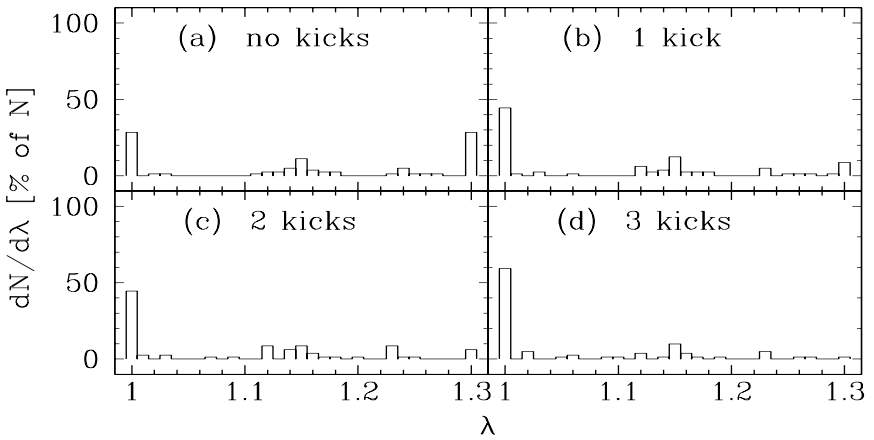

Figure 48: λ-histogram for initial heuristic scan and three consecutive parameter kicks. The success of parameter kicking is obvious, since after only three consecutive kicks the percentage of scans that converge within 1% of the optimal value of λ (in case of proper σ_k's $\lambda = 1$) is *doubled* from ∼30% to ∼60% Prša and Zwitter (2005a). As shown by Prša and Zwitter (2005), parameter kicking proves to be even more efficient in case of exclusively photometric observations, with improvement from ∼15% to ∼75% in convergence after three consecutive kicks.

in Fig. 48; it is shown that out of all heuristic scans only ∼30% initially converge to within 1% of optimal[17] value of λ, whereas this percentage steadily grows to ∼60% after three kicks. Figs. 49(b)–(d) show significant improvement to the solution introduced by these consecutive kicks. Parameter kicking is able to quickly escape from local minima and thus rapidly increase convergence efficiency of the whole NMS method. A down-side of parameter kicking is the time cost: each additional kick linearly adds to the overall execution time.

6.7.3 What happens to those oblivious of degeneracy?

A recent refereed publication (Hawkins et al., 2005) is an example of what may happen when the degeneracy is not handled properly. The modeled star V1128 Tauri is an overcontact W-type W UMa eclipsing binary at inclination $\sim 85^\circ$ that exhibits eclipses with amplitude $\sim$ 1mag and magnetic activity revealed by the O'Connell effect (O'Connell (1951); an effect where observed

[17]Note that the actual value of λ is not important; having under- or overestimated σ_k's, the value of λ will be less or more than 1. It is the relative offset from the minimal value of λ that is important.

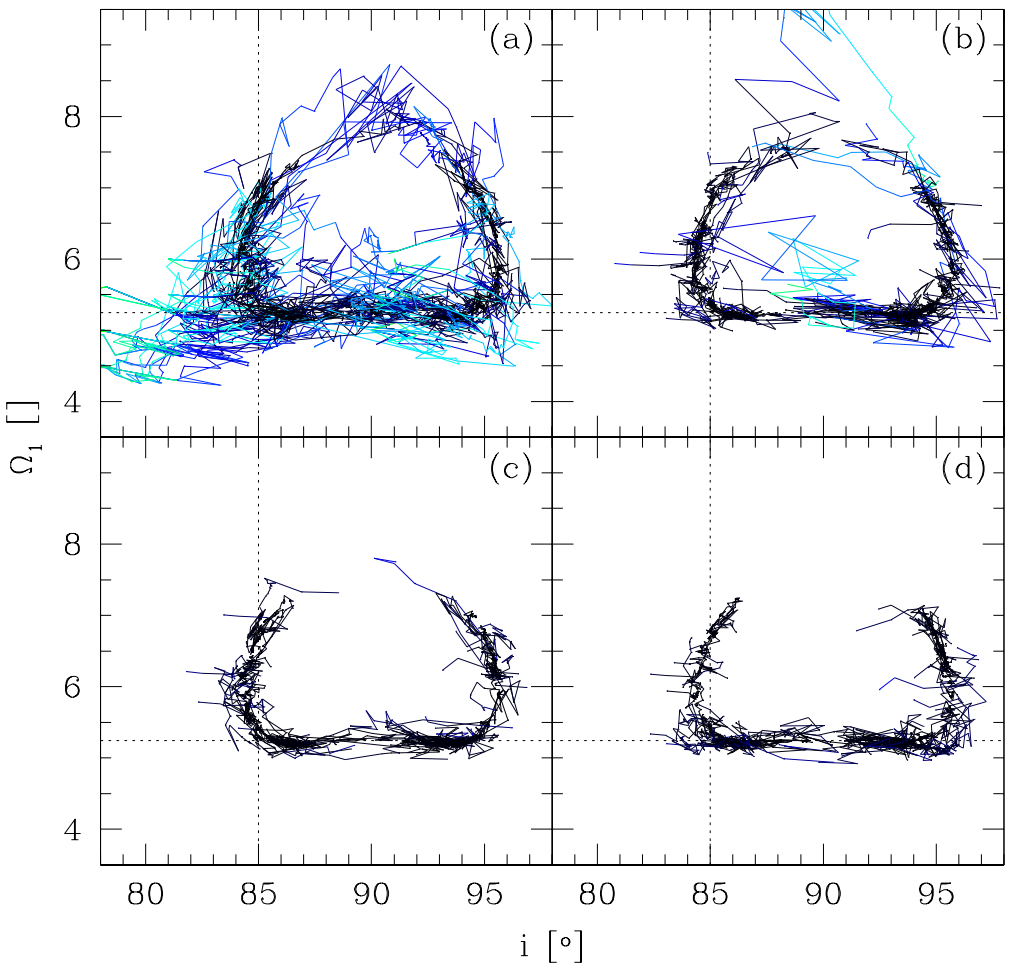

Figure 49: Convergence tracer for i-Ω_1 cross-section. Colors denote the value of the cost function: darker the trace, lower the value of χ^2. This particular case is a notorious example of very difficult-to-handle correlation between the inclination and effective potentials (hence the radii) of both components (only Ω_1 correlation is depicted for brevity). Individual plots denoted with letters (a) through (d) show the result of NMS heuristic scanning from zero to three consecutive parameter kicks. Cross-hairs mark the position of the true minimum. Attractors are symmetric to $i = 90°$, but still very flat at $i \sim 85°$ to $90°$ interval, which means that the obtained NMS solution should not be blindly trusted; rather, additional constraining is needed.

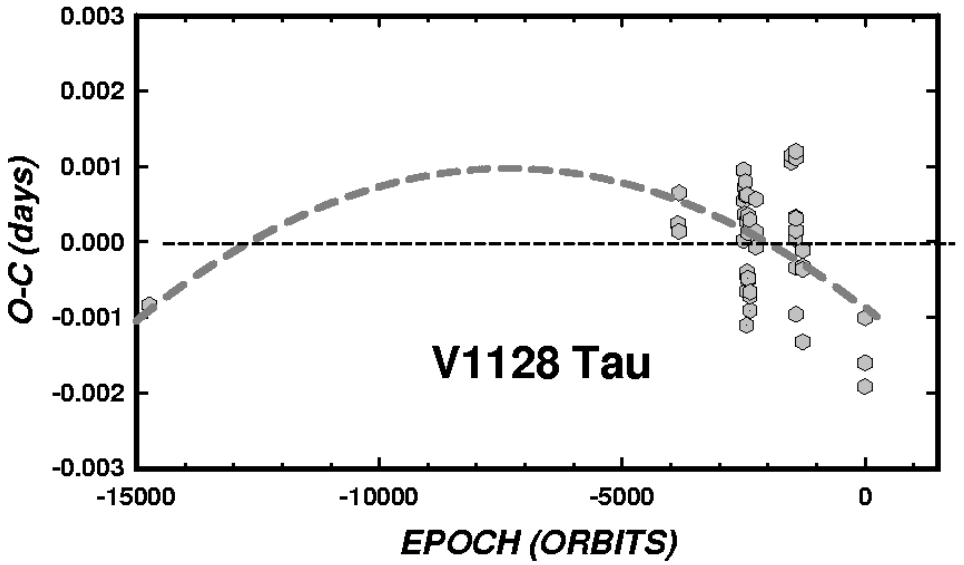

Figure 50: Period change observations (points) and the fit (line) for V1128 Tauri. Taken from Hawkins et al. (2005).

flux at quarter-phases differs due to magnetic activity of W UMa stars). Let us point out the traps of the EB field that have sprung on this paper:

1. The data used in this study was *exclusively* photometric: no spectra, no radial velocities. Without radial velocities it is virtually impossible to obtain a filling factor (see Eq. (3.24) for its definition) accurately; as a consequence, there is no solid handle on the value of the surface potential of the binary, so the correlation between Ω and the inclination i is very strong. The implications of this correlation have been described in Section 6.7.

2. Magnetic activity implies adding spots to the model. With proper tuning, spots may account for *any* flux variation that is exhibited in light curves, be it of magnetic origin or not. A non-eclipsing system may be easily mimicked to be an eclipsing system by putting the right spots at the right places on the stellar surface. One should thus *never* add spots to the model if there is no firm evidence that points to it, e.g. accurate Doppler tomography based on high-resolution spectroscopy (Section 2.3.4). The paper introduces a large spot ($\varrho_{\rm sp} = 25°$) on the primary star without any strong backing evidence.

3. Secular changes of the period are common in overcontact systems. Modeling these changes is usually done by trying to fit the times of

primary and secondary minima with some smoothly varying function, most commonly a straight line. Fig. 50 shows a fit to the data as is suggested by the paper. Not only does the fit look bad, it is fitting a second-order function to the data-set where the central parts are missing. There is no obvious justification for such a secular change.

4. Primary star temperature was *fixed* prior to analysis to 6000K, according to the spectral classification. This approach almost yields the wrong color indices, as our discussion in Section 7.2.2 will show. This means that the solution is discordant in color with observations.

5. To top everything off, the paper gives error estimates of the secondary star temperature to be 1K, of the inclination 0.06°, of the mass ratio 10^{-3}, on the spot position 1° and size 0.3°. These error estimates are significantly underestimated.

Hopefully this work will contribute a bit to raising the awareness of the EB community towards issues of degeneracy.

7 PHOEBE - PHysics Of Eclipsing BinariEs

We have so far covered modeling principles upon which the Wilson and Van Hamme (2003)'s WD code is built and described several approaches to the solution-seeking process. We now proceed with formally introducing a new facility for modeling eclipsing binaries.

So why would one build yet another modeling program? The answer is simple: one would not. Tackling the same old problems all over again makes no sense; rather, one builds on the basis of what has already been done. This is what our effort is all about: to create a modeling package built on top of the Wilson-Devinney code, introducing new enhancements, while still retaining 100% WD compatibility. Enhancements include new physics (proper handling of color indices and therefore temperatures in absolute units; conditional constraining; interstellar reddening effects), existing minimization scheme add-ons (stability and convergence improvements), and new minimization schemes aiming to fully automate the first steps of solution seeking (an issue of utmost importance for ambitious space scanning missions such as Gaia (Perryman et al., 2001)). We discuss the main characteristics of this new package, called PHOEBE: PHysics Of Eclipsing BinariEs.

7.1 What is it all about?

There have been many codes that have been derived from WD (forks) in the last 20 years, e.g. Binary Maker (http://www.binarymaker.com), Kallrath and Linnell (1987)'s WD87, Kallrath et al. (1998)'s WD98K93, Terrell's (unpublished) WDLC, which only shows the interest and appreciation of the community towards WD. We attempt to recognize some of the problems that these forks were facing and avoid them in PHOEBE.

1. Commercial code. Binary Maker by D. Bradstreet is sold for $100; although commercial software usually comes with warranty and support, it lacks the one thing a scientist needs: source code. Users are *restricted* to only using the code, not being able to modify it, enhance it or understand its subtleties.

2. Obfuscated code. If the code is supposed to do science, it should not be bloated with interwoven numerical algorithms and inline switches which demand recompiling of the entire program for each modeled binary.

3. Unportable code. The code that runs only under certain operating

systems (even worse, under only *commercial* operating systems), causes inconvenience, to say the least, by forcing the users to change their preferred environment just to be able to run the code.

4. Restrictive code. The layout of the code may be appealing, but because of the interface design the list of actions supported by the code is very limited, constraining the user to do only what the author of the program had conceived.

5. Backwards-incompatible forks. A very important point often overseen, the modifications introduced to the original code made it incompatible with the original WD, which is still being actively developed by R. E. Wilson and W. van Hamme. This means that whenever a new WD version comes out, there is a strong overhead imposed on the forks to re-do all hand-made changes to WD so as to remain compliant with the rest of the community.

When designing PHOEBE, we took all of the above considerations into account, trying to overcome the described problems. Technically speaking, PHOEBE's engine is a strict LALR(1) scripting language[18] especially designed for modeling eclipsing binaries. Although it currently uses WD as back-end, it can accomodate any physical model instead or in addition to WD. Being a scripting language makes it fully flexible to users' needs. It is written in ANSI C, which makes it fully portable to any platform and any compiler around. It is released under GNU General Public License, which makes it free and available to any interested parties. Finally, it features a full-fledged graphical user interface, which brings intuitivity and ease of clicking to the EB community.

PHOEBE is built in three layers: the lowermost layer is the modeling engine, currently employing WD. On top of it is the extension layer, where all scientific, numerical and technical extensions are incorporated. The topmost layer is the user interface layer, which serves as a bridge between the user and the model. In this Section we proceed by describing most important aspects of the extension layer that have never before been used in modeling eclipsing binaries.

7.2 What is different?

WD's extensive list of more than 30 adjustable parameters is an overwhelming indicator of how sophisticated the model has become in 35 years of devel-

[18] See Aho and Ullman (1977) for thorough discussion on computer language theory.

opment. Nevertheless, accuracy is crucial for a model to describe such a wide diversity of intrinsically different binaries. An accurate model should contain all relevant physical contributions for which the governing laws are well-known. We start the discussion by introducing new physical ties and constraints to parameter extracting schemes that are implemented in PHOEBE. It should be stressed that all these constraints are *optional* and it is up to the user to select the ones that are of interest.

7.2.1 Building a synthetic binary

To demonstrate some of the innovations PHOEBE brings to the EB field, a synthetic binary model is created. Testing the methods against a synthetic model may seem artificial, but the obvious advantage of knowing the right solutions is the only true way of both qualitative and quantitative assessment. Some preliminary results of using PHOEBE on true observations were already presented by Prša (2003) and will be overviewed in the next Section.

Our synthetic binary consists of two main-sequence F8 V–G1 V components with their most important orbital and physical parameters listed in Table 4. It is a partially eclipsing detached binary with only slight shape distortion of both components ($R_{1,\mathrm{pole}}/R_{1,\mathrm{point}} = 0.974$, $R_{2,\mathrm{pole}}/R_{2,\mathrm{point}} = 0.979$). Light curves are generated for Johnson B and V passbands in 300 phase points with Poissonian scatter ranging from $\sigma_{\mathrm{V}} = 0.005$ to $\sigma_{\mathrm{V}} = 0.025$. Radial velocity (RV) curves are generated in 50 phase points with Gaussian scatters ranging from $\sigma_{\mathrm{RV}} = 1\,\mathrm{km\,s^{-1}}$ to $\sigma_{\mathrm{RV}} = 25\,\mathrm{km\,s^{-1}}$. Light curves in B and V with $\sigma_{\mathrm{V}} = 0.015$ and both RV curves with $\sigma_{\mathrm{RV}} = 15\mathrm{km\,s^{-1}}$ are depicted in Fig. 51. Passband transmission curves were taken from ADPS (Moro and Munari, 2000).

This model binary will be used for demonstrating all PHOEBE's capabilities that are novel to the field of EBs.

7.2.2 Color-indices and effective temperatures

One of the main difficulties of modeling eclipsing binaries is accurate determination of individual temperatures of both components. Frequent practice in literature is to *assume* the temperature of one star (e.g. from spectra or color indices) and fit the temperature of the other star. This approach is often inadequate, particularly for binaries with similar component temperatures and luminosities: in such cases, the contribution of both components to

Parameter [units]	Binary	
	F8 V	G1 V
P_0 [days]	1.000	
a $[R_\odot]$	5.524	
$q = m_2/m_1$	0.831	
i [°]	85.000	
v_γ [km s^{-1}]	15.000	
$T_{\rm eff}$ [K]	6200	5860
L $[L_\odot]$	2.100	1.100
M $[M_\odot]$	1.239	1.030
R $[R_\odot]$	1.260	1.020
Ω [−]	5.244	5.599
$\log g/g_0$ [−]	4.33	4.43
x_B [−]	0.818	0.833
y_B [−]	0.203	0.158
x_V [−]	0.730	0.753
y_V [−]	0.264	0.242

Table 4: Physical parameters of the F8 V–G1 V test binary star. Spectral type – temperature relation taken from Cox (2000). Linear (x) and non-linear (y) coefficients of the logarithmic limb darkening law for Johnson B and V passbands, taken from van Hamme (1993).

the system luminosity is significant and it is difficult to accurately estimate the contribution of only one star in advance.

Before we propose a method capable of providing individual temperatures from standard photometry observations without any a priori assumptions, it proves useful to introduce a concept of effective temperature *of the binary*. A binary may be regarded as a point-source, the effective temperature of which varies in time. Both components contribute to this effective temperature according to their sizes and individual temperatures, and the inclination. Effective temperature of the binary is directly revealed by the color index, so its observational behavior is well known. If a model is to accurately reproduce observations, the composite of contributions of both components must match this behavior.

The observational light curve quantity (dependent variable) WD works with is *flux*, scaled to an arbitrary level (which could also be in absolute physical units, i.e. W/m^2 per wavelength interval). The model adapts to this level by determining the corresponding passband luminosity L_1^i, one for each passband. However, these passband luminosities are completely decoupled

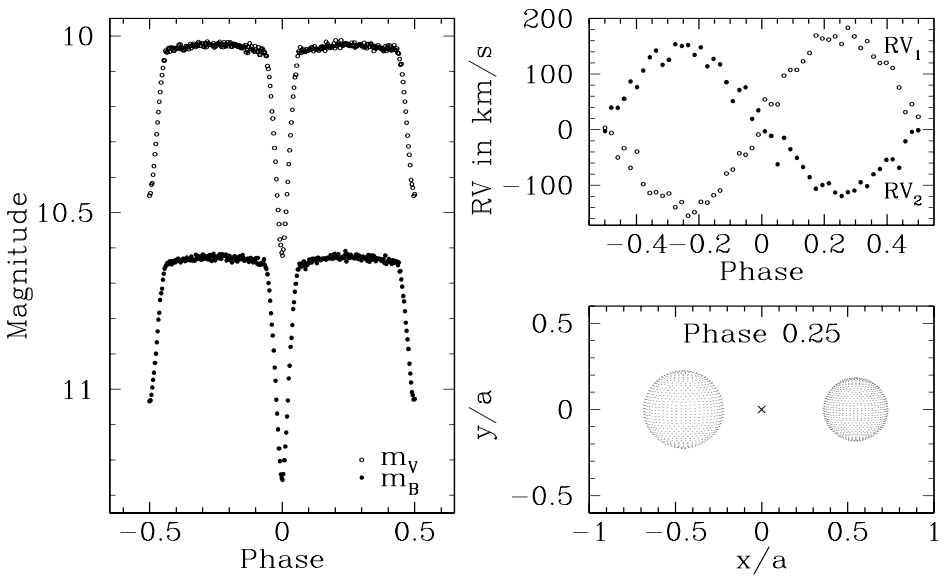

Figure 51: F8 V–G1 V test star data. Light curves are computed for Johnson B (filled dots) and V (empty dots) passbands in 300 phase points with $\sigma_{\rm V} = 0.015$ (left panel). RV curves are computed in 50 phase points with $\sigma_{\rm RV} = 15\,{\rm km\,s^{-1}}$ (upper right panel); eclipse proximity effects are turned off. Star plot is computed at quarter phase, cross denotes the center-of-mass (lower right panel).

from one another, so any color information that might have been present in the data is discarded. Since the effective temperature of a binary is observationally revealed by its $B-V$ (or any other suitable) color index[19], some of the relevant temperature information is lost. Transformation to fluxes in absolute units would not suffice for properly determining the corresponding passband luminosities – one needs a *physical relation* between those luminosities. Neglecting this additional relation results in discordant colors between the temperatures obtained by the fit (assuming that T_1 is à priori known) and the ones determined by the binary's effective temperature. This relation is nothing else than the color index and may thus be accurately determined from observations.

In the last decade substantial effort was made to scan the sky for standard stars to be used for photometric calibration: Landolt (1992) covering celestial equator, Henden and Honeycutt (1997) and Bryja and Sandtorf (1999) covering fields around cataclysmic variables, Henden and Munari (2000) cov-

[19]Useful relations among color indices are given in Caldwell et al. (1993). Although color-indices depend also on $\log g/g_0$, metallicity and rotational velocity, their effect is much smaller than the temperature.

ering fields around symbiotic binaries, to name just a few. These efforts help overcome the problem of small CCD fields with respect to all-sky photometry, since in many fields there are now cataloged standard stars that may be used to extract color indices for EBs. In context of PHOEBE, this means that using measured color indices as additional information is plausible even if the data were not obtained under photometric conditions.

PHOEBE initially regards L_1^i as simple level-setting quantities – physical context comes in only after the color index constraint is set. For the sake of simplicity, consider that input observational data are supplied in magnitudes rather than fluxes, without any arbitrary scaling of the data: colors must be preserved.

The physical quantity PHOEBE works with is inherited from WD, which is flux. PHOEBE uses a single, passband-independent parameter m_0 to transform *all* light curves from magnitudes to fluxes. The value of m_0 is chosen so that the fluxes of the dimmest light curve are of the order of unity. It is *a single quantity* for all light curves, which immediately implies that the magnitude difference, now the flux ratio, is preserved; hence, the color index is preserved. If the distance to the binary is known (e.g. from astrometry), m_0 immediately yields *observed* luminosities in physical units; intrinsic luminosities in physical units are obtained if the color excess $E(B-V)$ is also known.

This is where physics comes in: from such set of observations, the calculated L_1^i are indeed passband luminosities, the ratios of which are the constraints we need: passband luminosities of light curves are now connected by the corresponding color indices. Once the color constraint is set, PHOEBE makes sure that the ratio between L_1^i is kept constant.

Now that the color indices are preserved, effective temperature of the binary may be obtained from a color–temperature calibration. PHOEBE uses updated Flower (1996) tables with coefficients given in Table 5. It should be stressed that the color constraint is applicable only if the data are acquired on (or properly transformed to) a standard photometric system.

Applying the color constraint, effective temperatures of individual components may be readily disentangled by the minimization method. The method is now able to find only those combinations of parameters that *preserve* effective temperature of the binary and hence the color index. Since the relation between effective temperatures of individual components is fully determined by the light curve shape (predominantly by the primary-to-secondary eclipse depth ratio) and since the sum of both components' contributions must match the effective temperature of the binary, the color-constrained minimization

Coefficient:	V, IV, III, II	I
C_0	3.979145	4.012560
C_1	-0.654992	-1.055043
C_2	1.740690	2.133395
C_3	-4.608815	-2.459770
C_4	6.792600	1.349424
C_5	-5.396910	-0.283943
C_6	2.192970	–
C_7	-0.359496	–

Table 5: Coefficients of the empirical $\log T_{\rm eff}$ $(B-V)$ relation given by the 7th degree polynomial fit $\log T_{\rm eff} = \sum_{i=0}^{7} C_i (B-V)^i$ (Flower 2004, private communication). The second column applies to main-sequence stars, subgiants and giants, the third column applies to supergiants.

method yields effective temperatures of individual components without any à priori assumptions.

Simulation.

Before we get into details about the actual simulation, we should point out a common point of confusion when working with PHOEBE or WD: how is the total flux that is computed by the model normalized and how is it connected to passband luminosity L_1^i? The flux at reference phase (usually quarter-phase) is given by:

$$J^i_{\rm ref} = \frac{L^i_1}{4\pi}\left(1+\frac{L^i_2}{L^i_1}\right), \tag{7.1}$$

where L_1^i and L_2^i are passband luminosities of the primary and secondary component in the i-th passband, respectively, and the term 4π comes from the definition of emergent intensity per steradian's worth of area. This means that by setting $L_1^i = 4\pi$ and assuming that the luminosity of the secondary star is negligible, the flux value at reference phase would be 1.0. If on the other hand we used two stars which are exactly the same, the flux value at reference phase would be 2.0. This relative flux can be expressed in physical units only after the distance to the binary and at least one of the temperatures are known. Such convention, although trivial, has caused more than its rightful share of confusion, that is why we stress it here.

The simulation logic is as follows: we take Kurucz's spectral energy distribution (SED) function for both components from the spectra database

compiled by Zwitter et al. (2004), doppler-shift them to the reference phase, sum their SEDs weighted by their corresponding luminosity and convolve the sum with the passband response functions of Johnson B and V filters. This enables us to compute the B-V color-index, which needs to be zero-corrected with respect to spectral type A0 (adopted temperature 9560 K). Once this is done, we have obtained a synthetic prediction of the color index. Alternatively, the same result may be obtained by using color calibrations, e.g. Flower (1996) corrected tables given in Table 5. The color indices may now be readily transformed to the ratio of passband fluxes $J^V_{\rm ref}/J^B_{\rm ref}$. We set the value $L^V_1 = 4\pi$ (this does not imply any assumptions, it only sets the normalization point of the total flux) and color-consistent value for L^B_1 follows directly from Eq. (7.1).

Once the light curves are built so that the color index is preserved, we follow the described color-index constraining principle to assess the implications of erroneous *assumed* value of $T_{\rm eff1}$. The model without color-index constraining will yield a satisfactory solution even for erroneous absolute values of temperatures because the passband luminosities are completely decoupled from one another, whereas they should be constrained by the color index.

Results.

Our analysis brings us to the following conclusions:

1. Individual temperatures without the imposed color-index constraint are fully correlated. Fig. 52 depicts a $T_{\rm eff1}$-$T_{\rm eff2}$ cross-section of the parameter hyperspace, where this correlation is clearly visible. The reason for this is the degeneracy between the temperatures and passband luminosities L^i_1: local effects of slightly different temperatures on the *shape* of the light curve are very small, hardly noticeable (they scale roughly with the ratio of both temperatures), so the χ^2 cost function doesn't *feel* their influence. However, even slightly different temperatures cause an additional effect which is an order of magnitude stronger: they scale both light curves, thus changing the color index. If this change is not constrained, the model relies only on secular effects, which are almost always buried in data noise and parameter degeneracy. Without color-constraining there is thus *no way* to pinpoint a location in the $T_{\rm eff1}$-$T_{\rm eff2}$ cross-section that corresponds to the right solution.

2. Unless the luminosity of one component is overwhelming, there is no guarantee that the *assumed* value of temperature is in agreement with

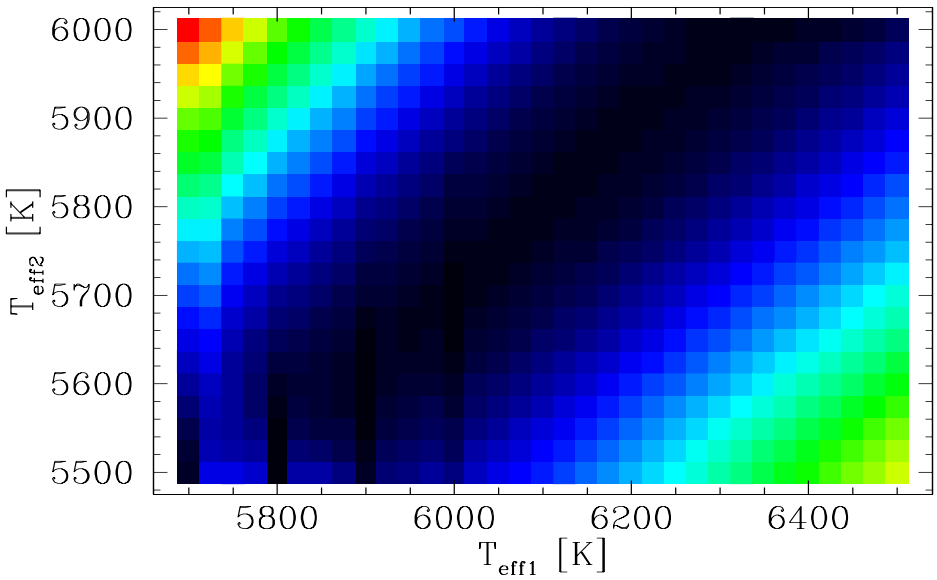

Figure 52: T_{eff1}-T_{eff2} cross-section of the parameter hyperspace. Different colors represent the value of the χ^2 cost function: black corresponds to the lowest χ^2 value and red corresponds to the highest χ^2 value on the plot. The simulation was done for the synthetic binary presented in Section 7.2.1, with surface potentials Ω_1, Ω_2 and passband luminosities L_1^B, L_1^V obtained by the χ^2-minimization in each mesh point.

reality. Fig. 53 shows a range of assumed values for T_{eff1} and the yielded color indices by the model which is *not* color-constrained. Since the shapes of light curves determine the ratio of luminosities of individual stars, it has to remain approximately constant. To achieve this with changing temperatures, the model adapts passband luminosities (first order effect) and stellar radii (second order effect) accordingly. The problem now becomes immediately evident: if we are to assume a primary star temperature from the quarter-phase color index, it would be roughly $T_{\text{eff1}}^{\text{assumed}} = 6080\,\text{K}$, around 120 K off just because the luminosity of the secondary star is not negligible. In principle, the solution could then be *manually* re-iterated by computing the predicted color-index from the solution, comparing it to the observed color index and then modifying the assumed temperature to get closer to the right solution. This is tedious and prone to subjective considerations, it should thus be avoided.

3. Adopting the color-constraint means fixing the ratio of passband luminosities L_1^V/L_1^B to the value which is in agreement with the observed color index. This means that *only* L_1^V is adjusted to reproduce the V

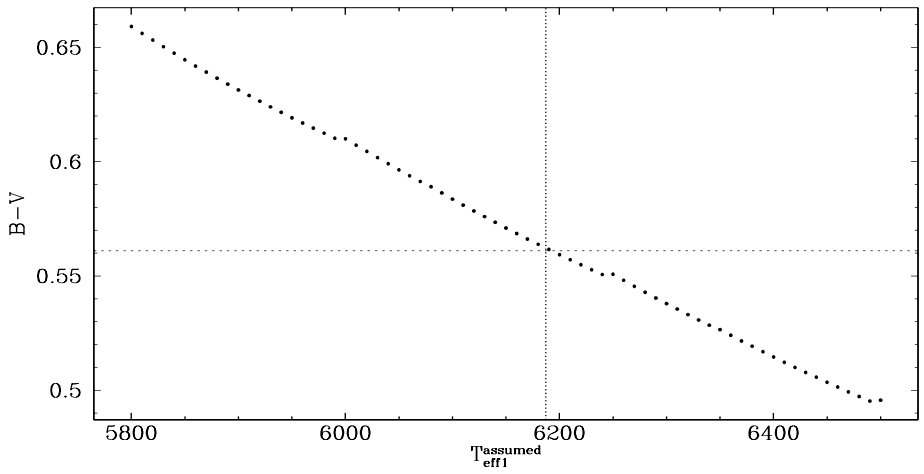

Figure 53: Color index dependence on the assumed value of the primary star temperature. If color-constraining is not applied, all depicted points may be satisfied by the model. If we are to assume the value of T_{eff1} from the color index at quarter-phase, it would yield $T_{\text{eff1}} = 6080\,\text{K}$, a value which is $\sim$120 K off from the correct value. If on the other hand we apply color-constraining, we immediately get a handle on which color index corresponds to the temperatures yielded by the model. Cross-hairs denote the solution obtained by color-constraining, which gives $T_{\text{eff1}} = 6187 \pm 32\,\text{K}$.

light curve and L_1^B (and other L_1^i for subsequent passbands) is then computed from this constraint. By this constraint the degeneracy between the temperatures and the passband luminosities is broken: we obtain a straight horizontal line over Fig. 53 which best represents the color-index. Thus, we obtain the primary temperature *without any assumptions*, and the secondary temperature follows directly from the model. Applying this to our test binary, we obtain individual temperatures $T_{\text{eff1}} = 6\,187\ \text{K} \pm 32\,\text{K}$ and $T_{\text{eff2}} = 5\,868\,\text{K} \pm 31\,\text{K}$. Comparing these values to true values $T_1 = 6\,200\,\text{K}$ and $T_2 = 5\,860\,\text{K}$ is very encouraging.

4. Finally, let us consider the correlation between the temperatures and the radii of the binary system components. We have mentioned earlier that this is a second order effect, but it is still very important to quantify the correlation between those two parameters. Since the radii come into the model via surface potentials Ω, we need to consider the correlation between the ratio of temperatures T_2/T_1 and surface potentials. Fig. 54 shows the convergence tracer for the T_2/T_1-Ω_2 cross-section, where we see that the correlation does exist (the off-diagonal element is 0.2), so it is important to be aware of this degeneracy.

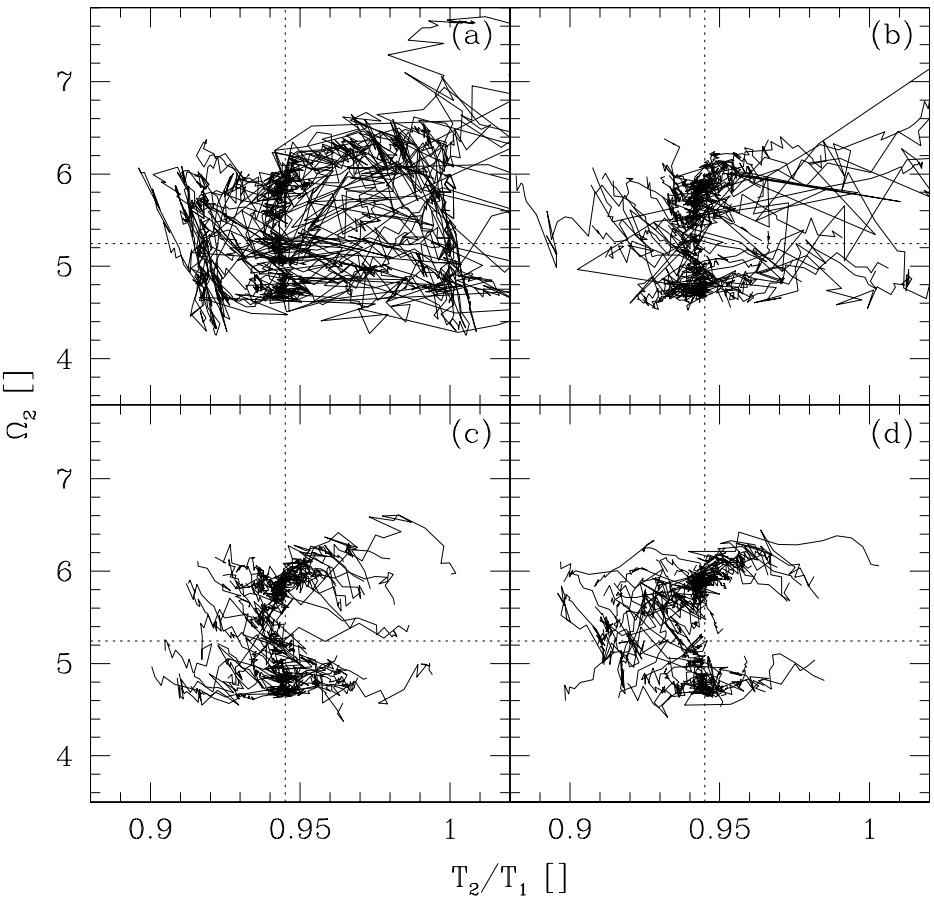

Figure 54: Convergence tracer for the $T_{\rm eff2}/T_{\rm eff1}$-$\Omega_2$ cross-section. Cross-hairs denote the correct solution. Panels (*a*) to (*d*) correspond to the solution obtained by NMS for 0, 1, 2 and 3 parameter kicks.

We have demonstrated how severe the implications of subjectively assuming a primary star temperature from the color index may be if special care is not taken to submit the acquired solution to manual re-iteration until the solution corresponds to the observed color indices. We have facilitated this task in PHOEBE, it is now readily available as part of the default reduction and analysis pipeline. The effect is already very pronounced for a modest case of two similar main-sequence components and it would be significantly greater e.g. for a hot main-sequence–cool giant system, where both stars have similar luminosities; in those cases the published solution may be off by as much as ∼1000 K. By having this method for objective determination of individual temperatures in place, we hope to raise awareness of this issue in future solution-seeking analyses.

7.2.3 Spectra as independent data source

Traditionally, spectra have been used only indirectly, e.g. for extracting radial velocities or determining effective temperatures. Several recent studies of individual EBs have shown that including flattened spectral energy distributions (SED) may be used as external check of the model solution (see Siviero et al. (2004) and Marrese et al. (2004b) for examples), where individual spectral lines of echelle spectra are compared with Kurucz (1993) model atmospheres.

Since the Kurucz's model atmosphere program runs only under VAX/VMS in its distributed form, several databases of precomputed spectra have been assembled for practical use (e.g. Zwitter et al. (2004) covering the spectral range 765–875nm, Murphy and Meiksin (2004) covering 300–1000nm, Munari et al. (2004a) covering 250–1050nm). Such databases bring stellar atmospheres to non-VAX/VMS equipped users. In recent years significant effort has been made to port Kurucz's model atmospheres code to Linux (see e.g. CCP7 initiative at `http://ccp7.dur.ac.uk`, Sbordone et al. (2004) and others). Such initiatives enable users to include SED data in solving the inverse EB problem. PHOEBE already takes a step in that direction by using a synthetic spectra database to test whether flattened, wavelength-calibrated spectra match synthetic spectra within a given level of significance.

One very important caveat that should be stressed: it is not feasible to compare observational SEDs to synthetic SEDs over the full spectral range. The problems occur because of Earth's atmosphere (significant parts of the spectrum are dominated by telluric lines, which the model does not handle). By default, PHOEBE uses the Zwitter et al. (2004) grid of 61 196 synthetic spectra covering the 765–875 nm interval at a resolving power $R = 20\,000$. A simple interpolation may be used to obtain the spectrum characterized by any combination of $T_{\rm eff}$, $\log g/g_0$, [M/H] and $v_{\rm rot}$ with the accuracy better than 25 K in temperature, 0.05 dex in $\log g/g_0$ and metallicity and 1 $\mathrm{km\,s^{-1}}$ in rotational velocity. These uncertainties are smaller than the uncertanties of the Kurucz's model for parameters of our test binary, so interpolation does not induce any systematic errors.

To demonstrate the current level of SED implementation in PHOEBE, consider again our test binary. Parametric vectors $(T_{\rm eff}, \log g/g_0, v_{\rm rot})_{1,2}$ of both EB components are determined by the model solution from photometric and RV data. These are used to obtain synthetic spectra by linear interpolation in $T_{\rm eff}$, $\log g/g_0$ and $v_{\rm rot}$ from the grid. For the "true" simulated spectrum, solar abundances ([M/H] = 0.0), corotation ($v_{\rm rot_1} = 64\mathrm{km\,s^{-1}}$, $v_{\rm rot_2} = 52\mathrm{km\,s^{-1}}$) and microturbulence $v_{\rm turb} = 2\mathrm{km\,s^{-1}}$ are assumed. Effective spectrum of the

binary is computed in out-of-eclipse phase (e.g. quarter-phase) by Doppler-shifting and convolving the spectra of the two stars.

After each solution of the NMS heuristic scan, a synthetic spectrum is built[20] from that solution. It is then compared with the "true" spectrum by the χ^2 cost function. Effective temperature is the dominant parameter that governs SED shape, but this is of little use for our case: recall from Fig. 47 and the discussion in Section 7.2.2 on color indices that individual temperatures are well determined from photometry alone. Rather, our solution suffers from degeneracy in effective potentials Ω_1, Ω_2 and inclination i (Fig. 49). It would be beneficial if the SEDs could break this degeneracy. Since the mass ratio and semi-major axis of the model are effectively held constant by the RVs, Ω_1 and Ω_2 depend only on the radii of individual components. Thus, different Ω's imply different $\log g/g_0$ and, by assuming corrotation, also $v_{\rm rot}$. Fig. 55 shows the $v_{\rm rot1}$-$v_{\rm rot2}$ cross-section, demonstrating that, as we hoped, the SED analysis indeed *constrains* the solution to smaller intervals for $v_{\rm rot1}$ and $v_{\rm rot2}$, thus smaller intervals for Ω_1 and Ω_2.

The $v_{\rm rot1}$-$v_{\rm rot2}$ cross-section may sometimes do even more than only break the degeneracy between Ω_1 and Ω_2. If the radii are well determined, e.g. by total eclipse geometry, such analysis yields synchronicity parameters F_1 and F_2, since the only way to compensate the change in rotational velocities for any predetermined radii is to break the corotation presumption. This may be especially important in analysis of well detached systems, as demonstrated by Siviero et al. (2004).

It should be noted that there is *no support* for extracting $T_{\rm eff}$, $\log g/g_0$, [M/H] or $v_{\rm rot}$ from spectra at the moment, only a weighted χ^2 test is done to confirm or reject the particular set. As such, the current implementation forms the base of spectral analysis for EBs, but it still does not contribute fully to minimization. Once we are capable of building stellar spectra without presuming spherically-symmetrical stars in LTE, full SED will be introduced to the minimization process as well. Such a scheme will have to weight properly individual wavelengths, since there is much less information in the continuum of the spectrum than it is, in example, in central parts and wings of spectral lines. However, even the present implementation of SED analysis finds the values of physical parameters which have not usually been attainable by light and RV curve analysis, namely metallicity and rotational velocity (see Terrell et al., 2003).

[20] At present the spectrum may be generated for any orbital phase outside of eclipses.

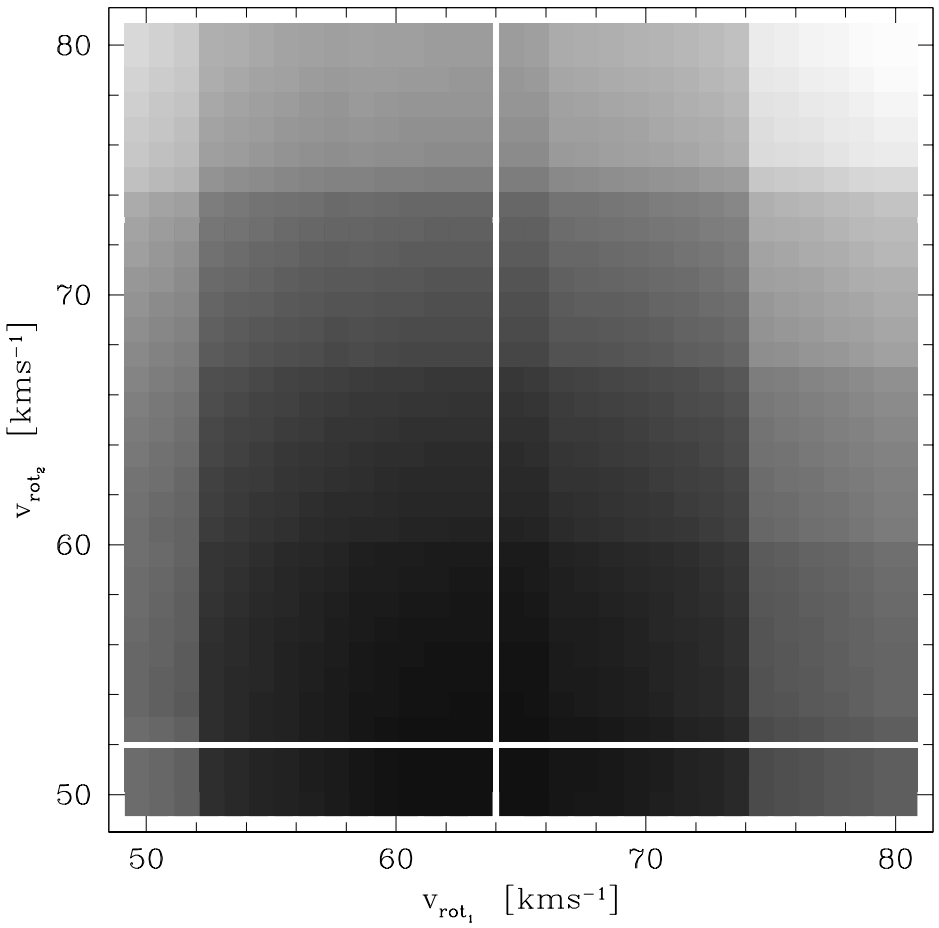

Figure 55: Result of the χ^2 comparison of the "true" spectrum against Zwitter et al. (2004) database. Out of all cross-sections, v_{rot_1}-v_{rot_2} cross-section is most interesting, because it helps break the degeneracy between effective gravitational potentials Ω_1 and Ω_2. The levels of gray in the mesh are linear in χ^2 and denote the quality of the fit: black color corresponds to the best fit, white color corresponds to the worst fit. Cross-hairs denote the position of the true values of rotational velocities.

7.2.4 Main sequence constraints

In cases where SED observations are not available, or where they are used only to extract RVs, the degeneracy among parameters may still be so strong that neither heuristic scan nor parameter kicking can break it. In such cases we stand no chance of obtaining *any* satisfactory solution without further constraining the modeled binary.

WD features 8 modes of operation that determine the morphology of the binary. By deciding on the mode of operation, the user imposes a set of physical constraints; for example, both components of over-contact systems have equal potentials. PHOEBE refers to these constraints as *morphological* constraints. If a morphological constraint is not chosen properly, the model may converge to a physically implausible solution.

On the other hand, we can sometimes make an assumption, not being certain it is correct. In case of degeneracy, a solution based on an assumption may be better than having no solution at all. One assumption might be the age of the coeval components. Assuming a particular type of evolutionary track, the luminosities from stellar evolution models may then be obtained (Pols et al., 1995). Another such assumption could be the distance to the binary, e.g. from astrometry. Yet another assumption may be that either or both components are main-sequence stars. Since a significant percentage of all stars are on the main-sequence, there is a fair chance that our assumption is correct.

Applying main-sequence constraint to component(s) of the modeled binary means imposing M-L-T-R relations for main-sequence stars (see e.g. Harmanec (1988) and Malkov (2003) for such relations specific to EBs). In consequence, given a single parameter (e.g. component's effective temperature), all other parameters (its mass, luminosity and radius) are calculable. This in turn implies that, in case of circular and nearly-circular orbits, effective potential of the constrained component is fully determined. Main-sequence constraint may be used for testing whether either or both stars may plausibly be main-sequence stars: depending on behavior of the χ^2 value, such hypothesis may be accepted or rejected.

Such additional constraints are not as straight-forward as was the case with morphological constraints. For example, by implying the condition: *let the modeled binary be a main-sequence binary*, we break the degeneracy by selecting the one solution that corresponds to that condition. This is why PHOEBE refers to these constraints as *conditional* constraints (CC). It is very important to emphasize that using conditional constraints improperly may lead to creating and propagating a circular argument: EBs provide absolute parameters for stars, which can then be used to establish various calibrations. Conditional constraints on the other hand use calibrations to constrain derived parameters. Conditionally constrained solutions should thus never be used to establish calibrations upon which they were constrained.

Recall from Fig. 49 that the solution from photometric and RV observations of our test binary indeed suffered from degeneracy in inclination and potentials. If we conditionally constrain both modeled components with the

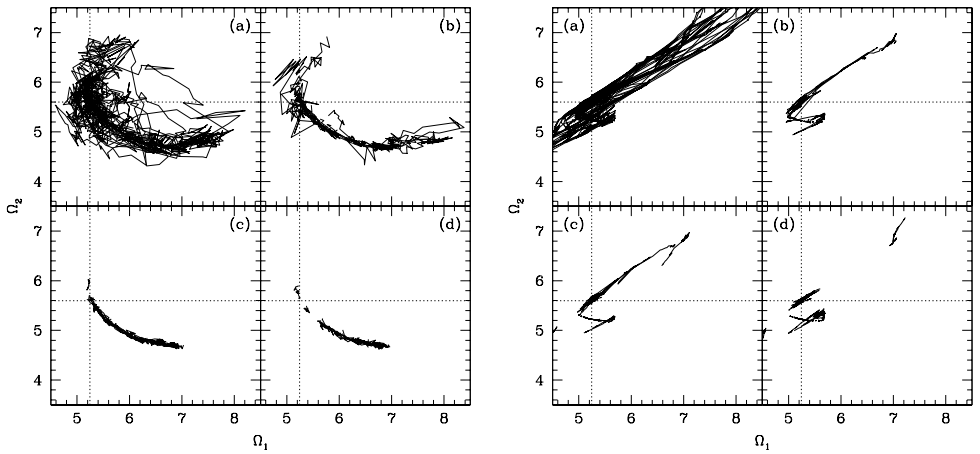

Figure 56: Convergence tracers for Ω_1-Ω_2 cross-section without (left) and with (right) the main-sequence constraint imposed on the model. Similar to Fig. 49, panels (a) through (d) denote successive number of kicks (zero to three) and cross-hairs mark the correct solution. Comparing these results immediately shows that the intersection of the two attractors yields the correct solution. Note that there are two intersections because of the model symmetry to the labeling of the two components (primary and secondary roles of both stars may be interchanged).

main sequence constraint, potentials Ω_1 and Ω_2 are calculable and thus exactly known. The variation in their values is only a consequence of the variation in either of the main-sequence parameters (M, L, T or R) that accomodate for different orbital inclinations during the fit. Fig. 56 shows convergence tracers for a similar NMS heuristic scan as in Fig. 49, this time for Ω_1-Ω_2 cross-section without (left) and with (right) the main-sequence constraint imposed on the model. Since the main-sequence constraint is very strong, there is no practical need for heuristic scan or parameter kicking (both Ω_i's are calculable for the given inclination and convergence is thus assured from practically *any* point in the hyperspace); Fig. 56 (right) still depicts both heuristic scan and consecutive parameter kicks for comparison between convergence tracer shapes and slopes of unconstrained and main-sequence constrained model. It is evident that both solutions intersect, yielding the right solution. This is of course expected, since our test binary is in fact composed of two main-sequence components.

One would hope that total eclipses reduce the degeneracy, but this also does not necessarily happen. If stars have comparable sizes (as is the case of our test binary), the duration of the eclipse totality is very short and limb darkening may obscure its flatness. Since geometrical parameters in case

of total eclipses are better constrained (the corresponding hyperspace cross-sections feature very narrow valleys), parameter kicking may work to our disadvantage, knocking the solution far from the minimum by only a small parameter displacement.

By using conditional constraining, we select a preferred subspace of model solutions. This is why extra care should be taken for the choice of adopted CCs.

7.2.5 Interstellar and atmospheric extinction

Although interstellar extinction has been discussed in many papers and quantitatively determined by dedicated missions (IUE, 2MASS and others), there is a lack of proper handling in the field of eclipsing binaries. Its influence on light curves was first quantified by Prša and Zwitter (2005b) and implemented in PHOEBE.

The usually adopted approach found in literature is to compute the amount of reddening from the observed object's coordinates and its inferred distance and to subtract it uniformly, regardless of phase, from photometric observations. Here we will show why this approach is inadequate, especially for objects where interstellar extinction and the color difference between both components are significant. Atmospheric extinction is a better-posed problem: similarly as interstellar extinction depends on $E(\mathrm{B}-\mathrm{V})$, atmospheric extinction depends on air-mass, which is a measurable quantity, whereas $E(\mathrm{B}-\mathrm{V})$ has to be estimated. The down-side of atmospheric extinction compared to interstellar extinction is its chaotic time variability: due to the changing presence of cirrus clouds and water vapors air-mass changes unpredictably during the course of observations.

To estimate the effect of reddening on eclipsing binaries, we use the synthetic binary constructed in Section 7.2.1, with a notable difference of adopting $i = 90^\circ$ instead of 85°, to enhance the effect of reddening on light curves. The simulation logic is as follows: for the given phase, we compute the effective spectrum of the binary by convolving Doppler-shifted individual spectra of the visible surfaces of both components. To this intrinsic spectrum we rigorously apply interstellar and atmospheric extinctions (both as functions of wavelength). We then convolve this reddened spectrum with instrumental response function (composed of the filter transmission and detector response functions) and integrate over the passband wavelength range to obtain the flux. In contrast, we use the same intrinsic spectrum without rigorously ap-

plying the reddening. To simulate the subtraction[21] of a reddening *constant* from photometric observations, we simply divide the intrinsic spectrum by the flux that corresponds to this constant. Finally, we calculate the flux in the same manner as before and compare it to the flux obtained by applying rigorous reddening. To evaluate the impact of reddening on photometric light curves exclusively, all second-order effects (limb darkening, gravity brightening, reflection effect) have been turned off.

The simulation.

We take Kurucz's synthetic spectra ($R = 20000$) from precalculated tables by Zwitter et al. (2004). The used $(UBV)_{\rm J}(RI)_{\rm C}$ response data (filter $\times$ detector) are taken from ADPS (Moro and Munari, 2000), where we apply a cubic spline fit to obtain the instrumental response function.

For interstellar extinction, we use the Cardelli et al. (1989) empirical formula with the extinction coefficient $\mathcal{R}_{\rm V} = 3.1$ assumed throughout this study. Formula by Cardelli et al. (1989) is split into three regions, depending on the wavelength:

Region:	λ-interval:	$x = (1/\lambda)$-interval:
UV:	$170\,\mathrm{nm} \leq \lambda < 303\,\mathrm{nm}$	$3.3\,\mu\mathrm{m}^{-1} \leq x < 5.9\,\mu\mathrm{m}^{-1}$
Optical/NIR:	$303\,\mathrm{nm} \leq \lambda < 910\,\mathrm{nm}$	$1.1\,\mu\mathrm{m}^{-1} \leq x < 3.3\,\mu\mathrm{m}^{-1}$
IR:	$910\,\mathrm{nm} \leq \lambda < 3330\,\mathrm{nm}$	$0.3\,\mu\mathrm{m}^{-1} \leq x < 1.1\,\mu\mathrm{m}^{-1}$

The amount of interstellar extinction at given wavelength is determined by the interpolation formula:

$$\left\langle \frac{A(\lambda)}{A_V} \right\rangle = a(x) + b(x)/\mathcal{R}_{\rm V}, \tag{7.2}$$

where $A(\lambda)$ is extinction in magnitudes at the given wavelength, expressed relative to the visual extinction A_V; $x = 1/\lambda$ is expressed in $\mu\mathrm{m}^{-1}$. Coefficients $a(x)$ and $b(x)$ are given by the following expressions:

[21] To emphasize that this constant is *subtracted* from photometric observations (given in magnitudes), we shall use the term *constant subtraction* throughout this study, although we are *dividing* when operating with fluxes.

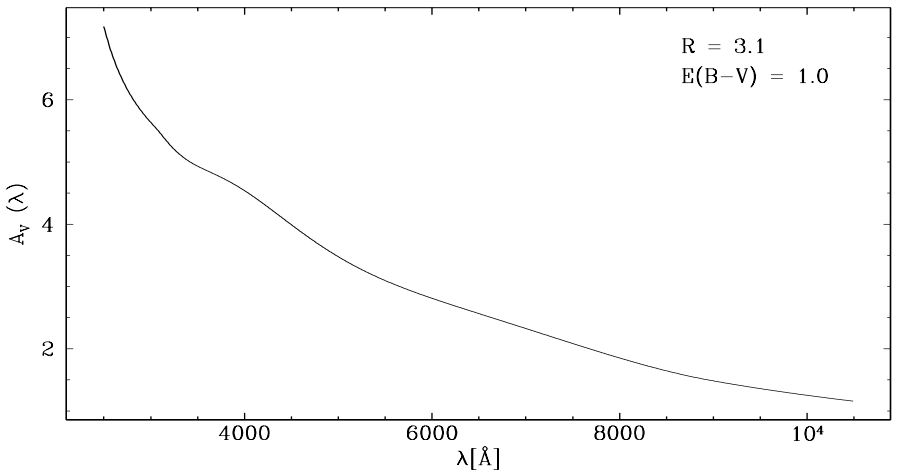

Figure 57: The reddening law adopted from Cardelli et al. (1989).

Region:	
UV:	$a(x) = 1.752 - 0.316x - 0.104/[(x-4.67)^2 + 0.341] - $ $-0.04473(x-5.9)^2 - 0.009779(x-5.9)^3$
	$b(x) = -3.090 + 1.825x + 1.206/[(x-4.62)^2 + 0.263] + $ $+0.2130(x-5.9)^2 + 0.1207(x-5.9)^3$
Optical/	$y := (x - 1.82)$
NIR:	$a(x) = 1 + 0.17699y - 0.50447y^2 - 0.02427y^3 + 0.72085y^4 + $ $+0.01979y^5 - 0.77530y^6 + 0.32999y^7$
	$b(x) = 1.41338y + 2.28305y^2 + 1.07233y^3 - 5.38434y^4 - $ $-0.62251y^5 + 5.30260y^6 - 2.09002y^7$
IR:	$a(x) = 0.574x^{1.61}$
	$b(x) = -0.527x^{1.61}$

Fig. 57 shows wavelength dependence of such an extinction formula.

For atmospheric extinction we use the equation triplet for Rayleigh-ozone-aerosol extrinction sources given by Forbes et al. (1996) and summarized by Pakštiene and Solheim (2003):

$$k_{\text{total}} = k_{\text{Rayleigh}} + k_{\text{ozone}} + k_{\text{aerosol}}. \tag{7.3}$$

In our simulation we neglect any effects of cirrus clouds and water vapors.

Rayleigh scattering is given by the following expression:

$$k_{\text{Rayleigh}} = k^{\text{STP}}_{\text{Rayleigh}} \left(\frac{P}{P_{\text{STP}}} \right) \left(\frac{T_{\text{STP}}}{T} \right), \tag{7.4}$$

where P and T are the actual pressure and temperature during observations, $P_{\rm STP} = 101300\,{\rm Pa}$ and $T_{\rm STP} = 273.15\,{\rm K}$ are *Standard Temperature* and *Pressure* values, respectively. Rayleigh scattering for these standard values is given by:

$$k^{\rm STP}_{\rm Rayleigh} = 9.4977 \cdot 10^{-3}\, e^{-h/7.996}\, \frac{1}{\lambda^4} \left(\frac{n(\lambda) - 1}{n(\lambda = 1\mu{\rm m}) - 1} \right)^2, \qquad (7.5)$$

where λ is the wavelength in μm. The formula is normalized to $\lambda = 1\mu$m, with n being the refractive index and the coefficient $9.4977 \cdot 10^{-3}$ corresponding to the optical thickness of the atmosphere at $\lambda = 1\mu$m. This is adjusted for the height h (in km) of the observatory above sea-level with the density scale-height for the lower troposphere assumed to be 7.996 km (Forbes et al., 1996). The normalized index of refraction term may be expressed in terms of wavelength by an empirical relation proposed by Penndorf (1957):

$$\left(\frac{n(\lambda) - 1}{n(\lambda = 1\mu{\rm m}) - 1} \right) = 0.23465 + \frac{107.6}{146 - \lambda^{-2}} + \frac{0.93161}{41 - \lambda^{-2}}. \qquad (7.6)$$

Ozone extinction depends on the amount $\alpha_{\rm ozone}$ of ozone in the vertical column of the atmosphere with cross-section $1\,cm^2$ and the ozone absorption coefficient $\kappa_{\rm ozone}(\lambda)$:

$$k_{\rm ozone} = 1.1\, \alpha_{\rm ozone}\, \kappa_{\rm ozone}(\lambda), \qquad (7.7)$$

where 1.1 corresponds to the ozone optical thickness at 320 nm. Values of $\kappa_{\rm ozone}$ are tabulated e.g. in Cox (2000).

Aerosol scattering on particles with size of the same order of magnitude as the wavelength is the most complicated contribution to the overall atmospheric extinction. It is modeled by the empirical relation:

$$k_{\rm aerosol} = A\lambda^{-b}, \qquad (7.8)$$

where A is the extinction at zenith for $\lambda = 1\,\mu$m and b is the coefficient that depends on the size and distribution of aerosol particles. These two parameters are very difficult to assess; fortunately, the aerosol contribution is usually very small, even negligible (Pakštiene and Solheim, 2003). We neglect its influence in our simulation.

To rigorously deredden the observations for the given $\mathcal{R}_V$ and $E({\rm B}-{\rm V})$, it is necessary to determine the reddening for each wavelength of the spectrum. Correcting differentially and integrating over the filter passband then yields the dereddened flux of the given filter. However, without spectral observations, it is difficult to calculate properly the flux correction. Since Cardelli et al. (1989) formula depends on the wavelength, the usually adopted approach found in literature is to use the effective wavelength $\lambda_{\rm eff}$ of the passband transmission curve to calculate the reddening correction.

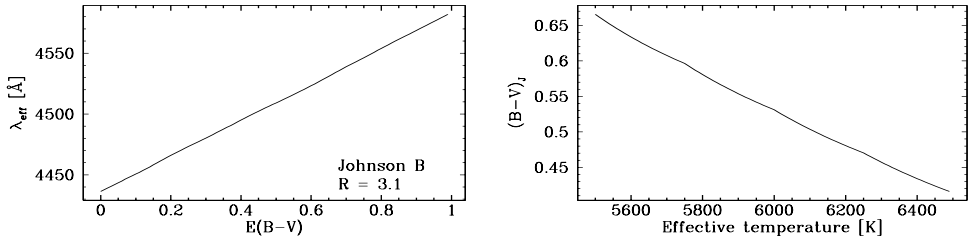

Figure 58: Left: The change of the effective wavelength of the Johnson B filter due to reddening of the simulated binary. Right: The $(\mathrm{B}-\mathrm{V})_\mathrm{J}$ color index on the 5500 K–6500 K temperature interval, calculated by integrating the spectrum over both filter passbands.

Interstellar extinction.

By comparing the rigorously calculated fluxes against intrinsic fluxes with a simple constant subtracted, we come to the following conclusions:

1. Taking the effective wavelength of the filter passband is wrong. Since the flux is the integral over the filter passband, λ_{eff} has a *conceptually* different meaning. Furthermore, λ_{eff} of the given filter depends heavily on the effective temperature of the observed object and on the color excess $E(\mathrm{B}-\mathrm{V})$ (Fig. 58). To determine the subtraction constant, one has to make sure that *the integral* (rather than any particular wavelength) of the both curves is the same. Fig. 59 shows the discrepancy between the properly calculated light curve and the one obtained by subtracting a λ_{eff}-calculated constant. Table 6 summarizes the differences between the rigorous treatment and approximative approaches.

2. Even if the subtraction constant is properly calculated, the light curves still exhibit measurable differences in both minima (Figs. 59, 60). This is due to the effective temperature change of the binary system during eclipses. For the analysed case, the difference in B magnitude is $\sim$ 0.01mag, which is generally observable.

3. If light curves in three or more photometric filters are available, it is possible to *uniquely* determine the color excess value $E(\mathrm{B}-\mathrm{V})$ by comparing different color indices in-and-out of eclipse. The reddening may thus be properly introduced to the fitting scheme of the eclipsing binary analysis program by using Eqs. (7.2)-(7.6). This was done in PHOEBE.

Approach:	λ_{eff}	Δm_B	$\epsilon_{\Delta m_B}$
Rigorously calculated value:	4470.2Å	4.03	0.00
Filter transmission:	4410.8Å	4.09	0.06
Filter transmission + reddening law:	4452.1Å	4.05	0.02
Intrinsic spectrum:	4436.3Å	4.06	0.03
Effective (reddened) spectrum:	4583.6Å	3.90	-0.13

Table 6: The summary of different approaches to calculate the wavelength to be used for the dereddening constant. λ_{eff} is determined by requiring that the area under the spectrum on both sides is equal. Δm_B is the value of extinction in B filter and $\epsilon_{\Delta m_B}$ is the deviation from the rigorously calculated value. All values are calculated for $E(\text{B}-\text{V}) = 1$ at quarter phase. Note that Δm_B is smaller than $\mathcal{R}_\text{V} + E(\text{B}-\text{V}) = 4.1$, since our simulated binary is cooler than 10000 K.

Atmospheric extinction.

Atmospheric extinction is comprised of three different sources: the Rayleigh scattering, the aerosol scattering and ozone absorption (Forbes et al., 1996). It depends on the wavelength of the observed light and on the air-mass of observations, which is of course the same for both binary components; we are thus left only with wavelength dependence at some inferred air-mass. To assess the impact on the photometric data, we compare the flux change imposed on the intrinsic spectrum by reddening and by atmospheric extinction (Fig. 61). We conclude that for weakly and moderately reddened eclipsing binaries the atmospheric extinction dominates the blue parts of the spectrum due to Rayleigh scattering, but for larger color excesses ($E(\text{B}-\text{V}) \gtrsim 0.5$) the reddening is dominant throughout the spectrum. Since the air-mass can be unambigously determined from observations of several comparison stars, the effect of atmospheric extinction may be removed by the model prior to interstellar extinction, so that the two reddening contributions may be treated separately.

7.2.6 Suggested optimizations to WD solving method

WD's DC code, as the name suggests, uses Differential Corrections (DC) method complemented by the Levenberg-Marquardt algorithm to solve the inverse problem (Wilson, 1993). It is especially suited for EBs and is one of the fastest codes around. In cases when the method does not converge, the Method of Multiple Subsets (MMS) may be used to relax the system to the nearest minimum (Wilson and Biermann, 1976).

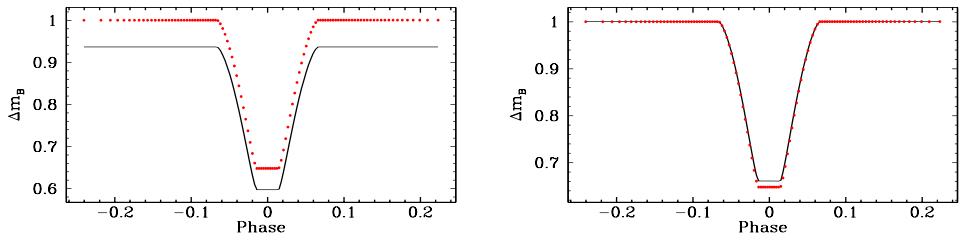

Figure 59: Left: The discrepancy due to simplified constant subtraction approach (solid line) compared to the rigorously applied reddening (points) for a model binary. The subtracted constant was obtained from the effective wavelength ($\lambda_{\text{eff}} = 4410.8$Å) of the Johnson B transmission curve. Right: Overplotted light curves with the subtraction constant calculated so that the magnitudes in quarter phase are aligned. There is still a *measurable* difference in eclipse depth of both light curves. $E(\text{B}-\text{V}) = 1$ is assumed.

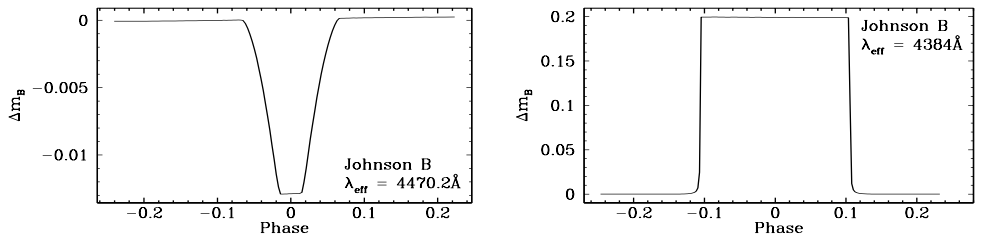

Figure 60: The difference between the rigorously calculated reddening and a constant subtraction in Johnson B filter for the G9 V–F5 V binary (left) and a B8 V–K4 III binary (right) during primary minimum. $E(\text{B}-\text{V}) = 1$ is assumed.

A DC program reads in a user-supplied input file consisting of **a)** a set of initial parameters that define physical and geometrical properties, **b)** observational data and **c)** switches that define the way a minimization algorithm is run (refer to the booklet by Wilson and Van Hamme (2003) accompanying WD code for details on DC input files). Within one iteration, the values of parameters set for adjustment are improved and returned for user inspection. In case of convergence, the user manually resubmits the new parameter set to the next iteration. The measure of the quality of the fit (the cost function) is the sum of squares of weighted $O-C$ residuals.

WD's list of more than 30 adjustable parameters includes passband luminosities L_1^i for i light curves (with their WD name HLA), that have a unique property of *linearly* scaling the level of light curves. DC (or any other minimization algorithm) fits these luminosities the same way it fits all other

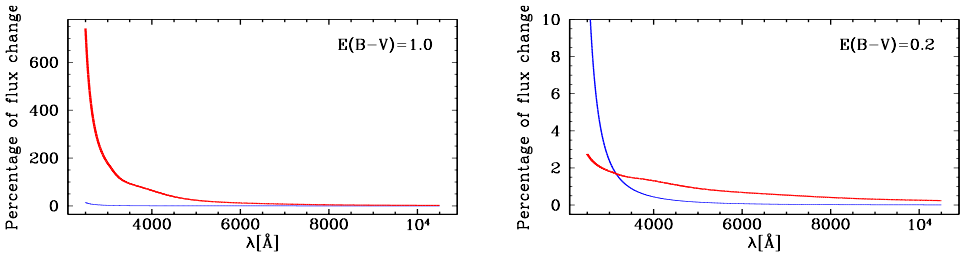

Figure 61: The percentage of the flux change imposed on the intrinsic spectrum by reddening (red line) and atmospheric extinction (blue line). The observatory altitude $h = 0$ km and the zenith air-mass are assumed throughout the study. If the color excess is large, the reddening completely dominates the spectrum (left), but if the color excess is moderate, the blue part of the spectrum is dominated by the Rayleigh scattering (right).

physical parameters: softly. This means that within one iteration, the values of L_1^i are *not* fully adjusted, only improved. Since L_1^i determine vertical offset of light curves, this raises two specific problems: **1)** The soft change of L_1^i in every iteration step causes *artificial* changes of other physical parameters: rather than fitting the shape of the data curve, other parameters fit the *discrepancy* between the model and the data, induced by the softness of L_1^i fit. It is like driving a very old car on a very bumpy road - each bump on the road causes wobbling of the whole car with slow attenuation. **2)** Changes of adjusted parameters calculated by DC will properly contribute to the cost function *only* if the model is aligned with the data: the average $O - C$ value must be approximately 0. This alignment is governed by L_1^i for light curves. If this alignment is not computed correctly, the cost function is *misleading* DC instead of aiding it. This causes under-estimation of formal errors due to L_1^i softness error propagation and even convergence problems.

PHOEBE solves this problem by supplying an option to *compute* L_1^i instead of minimizing them, thus increasing their stiffness with respect to other parameters. The alignment is calculated so that the average $O - C$ value is *exactly* 0. The time cost of this computation is not only negligible, it actually speeds up the overall algorithm, since the dimension of the parameter subspace submitted to DC is reduced. Fig. 62 demonstrates the iteration sequence with the original method (left) and the proposed method (right) for a case of 7 simultaneously fitted parameters displaced by at most 50% from their true value. In the latter case parameters converge quickly and in a smooth fashion. Similar simulations that test convergence behavior in cases when both temperatures are fitted or when other individual parameters are kept constant have also been performed; they confirm or even amplify the conclusion of Fig. 62 and their results are thus omitted on account of brevity.

Note however that stiffening L_1^i does not guarantee convergence to the global minimum, it only solves the inverse problem more efficiently. It should also be stressed that calculating L_1^i instead of fitting them might not always affect convergence as noticeably, particularly in cases where relative corrections of parameter values are small.

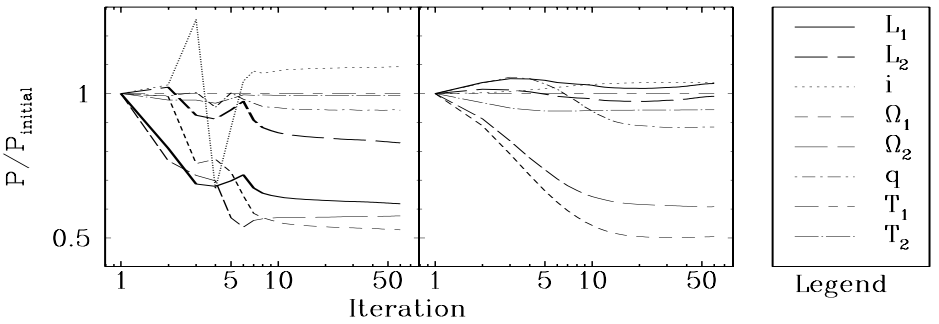

Figure 62: Soft vs. stiff curve leveling. Iteration sequence for 7 physical parameters of our test binary for soft L_1^i scheme (left) and stiff L_1^i scheme (right). The x-axis is given in log-scale to amplify the part where the impact of stiffening is largest. Unity on y-axis corresponds to parameter's initial value. L_1 and L_2 are passband luminosities in B and V filter, respectively, i is the system inclination, Ω_1 and Ω_2 are gravity potentials, q is the mass ratio and T_1 and T_2 are surface temperatures. Temperature T_1 is kept constant throughout the fit, simulating the usual practice of determining one temperature and fitting the other. Adopted from Prša and Zwitter (2005a).

By calculating L_1^i instead of fitting them, the χ^2 criterion is not used and the corresponding formal errors of L_1^i are not calculated. To obtain them, one would simply revert from calculating to fitting L_1^i at the very end of the minimization process and submit them to the final iteration of the DC.

Systemic velocity v_γ. The levels of RV curves are determined by the systemic velocity v_γ: changing it vertically shifts those curves. Although v_γ is not as correlated with other parameters as is the case for L_1^i and the problem is thus not as severe, alignment between the model and the data is still crucial. `PHOEBE` allows v_γ calculation following the same logic as before for L_1^i – by demanding that the average $O - C$ value is exactly 0.

Limb darkening coefficients. The native `WD` code supports linear, logarithmic and square root limb darkening (LD) laws. Their coefficients primarily depend on the given passband, effective temperature, gravity acceleration

log g/g_0 and metallicity [M/H]. WD does not constrain the choice of these coefficients, so people have traditionally used LD tables computed by, e.g., van Hamme (1993) or Claret (2000a).

Following a similar argument to the one mentioned before for L_1^i and v_γ, PHOEBE implements an optional dynamical LD computation. After each iteration that induces changes to any of the $T_{\rm eff}$, log g/g_0, [M/H] or related parameters, the LD coefficients need to be modified accordingly. PHOEBE uses van Hamme (1993) tables for this purpose, dynamically reading out tabulated values and linearly interpolating to obtain proper values automatically. The implications are not as severe as for the L_1^i and v_γ because LD contributions are orders of magnitude smaller and insensitive to small changes in the above mentioned parameters. Still, this guarantees that LD coefficients of the final solution are in agreement with the overall physical picture. This is an important merit when compared to WD, where values of LD coefficients are unconstrained and may thus converge to a physically unmeaningful solution.

8 Using PHOEBE on real data

In this final section we demonstrate PHOEBE's capabilities on real stars. PHOEBE has already been employed on well over 100 different binary stars (both individually and as part of testing pipelines for automatic EB analysis, e.g. Prša (2003)). Out of this group we selected several stars to present here which are most interesting from the astrophysical point of view: not only to contribute to catalogs of absolute physical parameters, but to have a deeper impact on EB field in general. We do not go thorougly through the analyses because the details have already been published or are in process of being published. We do however stress the peculiarities of each modeled binary that would not have been realized if an accurate model had not been applied.

8.1 BF Aurigae: a near-contact textbook binary

We start off with an example of a *well behaved* binary BF Aurigae. This does not mean that the star is not astrophysically challenging or that the interpretation of the model results are trivial: BF Aurigae is a close binary nearly in contact, at the onset of mass-transfer. By *well behaved* we characterize *computational* convergence behavior and solution reliability in terms of parameter degeneracy.

BF Aurigae (HD 32419, BD +41°1051) is a long-known eclipsing binary discovered by Morgenroth (1935) and thoroughly studied ever since (see Kallrath and Kaemper (1992) for a historical overview). It was classified as a B5 V main-sequence binary by Popper (1980). Spectroscopic data was acquired with Coudé spectrograph mounted on 0.9 m Kitt Peak National Observatory telescope. Photometric data was obtained with 0.75 m Vienna Observatory automatic telescopes situated in Arizona. Both data-sets are adopted from Kallrath and Strassmeier (2000a), who have made the data electronically available from VizieR service. A very reliable model was developed by Kallrath and Strassmeier (2000b) to a very high accuracy. This is why we decided to test PHOEBE on this binary.

There are two small deficiencies of Kallrath and Strassmeier (2000b)'s model: they have used normalized light curves, disregarding the information contained in color indices (refer to our discussion in Section 7.2.2) and they *assumed* the temperature of the primary star to correspond to B5 V spectral type, which could lead to systematic effects. As the first step in modeling we wanted to determine surface temperatures of the binary using color-constraining. Fig. 63 shows a χ^2-weighted histogram of the secondary-to-

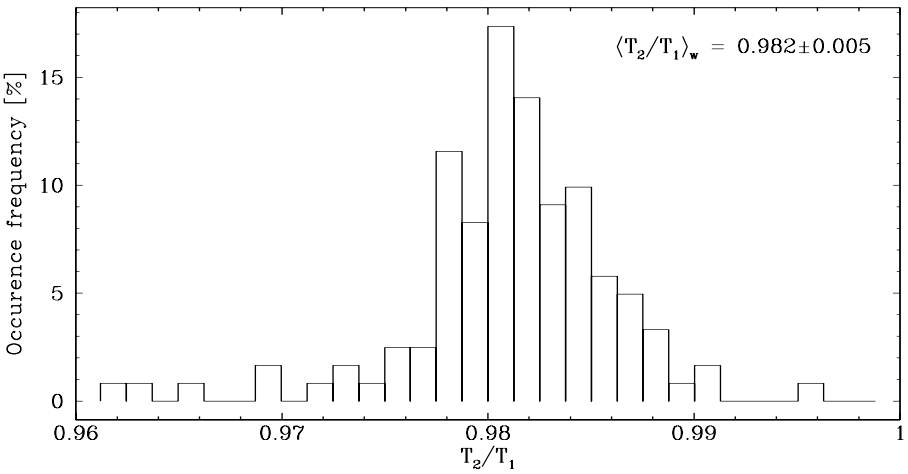

Figure 63: χ^2-weighted histogram of the secondary-to-primary star temperature ratio. The histogram was computed from heuristic scanning in Ω_1-Ω_2-L_1^i-i parameter space. The average value $\langle T_2/T_1\rangle = 0.982$ indicates that both stars are very similar.

primary star temperature ratio with its mean value $\langle T_2/T_1\rangle = 0.982 \pm 0.005$. This indicates that the two components are very similar both in size and in temperature, thus having comparable luminosities. As we have indicated in Section 7.2.2, in such a situation it is not desireable to assume primary temperature from color indices, which was the adopted strategy of the study of Kallrath and Strassmeier (2000b); the direct consequence of this is the color-index disparity between the model and observations. The authors could not have rectified this issue adequately because they based their model on normalized flux.

Unfortunately, the data made available by the authors is also flux-normalized, although the observations were done in all-sky photometric regime. That is why we cannot directly obtain individual temperatures, but we can assess the systematic error that might be present in their study. Fig. 64 depicts the effective $B-V$ color-index of the binary (both SEDs properly convolved) for the assumed values of primary star temperatures on the interval $[13000K, 14000K]$. It follows that the assumption made by Kallrath and Strassmeier (2000b) of the primary star temperature yields by $\sim 120\,\mathrm{K}$ discordant color-index effective temperature. This in turn implies that the value of T_1 is closer to 13630 K, so that the effective temperature of the binary is $\sim 13500\,\mathrm{K}$. It should be stressed however that Kallrath and Strassmeier (2000b) do verify their color-index accordance against color-temperature calibrations, but only to find concordance within estimated uncertainty of the calibrations themselves. This may very well be true (calibrations are hardly

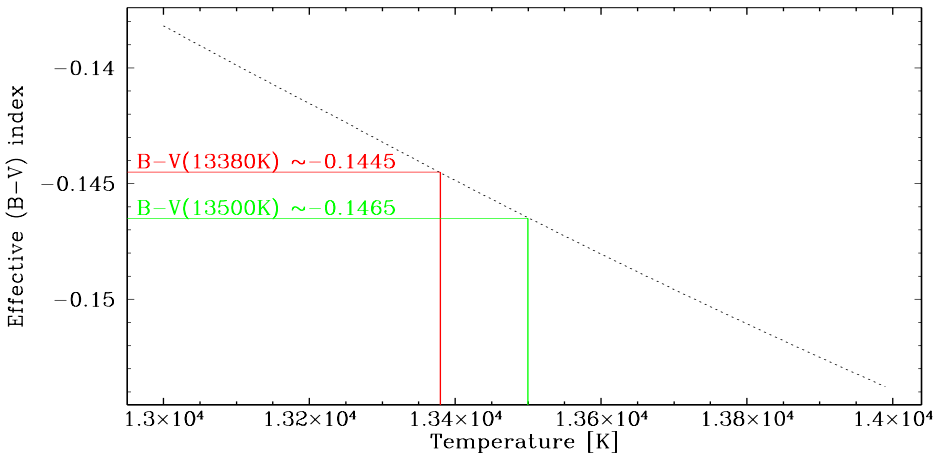

Figure 64: Effective $B-V$ color-index of the binary as function of the effective temperature of the binary on the interval $[13000K, 14000K]$. Red line denotes effective temperature that is yielded by the Kallrath and Strassmeier (2000b)'s adopted value $T_1 = 13500\,\mathrm{K}$ and the green line denotes effective temperature of the binary that would be yielded by $T_1 = 13630\,\mathrm{K}$. If we take the classification by Popper (1980) to be correct, then Kallrath and Strassmeier (2000b)'s solution is systematically wrong for $\sim 130\,\mathrm{K}$. Comparing this to their projected error estimate of 30 K sounds very significant.

expected to be accurate to $\Delta(B-V) \sim 0.02$, c.f. Fig. 64), but the consequence of this point is broader: do not be certain that the temperatures yielded by the fit are well determined; their *ratio* is pretty well determined (recall Fig. 63), but their absolute values may drift synchronously within the errors of the calibration, which can be $\sim 500\,\mathrm{K}$ or even more at these values of $B-V$. This conclusion could have a large potential impact on the placement of solutions on the H-R diagram and therefore on evolutionary tracks determined for the binary.

The next task was to explore the shape of parameter hyperspace by heuristic scanning. We chose 4 parameters for the scanning: inclination i, both surface potentials Ω_1, Ω_2 and (automatically computed) passband luminosities L_1^i. The result of this scanning is depicted in Fig. 65: convergence tracers for the "usual" high-correlation suspects. Here we establish a solid evidence of well-behaved convergency in all parameters, which is mostly due to the presence of RV curves and high photometric data accuracy. Such convergence tracers indeed make us confident enough to claim that the error bars on physical parameters are properly estimated (you may recall our discussion in Section 6.7.1 on this topic). Table 66 lists most important physical parameters of BF Aurigae obtained with PHOEBE. We give *formal* errors of

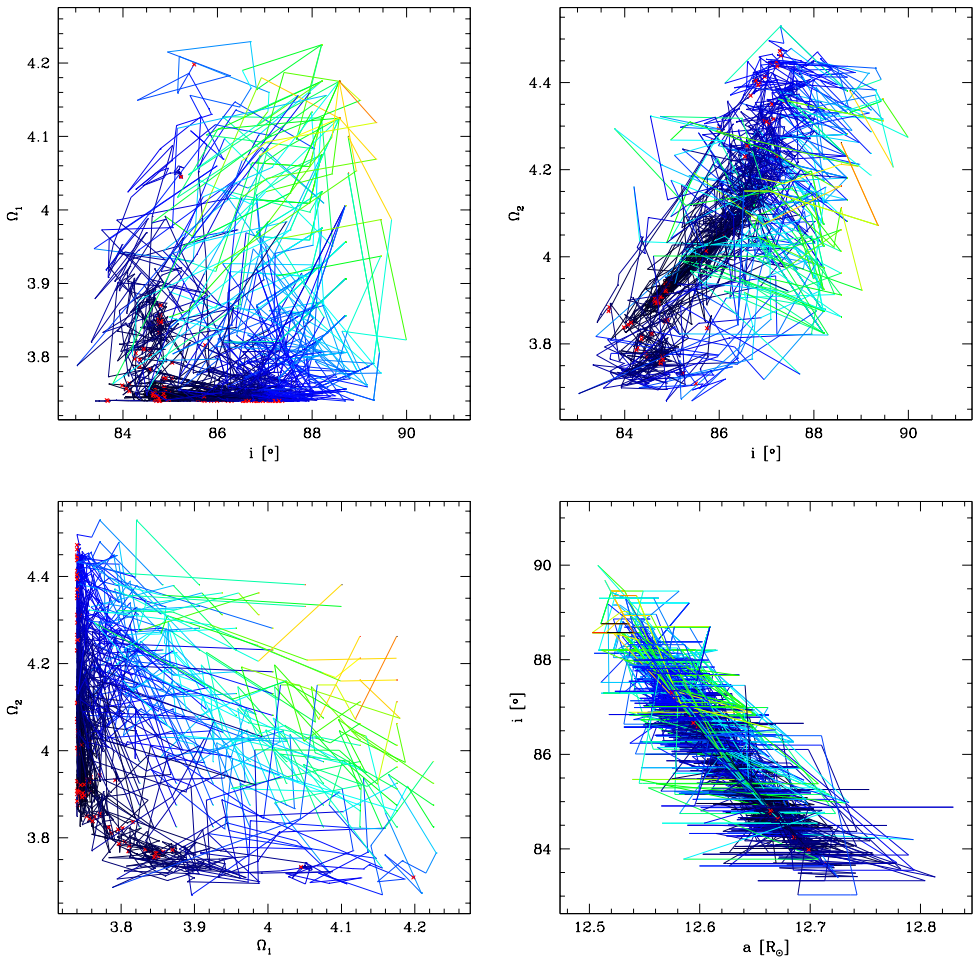

Figure 65: Convergence tracers for BF Aurigae. Each of the 4 panels represents a cross-section of the parameter hyperspace: i-Ω_1 (upper left), i-Ω_2 (upper right), Ω_1-Ω_2 (lower left) and a-i (lower right). We explored only the detached case scenario to conform to the solution found by Kallrath and Strassmeier (2000b), that is why a sharp edge in Ω_1 is present at ≈ 3.75. Convergence tracers were computed with the semi-constrained NMS method (see Section 6.4 for details).

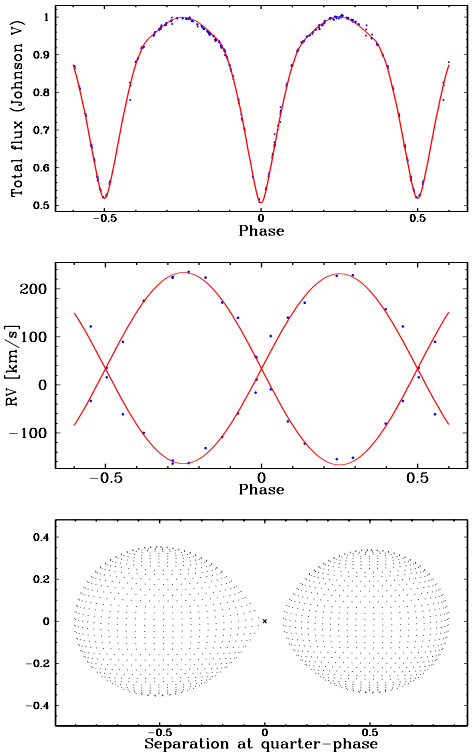

Parameter:	Value:
P_0 [days]	1.58322519(2)
a $[R_\odot]$	12.66 ± 0.23
$q = m_2/m_1$	1.012 ± 0.001
i [°]	84.75 ± 0.05
v_γ [km s^{-1}]	33.68 ± 2.5
$T_{\rm eff1}$ [K]	13630 ± 17
$T_{\rm eff2}$ [K]	13380 ± 16
Ω_1 [−]	3.77 ± 0.01
Ω_2 [−]	3.92 ± 0.01
$M_1^{\rm bol}$	-2.32 ± 0.03
$M_2^{\rm bol}$	-2.12 ± 0.04
M_1 $[M_\odot]$	5.21 ± 0.05
M_2 $[M_\odot]$	5.28 ± 0.04
R_1 $[R_\odot]$	4.73 ± 0.06
R_2 $[R_\odot]$	4.49 ± 0.06

Figure 66: Johnson V light curve, RV curve, quarter-phase shape and most important parameters of BF Aurigae. Errors of parameter values are *formal*, coming from the numerical method alone rather than heuristic scanning. As such, these errors are likely to be underestimated.

the solution in the table, coming only from the numerical method. Johnson V light curve, RV curve and quarter-phase shape are also depicted.

8.2 UV Leonis: a spotted star

There is much controversy that surrounds modeling spots from photometric data. We have already stated some of the reasons for this controversy in Section 5.3, namely that spots are very difficult to observe photometrically (since we do not resolve stellar surfaces) and that they may introduce a great deal of degeneracy in the solution. Here we try to do just that: establish that the binary given as example is magnetically active and speculate on the size and position of spots on the surface of the active component.

UV Leonis is a $V = 8.9$ eclipsing binary that consists of two solar-type G0 and G2 stars ($M_1 = 1.13M_\odot$, $M_2 = 1.09M_\odot$, $R_1 = 1.081R_\odot$, $R_2 = 1.186R_\odot$,

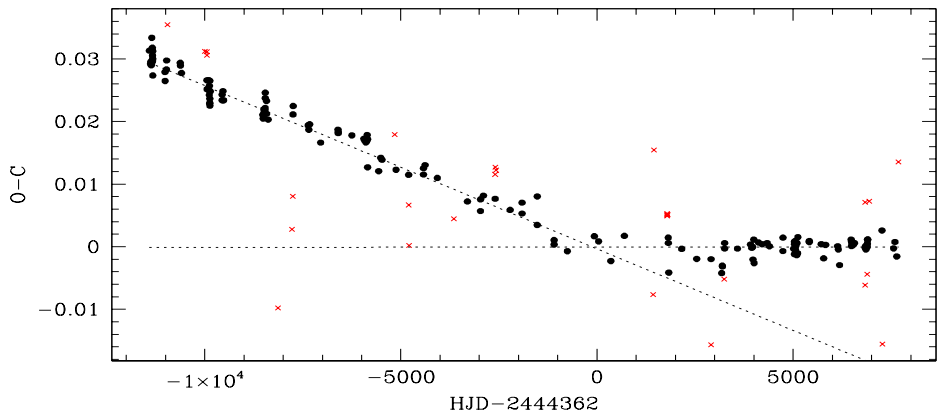

Figure 67: $O - C$ diagram for UV Leonis. Dashed lines represent the ephemeris before – Eq. (8.1) – and after – Eq. (8.2) – the sudden period change at HJD $\sim$ 2444362 (May 1980). Data taken from Kreiner et al. (2001) and our study. The points marked with a cross were considered as outliers and were not used in ephemeris computation.

$T_1 = 5916K$, $T_2 = 5861K$; Frederik and Etzel (1996)) for which period change and surface activity have already been reported by Wunder (1995), Frederik and Etzel (1996), Popper (1997) and Snyder (1998). We present the results based on a thorough photometric study conducted at the Črni Vrh observatory along with the published O-C catalog by Kreiner et al. (2001). We obtained Johnson B and V photometric measurements of UV Leonis from Feb 27, 2000 to Apr 04, 2001 with a 19-cm, f/4 flat field S-C telescope and HiSys-44 CCD imaging detector: in total 1564 measurements in B and 1579 in V filter.

Period change.

In recent years a significant effort is being made to estimate the $O - C$ behavior as a function of time: a sudden change in period was suggested by Wunder (1995), a sine function fitted to the quadratic change of O-C by Snyder (1998). By inspecting the $O - C$ catalog by Kreiner et al. (2001) with added data from this paper, we find that the sudden (discrete) change in period is a preferable assumption, as demonstrated by Fig. 67. A sudden change in period seems to have appeared at HJD $\sim$ 2444362 (May 1980) with

the following ephemeris deduced before and after the change:

$$\mathrm{HJD}_{\min} = 2437616.2091(4) + 0.6000849(21)E \qquad \text{for HJD} < 2444362, \tag{8.1}$$

$$\mathrm{HJD}_{\min} = 2448617.5761(3) + 0.6000864(12)E \qquad \text{for HJD} > 2444362. \tag{8.2}$$

Error estimates are based on the accuracy of the minima determination for HJD and $O - C$ dispersion for period. They are given in parentheses to show the accuracy of the last decimal place. Ephemeris are generally consistent with the results of Wunder (1995), though observations obtained in the last 6 years contribute to a more reliable linear solution since the period change.

To try to understand the underlying physics that could govern such a sudden period change, we made a crude estimate of the mass loss that could cause such a change. From the equation of total orbital angular momentum (L) and the Kepler's law we obtain the following relationship:

$$\frac{dL}{L} = \left[\frac{2}{3} + \frac{q}{3(1+q)}\right]\frac{dM_1}{M_1} + \left[1 - \frac{q}{3(1+q)}\right]\frac{dM_2}{M_2} + \frac{1}{3}\frac{dP}{P}, \tag{8.3}$$

where $q = M_2/M_1$ is the mass ratio and P is the period of UV Leonis. The angular momentum change dL can only be 0 or negative and the mass ratio is close to 1 so both square brackets have the value of 5/6. In order to cause the period change of $dP/P = 2.5 \times 10^{-6}$ the total mass lost from the system had to be no less than 1.9×10^{24} kg or a third of the mass of the Earth. Since our binary consists of two main sequence stars that appeared undisturbed around HJD 2444362, we see no plausible physical background to justify such a significant mass loss effect. The period change might, on the other hand, be assigned to the near-periastron passage of an unobserved third body of a low mass. We plan to investigate this assumption further.

Surface activity.

Our measurements were obtained in two consecutive seasons, the first one in 2000 (1973 measurements) and the second one in 2001 (1176 measurements). The unmistakable vertical shift in light curves between the two seasons (c.f. Fig. 68) shows the sign of UV Leonis' surface activity. The magnitudes of standard stars remained constant at all times, so instrumental errors are ruled out; the vertical shift is real.

The magnitude offset shown in Fig. 68 is $\sim 0.03 - 0.05$, the second season measurements being *brighter* than the first season. This yields a

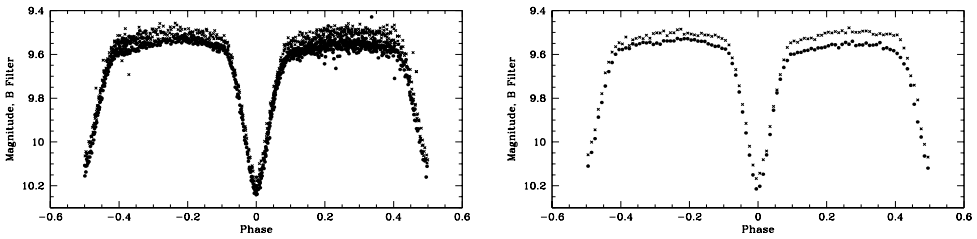

Figure 68: Complete (left) and binned (right) Johnson B light curve acquired in 2000 (filled circles) and 2001 (crosses). Binning was done to establish a clear argument that a vertical shift alone accomodates for the seasonal difference of light curves.

flux difference of $\sim 3\%$ to 5% or a total surface temperature difference of $dT/T \sim 0.01$. If we adopt the average temperature factor of dark spots from Frederik and Etzel (1996) ≈ 0.85 ($dT/T \sim 0.15$), then such spots should cover $\sim 1/15 \approx 7\%$ of stellar surfaces. To obtain a strict vertical shift, two plausible distributions make sense: 1) large near-polar spots which do not get eclipsed at any time and 2) a fair amount of small, uniformly distributed spots over the visible surface.

This is the point where PHOEBE enters into play. As we have mentioned above, polar spots could reproduce observations pretty well, but is their existence physically valid? We know that magnetic spots on our Sun are confined to $\sim 20^\circ - 25^\circ$ around the equator, so why would other stars prefer polar to equatorial spots? First indications of the presence of polar spots came from Doppler tomography, which was discussed in Section 2.3.4. Starting from Vogt and Penrod (1983)'s observation of RS CVn, 18 out of 27 late-type stars for which Doppler maps were constructed feature polar spots (Strassmeier, 1996). The main theoretical layout for existence of polar spots was first laid out by Schüssler and Solanki (1992), who predict their existence in rapidly rotating stars due to the Coriolis force overpowering bouyonce. To make things more complicated, Byrne (1996) had shown that the same effect on Doppler maps as is attributed to polar spots could also be caused by the overall chromospheric activity (in particular by flattening the bottom parts of line profiles (Bruls et al., 1999)). Eclipsing binaries now readily enter this discussion: they have every right to be regarded as rapid rotators due to their common synchronous rotation. If the model can confirm or reject the existence of a polar spot, it can contribute to solving the puzzle of polar spots. Fig. 69 shows a successful attempt to reconcile model with the observations by adding polar spots to one star. Although it does not unanimously decide in favor of the polar spot scenario, it does tag it as physically plausible with respect to binary star light curves.

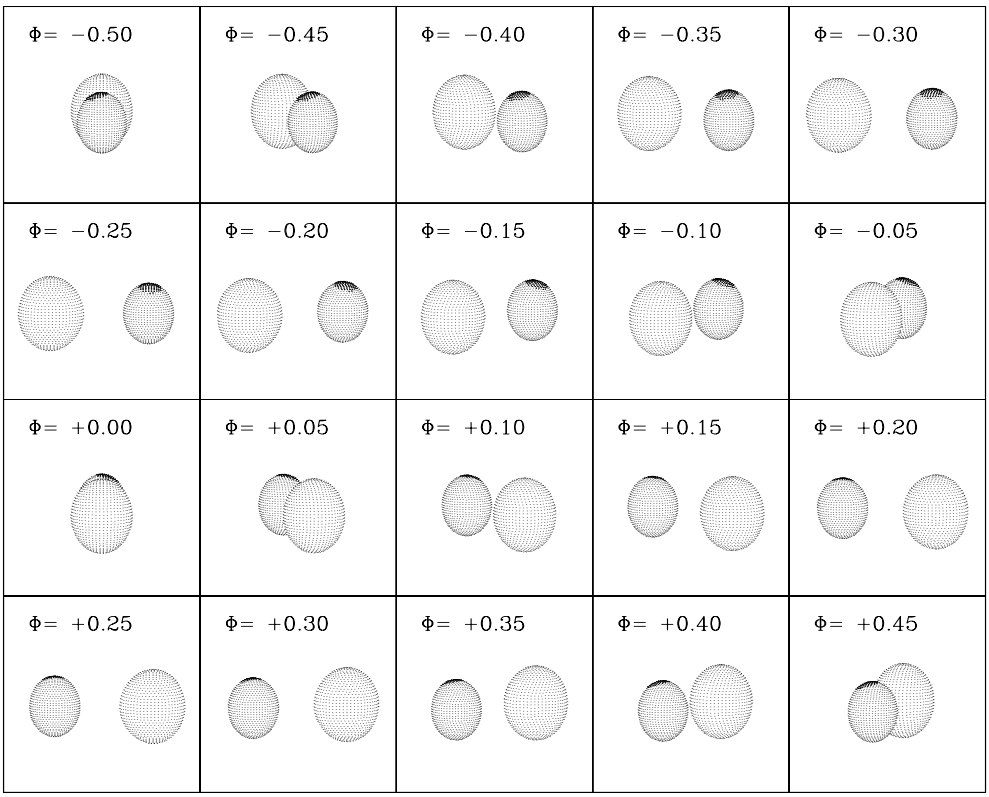

Figure 69: A polar spot model computed by PHOEBE to reproduce asymmetric light curves in Fig. 68. For further information on the solution see Prša et al. (2006), in preparation.

8.3 GK Draconis: an intrinsically variable component

Eclipsing binaries are ideal test-beds for variability studies, because modeling intrinsically variable components in binary systems yields their masses, luminosities and radii as function of time. As an example of such an intrinsic variable in eclipsing binary system we present GK Draconis.

GK Draconis (HIP 82056, HD 152028, spectral type G0) has been discovered to be an eclipsing system by the Hipparcos satellite ($V_{T,\max} = 8^m.81$, $B_{T,\max} = 9^m.21$, $\Delta m = 0.4$ mag and almost equal depth of primary and secondary eclipses; ESA SP-402 (1997)), that provided the following ephemeris for the primary eclipses:

$$\text{Min.} = 2448515.6 + 16^d.96 \times E. \tag{8.4}$$

No other information existed in the literature for this star, and we decided in 1999 to place it on the Asiago eclipsing binary program (Marrese

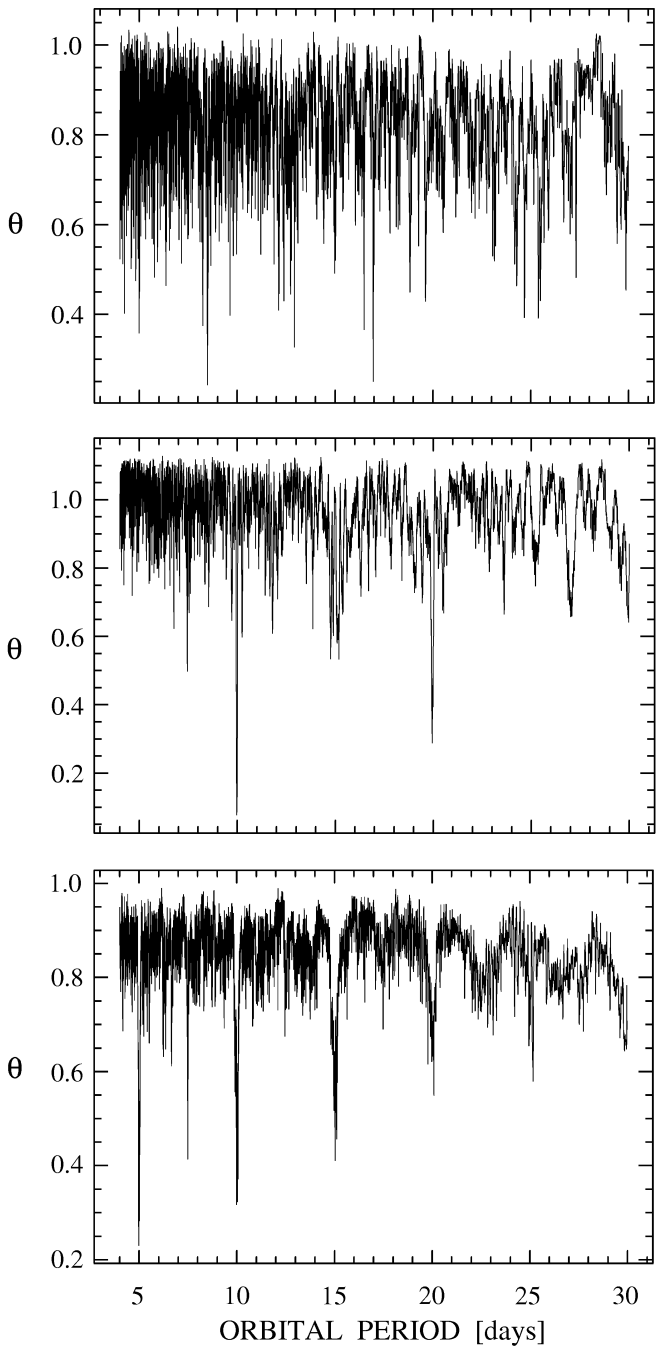

Figure 70: GK Draconis period search using Phase dispersion minimization (Stellingwerf, 1978). The three panels depict PDM results on three different data-sets: 124 Hipparcos observations in H_P band, 35 spectroscopic RV data points and 1323 ground-based photometric observations by Dallaporta et al. (2002), from top to bottom respectively. Hipparcos data favor the 16.96-day period, while spectroscopy and dedicated photometry identify the correct value of 9.97-days. Adopted from Zwitter (2003).

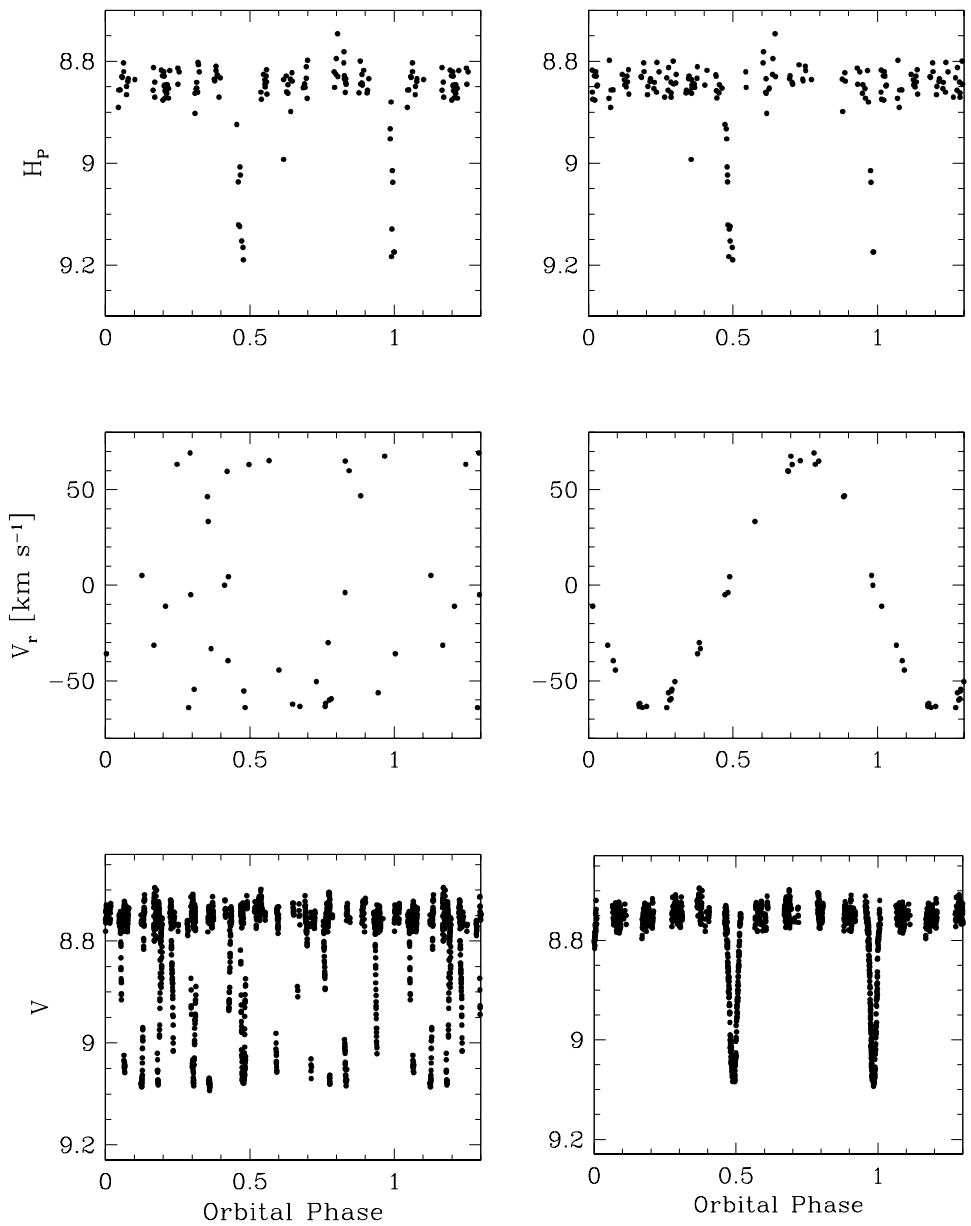

Figure 71: Folding GK Draconis data to orbital phase. Left panels depict Hipparcos determined period of 16.96 days and right panels depict the correct period 9.9742 days. Following from top to bottom: Hipparcos, spectroscopic and ground-based photometric observations. It is evident that Hipparcos period determination cannot be blamed because of poor eclipse coverage; this is yet another example of how important spectroscopy is, where each point contributes significantly to period determination.

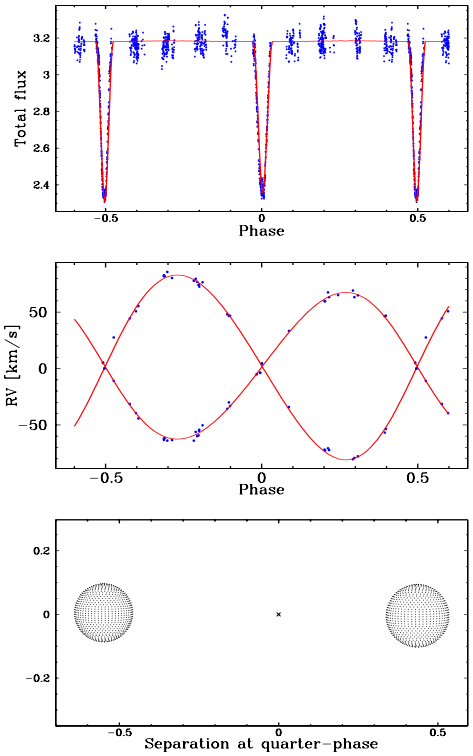

Parameter:	Value:
P_0 [days]	9.97420(1)
a $[R_\odot]$	29.0 ± 0.03
e []	0.063 ± 0.001
ω []	4.553 ± 0.015
$q = m_2/m_1$	1.26 ± 0.003
i [°]	85.8 ± 0.22
v_γ [km s^{-1}]	1.8 ± 0.06
$T_{\rm eff1}$ [K]	6960 ± 92
$T_{\rm eff2}$ [K]	6860 ± 89
Ω_1 [−]	12.26 ± 0.23
Ω_2 [−]	13.69 ± 0.24
$M_1^{\rm bol}$	1.86 ± 0.07
$M_2^{\rm bol}$	1.76 ± 0.07
M_1 $[M_\odot]$	1.46 ± 0.06
M_2 $[M_\odot]$	1.84 ± 0.08
R_1 $[R_\odot]$	2.66 ± 0.04
R_2 $[R_\odot]$	2.87 ± 0.05

Figure 72: Johnson B light curve, RV curve, quarter-phase shape and most important parameters of GK Draconis. Errors of parameter values are *formal*, coming from the numerical method alone rather than heuristic scanning. As such, these errors are likely to be underestimated.

et al., 2004b; Siviero et al., 2004). Altogether we obtained 1309 observations in B and 1328 in V from April 2000 to February 2002. Typical error for both B and V observations is $0^m.01$. The results of the preliminary photometric analysis were published by Dallaporta et al. (2002) and the detailed spectrophotometric study is being submitted, parts of which we present here.

The first problem we encountered was the ephemeris reported by Hipparcos. Phase dispersion minimization (PDM) based on Stellingwerf (1978)'s algorithm that is built into PHOEBE gives the erroneous period of $P_0 = 16^d.96$ for Hipparcos data (see Fig. 70). PDM applied to the Dallaporta et al. (2002) data, on the other hand, gives the correct value $P_0 = 9^d.9742$, as is evident from Fig. 71. This period re-determination yields the corrected ephemeris:

$$\text{Min.} = 2452005.56(1) + 9^d.9742(1) \times E, \tag{8.5}$$

where the number in parentheses denotes the error of parameter determination.

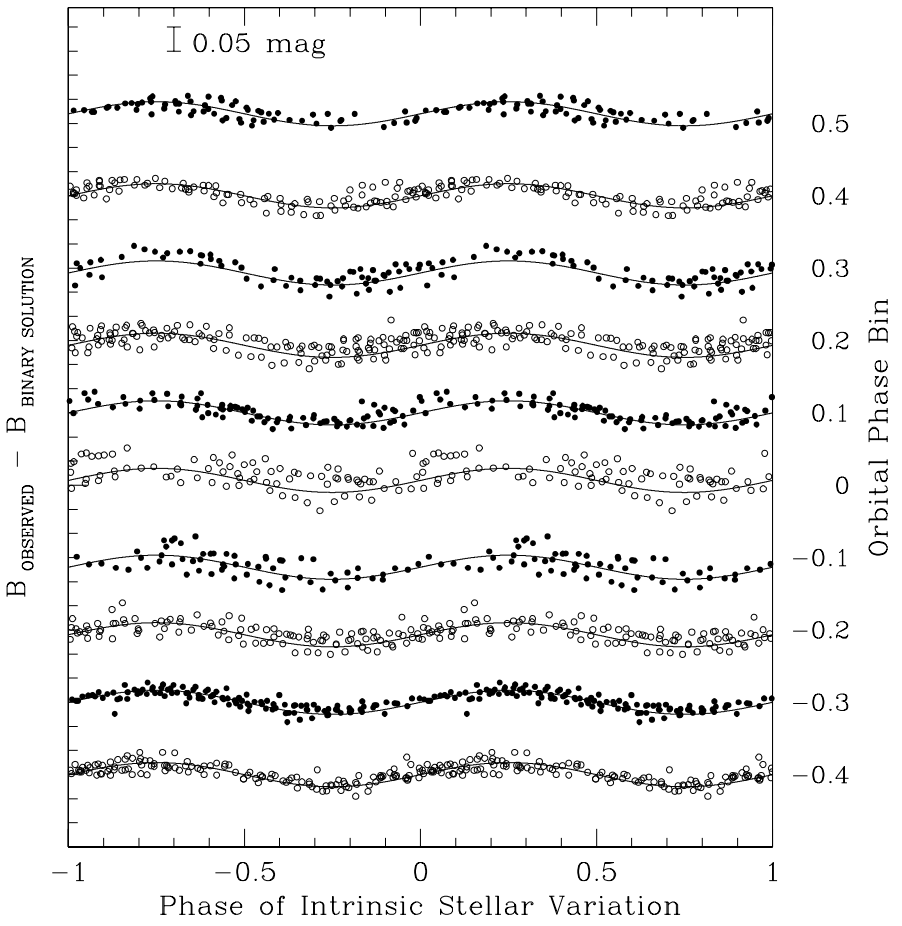

Figure 73: The difference between the observed B magnitudes of GK Dra (Dallaporta et al., 2002) and the ones generated from PHOEBE's binary system solution, folded on an intrinsic stellar variation period of $\sim$ 170 minutes. Differences pertaining to different orbital phase bins (P_{orb} = 9.97 days) are marked by different symbols and vertically offset for clarity. Note that a sinusoidal variation with a peak-to-peak amplitude of $\sim$ 0.05 mag is present throughout the orbital cycle and maintains its phase coherence.

The next significant observation is the offset of the secondary eclipse from phase $\Phi = 0.5$ to $\Phi = 0.493$, which according to the formalism developed in Section 3.5.2 indicates orbital eccentricity of the binary. The effect of eccentricity is visible on RV curve as well, depicted on Fig. 72. Orbital eccentricity has been derived to be $\varepsilon = 0.0632 \pm 0.001$.

But what seems to be the most puzzling are noisy photometric data, especially if the claim of achieving $0^m.01$ accuracy is valid. To inquire on the

source of this scatter, the model must compute all binary-related effects in detail, so that subsequent analysis of observed – computed ($O - C$) curves regards only intrinsic variability effects. Fig. 73 shows the $O - C$ difference between the observed light curves and PHOEBE modeling results; clearly there is regular sinusoidal variation present in the data. Submitting these variations to the PDM method yields the following ephemeris:

$$\text{Min.} = 2450005.528(1) + 0^d.117775(2) \times E. \tag{8.6}$$

Judging by the pulsation shape (regular sinusoidal, exhibited amplitude of $0^m.05$) and frequency (~ 0.12 days), the secondary star is most likely a δ-Scuti type variable.

The analysis of these superimposed oscillations would never have been possible if it weren't for the accurate modeling formalism in treating eccentric binaries.

8.4 V945 Centauri: an ellipsoidal binary

Although PHOEBE is primarily designed to model eclipsing binaries, it can actually model *any* binary system. To show this, as a concluding example we overview the model of the nearly pole-on ellipsoidal binary V945 Centauri. As we explain below, PHOEBE played an important role in rectifying the misclassification of this star.

The success of the ESA Hipparcos mission (ESA SP-402, 1997) led, among other things, to discoveries of many new variables (Eyer and Grenon, 1997; Kazarovets et al., 1999). Waelkens et al. (1998) attempted to classify the periodically variable B stars among them. The star V945 Centauri (HD 112409), a bright (V= 5.2) B8.5V variable with a period of some 8 hours is on their list. Such a short-period light variability can be caused by several possible phenomena: (1) a non-radial gravity mode as in the slowly pulsating B stars (De Cat and Aerts, 2002), rotational modulation in chemically peculiar B stars (Briquet et al., 2004), by duplicity of the star in question (De Cat et al., 2000) or by a combination of more of the above possibilities. Waelkens et al. (1998) tentatively classified V945 Centauri as a slowly pulsating B star. However, since this star was one of a very few new B8–9 IV–V suspects for slowly pulsating B stars, a separate spectroscopic 5-day campaign was carried out by the Leuven team to search for possible line-profile variations of three such stars, using FEROS echelle spectrograph mounted on the 2.2 m ESO telescope. In adition, we obtained Geneva 7-color high-precision photometry of V945 Centauri during one campaign with a 3-week duration and

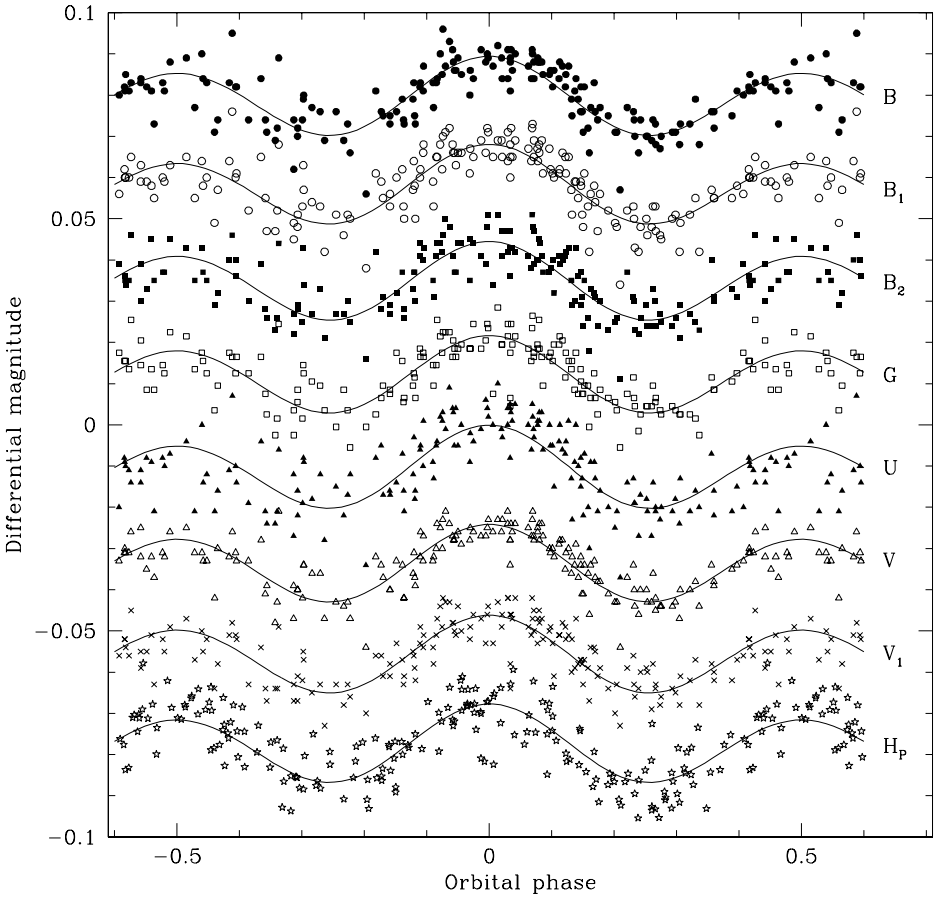

Figure 74: Light curves of V945 Centauri acquired in Hipparcos H_p filter and Geneva filter-set in a campaign thoroughly described by Aerts and Kolenberg (2005). Solid lines are the solutions obtained by PHOEBE.

one campaign of 9 weeks within one season. The integration times were typically 3 minutes, resulting in a precision of about 5 mmag per measurement. Altogether, we obtained 160 observations over a time span of 121 days. We also use all Hipparcos H_p broad-band photometric observations with error flags 0 and 1 (ESA SP-402, 1997). To the best of our knowledge, there are no other published photometric observations of this object with known times of observations. Figs. 74 and 75 show photometric and radial velocity data and the fit obtained by PHOEBE.

V945 Centauri's B-type components and a very short orbital period (see Table in Fig. 76) make this star an interesting astrophysical test-case. Since the orbital inclination is very low ($\sim 20°$), the only binarity effect we observe

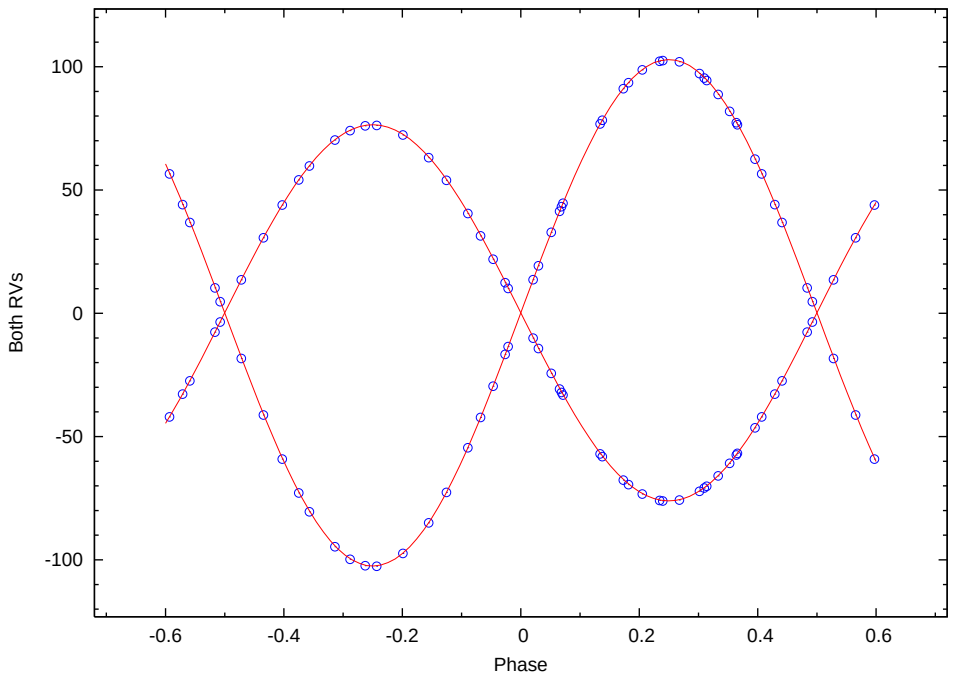

Figure 75: Radial velocity curves extracted from FEROS spectra with KOREL (Drechsel et al., 1997). Solid lines are the solutions obtained by PHOEBE.

is ellipsoidal variation due to distortion of stellar shapes of both components (recall Section 4.6). Fig. 76 (left) depicts the model of V945 Centauri as seen from Earth.

Since there are no eclipses, the inclination i and the semi-major ratio a are completely correlated. To overcome this, conditional constraining is used: we take the T-M relation for main-sequence stars computed by Harmanec (1988) to set the semi-major axis to the value that yields consistent masses. Since $a \sin i = \text{const}$ value is very well determined from RV fit, we directly obtain the inclination of the system. The other degeneracy is the choice of effective temperatures, but since photometry was acquired in calibrated Geneva filter-set, color-constraining (see Section 7.2.2) was used to pinpoint both temperatures objectively. The model could now be uniquely solved; Figs. 74 and 75 depict the obtained solution and Table in Fig. 76 lists the most important model parameters.

The model seemed to have achieved a remarkable agreement with the observations; however, a detailed spectroscopic analysis revealed a presence of the *third* line component, as is depicted in Fig. 77. This line has a virtually constant, very low amplitude of the radial velocity throughout the phase

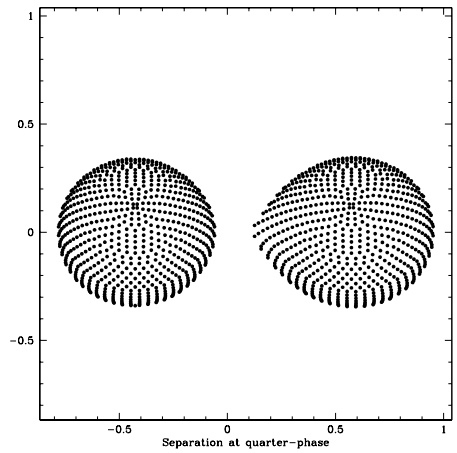

Parameter:	Value:
P_0 [days]	0.6495931845(5)
a $[R_\odot]$	5.70 ± 0.06
$q = m_2/m_1$	0.736 ± 0.002
i [°]	23.9 ± 0.23
v_γ [km s^{-1}]	0.2 ± 0.8
$T_{\rm eff1}$ [K]	13200 ± 21
$T_{\rm eff2}$ [K]	10890 ± 15
Ω_1 [−]	3.52 ± 0.01
Ω_2 [−]	3.60 ± 0.01
$M_1^{\rm bol}$	-0.43 ± 0.03
$M_2^{\rm bol}$	0.67 ± 0.04
M_1 $[M_\odot]$	3.403 ± 0.04
M_2 $[M_\odot]$	2.505 ± 0.04
R_1 $[R_\odot]$	2.12 ± 0.03
R_2 $[R_\odot]$	1.74 ± 0.03

Figure 76: The shape and most important parameters of V945 Centauri. Errors of parameter values are *formal*, coming from the numerical method alone rather than heuristic scanning. As such, these errors are likely to be underestimated.

cycle. Its origin could have been attributed to the field star behind V945 Centauri, but after a comprehensive search failed to identify a possible source, this hypothesis was discarded.

This means that we need a source that does not move in phase, is very hot (judging by the presence of helium lines) and cold (judging by the presence of iron and titanium lines) at the same time. It obviously cannot be a circumstellar cloud, both because of low-amplitude of radial velocity and because of the presence of hot lines. It is unlikely to be a hot-spot due to mass exchange, because the solution does not indicate any ongoing mass transfer. By consulting the literature on B stars we find that such lines may be a strong evidence for colliding hot winds coming from both components (see e.g. Pfeiffer and Stickland (2004) for a similar analysis on EM Carinae and Fig. 5 therein, which we reproduce for the sake of completeness here in Fig. 78). Since we are observing the binary nearly pole-on (see Fig. 76), we look vertically along the collision area at virtually every phase. This means that we expect to see a range of temperature-dependent lines throughout the phase period, and the unusual strength of these lines may be attributed to the optical depth of the colliding region. This currently ongoing analysis will be published by Aerts et al. (2005).

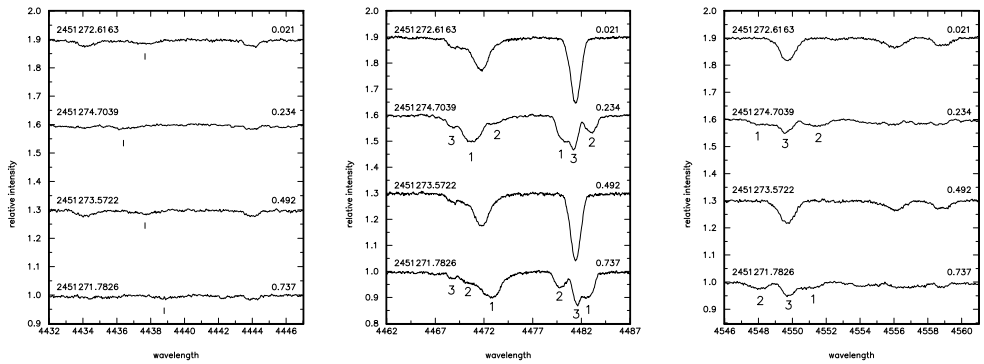

Figure 77: Four sample segments of the V945 Centauri spectra near some interesting spectral lines. Heliocentric Julian dates and orbital phases of the spectra are given in each panel. For better clarity, the continua of subsequent spectra are shifted for 0.3 in intensity. The left panel shows the region near He I (4437.551 Å) line (the position of which is shown by a bar), the central panel shows the neighbourhood of He I (4471.508 Å) and Mg II (4481.228 Å) lines and the right one shows Fe II (4549 Å) line. It is obvious that the observed spectrum is actually a combination of three different spectra, identified as components 1, 2 and the stationary line 3 for the spectra taken at both elongations of the 0.65-d binary.

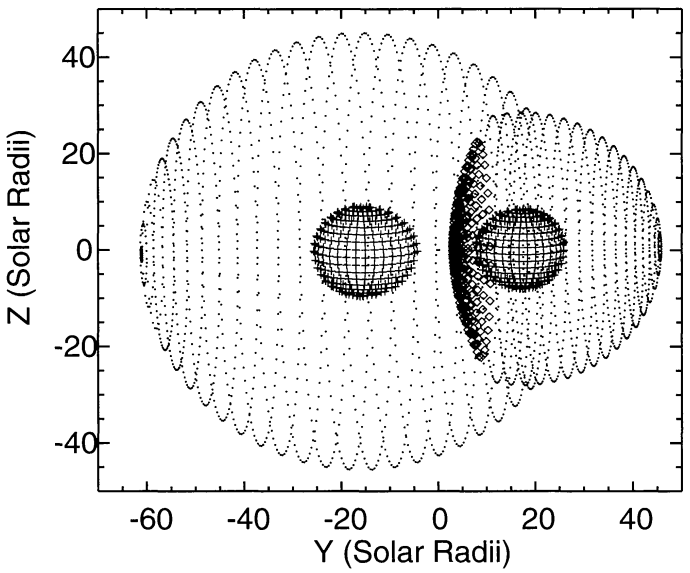

Figure 78: The model of colliding hot stellar winds of O- and B-type stars. The depicted binary is EM Carinae, adopted from Pfeiffer and Stickland (2004).

9 Prospects for the future

PHOEBE is far from being complete, it merely represents a solid base upon which new scientific and technical enhancements may be incorporated. We list below some of the work in progress and ideas that have yet to take shape in the near future.

9.1 In situ stellar atmospheres

One of the most desired extensions in EB community is the proper inclusion of spectral energy distribution (SED) functions. Currently PHOEBE relies on linear interpolation of gridded SEDs, as was thoroughly discussed in Section 7.2.3; this is inadequate in many respects:

- Gridded spectra are computed for a single-star spherical model. This means that, strictly speaking, using SEDs is applicable only for widely detached binaries that don't exhibit any significant shape distortion.
- All spectra are computed in LTE regime, which is not a plausible assumption for a variety of early-type and contact binary stars.
- There is no support for treating oblateness or surface brightness distribution in computing SEDs, so all effects described in Section 5.3 must be neglected.

Chances of changing this situation were bleak until recently; the chosen Kurucz's model atmosphere code ran only under VAX/VMS and was thus incompatible with other platforms. Lately Sbordone et al. (2004) has successfully ported Kurucz code to Linux, which is a start: we can now collaborate with model atmospheres people (see e.g. proceedings from Trieste meeting in Aug 2005, in print) to add convection effects, the description of distortion of stellar surfaces and NLTE. All these extensions are well-studied and successfully described analytically, so the only barrier to incorporate SEDs properly is the modification of the Kurucz code itself. A member of our research group (U. Jauregi) is working on rotational distortion, whose work is expected to be completed in the near future.

Having such SEDs available for real-time computation, a range of "around-the-corner" solutions currently incorporated into the model will have been removed: limb darkening will have become obsolete, Legendre fits of emergent

normal intensity will not have been necessary, and color-index constraining will have come naturally from the model. This is definitely something to look forward to.

9.2 More minimization algorithms

In Section 6 we have concentrated on numerical methods that have already been implemented in PHOEBE; still, many new powerful methods are emerging and they deserve to be evaluated for suitability of solving the inverse problem for eclipsing binaries. Due to numerical stability we have limited ourselves to examining derivativeless methods (NMS, Powell's direction set method), yet there are two two distinct groups of algorithms that may very well prove to be superior:

Gradient methods, such as Fletcher (1964) or Polak and Ribiere (1969) conjugate gradient algorithms ...

Probabilistic (Bayesian) methods, such as Monte Carlo Markov Chains (Chen et al., 2000), neural networks, genetic algorithms ...

Both of these families of algorithms have their pros and cons, but until we assess their performance on eclipsing binaries, there is no obvious way to characterize them a priori. Function:

$$f(x,y) = (x^2-1)\cos(4\pi x)(y^2-1)\cos(2\pi y) \tag{9.1}$$

proves to be a solid initial test because it is "bumpy" and degenerate. If the method can cope with such a function, it might perform well for eclipsing binaries as well. Fig. 79 depicts this function and Fig. 80 shows the results of heuristic scanning for the already implemented algorithms: NMS, Powell's direction set and adaptive simulated annealing.

9.2.1 Principal component analysis

Another method that could significantly improve convergency to the solution is Principal component analysis (PCA). PCA is *not* a minimization method, it is an algorithm to find orthogonal directions in parameter hyperspace. Correlations in EB hyperspace are not all due to non-linearity of the problem, some are also induced by poorly considered parameter definitions which

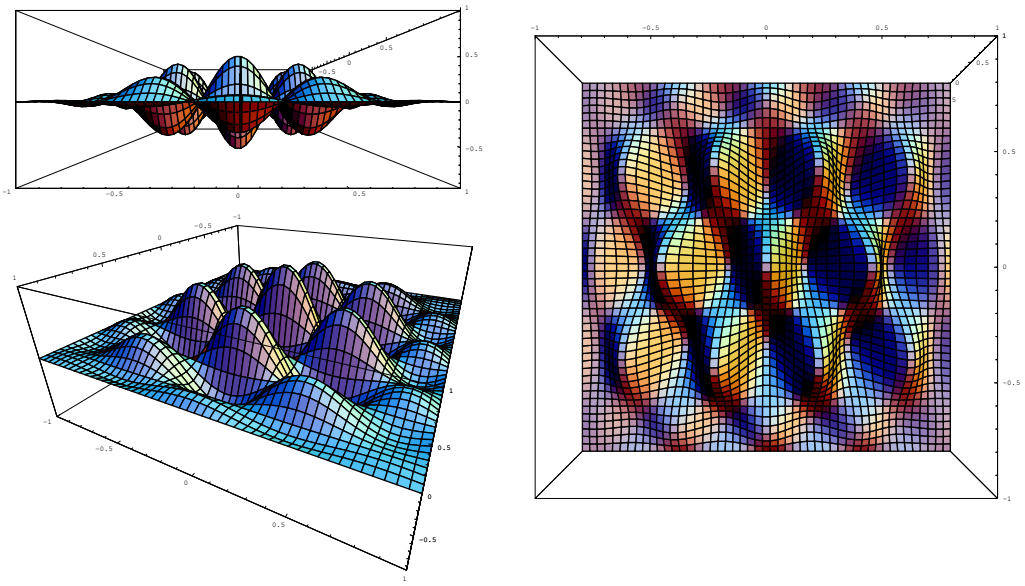

Figure 79: An example of a test function given by Eq. (9.1).

cannot be changed for historical reasons. Take the definition of Kopal's potentials given by Eq. (3.16), for example: $\Omega(\rho; q, F)$ is a function of the mass ratio q, yet both the mass ratio and the potential enter the model as independent parameters. The correlation between them is induced only by the awkward selection of input parameters. The way out without changing historically determined set of parameters is to use PCA: by finding orthogonal directions in parameter hyperspace, we would reduce the artificially induced correlations in parameter hyperspace. We wouldn't be able to remove it, at least not with a generic PCA technique, because the relations between some parameters are non-linear, whereas generic PCA uses linear combinations of parameters. An advanced, non-linear PCA method could be devised that would be able to transform input parameters into a more orthogonal hyperspace, solve the model, and then transform the working parameters back to physical ones and report them to the user.

9.3 Planetary transits

At the time of this writing, according to Extrasolar Planets Encyclopaedia, `http://www.obspm.fr/planets`, there have been 160 extrasolar planets discovered. One of the most reliable methods for discovering an extrasolar planet is hunting planetary transits. This astronomical field virtually exploded in the last 15 years as the first extrasolar planet candidate was dis-

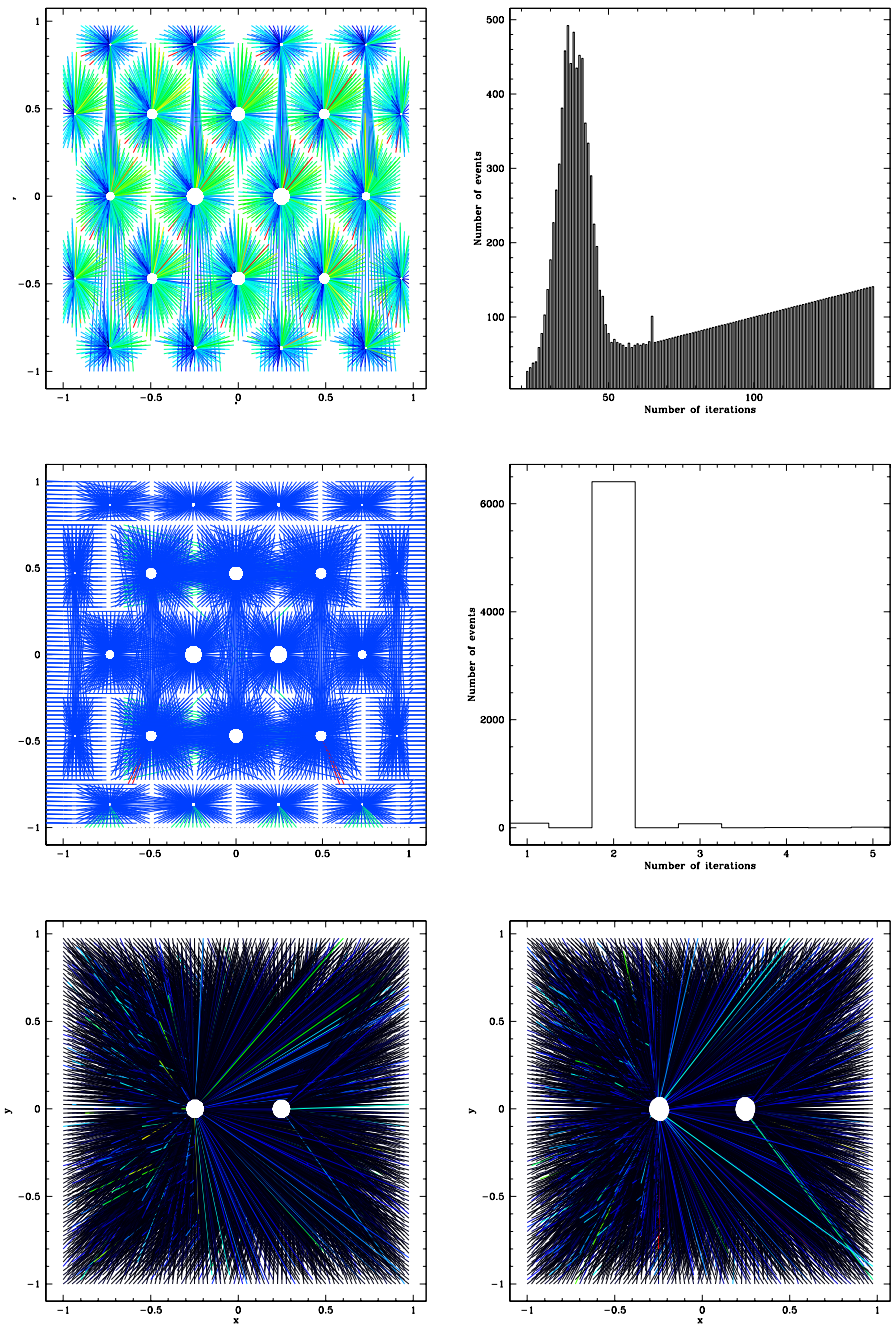

Figure 80: Heuristic scanning test results for NMS (top row), Powell's direction set method (middle row) and Adaptive simulated annealing (bottom row) for slow (left) and fast (right) cooling constant. The number of steps required for convergence for NMS and Powell's method are shown in histograms; it is more than obvious that Powell's method is completely superior for solving the test function.

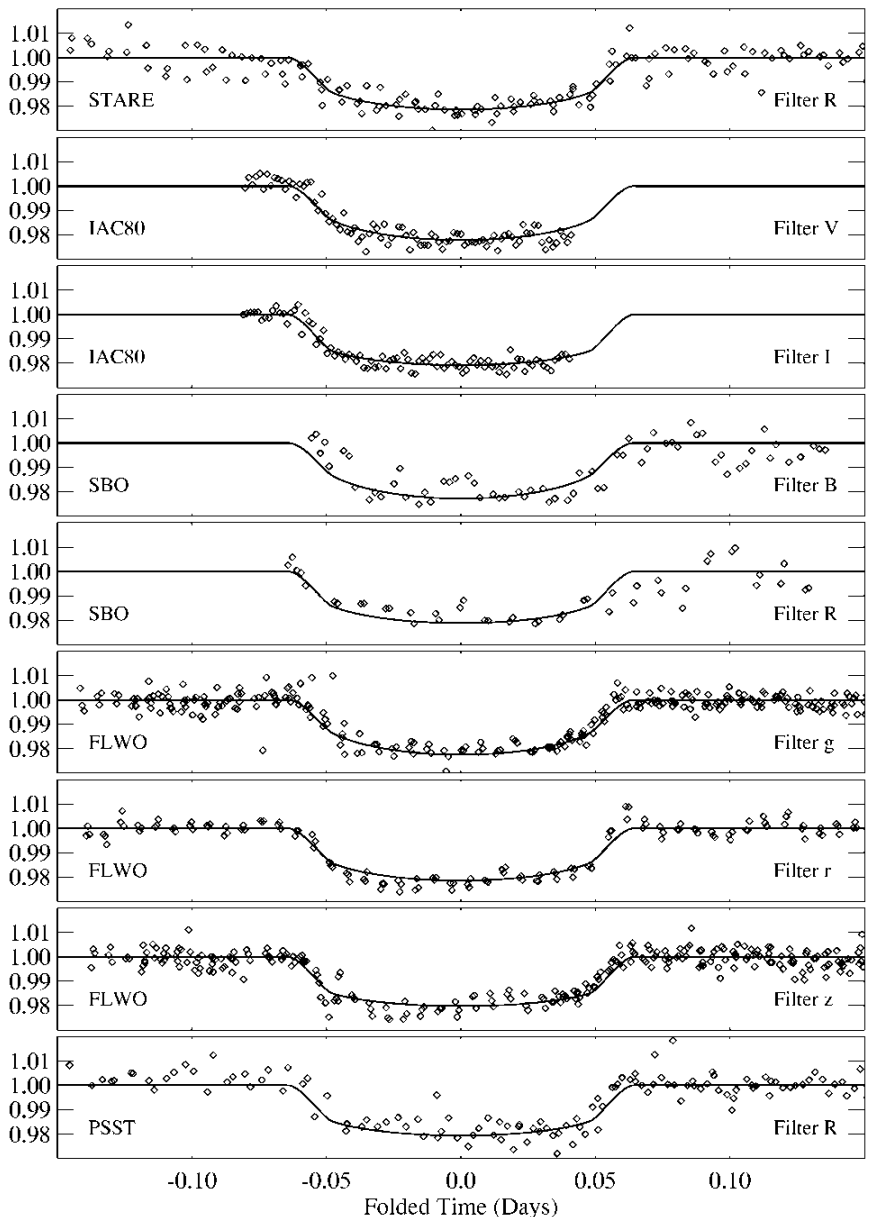

Figure 81: The first planetary transit discovered by the `TrES` mission (Alonso et al., 2004).

covered by Latham et al. (1989). There are several tens of ground-based missions that are trying to detect transiting planets; space mission CoRoT (Weiss et al., 2004) had changed its focus from stellar analysis to search for planets. This only shows how immensely interesting and attractive this field is.

Planetary transits are in principle simplified versions of eclipsing binary stars, where the secondary is much lighter, much smaller and much cooler than the primary. The transiting planet represents a tiny black disk over the stellar surface; this is in principle very easy to model, since the radius may be determined very accurately (each transit is the total eclipse) and the computation is insensitive to absolute values of the temperature (planet will appear black regardless of its temperature). Fig. 81 shows the first discovered planetary transit by the TrES mission (Alonso et al., 2004).

So how does PHOEBE fit into this? Unfortunately it doesn't. You may recall from Section 5.1 that we *sample* stellar parameters in discrete points over the surface and neglect effects whose size is smaller than the grid size. Aiming to properly model a transiting planet would imply significantly denser grids, which would be devastating for the computation - all the merits of abandoning complete numerical integration would be lost. Yet we are not prepared to give up on extrasolar planets; not only are they interesting from a sociological point of view (attractive for the general audience as well, not only hard-core astrophysicists), transiting planets can be readily used to directly measure surface brightness distribution of the transited star. This in turn directly feeds back into the model by improving gravity brightening and limb darkening laws. It would thus seem worthwhile to implement an analytical solver next to the discrete one that is already in place that could use general properties of planetary transits mentioned in the previous paragraph. Another alternative would be to preserve the existing code, but to modify the point-sampling strategy described in Section 5.1 to cover the transit points to a substantially larger extent and to thus retain the needed accuracy for a proper description. The author's honest bet is that extrasolar planets is the way to go.

9.4 Automated analysis of large data-sets

So far we have concentrated on modeling transiting objects individually, one at the time. However, more and more medium-sized telescopes are refitted into fully automatic survey instruments. In the last decade a multitude of automatic surveys surfaced, most important are listed in Table 7.

Survey:	Passbands:	Target:
CAMS: Carlsberg Meridian telescope	V	meridian
UCAC: USNO CCD Astrometric Catalog	579–642 nm	southern sky
FASTT: Flagstaff Astrometric Scanning Transit Telescope	V	meridian
DENIS: DEep Near-Infrared Survey	I_C, J, K_S	southern sky
2MASS: Two-Micron All-Sky Survey	J, H, K	entire sky
ASAS: All-Sky Automated Survey	V, I_C	entire sky
LOTIS: Livermore Optical Transient Imaging System	B, V, R, I	northern sky
TASS: The Amateur Sky Survey	V, I_C	entire sky
APT: Automated Patrol Telescope	B, V, R, I	southern sky
QUEST: QUasar Equatorial Survey Team	B, V, R	equator
SDSS: Sloan Digital Sky Survey	u', g', r', i', z'	northern sky
RAVE: RAdial Velocity Experiment	spectroscopy	southern sky

Table 7: Most important on-going sky surveys of the last decade. Other surveys such as MACHO, OGLE, HDF, ROTSE, RAPTOR, LINEAR, NEAT and others are reviewed by Henden (2003).

These surveys produce a wealth of decently accurate photometric data which, accompanied by dedicated spectroscopy and/or additional follow-up observations, may be used for studying objects statistically, both in numbers as well as in time, due to prolonged and complementing time spans of these surveys. PHOEBE is already well-suited for modeling large data samples thanks to its scripting facility; a study based on TASS data (Richmond et al., 2000) is now underway that will establish an automated script to analyse and model a sample of 200 overcontact W UMa-type binaries.

9.4.1 Gaia

Gaia is an ambitious ESA cornerstone mission to chart a three-dimensional map of our Galaxy, in the process revealing its composition, formation and evolution (Perryman et al., 2001). Gaia will provide unprecedented positional and radial velocity measurements with the accuracies needed to produce a thorough stereoscopic and kinematic census of about one billion stars in our Galaxy and throughout the Local Group. This amounts to about 1 per cent of the Galactic stellar population. Combined with astrophysical information for each star, provided by on-board multi-colour photometry and spectroscopy, these data will have the precision necessary to quantify the early formation, and subsequent dynamical, chemical and star formation evolution of the Milky Way Galaxy. It is the successor of ESA's very successful pioneering mission Hipparcos ESA SP-402 (1997). Table 8 summarizes Gaia's scope extent with respect to that of Hipparcos.

	Hipparcos	Gaia
Magnitude limit	12^{mag}	$20^{\mathrm{mag}} - 21^{\mathrm{mag}}$
Completeness	$7^{\mathrm{mag}} - 9^{\mathrm{mag}}$	$\sim 20^{\mathrm{mag}}$
Bright limit	$\sim 0^{\mathrm{mag}}$	$\sim 7^{\mathrm{mag}}$
Number of objects	120.000	26 million to 15^{mag}
		250 million to 18^{mag}
		1000 million to 20^{mag}
Effective distance limit	1 kpc	1 Mpc
Observed quasars	none	~ 500.000
Observed galaxies	none	1–10 million
Accuracy	1 mas	4 μas at 10^{mag}
		10 μas at 15^{mag}
		200 μas at 20^{mag}
Broad bands	B and V	4 bands to 20^{mag}
Intermediate bands	none	11 bands to 20^{mag}
Radial velocities	none	1–10 km/s at 17^{mag}
Observing program	predefined	unbiased

Table 8: Comparison between the currently most successful mission Hipparcos (ESA SP-402, 1997) and Gaia (Perryman et al., 2001).

With photometry complete down to 20^{mag} and spectroscopy to 15^{mag}, one may expect to detect roughly 7 *million* eclipsing binaries (Munari et al., 2001). Out of those, $\sim 400\,000$ will be brighter than 15^{mag}, thus within reach for both photometry and spectroscopy. At an average G7 spectral type it may be estimated that 25% of them will be double-lined, which makes it $\sim 100\,000$ double-lined spectroscopic binaries. Even if only 10% of those binaries are viable for accurate modeling, they will still have meant an enormous breakthrough in our knowledge and understanding of eclipsing binaries and their components.

Such a vast number should be dealt with all due vigilance, because reliable algorithms for data reduction, classification and physical analysis have yet to be constructed. This is our role in Gaia preparation: to create a fully automatic processing pipeline that would interoperate with other processing tasks (photometry, RVS, classification) during the mission. Our group has invested more than 100 nights on the echelle spectrograph mounted on 1.8 m Cima Ekar telescope in Asiago, securing high-resolution spectra of dozens of eclipsing binaries and using them to evaluate Gaia expected harvest (Munari et al., 2001; Zwitter et al., 2003; Marrese et al., 2004a; Milone et al., 2005). During that time we devised new numerical approaches that specifically concentrate on automatic analysis of simulated Gaia data (Prša, 2003, 2004; Prša

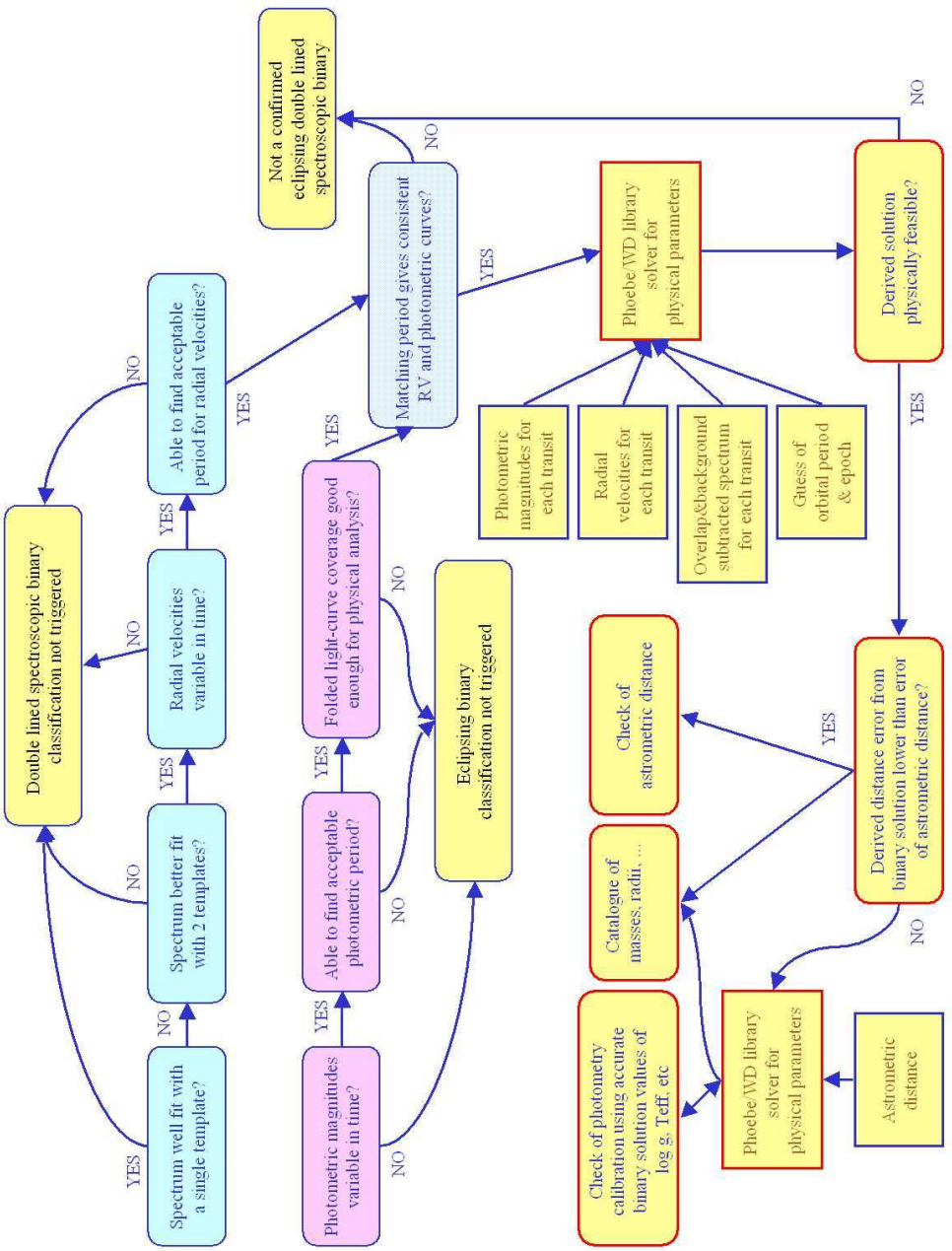

Figure 82: Draft of the proposed Gaia pipeline for double-lined spectroscopic eclipsing binaries (Courtesy of the RVS report by P. Marrese, U. Munari, A. Prša, D. Terrell, R. E. Wilson and T. Zwitter).

and Zwitter, 2005), which established our firm commitment and active collaboration with the rest of the Gaia community. On the 10th RVS workshop in Cambridge (Sep 2005) we presented our Letter of Intent and the proposal for incorporating processing pipeline of double-lined spectroscopic eclipsing binaries into the main Gaia pipeline, which was accepted. Fig. 82 shows a possible scheme for integrating eclipsing binary pipeline to the main pipeline, for validating astrometric distance measurements, spectra cross-correlation disentangling, classification and contributing to the final Catalog.

Gaia will by all means contribute a great deal to science; it is our responsibility to make sure eclipsing binaries don't lag behind, that is why constant improvement, thorough testing and critical judgement of the future `PHOEBE` development must not be neglected.

9.5 Get people to join in

From its very beginnings, `PHOEBE` was conceived to become a community-driven project. Its open-source license (GNU General Public License) welcomes anyone with interest to join in on future `PHOEBE` development. From a purely scientific code `PHOEBE` has grown into a fully grown, portable and reliable application; a lot of thought and effort has gone into organizing its structure to enable new developers to quickly pick up on the specifications and start concentrating on science rather than application programming interface (API). In this light three discussion mailing lists have been set up (`phoebe-announce`, `phoebe-discuss` and `phoebe-devel`), to facilitate interaction between users and developers. API documentation is strictly kept up to date and is publically available from `PHOEBE`'s homepage. There has been continuous expressed interest by several individuals to join `PHOEBE` development already, some of them (D. Terrell, M. Bauer, G. Matijevič) have already taken part in it. Developing open-source code with fellow scientists is very rewarding both from a scientific point of view (more people get more work done) and a social point of view (just imagine the fun and the number of internal jokes we share at EB conferences!). Sounds attractive? Join us in making `PHOEBE` better and better!

10 Wrapping it up

As we have shown throughout this work, eclipsing binary stars are renowned for their typical geometrical layout and well-understood underlying physics, enabling us to build and use numerical models to accurately determine values of various physical parameters. Solving the inverse problem for detached eclipsing binaries has become an indispensable tool for obtaining absolute dimensions of individual stars (their masses, radii, temperatures and luminosities). The impact of this fact is very broad and powerful: eclipsing binaries are used to establish color calibrations (see Popper (1980); Harmanec (1988); Flower (1996); Popper (1998)), evolutionary properties based on exact coevality of both components (Ribas et al., 2000; Lastennet and Valls-Gabaud, 2002), accurate distances (Paczynski (1997)) and relations between M-L-R-T quantities for different spectral types and luminosity classes (Gorda and Svechnikov, 1998; Malkov, 2003). It is thus very important to study eclipsing binaries thoroughly and to apply the model responsibly and as objectively as possible, otherwise it is likely that systematic errors may creep in and mislead any theoretical models built on those results. We tried to demonstrate that `PHOEBE`, the newly developed modeling package based on Wilson and Devinney (1971) code, aims to be scientifically undisputable, extensive, general and efficient; feedback from many people from various institutions indicates that we are on the right track. Yet a lot of work is still to be done and there is only one sentence that comes to mind, based on all the fun we had so far: "Bring it on!"

References

Abt, H. A.: 1983, *Ann. Rev. Astron. Astroph.* **21**, 343

Aerts, C. and Kolenberg, K.: 2005, *Astron. Astrophys.* **431**, 615

Aerts, C., Prša, A., Harmanec, P., and Yakut, K.: 2005, *Astron. Astrophys.* p. in print

Aho, A. V. and Ullman, J. D.: 1977, *Principles of Compiler Design*, Addison-Wesley, Reading, MA

Alencar, S. H. P. and Vaz, L. P. R.: 1997, *Astron. Astrophys.* **326**, 257

Alencar, S. H. P., Vaz, L. P. R., and Nordlund, Å.: 1999, *Astron. Astrophys.* **346**, 556

Alonso, R., Brown, T. M., Torres, G., Latham, D. W., Sozzetti, A., Mandushev, G., Belmonte, J. A., Charbonneau, D., Deeg, H. J., Dunham, E. W., O'Donovan, F. T., and Stefanik, R. P.: 2004, *Astrophys. J., Lett.* **613**, L153

Avery, P.: 1991, *Applied Fitting Theory I: General Least Squares Theory*, University of Florida

Bertone, E., Buzzoni, A., Chávez, M., and Rodríguez-Merino, L. H.: 2004, *Astron. J.* **128**, 829

Bessell, M. S.: 1990, *Publ. Astron. Soc. Pac.* **102**, 1181

Brent, R. P.: 1973, *Algorithms for Minimization without Derivatives*, Prentice-Hall, Englewood Cliffs, NJ

Briquet, M., Aerts, C., Lüftinger, T., De Cat, P., Piskunov, N. E., and Scuflaire, R.: 2004, *Astron. Astrophys.* **413**, 273

Bruls, J. H. M. J., Schüssler, M., and Solanki, S. K.: 1999, in *ASP Conf. Ser. 158: Solar and Stellar Activity: Similarities and Differences*, pp 182–+

Bryja, C. and Sandtorf, J. R.: 1999, *American Astronomical Society Meeting Abstracts* **194**,

Byrne, P. B.: 1996, in *IAU Symp. 176: Stellar Surface Structure*, pp 299–+

Caldwell, J. A. R., Cousins, A. W. J., Ahlers, C. C., van Wamelen, P., and Maritz, E. J.: 1993, *South African Astronomical Observatory Circular* **15**, 1

Cardelli, J. A., Clayton, G. C., and Mathis, J. S.: 1989, *Astrophys. J.* **345**, 245

Carroll, B. W. and Ostlie, D. A.: 1995, *An Introduction to Modern Astrophysics*, Vol. 2005, Addison-Wesley Publishing Company

Chandrasekhar, S.: 1933, *Mon. Not. R. Astron. Soc.* **93**, 462

Chen, M.-H., Shao, Q.-M., and Ibrahim, J. G.: 2000, *Monte Carlo Methods in Bayesian Computation*, Vol. ISBN 0-387-98935-8, Springer-Verlag

Claret, A.: 1999, in *ASP Conf. Ser. 173: Stellar Structure: Theory and Test of Connective Energy Transport*, pp 277–+

Claret, A.: 2000a, *VizieR Online Data Catalog* **336**, 31081

Claret, A.: 2000b, *Astron. Astrophys.* **359**, 289

Cousins, A. W. J.: 1976, *Mem. R. Astron. Soc.* **81**, 25

Cox, A. N.: 2000, *Allen's astrophysical quantities*, Allen's astrophysical quantities, 4th ed. Publisher: New York: AIP Press; Springer, 2000. Editedy by Arthur N. Cox. ISBN: 0387987460

Dallaporta, S., Tomov, T., Zwitter, T., and Munari, U.: 2002, *Informational Bulletin on Variable Stars* **5312**, 1

De Cat, P. and Aerts, C.: 2002, *Astron. Astrophys.* **393**, 965

De Cat, P., Aerts, C., De Ridder, J., Kolenberg, K., Meeus, G., and Decin, L.: 2000, *Astron. Astrophys.* **355**, 1015

Deutsch, A.: 1958, in *IAU Symp. 6: Electromagnetic Phenomena in Cosmological Physics*, pp 209–+

Diaz-Cordoves, J. and Gimenez, A.: 1992, *Astron. Astrophys.* **259**, 227

Djurasevic, G.: 1992, *Astrophys. Space. Sci.* **197**, 17

Drechsel, H., Weeber, M., Lorenz, R., and Hadrava, P.: 1997, in *Astronomische Gesellschaft Abstract Series*, pp 207–+

Eastman Kodak Company: 2000, *KAF-16801E 4096 (H) × 4096 (V) Pixel Performance Specification*, Technical report, Image Sensor Solutions, Rochester, New York 14650-2010

ESA SP-402: 1997, *VizieR Online Data Catalog* **1239**, 0

Etzel, P. B.: 1981, in *Photometric and Spectroscopic Binary Systems*, pp 111–

Euler, L.: 1755, *Institutiones Calculi Differentialis*, Mémoires de l'académie de sciences de Berlin

Eyer, L. and Grenon, M.: 1997, in *ESA SP-402: Hipparcos - Venice '97*, pp 467–472

Fletcher, R. and Reeves, C.: 1964, *Computer J.* 149

Flower, P. J.: 1996, *Astrophys. J.* **469**, 355

Forbes, M. C., Dodd, R. J., and Sullivan, D. J.: 1996, *Baltic Astronomy* **5**, 281

Frederik, M. C. and Etzel, P. B.: 1996, *Astron. J.* **111**, 2081

Galassi, M., Davies, J., Theiler, J., Gough, B., Jungman, G., Booth, M., and Rossi, F.: 2003, *GNU Scientific Library Reference Manual - Second Edition*, Network Theory Ltd.

Galičič, M.: 1999, *Ph.D. thesis*, University of Ljubljana, Dept. of Physics

Giménez, Á., Claret, A., and Cunha, N. C. S.: 1998, in *ASP Conf. Ser. 154: Cool Stars, Stellar Systems, and the Sun*, pp 2115–2117

Gorda, S. Y. and Svechnikov, M. A.: 1998, *Astronomy Reports* **42**, 793

Gray, D. F.: 1992, *The Observation and Analysis of Stellar Photospheres*, Cambridge UP, 2nd edition

Guinan, E. F., Ribas, I., and Fitzpatrick, E. L.: 2004, in *ASP Conf. Ser. 310: IAU Colloq. 193: Variable Stars in the Local Group*, pp 363–

Gustafsson, B.: 1983, *Mitteilungen der Astronomischen Gesellschaft Hamburg* **60**, 139

Hadrava, P.: 1990, *Contrib. Astron. Obs. Skalnaté Pleso* **20**, 23

Halbwachs, J. L. and Arenou, F.: 1999, *Baltic Astronomy* **8**, 301

Harmanec, P.: 1988, *Bulletin of the Astronomical Institutes of Czechoslovakia* **39**, 329

Hauschildt, P. H., Allard, F., and Baron, E.: 1999, *Astrophys. J.* **512**, 377

Hawkins, N. C., Samec, R. G., van Hamme, W., and Faulkner, D. R.: 2005, *Informational Bulletin on Variable Stars* **5612**, 1

Henden, A. and Munari, U.: 2000, *Astron. Astrophys. Suppl. Ser.* **143**, 343

Henden, A. A.: 2003, in *ASP Conf. Ser. 298: GAIA Spectroscopy: Science and Technology*, pp 365–+

Henden, A. A. and Honeycutt, R. K.: 1997, *Publ. Astron. Soc. Pac.* **109**, 441

Hilditch, R. W.: 2001, *An Introduction to Close Binary Stars*, Cambridge University Press, 392 pp.

Hilditch, R. W., Harries, T. J., and Hill, G.: 1996, *Mon. Not. R. Astron. Soc.* **279**, 1380

Hill, G. and Rucinski, S.: 1993, in E. F. Milone (ed.), *Modeling and Analysis of Eclipsing Binary Observations*, Vol. 135

Hubeny, I., Mihalas, D., and Werner, K. (eds.): 2003, *Stellar Atmosphere Modeling*

Ingber, L.: 1989, *Mathematical Computer Modelling* **12(8)**, 967

Ingber, L.: 1996, *Control and Cybernetics* **25(1)**, 33

Irwin, J. B.: 1947, *Astrophys. J.* **106**, 380

Johnson, H. L.: 1965, *Astrophys. J.* **141**, 923

Johnston, K.: 2000, in *IAU Colloq. 180: Towards Models and Constants for Sub-Microarcsecond Astrometry*, pp 392–+

Kõvári, Z. and Weber, M.: 2004, *Publications of the Astronomy Deparment of the Eotvos Lorand University* **14**, 221

Kallrath, J. and Kaemper, B.-C.: 1992, *Astron. Astrophys.* **265**, 613

Kallrath, J. and Linnell, A. P.: 1987, *Astrophys. J.* **313**, 346

Kallrath, J. and Milone, E. F.: 1999, *Eclipsing Binary Stars - Modeling and Analysis*, Springer Verlag, 355 pp.

Kallrath, J., Milone, E. F., Terrell, D., and Young, A. T.: 1998, *Astrophys. J.* **508**, 308

Kallrath, J. and Strassmeier, K. G.: 2000a, *VizieR Online Data Catalog* **336**, 20673

Kallrath, J. and Strassmeier, K. G.: 2000b, *Astron. Astrophys.* **362**, 673

Kazarovets, A. V., Samus, N. N., Durlevich, O. V., Frolov, M. S., Antipin, S. V., Kireeva, N. N., and Pastukhova, E. N.: 1999, *Informational Bulletin on Variable Stars* **4659**, 1

Kippenhahn, R.: 1977, *Astron. Astrophys.* **58**, 267

Klinglesmith, D. A. and Sobieski, S.: 1970, *Astron. J.* **75**, 175

Kopal, Z.: 1951, *Popular Astronomy* **59**, 395

Kopal, Z.: 1959, *Close Binary Systems*, Chapman & Hall, London

Kreiner, J. M., Kim, C.-H., and Nha, I.-S.: 2001, *An Atlas of O-C Diagrams of Eclipsing Binary Stars*, An Atlas of O-C Diagrams of Eclipsing Binary Stars / by Jerzy M. Kreiner, Chun-Hwey Kim, Il-Seong Nha. Cracow, Poland: Wydawnictwo Naukowe Akademii Pedagogicznej. 2001.

Kurucz, R. L.: 1970, *SAO Special Report* 309

Kurucz, R. L.: 1993, *VizieR Online Data Catalog* **6039**, 0

Kurucz, R. L.: 1996, in *ASP Conf. Ser. 108: M.A.S.S., Model Atmospheres and Spectrum Synthesis*, pp 160–+

Kwee, K. K. and van Woerden, H.: 1956, *Bull. Astron. Inst. Ned.* **12**, 327

Landi degl'Innocenti, E., Landi degl'Innocenti, M., and Landolfi, M.: 1988, *Astron. Astrophys.* **204**, 133

Landolt, A. U.: 1992, *Astron. J.* **104**, 340

Lapasset, E., Gomez, M., and Farinas, R.: 1996, *Publ. Astron. Soc. Pac.* **108**, 332

Lastennet, E. and Valls-Gabaud, D.: 2002, *Astron. Astrophys.* **396**, 551

Latham, D. W., Mazeh, T., Stefanik, H. P., Davis, R. J., Carney, B. W., Torres, G., and Laird, J. B.: 1992, in *ASP Conf. Ser. 32: IAU Colloq. 135: Complementary Approaches to Double and Multiple Star Research*, pp 158–161

Latham, D. W., Stefanik, R. P., Mazeh, T., Mayor, M., and Burki, G.: 1989, *Nature* **339**, 38

Levenberg, K.: 1944, *Quarterly of Applied Math.* pp 164–168

Limber, D. N.: 1963, *Astrophys. J.* **138**, 1112

Lucy, L. B.: 1967, *Zeitschrift fur Astrophysics* **65**, 89

Malkov, O. Y.: 2003, *Astron. Astrophys.* **402**, 1055

Marquardt, D.: 1963, *SIAM J. Appl. Math.* **11**, 431

Marrese, P. M., Boschi, F., and Munari, U.: 2003, *Astron. Astrophys.* **406**, 995

Marrese, P. M., Munari, U., Siviero, A., Milone, E. F., Zwitter, T., Tomov, T., Boschi, F., and Boeche, C.: 2004a, *Astron. Astrophys.* **413**, 635

Marrese, P. M., Munari, U., Sordo, R., Siviero, A., and Dallaporta, S.: 2004b, in *ASP Conf. Ser. 318: Spectroscopically and Spatially Resolving the Components of the Close Binary Stars*, pp 178–181

Martin, C., Mignard, F., Hartkopf, W. I., and McAlister, H. A.: 1998, *Astron. Astrophys. Suppl. Ser.* **133**, 149

Mathieu, R. D.: 1994, *Ann. Rev. Astron. Astroph.* **32**, 465

Metropolis, N., Rosenbluth, A. W., Rosenbluth, M. N., Teller, A. H., and Teller, E.: 1953, *J. Chem. Phys.* **21**, 1087

Milone, E. F., Munari, U., Marrese, P. M., Williams, M. D., Zwitter, T., Kallrath, J., and Tomov, T.: 2005, *Astron. Astrophys.* **441**, 605

Milone, E. F., Stagg, C. R., and Kurucz, R. L.: 1992, *Astrophys. J., Suppl. Ser.* **79**, 123

Morgan, W. W., Keenan, P. C., and Kellman, E.: 1943, *An atlas of stellar spectra, with an outline of spectral classification*, Chicago, Ill., The University of Chicago press [1943]

Morgenroth, O.: 1935, *Astronomische Nachrichten* **255**, 425

Moro, D. and Munari, U.: 2000, *Astron. Astrophys. Suppl. Ser.* **147**, 361

Munari, U., Castelli, and F.: 2004a, *VizieR Online Data Catalog* **3238**, 0

Munari, U.: 1999, *Baltic Astronomy* **8**, 73

Munari, U., Dallaporta, S., Siviero, A., Soubiran, C., Fiorucci, M., and Girard, P.: 2004b, *Astron. Astrophys.* **418**, L31

Munari, U. and Tomasella, L.: 1999, *Astron. Astrophys. Suppl. Ser.* **137**, 521

Munari, U., Tomov, T., Zwitter, T., Milone, E. F., Kallrath, J., Marrese, P. M., Boschi, F., Prša, A., Tomasella, L., and Moro, D.: 2001, *Astron. Astrophys.* **378**, 477

Murphy, T. and Meiksin, A.: 2004, *Mon. Not. R. Astron. Soc.* **351**, 1430

Nautical Almanac: 2005, *The Nautical Almanac for the year 2006*, The Nautical Almanac for the year 2006, Her Majesty's Nautical Almanac Office. London: The Stationary Office, 2005

Nelder, J. A. and Mead, R.: 1965, *Computer Journal* **7**, 308

O'Connell, D. J. K.: 1951, *Publications of the Riverview College Observatory* **2**, 85

Olson, E. C. and Etzel, P. B.: 1994, *Astron. J.* **108**, 262

Paczynski, B.: 1997, in *The Extragalactic Distance Scale*, pp 273–280

Pakštiene, E. and Solheim, J.-E.: 2003, *Baltic Astronomy* **12**, 221

Penndorf, R.: 1957, *Journal of the Optical Society of America* **47**, 176

Perryman, M. A. C., de Boer, K. S., Gilmore, G., Høg, E., Lattanzi, M. G., Lindegren, L., Luri, X., Mignard, F., Pace, O., and de Zeeuw, P. T.: 2001, *Astron. Astrophys.* **369**, 339

Pfeiffer, R. J. and Stickland, D. J.: 2004, *The Observatory* **124**, 117

Pickering, E. C. and Fleming, W. P.: 1895, *Astrophys. J.* **2**, 320

Pigulski, A. and Michalska, G.: 2002, *Informational Bulletin on Variable Stars* **5218**, 1

Pinfield, D. J., Dobbie, P. D., Jameson, R. F., Steele, I. A., Jones, H. R. A., and Katsiyannis, A. C.: 2003, *Mon. Not. R. Astron. Soc.* **342**, 1241

Pinfield, D. J., Jones, H. R. A., and Steele, I. A.: 2005, *Publ. Astron. Soc. Pac.* **117**, 173

Piskunov, N. E. and Wehlau, W. H.: 1990, *Astron. Astrophys.* **233**, 497

Polak, E. and Ribiere, G.: 1969, *Revue Francaise d'Informatique et de Recherche Operationnelle* **3**, 35

Pols, O. R., Tout, C. A., Eggleton, P. P., and Han, Z.: 1995, *Mon. Not. R. Astron. Soc.* **274**, 964

Popper, D. M.: 1980, *Ann. Rev. Astron. Astroph.* **18**, 115

Popper, D. M.: 1997, *Astron. J.* **114**, 1195

Popper, D. M.: 1998, *Publ. Astron. Soc. Pac.* **110**, 919

Pourbaix, D.: 2002, *Astron. Astrophys.* **385**, 686

Press, W. H., Flannery, B. P., Teukolsky, S. A., and Vetterling, W. T.: 1986, *Numerical Recipes: The Art of Scientific Computing*, Cambridge University Press, Cambridge (UK) and New York, 1st edition

Prša, A.: 2003, in *ASP Conf. Ser. 298: GAIA Spectroscopy: Science and Technology*, pp 457–+

Prša, A.: 2004, *Extraction and Analysis Algorithms*, Technical report, University of Ljubljana, Dept. of Astrophysics

Prša, A. and Zwitter, T.: 2005a, *Astrophys. J.* **628**, 426

Prša, A. and Zwitter, T.: 2005b, *Astrophys. Space. Sci.* **296**, 315

Prša, A. and Zwitter, T.: 2005, in *ESA SP-576: The Three-Dimensional Universe with Gaia*, pp 611–+

Rafert, J. B. and Twigg, L. W.: 1980, *Mon. Not. R. Astron. Soc.* **193**, 79

Ribas, I., Jordi, C., and Giménez, Á.: 2000, in *NATO ASIC Proc. 544: Variable Stars as Essential Astrophysical Tools*, pp 659–+

Ribas, I., Jordi, C., Vilardell, F., Giménez, Á., and Guinan, E. F.: 2004, *New Astronomy Review* **48**, 755

Rice, J. B. and Wehlau, W. H.: 1990, *Astron. Astrophys.* **233**, 503

Richmond, M. W., Droege, T. F., Gombert, G., Gutzwiller, M., Henden, A. A., Albertson, C., Beser, N., Molhant, N., and Johnson, H.: 2000, *VizieR Online Data Catalog* **2230**, 0

Roche, E.: 1849, *La Figure d'une Masse Fluide - Soumise á l'Attraction d'un Point Éloigné (Premiere Partie)*, Academie des Sciences et Lettres de Montpellier, 1847–1850

Rossiter, R. A.: 1924, *Astrophys. J.* **60**, 15

Sbordone, L., Bonifacio, P., Castelli, F., and Kurucz, R. L.: 2004, *Memorie della Societa Astronomica Italiana Supplement* **5**, 93

Schüssler, M. and Solanki, S. K.: 1992, *Astron. Astrophys.* **264**, L13

Shakhovskoi, N. M.: 1965, *Soviet Astronomy* **8**, 833

Siviero, A., Munari, U., Sordo, R., and Marrese, P. M.: 2004, in *ASP Conf. Ser. 318: Spectroscopically and Spatially Resolving the Components of the Close Binary Stars*, pp 182–185

Smart, W. M.: 1977, *Textbook on Spherical Astronomy*, Cambridge University Press, 6th Edition, 446 pp.

Snyder, L. F.: 1998, *Informational Bulletin on Variable Stars* **4624**, 1

Stellingwerf, R. F.: 1978, *Astrophys. J.* **224**, 953

Sterne, T. E.: 1939, *Mon. Not. R. Astron. Soc.* **99**, 451

Strassmeier, K. G.: 1996, in *IAU Symp. 176: Stellar Surface Structure*, pp 289–+

Taam, R. E. and Sandquist, E. L.: 2000, *Ann. Rev. Astron. Astroph.* **38**, 113

Taff, L. G.: 1985, *Celestial Mechanics: A Computational Guide for the Practitioner*, John Wiley & Sons

Terrell, D., Munari, U., Zwitter, T., and Nelson, R. H.: 2003, *Astron. J.* **126**, 2988

Tinbergen, J.: 1996, *Astronomical polarimetry*, Cambridge, New York: Cambridge University Press, —c1996, ISBN 0521475317

Tody, D.: 1986, in *Instrumentation in astronomy VI; Proceedings of the Meeting, Tucson, AZ, Mar. 4-8, 1986. Part 2 (A87-36376 15-35). Bellingham, WA, Society of Photo-Optical Instrumentation Engineers, 1986, p. 733.*, pp 733–+

Tohline, J. E.: 2002, *Ann. Rev. Astron. Astroph.* **40**, 349

van Hamme, W.: 1993, *Astron. J.* **106**, 2096

van Hamme, W. and Wilson, R. E.: 1986, *Astron. J.* **92**, 1168

van Hamme, W. and Wilson, R. E.: 2003, in *ASP Conf. Ser. 298: GAIA Spectroscopy: Science and Technology*, pp 323–+

Vaz, L. P. R.: 1985, *Astrophys. Space. Sci.* **113**, 349

Verbunt, F.: 1993, *Ann. Rev. Astron. Astroph.* **31**, 93

Vincent, A., Piskunov, N. E., and Tuominen, I.: 1993, *Astron. Astrophys.* **278**, 523

Vogt, S. S. and Penrod, G. D.: 1983, *Publ. Astron. Soc. Pac.* **95**, 565

Vogt, S. S., Penrod, G. D., and Hatzes, A. P.: 1987, *Astrophys. J.* **321**, 496

von Zeipel, H.: 1924, *Mon. Not. R. Astron. Soc.* **84**, 665

Waelkens, C., Aerts, C., Kestens, E., Grenon, M., and Eyer, L.: 1998, *Astron. Astrophys.* **330**, 215

Warner, B.: 2003, *Cataclysmic Variable Stars*, Cataclysmic Variable Stars, by Brian Warner, pp. 592. ISBN 052154209X. Cambridge, UK: Cambridge University Press, September 2003.

Weiss, W. W., Aerts, C., Aigrain, S., Alecian, G., Antonello, E., Baglin, A., Bazot, M., Collier-Cameron, A., Charpinet, S., Gamarova, A., Handler, G., Hatzes, A., Hubert, A.-M., Lammer, H., Lebzelter, T., Maceroni, C., Marconi, M., de Martino, D., Janot-Pacheco, E., Pagano, I., Paunzen, E., Pinheiro, F. J. G., Poretti, E., Ribas, I., Ripepi, V., Roques, F., Silvotti, R., Surdej, J., Vauclair, G., Vauclair, S., and Zwintz, K.: 2004, in *ESA SP-538: Stellar Structure and Habitable Planet Finding*, pp 435–444

Wilson, R. E.: 1979, *Astrophys. J.* **234**, 1054

Wilson, R. E.: 1990, *Astrophys. J.* **356**, 613

Wilson, R. E.: 1993, in *ASP Conf. Ser. 38: New Frontiers in Binary Star Research*, pp 91–+

Wilson, R. E.: 1998, *Computing binary star observables*

Wilson, R. E. and Biermann, P.: 1976, *Astron. Astrophys.* **48**, 349

Wilson, R. E. and Devinney, E. J.: 1971, *Astrophys. J.* **166**, 605

Wilson, R. E. and Liou, J.-C.: 1993, *Astrophys. J.* **413**, 670

Wilson, R. E. and Van Hamme, W.: 2003, *Computing Binary Star Observables*, Astronomy Dept., University of Florida, Gainesville, FL 32611

Wunder, E.: 1995, *Informational Bulletin on Variable Stars* **4179**, 1

Wyse, A. B. and Kron, G. E.: 1939, *Lick Observatory Bulletin* **19**, 17

Zucker, S. and Mazeh, T.: 1994, *Astrophys. J.* **420**, 806

Zwitter, T.: 2003, in *ASP Conf. Ser. 298: GAIA Spectroscopy: Science and Technology*, pp 329–+

Zwitter, T., Castelli, F., and Munari, U.: 2004, *Astron. Astrophys.* **417**, 1055

Zwitter, T., Munari, U., Marrese, P. M., Prša, A., Milone, E. F., Boschi, F., Tomov, T., and Siviero, A.: 2003, *Astron. Astrophys.* **404**, 333

A Mathematical symbols used in the book

ϱ	...	Radius-vector in units of a
θ	...	Stellar co-latitude
ϕ	...	Stellar longitude
$\Delta\theta$	...	Surface element width in co-latitude
$\Delta\phi$	...	Surface element width in longitude
λ	...	Direction cosine, $\lambda = \sin\theta\sin\phi$
μ	...	Direction cosine, $\lambda = \sin\theta\cos\phi$
ν	...	Direction cosine, $\lambda = \cos\theta$
Φ	...	Orbital phase
I_λ	...	Normal emergent intensity
$\mathcal{L}$	...	Limb darkening correction
$\mathcal{G}$	...	Gravity darkening correction
$\mathcal{R}$	...	Reflection correction
Ω	...	Kopal's Surface potential
Ω	...	Longitude of ascending node
Ω	...	Solid angle
β	...	Gravity darkening coefficient
γ	...	Angle between the surface element normal and radius vector
δ	...	Instantaneous separation between star centers in units of a
ϵ	...	Angle between the equator and the ecliptic
ε	...	Orbital eccentricity
ζ	...	Physical-to-relative surface potential scaling factor
$\bar{\kappa}$	...	Rosseland opacity coefficient
φ	...	Angle between surface normal and the line-of-sight
ϖ	...	Relative temperature factor, $\varpi = (T - T_{\rm ll})/(T_{\rm ul} - T_{\rm ll})$
$\mathcal{T}$	...	passband (filter) transmission function
$\boldsymbol{\omega}$	...	angular velocity
ω	...	argument of periastron
$\mathcal{F}$	...	lobe filling factor

Index

air-mass, 5, 119, 124
anomaly
  eccentric, 33
  mean, 33, 34
  true, 32, 33, 36, 37
apsidal motion, 32, 34, 41
argument of periastron, 29–31, 36, 37, 64
ascending node, 29
  longitude, 29, 30

binary
  effective temperature, 106
  morphology, 25, 27, 66, 68

conjunction
  inferior, 35
  superior, 35, 36
curve
  CCD response, 5, 6
  Johnson B, 125
  passband transmission, 5, 6, 105, 122
  telescope responce, 5
curves
  light, 6, 7, 36–39, 53, 59, 60, 83, 86, 95, 96, 98, 101, 105, 107, 119, 120, 123, 125
  radial velocity, 12, 14, 64, 83, 86, 105, 107

descending node, 31
distance
  astrometric, 14
  to the binary, 4, 15, 119

eccentricity, 64
epoch
  critical, 36

flux
  bolometric, 5
  instrumental, 5
  irradiating, 56
  monocromatic, 46, 47
  passband, 47, 48
  Planck, 47

heliocentric Julian date, 6, 40–41
HJD0, 6, 41, 64

inclination, 4, 29–31, 37–39, 59, 60, 64, 79, 95, 96, 98–102
intensity
  normal emergent, 43, 45–48, 54–56
  passband, 73, 76

Kepler
  law, 22, 28
  problem, 32–40

limb darkening
  bolometric, 77

node
  ascending, 30
  descending, 31

observations
  astrometry, 14–16
  doppler tomography, 13–14
  photometry, 5–8
  polarimetry, 16–18
  radial velocities, 10–13
  spectroscopy, 8–10
orbital period, 4, 6, 28, 29, 33, 34, 41, 64
  change rate, 4, 64

phase
  conjunction, 37
  orbital, 34, 35, 37, 41, 72, 79, 169
  periastron, 36
phase shift, 41, 64

relation
    mass-luminosity, 3, 117, 157
    spectral type-magnitude, 106
    temperature-mass, 144
Roche, 19

scatter
    Gaussian, 105
    Poissonian, 105
star
    primary, 31, 35, 37–39, 56, 57, 59, 67, 79, 96, 101, 102
    secondary, 31, 35, 56, 57, 59, 67, 79, 102